

学位論文

Understanding Oscillation Phenomena  
Induced by Non-linear Magma Rheology

(非線形マグマレオロジーに起因する波動現象のメカニズム探究)

平成 27 年 12 月博士（理学）申請

東京大学大学院理学系研究科

地球惑星科学専攻

黒川 愛香



# Understanding Oscillation Phenomena Induced by Non-linear Magma Rheology

Aika Kurokawa

Department of Earth and Planetary Science

The University of Tokyo

A thesis submitted for the degree of

*Doctor of Philosophy*

February 13, 2016

## Acknowledgements

First of all, I appreciate Prof. Kei Kurita for providing me the interesting subjects for study and discussing willingly any time for five years. Dr. Mie Ichihara helped and supported me under many circumstances whenever I was faced difficulties. I am special grateful to them and never forget their kindness and their stances on research with a wide vision.

During my internship in France, I have spent a great time thanks to people there, especially Dr. Sebastien Manneville, Dr. Valerie Vidal, Dr. Thibaut Divoux, Dr. Mathiew Leomach, Dr. Thierry Biben, Ines Eymard, Franco Tapia, and Clotilde Peschet. I say a big thank-you to them.

The study of the 1986 Izu-Oshima eruption gave me priceless opportunities to discuss with many researchers who have worked on the eruption. Above all, Dr. Minoru Takeo gave treasurable data and fruitful advice. Dr. Yuichi Morita, Dr. Yoshiaki Ida, Dr. Toshitsugu Fujii, Dr. Hidefumi Watanabe also suggested important points of the study. The work was progressed thanks to valuable data provided by Dr. Koshun Yamaoka, Japan Meteorological Agency, and National Research Institute for Earth Science and Disaster Prevention.

Dr. Tomotaka Saruya, Dr. Rina Noguchi, Dr. Daigo Shoji, Mr. Yasuhiro Nishikawa, Mr. Rintaro Kamata, Ms. Akari Yoshida, Ms. Miki Okano, Mr. Masahiro Yoda, Mr. Yoshitaka Kon, Mr. Yo Kanno, Mr. Sato, Mr. Uchida, and secretaries at ERI have supported me in various ways. The members of thesis committee helped in improving this thesis. Especially, Dr. Ryosuke Ando gave fruitful advice to consider the mechanism of experimental results. I really thank all their supports.

Finally I would like to convey great thankfulness to my families and friends who have always supported me and cheered me up. I could have not written this thesis without their warm support.

*This work was supported by JSPS and CNRS under the Japan-France Research Cooperative Program (PRC CNRS/JSPS RheoVolc) and JSPS Kakenhi Grant No. 265204.*

# Abstract

Movement of magmatic fluid has been widely recognized as a key process to induce volcanic tremor and long-period (LP) event. Since these magma-driven oscillation phenomena often precede eruptions, they have drawn wide attentions in terms of prediction of volcanic eruption. Their models proposed until now mainly describe interactions between magma flowing and elasticity of volcanic system and/or bubbles on the assumption that magma flows in a simple way. However, magma in itself has complex non-linear rheology, which can cause self-induced oscillation related to rheological multiplicity. For that reason, this study aimed to explore possible link between magma-driven volcanic oscillations and non-linear magma rheology. In order to achieve the goal, two approaches were adopted. One is experimental study to understand underlying physics of flow instabilities in non-linear fluids, which have the rheological multiplicity. The other is analysis of volcanic tremors and LP events.

First, two fluctuation phenomena, which are pressure perturbation in the pipe flow and persistent stress fluctuation coupled to the local dynamics, were substantiated in the experiments. Although different mechanisms were proposed by linking to rheological properties, the important factor to generate the both phenomena is the multiplicity caused by aging. This common point suggests a relation between non-linear magma rheology and volcanic oscillation phenomena.

As another approach, analysis of volcanic tremors and LP events accompanied by the 1986 Izu-Oshima eruption was also performed for the purpose of understanding actual phenomena. The results demonstrated the apparent relation between temporal variations in eruption style and characteristics of LP events and tremors in terms of the waveform and the source location. Especially the temporal variation in volcanic oscillations below the summit is interpreted as indication of rheological change in magma inside the conduit with time.

Based on the results by the two approaches, finally a possible link between non-linear magma rheology caused by the change in crystal alignment and temporal shift in magma-driven volcanic oscillations at Izu-Oshima volcano was discussed. Although the proposed mechanism is an interpretation at the present stage, this study proposes the importance of aging in order to understand volcanic oscillation phenomena caused by non-linear magma rheology.

# Contents

<b>Contents</b>	<b>iii</b>
<b>List of Figures</b>	<b>vi</b>
<b>1 Introduction</b>	<b>1</b>
1.1 Volcanic Oscillation Phenomena Induced by Magma Movement . . . . .	1
1.1.1 Characteristics . . . . .	2
1.1.2 Proposed Generation Mechanism . . . . .	7
1.2 Magma Rheology . . . . .	12
1.2.1 What is Rheology? . . . . .	12
1.2.2 Magma as Non-linear Complex Fluid . . . . .	13
1.3 Multiplicity . . . . .	16
1.3.1 Multiplicity in Elastic Fluid . . . . .	17
1.3.2 Multiplicity in Gas-liquid System . . . . .	18
1.3.3 Multiplicity in Solid-liquid Magma . . . . .	23
1.4 Aim and Framework of This Thesis . . . . .	24
<b>2 Experimental Study 1: Undershoot of Pressure Difference</b>	<b>26</b>
2.1 Overview . . . . .	26
2.2 Materials . . . . .	27
2.2.1 Microstructure . . . . .	27
2.2.2 Fundamental Rheology . . . . .	29
2.3 Experimental Setup . . . . .	31
2.4 Results . . . . .	33
2.4.1 Start-up Flow with Pump . . . . .	33
2.4.2 Start-up Flow without Pump . . . . .	37
2.4.3 Linking Rheology and Pipe Flow in Terms of Aging . . . . .	41
2.5 Interpretation and Consideration . . . . .	43
2.5.1 Characterization of LE and TR fluids . . . . .	44

2.5.2	Remaining Questions to the Next Step . . . . .	47
<b>3</b>	<b>Experimental Study 2: Shear-induced Stress Fluctuation</b>	<b>49</b>
3.1	Overview . . . . .	49
3.2	Materials . . . . .	49
3.2.1	Particle Interaction . . . . .	50
3.2.2	Microstructures . . . . .	52
3.3	Methods . . . . .	54
3.3.1	Experimental Instruments and Setup . . . . .	54
3.3.2	Experimental Protocol . . . . .	56
3.4	Results . . . . .	57
3.4.1	Fundamental Rheology . . . . .	57
3.4.2	Global Rheology and 1D Velocity Profiles . . . . .	58
3.4.3	Flow State Diagram . . . . .	61
3.4.4	Linking Global Rheology to Local Dynamics . . . . .	64
3.4.5	Local Scenario of Stress Fluctuation . . . . .	70
3.4.6	Local Scenario of Flow Curve . . . . .	72
3.4.7	Difference in Rate-control and Stress-control . . . . .	73
3.5	Interpretation and Consideration . . . . .	74
3.5.1	Common Characteristics of Stress Fluctuation . . . . .	74
3.5.2	How is Stress Fluctuation Induced? . . . . .	79
3.5.3	Implication for Oscillation Induced by Non-linear Magma Rheology . . . . .	82
<b>4</b>	<b>Analysis of Volcanic Oscillations Accompanied by 1986 Izu-Oshima Eruption</b>	<b>84</b>
4.1	Overview . . . . .	84
4.2	Sequence of 1986 Izu-Oshima Eruption . . . . .	85
4.3	Analytical Methods . . . . .	86
4.3.1	Data . . . . .	86
4.3.2	Estimation of Source Location . . . . .	87
4.4	Results and Consideration . . . . .	90
4.4.1	Volcanic Tremor in Active Eruption Stage . . . . .	90
4.4.2	LP Events and Volcanic Tremor in Terminal Stage . . . . .	102
4.4.3	Summary of Temporal Variation in Volcanic Oscillations . . . . .	112
<b>5</b>	<b>Discussion</b>	<b>114</b>
5.1	Difference in Aging Effect on the Two Fluctuations . . . . .	114
5.2	Understanding Mechanism of the Stress Fluctuation . . . . .	119

5.2.1	Link to the Multiplicity . . . . .	119
5.2.2	External Factors of the Stress Fluctuation . . . . .	120
5.2.3	Suggestion of Kinetic Model for the Stress Fluctuation . . . . .	122
5.3	Implication for Future Works . . . . .	125
5.3.1	Possible Link between Stress Fluctuation and LP Event . . . . .	125
5.3.2	Proposal of Rheological Measurements in Non-linear Magma . . . . .	126
<b>6</b>	<b>Conclusions</b>	<b>128</b>
	<b>Appendix</b>	<b>130</b>
	<b>Bibliography</b>	<b>141</b>



# List of Figures

1.1	Waveform examples observed at Redoubt Volcano [78]. (a) High-frequency volcano-tectonic earthquake, (b) mixed-frequency event, (c) LP event, and (d) volcanic tremor. . . . .	2
1.2	Ground velocities of UD component and the spectrograms for LP, VT and hybrid events, and tremor observed at Redoubt Volcano [16]. Warm colors define the dominant spectral amplitudes. . . . .	3
1.3	Time series of amplitude spectra at Montserrat showing evolution in characteristics of harmonic tremor during transitions to eruptions [53]. . . . .	4
1.4	Source location of tremor during the 1998 eruption on Piton de la Fournaise Volcano [7]. The source locations are divided into three plots with different colors depending on the periods. . . . .	6
1.5	Flow-induced model described by [54] (the picture in [56] is cited here). Incompressible viscous fluid flows in x-direction from bottom to top through a channel with imperfectly elastic walls. Two dynamical variables, $h(t)$ and $v(x, t)$ , are the channel thickness and the fluid flow speed, respectively. . . . .	8
1.6	Source geometry of fluid-filled model proposed by [15] (the picture in [58] is cited here). The gray zone indicates the place of application of the pressure transient that triggers resonance. . . . .	9
1.7	Bubble-coalescence conditions proposed by [101]. (a) Bubble layers rising freely coalesce in a larger bubble when hydrostatic pressure drops. (b) A bubble layer reaching a structural barrier is forced to coalesce and rises generating a hydrostatic pressure drop. . . . .	9
1.8	Illustration of proposed geyser model by [10] based on analysis of banded tremor at Etna. . . . .	10
1.9	Illustration of the model that describes mass and/or pressure transportation between two separated chambers as the source of LP events [90]. . . . .	11
1.10	Flow under shearing . . . . .	12
1.11	Classification of fluids . . . . .	13

1.12	Schematic image of effective shear viscosity $\mu_{eff}$ and yield stress $\tau_y$ vs crystal volume fraction of magma $\phi$ [105]. . . . .	14
1.13	Back-scattered electron image of quenched natural sample including plagioclase-chains [98]. The scale bar (white line) indicates 0.5 mm. . . . .	14
1.14	Shear banding . . . . .	15
1.15	Shear banding structure in eruption product [94] . . . . .	15
1.16	Time-dependent variations in viscosity derived from alkali olivine basalt from Matsuura district [50]. Thin black lines, thick gray lines, thick black lines, and thin gray lines represent rotation rate of 1, 2.5, 5, and 10 rpm. . . . .	16
1.17	Self-induced oscillations provided by the rheological (resp. or systemic) multiplicity in the relation between shear stress $\sigma$ (resp. pressure $P$ ) and shear rate $\dot{\gamma}$ (resp. flux $Q$ ). The figure in [74] is modified here. . . . .	17
1.18	A scheme of experimental geometry to induce spurt [74]. . . . .	17
1.19	Spectrum of pressure fluctuations [95]. The inset shows the temporal change of the normalized pressure with an optical microscope picture. . . . .	18
1.20	Graphic illustration of limit cycle of pressure-drop oscillation [55]. . . . .	19
1.21	Graphic illustrations of (a) occurrence regions and (b) typical waveform examples of ① density-wave oscillation and ② pressure-drop oscillation [55]. . . . .	20
1.22	Relation between pressure loss $\Delta p$ and flux $j_{in}$ of the gas-liquid system [35]. Comparison with the observed tilt step cycles is also indicated. . . . .	22
1.23	Graphic illustration of mechanism of tilt steps and caldera formation based on the pressure-drop oscillation model [35]. . . . .	22
1.24	Variations of flow field in multiplicity in the relation between shear stress $\sigma$ and shear rate $\dot{\gamma}$ in a suspension. . . . .	24
2.1	Structure of <i>p</i> -NIPAM aqueous suspension. . . . .	27
2.2	Analogy to magmatic system . . . . .	28
2.3	Images that show the size change of particle taken by a digital microscope (VHX-1000, Keyence Co., Ltd.). (a) Dried commercial particle in the air. (b)-(d) Time change of the particle 1-3 minutes after putting into the water, respectively. $r$ is the radius of the particle and red lines show the scale of 100 $\mu\text{m}$ . . . . .	29
2.4	Shear stress response $\sigma(t)$ at shear rate of $0.1 \text{ s}^{-1}$ . . . . .	30
2.5	Flow curve $\sigma$ vs $\dot{\gamma}$ after aging times (5 s–3 h). The data in (a) are taken before the start-up flow experiments and those in (b) are taken three weeks later. . . . .	30
2.6	Apparatus for start-up flow measurement. . . . .	32

2.7	(a) Temporal variations in the pressure difference for flow velocities of $1.3 \cdot 10^{-2} \text{ m}\cdot\text{s}^{-1}$ to $10.6 \cdot 10^{-2} \text{ m}\cdot\text{s}^{-1}$ . (b) Variations in the non-dimensional pressure difference with respect to the scaled time. Suspension concentration 1.0 gel wt.%; waiting 1 h. A rotary displacement pump (Hicera pump V series, Iwaki Co., Ltd.) is used for the flow velocity of $1.3 \cdot 10^{-2} \text{ m}\cdot\text{s}^{-1}$ ; a diaphragm pump (Liquiport, KNF Flodos AG) is used in the other three tests.	34
2.8	Pressure difference along the pipe $\Delta P$ and converted shear stress $\sigma$ vs. time $t$ and $\Gamma$ after different aging times of 5 s to 3 h. Suspension concentration 1.5 gel wt.%; mean flow velocity $2.6 \cdot 10^{-2} \text{ m}\cdot\text{s}^{-1}$ .	35
2.9	Pressure difference along the pipe $\Delta P$ and converted shear stress $\sigma$ vs. time $t$ and $\Gamma$ for configurations with (black line) and without (gray line) a chamber. Suspension concentration 1.5 gel wt.%; aging time 1 h; mean flow velocity $2.9 \cdot 10^{-2} \text{ m}\cdot\text{s}^{-1}$ .	36
2.10	Pressure differences at different sections along the pipe $\Delta P$ (top, middle, and bottom), and converted shear stress $\sigma$ vs. time $t$ and $\Gamma$ observed after different aging times of 5 s to 3 h. Suspension concentration, 1.5 gel wt.%; mean flow velocity $3.9 \cdot 10^{-3} \text{ m}\cdot\text{s}^{-1}$ .	38
2.11	Pressure profiles along the pipe for different aging times (5 s, 15 min, 30 min, 1 h, and 3 h from left to right). Measurements at each location are taken at 4 s intervals from 7 s to 125 s. Data measured at interval are shifted on the x-axis by 0.08 kPa from those of the previous interval.	38
2.12	Images and pressure changes recorded at different times. Suspension concentration 1.5 gel wt %; aging time 3 h.	40
2.13	The relation between the pressure gradient $\Delta P / \Delta z$ and the flow velocity $v$ for the aging time of 1 h and suspension concentration of 1.5 gel wt %. Gray area is the range of pressure difference estimated by two rheological measurements shown in Figure 2.5 while circles are results in start-up flow experiments. The left circle shows the result without using the pump.	42
2.14	Variation in the pressure difference $\Delta P$ with the aging time for mean velocity $3.9 \cdot 10^{-3} \text{ m}\cdot\text{s}^{-1}$ and suspension concentration 1.5 gel wt %. Blue dots are estimated by rheological data shown in Figure 2.5. Red squares are $\Delta P$ of the undershoots while green diamonds are $\Delta P$ in the steady state after the undershoot in the case without using the pump.	42
2.15	Models for the different behavior of fluid transport between aged and non-aged fluids.	44
2.16	Characterization of <b>LE</b> and <b>TR</b> by rheometer.	46

3.1	Example of interaction potential for 100 nm radius particles with a surface charge of 25 mV quoted from [80]. The thick line is the total potential, composed of the dispersion potential (dashed line) plus the electrostatic potential (thin line). . . . .	51
3.2	Illustration of layers in solution at the surface of a particle with reference to [80]. The Stern layer (double layer) and the electrostatic potential $\psi(r)$ (thick line) are indicated. . . . .	51
3.3	SEM images of (a) the commercial suspension (Ludox TM-40), and (b) the non-Brownian aggregates in the sample (the inset shows a typical aggregate of silica particles). (c)-(e) the microstructure at three different magnifications. The sample has been presheared for 2 min at $500 \text{ s}^{-1}$ , 10 minutes before being imaged. . . . .	53
3.4	Effect of shear history on the microstructure. The images show samples at rest, after a preshear of 2 min at $500 \text{ s}^{-1}$ and 10 min at $1000 \text{ s}^{-1}$ from the left. The scales are same with that of Fig. 3.3 (c). . . . .	53
3.5	Experimental system with reference to [77]. . . . .	55
3.6	(a) 1D-USV setup [77]. Ultrasonic pulses are incident on the stator with a given angle $\theta_0$ while $\theta$ is the incidence angle and $c_0$ , $c_p$ , and $c_w$ stand for the speed of sound in the sample, in Plexiglas, and in water, respectively. The inset shows the 1D transducer and the stator as seen above. (b) General view of 2D-USV setup [37]. . . . .	56
3.7	Elastic modulus $G'$ vs time $t$ after preshearing. Inset: same data set in semilogarithmic scales with viscous modulus $G''$ (red). . . . .	57
3.8	Flow curve $\sigma$ vs $\dot{\gamma}$ obtained by decreasing ( $\blacktriangledown$ ) and then increasing $\dot{\gamma}$ ( $\blacktriangle$ ). . .	58
3.9	(a) Shear stress response $\sigma(t)$ for different shear rates [color, $\dot{\gamma}$ ( $\text{s}^{-1}$ ): [ $\color{red}{-}$ , 100]; [ $\color{green}{-}$ , 150]; [ $\color{blue}{-}$ , 200]; [ $\color{purple}{-}$ , 250]. (b)-(e) Velocity profile $v(r)$ across the gap, where $r$ is the distance to the rotor at different times [symbol, time (s)]: [ $\circ$ , 200]; [ $\square$ , 400]; [ $\triangle$ , 800]; [ $\nabla$ , 1400]. Each color corresponds to each applied shear rate in (a). The rotor velocity corresponds to the upper bound of the vertical axis. The sample is left to age during $t_w = 60$ min before each experiment. . .	59
3.10	Excerpt data at shear rate $150 \text{ s}^{-1}$ and $t_w = 60$ min from Fig. 3.9. Shear stress response $\sigma(t)$ with velocity profiles $v(r)$ at different times are shown. .	60
3.11	(a) Shear stress response $\sigma(t)$ for different aging times $t_w$ [color, $t_w$ (min)]: [ $\color{red}{-}$ , 100]; [ $\color{green}{-}$ , 30]; [ $\color{blue}{-}$ , 5]; [ $\color{purple}{-}$ , 1]. Experiments performed at $\dot{\gamma} = 100 \text{ s}^{-1}$ . (b)-(e) Velocity profile at different times [symbol, time (s)]: [ $\circ$ , 30]; [ $\square$ , 400]; [ $\triangle$ , 800]; [ $\nabla$ , 1100]. Each color corresponds to each value of $t_w$ in (a). The rotor velocity corresponds to the upper bound of the vertical axis. . . . .	61

3.12 Flow state diagram in the (sample age  $t_w$ , applied shear rate  $\dot{\gamma}$ ) plane. In steady state, the sample may either be fully fluidized ( $\blacklozenge$ ) or display shear banding. Steady shear banding is represented in ( $\bullet$ ). Unsteady banding, which denotes flows where the band width and the slip velocity display significant fluctuations, is represented by ( $\blacklozenge$ ). . . . . 62

3.13 Numerous examples of the three types, full fluidization, unsteady shear banding, and steady shear banding indicated as  $\blacklozenge$ ,  $\blacklozenge$ ,  $\bullet$  in the flow state diagram (Fig. 3.12), respectively. The insets show each applied shear rate and waiting time. . . . . 63

3.14 Full fluidization observed for  $\dot{\gamma} = 150 \text{ s}^{-1}$  and  $t_w = 30 \text{ min}$ . (a) Shear stress  $\sigma$  and slip velocity  $v_s$  vs time. (b) Width  $\delta$  of the fluidized shear band normalized by the gap width  $e$  vs time. (c) Local shear rate within the shear band vs time. The horizontal dotted line indicates the global shear rate applied and measured by the rheometer. In (a)-(c), the vertical dashed line indicates the fluidization time while the blue lines show the peak times. . . . . 65

3.15 Unsteady shear banding observed for  $\dot{\gamma} = 50 \text{ s}^{-1}$  and  $t_w = 30 \text{ min}$ . (a) Shear stress  $\sigma$  and slip velocity  $v_s$  vs time. (b) Width  $\delta$  of the fluidized shear band normalized by the gap width  $e$  vs time. (c) Local shear rate within the shear band vs time. The horizontal dotted line indicates the global shear rate applied and measured by the rheometer. . . . . 66

3.16 Temporal change in velocity profile in the cases of full fluidization ( $\dot{\gamma} = 150 \text{ s}^{-1}$ ,  $t_w = 30 \text{ min}$  in Fig. 3.14) and unsteady shear banding ( $\dot{\gamma} = 50 \text{ s}^{-1}$ ,  $t_w = 30 \text{ min}$  in Fig. 3.15). The color variation from white to black indicates the elapsed time of the experiment. The velocity data are plotted at 5 s intervals. 68

3.17 Comparison between global rheology and local dynamics at  $\dot{\gamma} = 50 \text{ s}^{-1}$  and  $t_w = 30 \text{ min}$  during measurement time of  $2150 \text{ s} < t < 2730 \text{ s}$  (*ref.* Fig. 3.15). 69

3.18 (a) Stress  $\sigma$  vs time  $t$  during a single stress fluctuation ( $\dot{\gamma} = 180 \text{ s}^{-1}$ ,  $t_w = 1 \text{ min}$ ). (b) Spatiotemporal diagram of the velocity  $v(r_0, z, t)$  as a function of the vertical position  $z$  and  $t$  at  $r_0 = 0.7 \text{ mm}$  obtained with 2D-USV. The fluid velocity is color coded in  $\text{mm}\cdot\text{s}^{-1}$ . . . . . 71

3.19 (a) Stress  $\sigma$  vs time  $t$  during a single stress fluctuation ( $\dot{\gamma} = 200 \text{ s}^{-1}$ ,  $t_w = 1 \text{ min}$ ). (b) Spatiotemporal diagram of the velocity  $v(r_0, z, t)$  as a function of the vertical position  $z$  and  $t$  at  $r_0 = 0.7 \text{ mm}$  obtained with 2D-USV. The fluid velocity is color coded in  $\text{mm}\cdot\text{s}^{-1}$ . . . . . 71

3.20	Local dynamics of flow curves. (a) Shear rate $\dot{\gamma}$ and shear stress $\sigma$ vs time $t$ . (b) Width of shear banding at $z_0 \simeq 15$ mm vs time. (c) Spatiotemporal diagram of the velocity data $v(r_0, z, t)$ as a function of the vertical position $z$ and $t$ , at $r_0 = 0.5$ mm. The fluid velocity is color-coded in $\text{mm}\cdot\text{s}^{-1}$ . . . . .	73
3.21	Flow curve $\sigma$ vs $\dot{\gamma}$ obtained by decreasing ( $\blacktriangledown$ , $\blacktriangleright$ ) and then increasing $\dot{\gamma}$ or $\sigma$ ( $\blacktriangle$ , $\blacktriangleleft$ ). Black (resp. red) data indicate results of shear-rate (resp. shear-stress) controlled test. . . . .	74
3.22	Relation between times when the width of shear banding achieves the peak, $t_{\delta_{peak}}$ and when the stress reaches the peak, $t_{\sigma_{peak}}$ during experiments for the cases of observing fluctuations by both the rheometer and the 1D-USV. The line length represents the error. . . . .	75
3.23	Variable definition in fluctuation . . . . .	76
3.24	(a) Amount of stress drop $\Delta\sigma$ vs non-dimensional preparing time $t_p^n$ (b) Duration time of stress drop $t_d$ vs $t_p^n$ for all cases of stress fluctuations. . . . .	77
3.25	Peak stress $\sigma_p$ vs amount of stress drop $\Delta\sigma$ for all cases of stress fluctuations. . . . .	78
3.26	Flow curve, shear stress $\sigma$ vs. applied shear rate $\dot{\gamma}$ shown in Fig. 3.8 superimposed results of the stress fluctuations. As for the blue dots, stresses, at with the stress drops occur are measured by the rheometer while shear rates are local shear rates in the shear-banded part estimated by USV data. The dot size depends on the errors. . . . .	78
3.27	Graphic illustration of proposed mechanism of the stress fluctuation. The red lines show velocity profiles. . . . .	80
3.28	Images of rearrangement and fracturing processes of aggregated particles taken by a microscope (Wild Makroskop Mk20, Heerbrugg Co., Ltd., objective Makrozoom 1/5, Leica Co., Ltd.). . . . .	81
3.29	Temporal change in viscosity during crystallization at $0.042 \text{ s}^{-1}$ and $1162 \text{ }^\circ\text{C}$ [13]. The same measurement is repeated four times with different termination times. . . . .	83
3.30	Image of the product quenched after run 2 in Fig 3.29 with the corresponding crystal fraction across the sample in reference to [13]. The right image shows the crystallization front and two crystal-bearing zones with plagioclase aspect-ratio frequency plots. . . . .	83
4.1	Names and positions of the five seismic stations used in this analysis. The map of Izu-Oshima, which shows the locations of the summit crater (A) and the fissures (B and C) is based on [123]. The map left above indicates the location of the Izu-Oshima Island in Japan as red square. . . . .	87

4.2	(a) Magma discharge rate of November 15 – 22 given by [31]. Red, blue, and green lines indicate activities of the summit eruption at A crater, the fissure eruptions at B and C craters, respectively with reference to [106]. (b) RMS amplitude of volcanic tremor during November 13 – 25 at MBS calculated every 1 min. . . . .	91
4.3	Comparison of waveforms observed at OSK. (a) Example of continuous tremor starting at 1:00 am on November 19. Inset: magnified figure of the same data set. (b) Examples of episodic tremor starting at 9:32 am on November 23. . . . .	92
4.4	Comparison of spectra of waveforms in Fig. 4.3(a) and (b). Noises come from the tape characteristic are filtered out from the data. . . . .	92
4.5	Relation between source amplitude $A_{obs} \cdot s^{-1}$ and distance to the source $r$ , occurred from 8 pm for 15 minutes on November 15. The right insets show waveforms at the five seismic stations. The scale of y-axes is $\pm 0.3$ cm/s and the waveforms filtered from 1 Hz to 5 Hz are used in the AIM method. The left inset marks locations of the tremor source ( $\star$ ) and the seismic stations ( $\times$ ). . . . .	93
4.6	Temporal variations in source location on November 13 to November 23. The results shown here are 61.8 % of the total that meet the threshold condition. The color gradation represents the hour in a day and red cross marks indicate the locations of seismic stations. . . . .	96
4.7	Comparison between source locations of tremor and earthquake on November 13 to November 23. The color gradation of tremor sources shows the time in the day unit and red cross marks indicate the locations of seismic stations. Gray diamonds mark source locations of earthquakes during the same period with reference to [123]. . . . .	97
4.8	Temporal variation in source depth with the distance error estimated by Equation 4.5 on November 13 to November 23 is shown on a cross-section of the island. The color gradation of tremor sources shows the time in the day unit. The planar source locations are indicated in Fig. 4.6 and 4.7. . . . .	97
4.9	Examples of episodic tremors superimposed on the continuous tremor observed at all stations (MBS, NOM, NRM, OSK, SNK from the top to the bottom. The positions are shown in Fig. 4.1), which have y-axis range of $\pm 1$ cm.s <sup>-1</sup> . The figures show data at 6:42 am on November 17. . . . .	99
4.10	Source locations of 40 episodic tremors from 16:16 on November 16 to 4:20 on November 17. The color gradation shows the magnitude of source amplitudes and red cross marks indicate the locations of seismic stations. . . . .	100
4.11	Temporal change in tremor energies at the five stations $E$ (black to gray lines) and cumulative discharge weight ( $W$ in red) by reference to [31]. . . . .	101

4.12	Examples of LP waveforms observed by the long-period seismometer in November. The length between squares indicates 1 min. . . . .	103
4.13	Examples of LP waveforms observed by the long-period seismometer in December. The length between squares indicates 1 min. . . . .	104
4.14	RMS amplitudes of early and late LP events normalized by the sum total. $N$ is the number of events and each color represents each seismic station. Locations of the seismic stations are shown in Fig. 4.1. . . . .	106
4.15	Source locations of early and late LP events. Red dot and lines written as A, B and C, indicate the places where the summit eruption and the two fissure eruptions occurred. . . . .	106
4.16	Examples of early LP waveforms observed at MBS and OSK (ref. Fig. 4.1), which have y-axis range of $\pm 0.8 \text{ cm.s}^{-1}$ . The three events started at 15:56 on November 23, 6:47 on November 24, and 10:10 on November 25, from top to bottom. . . . .	108
4.17	Examples of late LP waveforms observed at MBS and OSK (ref. Fig. 4.1), which have y-axis range of $\pm 0.2 \text{ cm.s}^{-1}$ . The three events started at 1:10 am on December 19, 4:58 am on December 19, and 6:09 am on December 21, from top to bottom. . . . .	109
4.18	Source locations of tremors accompanied by the small summit eruption on December 18. Red dot and lines written as A, B and C, indicate the places where the summit eruption and the two fissure eruptions occurred. . . . .	110
4.19	Comparison of waveforms observed at MBS. (a) Examples of continuous tremor starting at 12:30 on November 18 during the large summit eruption. (b) Example of tremor starting at 16:43 on December 18 during the small summit eruption. . . . .	111
4.20	Time table, which shows the relation between eruption activities and volcanic oscillation phenomena during the 1986 Izu-Oshima eruption. . . . .	113
5.1	Graphic illustration of proposed mechanism of the stress fluctuation. Fig. 3.27 is modified here. The red lines show velocity profiles. . . . .	115
5.2	Elastic modulus $G'$ (black) and viscous modulus $G''$ (red) vs time $t$ after preshear at $23.5 \text{ }^\circ\text{C}$ . . . . .	117



5.3 Proposed mechanism of the stress fluctuation with the flow curve  $\sigma$  vs  $\dot{\gamma}$ .  $\sigma_{st}$  is the static yield stress above which the system starts flowing from the solid state [27]. Gray dot represents the apparent state, and red (resp. blue) dot shows the solid (resp. liquid) state in shear banding. The liquid state is defined as shear banded part. (a) describes the stress fluctuation process while (b) shows the fluidization process. . . . . 120

5.4 Stable shear banding observed for  $\dot{\gamma} = 80 \text{ s}^{-1}$  and  $t_w = 10 \text{ min}$  with the rough boundary condition. (a) Shear stress  $\sigma$  and slip velocity  $v_s$  vs time. (b) Width  $\delta$  of the fluidized shear band normalized by the gap width  $e$  vs time. 121

5.5 Conceptual diagram of the stress fluctuation model . . . . . 122

5.6 Graphic illustrations of the model where  $\sigma_c$  is the critical stress,  $v_0$  is the cut-off velocity,  $H$  is the gradient of positive slopes, and  $-h$  is that of negative slope. . . . . 124

1 Elastic ( $\Delta$ ) and viscous ( $\nabla$ ) moduli vs frequency  $f$ . The frequency sweep is performed at a constant strain  $\gamma = 0.5 \%$  and at different aging times  $t_w$  after preshear. [color,  $t_w$  (min)]: (-, 30); (-, 60); (-, 100). . . . . 132

2 Elastic ( $\Delta$ ) and viscous ( $\nabla$ ) moduli vs the strain amplitude  $\gamma$ . The strain sweep is performed at a fixed frequency  $f = 1 \text{ Hz}$  with an aging time of 8 s per point, and at different times  $t_w$  after the preshear. [color,  $t_w$  (min)]: (-, 30); (-, 60); (-, 100). . . . . 132

3 Shear stress response  $\sigma(t)$  and shear rate response  $\dot{\gamma}(t)$  in the start-up flow for different applied shear rates [color,  $\dot{\gamma}$  ( $\text{s}^{-1}$ )]: [-, 100]; [-, 150]; [-, 200]; [-, 250]. The sample is left to age during  $t_w = 60 \text{ min}$  before each experiment. 133

4 Shear stress response  $\sigma(t)$  and shear rate response  $\dot{\gamma}(t)$  in the start-up flow for different aging times  $t_w$  [color,  $t_w$  (min)]: [-, 100]; [-, 30]; [-, 5]; [-, 1]. Experiments performed at  $\dot{\gamma} = 100 \text{ s}^{-1}$ . Experiments performed at  $\dot{\gamma} = 100 \text{ s}^{-1}$ . 134

5 (a) Stress response  $\sigma(t)$  at  $\dot{\gamma} = 150 \text{ s}^{-1}$ ,  $t_w = 10 \text{ min}$ . Inset:  $\sigma(t)$  for the whole experiment. The signal of the main graph appears in red. (b) Spatiotemporal diagram of the velocity  $v(r, t)$  as a function of position  $r$  and  $t$  obtained with 1D-USV. The radial position  $r$  is measured from the rotor. (c) Spatiotemporal diagram of the velocity  $v(r_0, z, t)$  as a function of the vertical position  $z$  and  $t$  at  $r_0 = 0.2 \text{ mm}$  obtained by 2D-USV.  $z$  is measured from the top of the transducer. The velocity is color coded in  $\text{mm}\cdot\text{s}^{-1}$ . . . . . 135

6	1D and 2D velocity profiles of flow curves in rough b.c. (a) Shear rate $\dot{\gamma}$ and shear stress $\sigma$ vs time $t$ . (b) Spatiotemporal diagram of the velocity data $v(r, z_0, t)$ as a function of the distance $r$ to the rotor and $t$ , at $z_0 \simeq 15$ mm. (c) Spatiotemporal diagram of the velocity data $v(r_0, z, t)$ as a function of the vertical position $z$ and $t$ , at $r_0 = 0.5$ mm. The fluid velocity is color-coded in mm/s. . . . .	136
7	(a) Stress response $\sigma(t)$ to a shear startup experiment performed at $\dot{\gamma} = 50 \text{ s}^{-1}$ for different gap sizes: [color, gap (mm)] = [—, 2], [—, 1], [—, 0.5]. (b)-(d) Velocity profile, where $r$ is the distance to the rotor at different times in (a) [symbol, time (s)]: [○, 100]; [□, 800]; [△, 1200]; [▽, 2000]. The rotor velocity corresponds to the upper bound of the vertical axis. The sample is aged during $t_w = 10$ min before each experiment. . . . .	137
8	(a) Epicenters of earthquakes utilized in estimation of site amplification factors. Red, green, and blue dots represent those occurred in January 2013 (Tokyo Bay, Boso Peninsula, and Izu Peninsula, respectively) while gray stars are those happened in November 1986. (b) Normalized site amplification factors at the stations estimated by earthquakes in (a) with the same color coordination. . . . .	139
9	Seismic sources of earthquakes that occurred in January (left) and July (right) of 2014. White and black inverted triangles are the locations of hypocenters determined by ERI and JMA, respectively. The results of our estimation using AIM are shown as red dots. Seismic data recorded at five stations indicated by cross marks were used in the estimation. . . . .	140

# Chapter 1

## Introduction

### 1.1 Volcanic Oscillation Phenomena Induced by Magma Movement

Today, a number of volcanic oscillation phenomena have been observed all over the world and various kinds of the oscillations sometimes occur even at a volcano as shown in Fig. 1.1. Here the term of volcanic oscillation phenomena is defined as the phenomena detected by seismometers associated with volcanic activities. Since recent seismometers have a capability to detect motions with broad frequencies from the order of kHz to below mHz, the corresponding ground motions include various types of phenomena such as volcano-tectonic earthquakes, explosion earthquakes, volcanic tremors, long period (LP) events and ultra-long period events. Among them, volcano-tectonic earthquake is known to represent ordinary brittle failure on fault in volcanic edifice and explosion earthquake, which is often associated with a high frequency prior to shock wave generation at the vent, occurs during explosive eruption [56]. On the other hand, long-period event and volcanic tremor are other kinds of oscillations that have longer periods in the range of 0.2 - 2 s. Although the duration time of volcanic tremor (from few minutes to months) is longer than that of LP event (several tens of seconds), the two oscillation phenomena often show common characteristics [16]. The fact that LP event has a similar waveform and spectrum to volcanic tremor has led researchers to believe that tremor may be a superposition of LP event and suggests a possible common origin [32, 56]. Since both LP event and tremor activities occur in locations within volcanic systems where disturbances in the flow are encountered, those are regarded as seismic events originating in fluid processes [16]. However, compared to other volcanic oscillations such as volcano-tectonic earthquake and explosion earthquake, the generating mechanism of LP event and tremor is still under debate although researchers share the view that it should involve complicated interactions of magmatic fluids with the surrounding conditions [58].

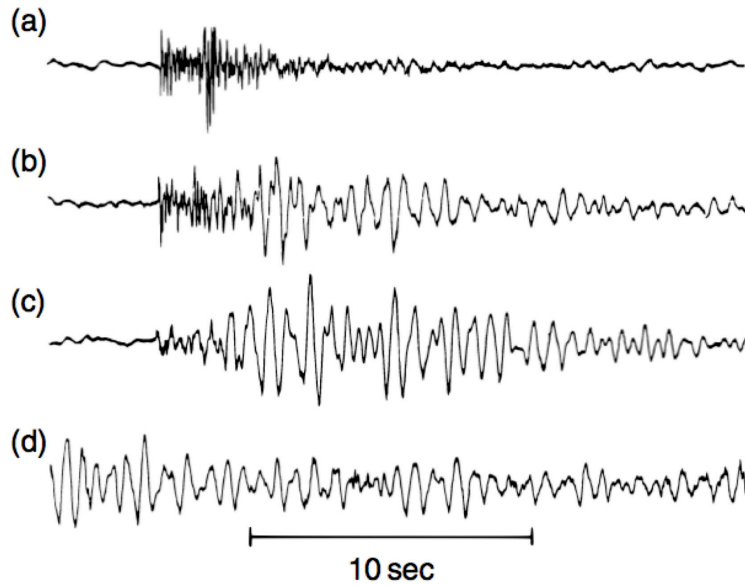


Figure 1.1: Waveform examples observed at Redoubt Volcano [78]. (a) High-frequency volcano-tectonic earthquake, (b) mixed-frequency event, (c) LP event, and (d) volcanic tremor.

### 1.1.1 Characteristics

#### Waveform and Spectrum

LP event and tremor have essentially the same temporal and spectral components in many cases, suggesting that a common source, which has a difference only in duration [16, 17]. Fig. 1.2 supports the idea. In the figure, tremor is closely analogous to LP event in terms of waveform and spectrum (the same dominant frequency around 1.5 Hz) except for the duration time, while the similarity is not seen in volcano-tectonic (VT) or hybrid events. With respect to hybrid events that have high-frequency onsets followed by low-frequency oscillation, one considers that the generation is explained by brittle-failure without consideration of fluid processes [41]. As other unique spectral properties of LP event and tremor that are not found in Fig 1.2, the spectrum structure composed of harmonics and the time variation in the spectrum are reported [53].

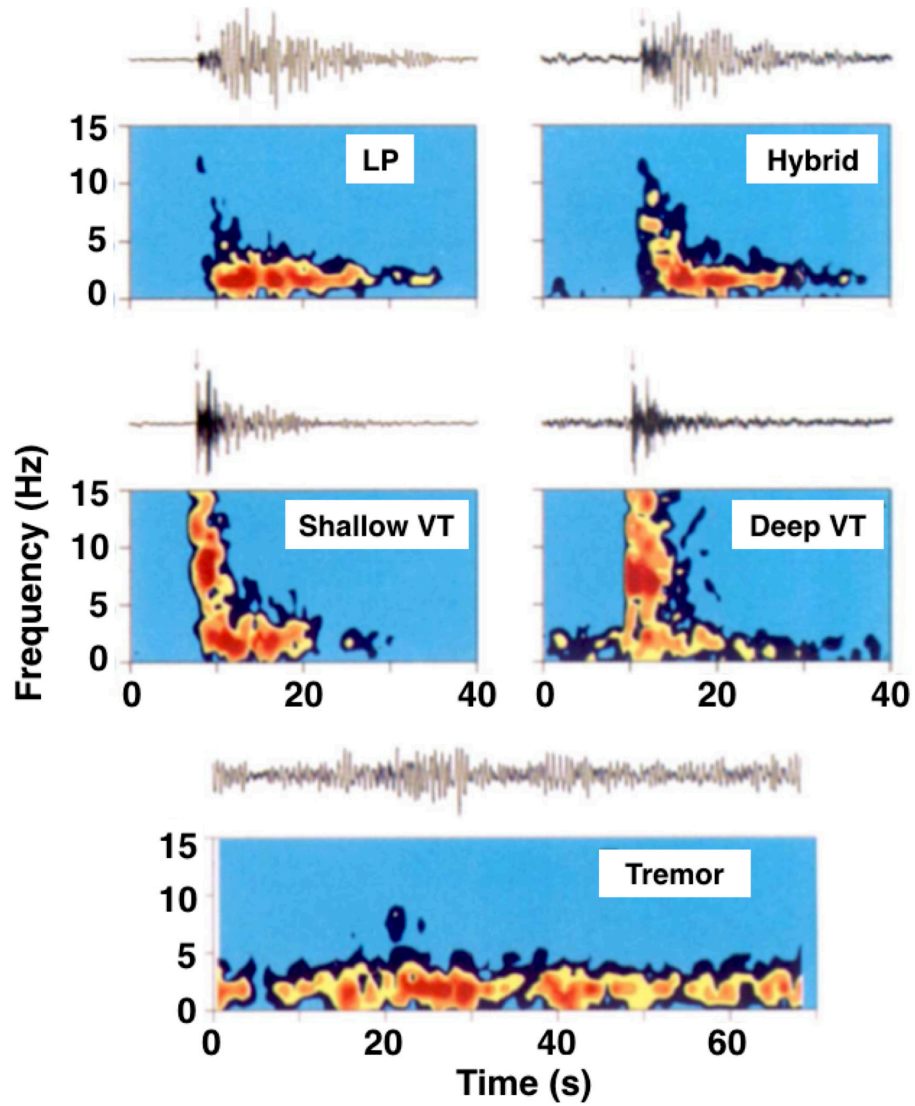


Figure 1.2: Ground velocities of UD component and the spectrograms for LP, VT and hybrid events, and tremor observed at Redoubt Volcano [16]. Warm colors define the dominant spectral amplitudes.

---

Nowadays, hundreds of volcanoes are seismically monitored all over the world and over 600 scientific publications have been written for describing properties of volcanic tremor. The previous works reveal that there are a wide variety of volcanic tremors as some following examples.

#### *Monochromatic tremor*

Monochromatic tremor is a simple tremor that has one dominant frequency in its spectrum. It is observed at Kuchierabujima Volcano and Villarrica Volcano, for instance [49, 102].

#### *Harmonic tremor*

The spectrum of harmonic tremor is composed of a fundamental frequency together with associated overtones. Time variations of the dominant frequencies, which are often observed at different volcanoes (*e.g.* Fig. 1.3), supports the fact that volcanic tremor is generated not only by volcanic geometry as a resonance system but also by fluid processes.

Since harmonic tremor is also observed as infrasonic signal frequently, switching between seismic-only harmonic tremor and seismo-acoustic harmonic tremor may indicate important changes in shallow conduit conditions. Subtle changes in magma properties and supply rate during degassing process are regarded as important factors and intermediate magma viscosity in which stable degassing pathways open to the atmosphere will allow harmonic tremor generated in the conduit to be transmitted into the atmosphere [71].

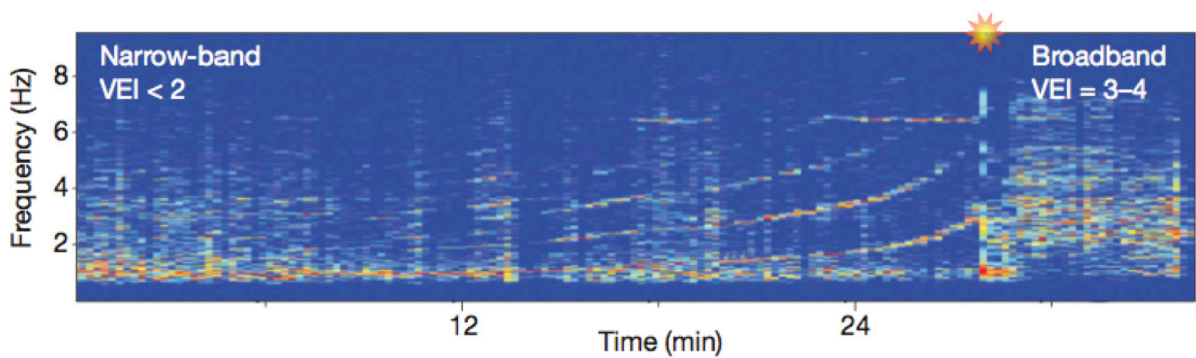


Figure 1.3: Time series of amplitude spectra at Montserrat showing evolution in characteristics of harmonic tremor during transitions to eruptions [53].

---

### *Episodic tremor*

Tremor, which appears intermittently and observed as a stripe pattern in monitor recordings is categorized into episodic tremor, which is also known as intermittent tremor or banded tremor [10].

### *Continuous tremor and LP event*

Continuous tremor persists for a prolonged time without ceasing whereas LP event is a single-shot oscillation sharing waveform similarity with continuous tremor. Usually the both oscillations dominate with volcanic activities.

## **Source Migration**

Source location of volcanic oscillation phenomena provides important information. At volcanoes where dense seismic network is operated, the source locations are believed to represent magma path-way so that its temporal migration represents clue about the resultant eruption. Fig. 1.4 shows migration of tremor sources during several eruptions at Piton de la Fournaise Volcano, Reunion Island in 1998 [7]. The source locations are performed by approximating decay of the seismic amplitude as a function of the hypocentral distance. Kapor, Krafft, and Hudson vents are active in March while only Kapor vent has kept energetic activity in April. From July to September, activity outside the Enclos Fouque becomes pronounced. Fig 1.4 tells that the migration of tremor sources is accompanied by the change in the eruption position. Although it is uncertain which precedes under this time resolution, the fact supports the general argument that movements of magma are related to generation of volcanic tremor. The correlation is also reported at other volcanoes, such as Meakandake Volcano [93].

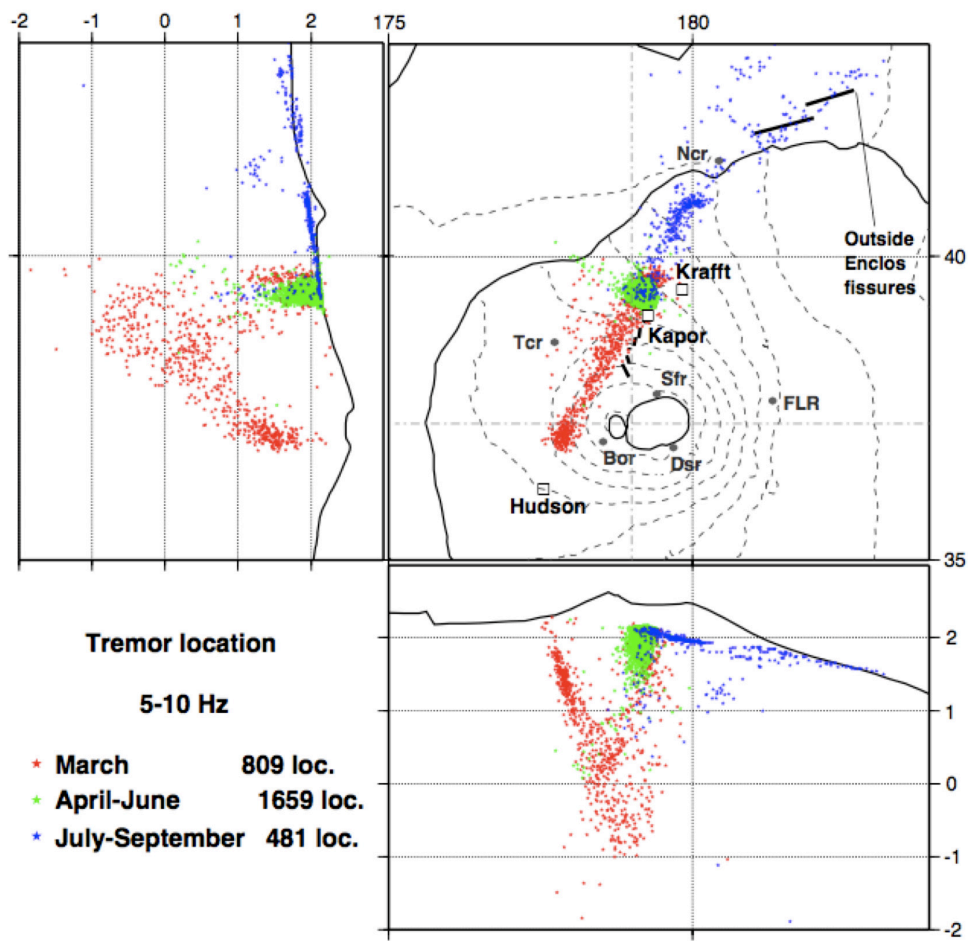


Figure 1.4: Source location of tremor during the 1998 eruption on Piton de la Fournaise Volcano [7]. The source locations are divided into three plots with different colors depending on the periods.



---

### 1.1.2 Proposed Generation Mechanism

Since volcanic tremor and LP event have potential value as tools for better understanding dynamic processes inside volcanoes and forecasting eruptions, various generation models have been proposed so far. The models can be classified into four main groups [58]: (a) fluid-flow-induced oscillations of conduits transporting magmatic fluids, (b) excitation and resonance of fluid-filled cracks, (c) bubble growth or collapse due to hydrothermal boiling of groundwater as well as vesiculation in magma, (d) oscillations of magma bodies with different geometries. The difference in duration of LP event and tremor is believed to be explained by the duration of the excitation mechanism [14, 32, 114]. Examples of the four types are introduced here.

#### (a) Fluid-flow-induced oscillations of conduits transporting magmatic fluids

A model of fluid-induced oscillations inside a vertical crack transporting magmatic fluid is proposed as a possible generating mechanism for volcanic tremor [54]. The model assumes that melt is incompressible fluid with basaltic viscosity, the channel walls are imperfectly elastic represented by a spring and a dashpot, and the channel thickness and the fluid flow speed are variable (see Fig. 1.5). The numerical result indicates a cyclic change in conduit thickness by the following mechanism: 1) an increase in flow speed results in a decrease in fluid pressure due to the Bernoulli effect,  $p + \rho v^2/2 = const.$  2) The walls move towards each other constricting the flow. 3) The pressure builds up again forcing the walls apart again because of the same reason. The change causes a decrease in the pressure and an increase in the flow to go back to 1). This positive feedback induces the oscillation. As this model represents, (a)-type model presumes elastic conduit and one-phase fluid, which has a constant density.

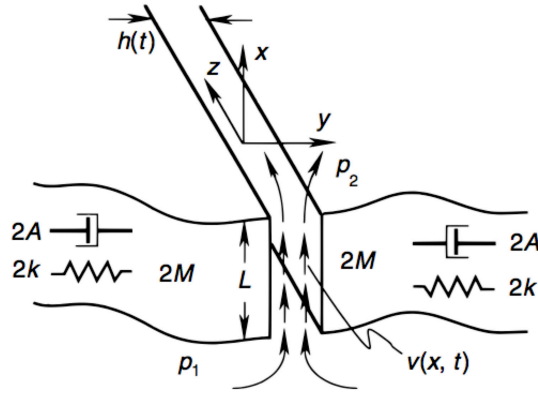


Figure 1.5: Flow-induced model described by [54] (the picture in [56] is cited here). Incompressible viscous fluid flows in  $x$ -direction from bottom to top through a channel with imperfectly elastic walls. Two dynamical variables,  $h(t)$  and  $v(x, t)$ , are the channel thickness and the fluid flow speed, respectively.

### (b) Excitation and resonance of fluid-filled cracks

The displacement of walls of a fluid-filled crack caused by a pressure disturbance in the fluid is proposed as a model for generation of LP events as well as tremor in [15]. As illustrated in Fig. 1.6, the viscous compressible fluid exits in the crack and the resonance of the crack is induced by an impulsive pressure transient. The model succeeds to produce both longitudinal and lateral modes of oscillation in only one crack without inflow and outflow depending on some parameters such as the crack geometry, the position and the area over which the pressure disturbance happens, the crack stiffness  $C = bL/\mu d$ , and the fluid-solid impedance contrast  $Z = \rho_s \alpha / \rho_f a$  [ $b$  is the bulk modulus of the fluid,  $\mu$  is the rigidity of the solid,  $L$  is the crack length,  $d$  is the crack thickness,  $\rho_s$  (resp.  $\rho_f$ ) is the density of the solid (resp. fluid) with its P-wave velocity  $\alpha$  (resp.  $a$ )]. The duration of the signal is a function of the fluid viscosity, area of the crack, and amplitude of the pressure transient.

### (c) Bubble growth or collapse due to hydrothermal boiling of groundwater

At shallow depth, deformations and fragmentations of bubbles that obtain high compressibility take place [1, 47]. Under the condition, the existence of gas bubbles in volcanic system is one of the considerable factors to generate oscillation phenomena and plenty of models that took account of the effect of bubbles have been described so far. The bubble models can be classified depending on which fluid is involved, magma or hydrothermal fluid at each volcanic system. One focuses on bubbles in magma. Magma ascended from a deep part reaches a shallower part decreasing density by generation of bubbles. There bubbles in magma play an important role as seismic source. Bubble dynamics model for shallow volcanic tremor at Stromboli is proposed in [101] and the schematic illustration is shown

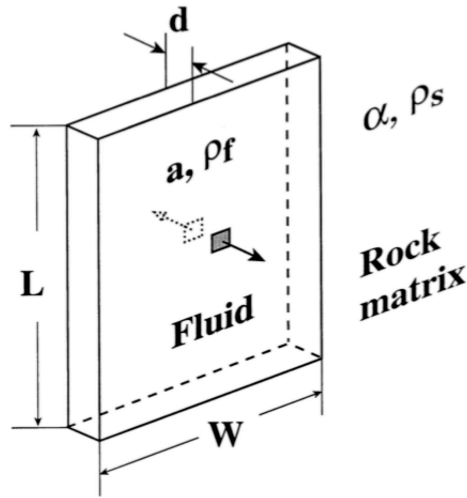


Figure 1.6: Source geometry of fluid-filled model proposed by [15] (the picture in [58] is cited here). The gray zone indicates the place of application of the pressure transient that triggers resonance.

in Fig. 1.7. The model considers two steps, first gas coalescence, and then gas bursting. Within the two steps, seismic signals are related to the first coalescence while infrasonic signals are linked to the latter bursting. They propose that the shallow volcanic tremor could be induced by the viscoelastic reaction of magma to the pressure decrease.

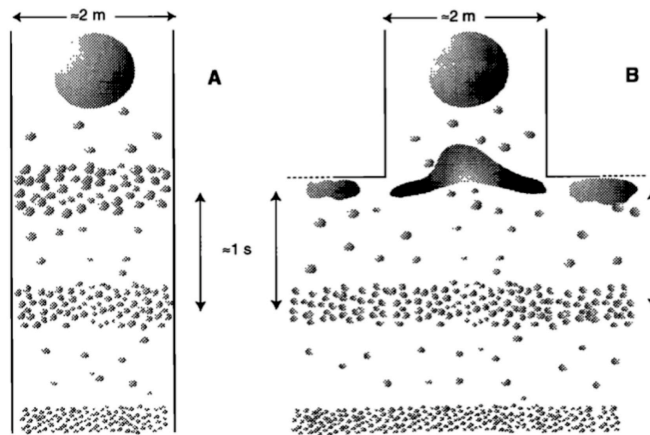


Figure 1.7: Bubble-coalescence conditions proposed by [101]. (a) Bubble layers rising freely coalesce in a larger bubble when hydrostatic pressure drops. (b) A bubble layer reaching a structural barrier is forced to coalesce and rises generating a hydrostatic pressure drop.

The other type of bubble model is boiling groundwater in geysers and aquifers [57]. A model is proposed on the basis of analysis of episodic tremor activity [10]. It suggests that the tremor happens due to “perturbations” in shallow aquifers such as bubble growth or collapse because of hydrothermal boiling triggered by heat and hot fluid transfer from

---

underlying magma bodies (Fig. 1.8).

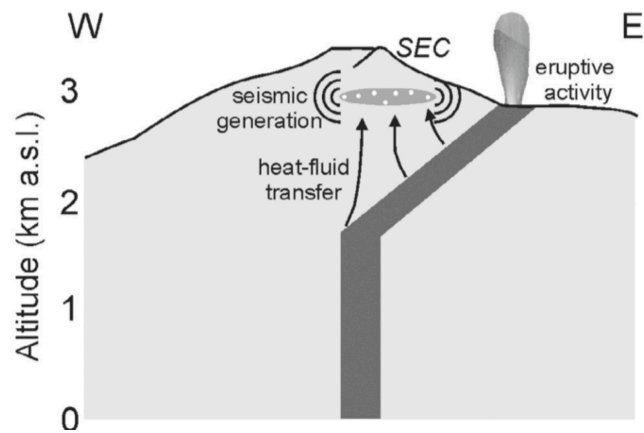


Figure 1.8: Illustration of proposed geyser model by [10] based on analysis of banded tremor at Etna.

In this way, bubble models can explain volcanic oscillations at shallower parts and relations between seismic and acoustic signals well, although the models cannot apply to oscillations at deeper parts where bubbles and water do not exist, or when magma does not have sufficient amounts of volatile component.

---

(d) Oscillations of magma bodies with different geometries

Specific geometrical conditions of volcanic system also affect movement of magma. Here a model for LP events accompanied by the 1998 activity at Iwate Volcano is introduced [90]. The study describes a source mechanism of mutual deflation and inflation of two chambers located at western and eastern edges of the source region on the bases of results of moment tensor inversions. It infers that mass and/or pressure transportation and movement of magmatic fluid between the two separated chambers generates LP events as shown in Fig. 1.9.

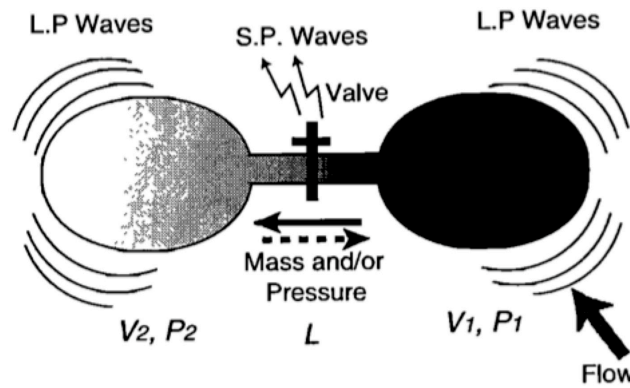


Figure 1.9: Illustration of the model that describes mass and/or pressure transportation between two separated chambers as the source of LP events [90].

As introduced above including concrete examples, models proposed so far have mainly taken account of effects of elasticity of bubbles and volcanic body as “reservoir”. Although they play important roles in generating oscillations, on the other hand, there is a common view among researchers regardless of model type that volcanic tremor and LP event are related to fluid movement in itself. Therefore finding a possible link between magma rheology and magma-derived oscillations such as LP event and tremor would be also important.

---

## 1.2 Magma Rheology

### 1.2.1 What is Rheology?

Rheology is *the study of the deformation and flow of matter*. This definition was accepted when the American Society of Rheology was founded in 1929 [5]. So as to express rheological characteristics, three physical quantities, shear stress, shear rate, and viscosity, are basically employed. The shear stress  $\sigma$  is the force per unit area required to produce the motion, the shear rate  $\dot{\gamma}$  is the velocity gradient, and the constant of proportionality is the viscosity  $\eta$  [5]. The viscosity is an internal property of a material that offers resistance to flow. The quantities are expressed as  $\sigma = F/S$ ,  $\dot{\gamma} = V_0/h$ , and  $\eta = \sigma/\dot{\gamma}$  by using symbols in Fig. 1.10. In general, rheological measurements are performed by controlling  $\sigma$  or  $\dot{\gamma}$ .

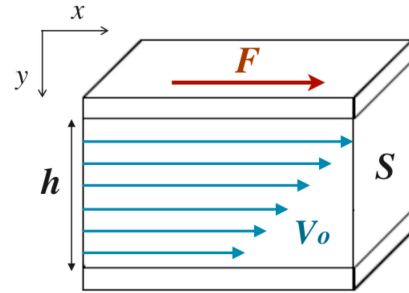


Figure 1.10: Flow under shearing

Fluids are classified according to the relation between  $\sigma$  and  $\dot{\gamma}$  as shown in Fig. 1.11. Newtonian fluid is a fluid where the rate of deformation is proportional to the force, or it has a fixed viscosity. The behavior becomes more complex when it comes to non-Newtonian (non-linear) fluid. Fig. 1.11 describes behaviors of three basic types of non-linear fluids. Yield stress fluid has the yield stress that is defined as the stress at which the fluid *just* starts/stops flowing ( $\sigma_0$  in Fig. 1.11) [85]. Therefore in order to make a yield stress fluid flows,  $\sigma$  that is larger than the yield stress  $\sigma_0$  should be imposed. Shear-thinning (resp. shear-thickening) means that  $\eta$  decreases (resp. increases) with increase in  $\dot{\gamma}$ . As familiar examples, ketchup and blood are shear-thinning fluids while mixture of starch and water is shear-thickening fluid. Note that these non-linear characteristics are not independent and fluids, which have yield stress and show shear-thinning/shear-thickening behavior, exist. Moreover there is a fluid that has a finite yield stress and behaves as a Newtonian fluid once it flows (Bingham fluid) [8] and Newtonian fluids can turn into non-linear fluids by adding particles or bubbles [69]. Magma also shows diverse rheological properties depending on the condition.

Another important nature in non-linear rheology is thixotropy, which describes time-variable nature of rheology caused by a reversible cycle of the formation and the destruction of microstructure. In a precise sense, slow increase in viscosity with time (aging) and viscosity decrease with time (rejuvenation) are two aspects of the phenomenon: the build-up and destruction of the microstructure [85].

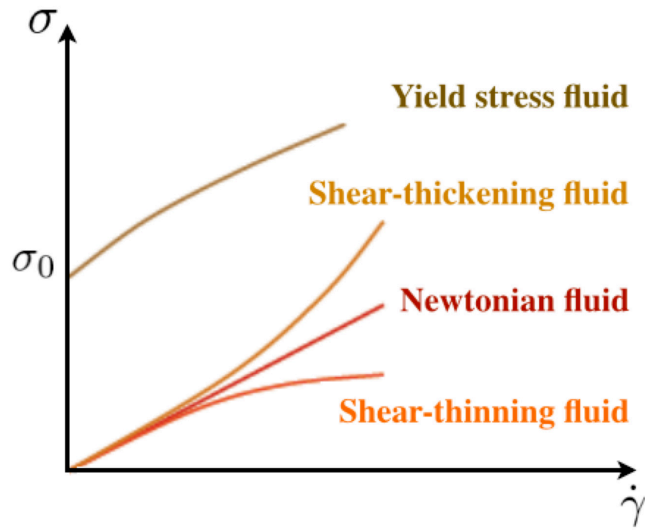


Figure 1.11: Classification of fluids

### 1.2.2 Magma as Non-linear Complex Fluid

Volcano is where magma is effused on the Earth's surface as lava flows, ashes, gases, and rocks [107]. As with the wide variety of eruptive products, magma rheology also changes as a function of many factors. The greatest characteristic of magma is that it is a mixture of melt, crystals, and bubbles. In general, magma starts melting with increasing temperature/pressure and it yields bubbles with decreasing pressure. Although the relation between the three phases is important, this study focuses on solid-liquid magma, which still has many undiscovered properties with potential to cause oscillation phenomena.

As in Fig. 1.12, solid-liquid magma varies from a simple Newtonian fluid to a non-linear complex fluid with increasing particle volume fraction  $\phi$ . The non-linear properties emerge when the particle volume fraction reaches critical volume fraction  $\phi_c$  at which the yield stress ( $\sigma_0$  in Fig. 1.11) first appears. Magma is known to possess lower  $\phi_c$  than that of interaction-free suspensions because crystals connect each other and form networked structures even under poor crystal conditions unlike with simple hard-sphere particles as in Fig. 1.13 [46, 98]. In this way, non-linear rheology of magma is attributed to interaction and/or arrangement of crystals.

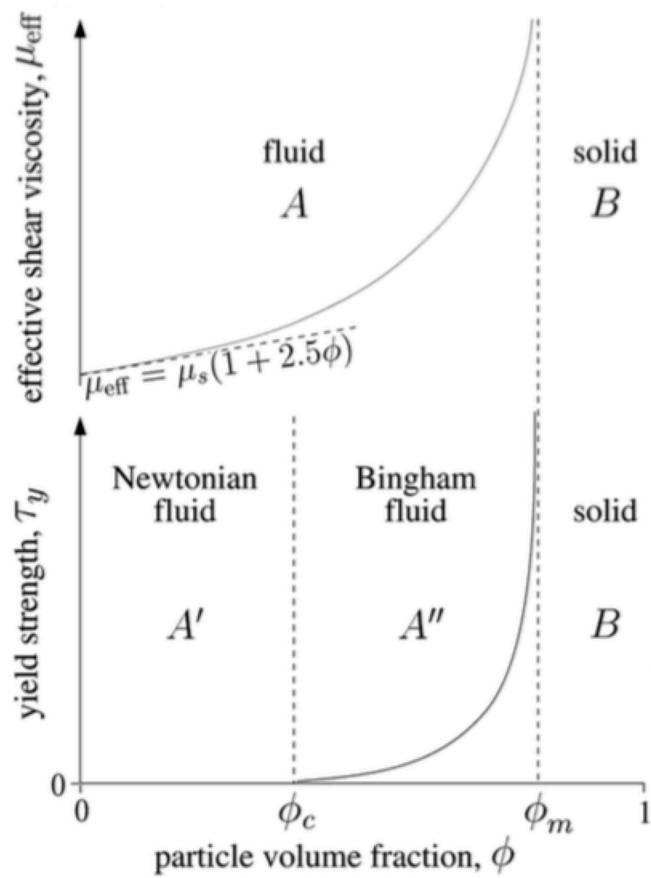


Figure 1.12: Schematic image of effective shear viscosity  $\mu_{eff}$  and yield stress  $\tau_y$  vs crystal volume fraction of magma  $\phi$  [105].

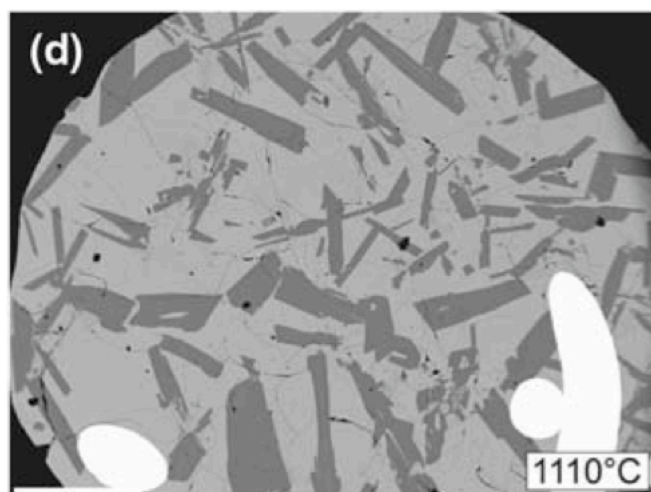


Figure 1.13: Back-scattered electron image of quenched natural sample including plagioclase-chains [98]. The scale bar (white line) indicates 0.5 mm.



Under simple shear condition, magma may separate into bands of widely different viscosities that is known as “shear banding”, due to crystal arrangements (Fig. 1.14). In fact, evidences of shear banding in eruptive products are found as seen in Fig. 1.15 [94]. The phenomenon involves inhomogeneous flows where macroscopic bands bearing different shear rates or shear stresses coexist. Although it was revealed that shear banding is attributed to an underlying shear-induced transition from a given microscopic organization of the fluid structure to another, plenty of theoretical and experimental challenges are still required even in the field of non-linear rheology [76]. It is all the more as for shear banding in magma, which has received little attention until now.

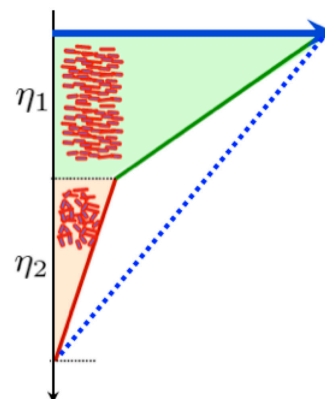


Figure 1.14: Shear banding

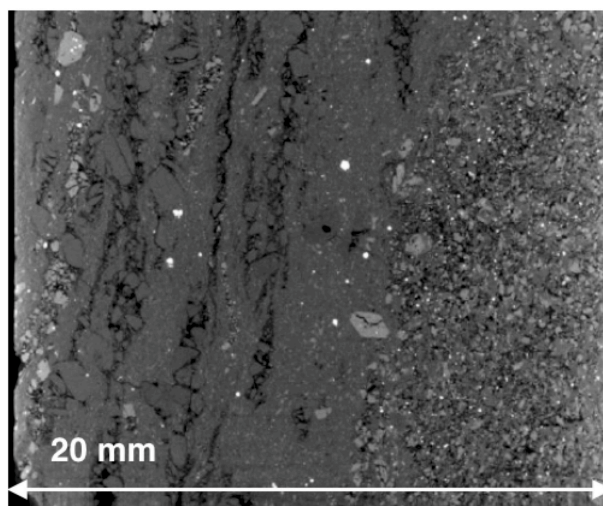


Figure 1.15: Shear banding structure in eruption product [94]

Effect of crystal arrangements is seen not only as the shear banding but also as non-linear characteristics in its rheology. Fig 1.16 shows two non-linear characteristics of magma rheology due to the change in crystal arrangements [50]. One is a decrease in viscosity over time even at a constant shear rate, which is a rejuvenation process. This characteristic indicates rearrangement of crystals to the direction parallel to the flow with time by constant shear. The other is shear-thinning (a decrease in viscosity with increasing the shear rate), which also comes from changes in crystal arrangement to flow easily with increase in shear rate. As the two properties appeared in magmas at many volcanoes, non-linear magma rheology is universally-present [19, 51, 105, 119]. Based on the non-linearity in magma

rheology, it won't be surprised if magma shows a reverse process, or rearrangement of crystals to random directions interacting and connecting each other at rest or by slight shear. In reality, the initial conditions of magma before the rheological measurements in which crystals are connected, strongly suggest the idea. These quasi-static changes are related to “aging”, which is variation in rheological properties at rest with time [62]. From the perspective that apparent rheological changes are observed during aging process of fluids in the field of non-linear rheology [24, 26], magma should not flow smoothly at all times and the link between non-linear magma rheology and unsteady flow exists. The next Section 1.17 focuses on a key concept to explore the link.

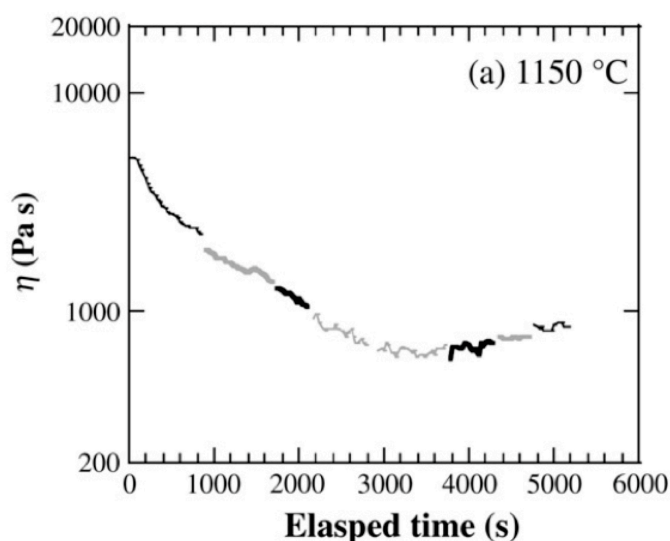


Figure 1.16: Time-dependent variations in viscosity derived from alkali olivine basalt from Matsuura district [50]. Thin black lines, thick gray lines, thick black lines, and thin gray lines represent rotation rate of 1, 2.5, 5, and 10 rpm.

### 1.3 Multiplicity

It is known that oscillation is produced under the condition that the relation between driving force (shear stress or pressure) and flow rate (shear rate or flux) has a negative slope, which is referred to as “multiplicity” (Fig. 1.17). In this state, several flow rates exist at certain driving force, and jumps between high and low flow rates generate self-induced oscillations. To become the state, using a material that has the multiplicity in its rheology or using a system that shows the multiplicity in the relation between shear stress (resp. pressure) and shear rate (resp.  $\dot{Q}$ ) are necessary. In short, there exists rheological multiplicity and systemic multiplicity. Especially since the rheological multiplicity is not very intuitive, many researchers had resisted the idea and a statement that has been revisited and reversed

by the same author almost 40 years later [12]. However in proportion as an increase in experimental studies, which show self-induced oscillations by the multiplicity, it becomes a common concept to describe oscillation phenomena [73, 74]. This section gives existing ideas of multiplicity and explains proposed mechanisms.

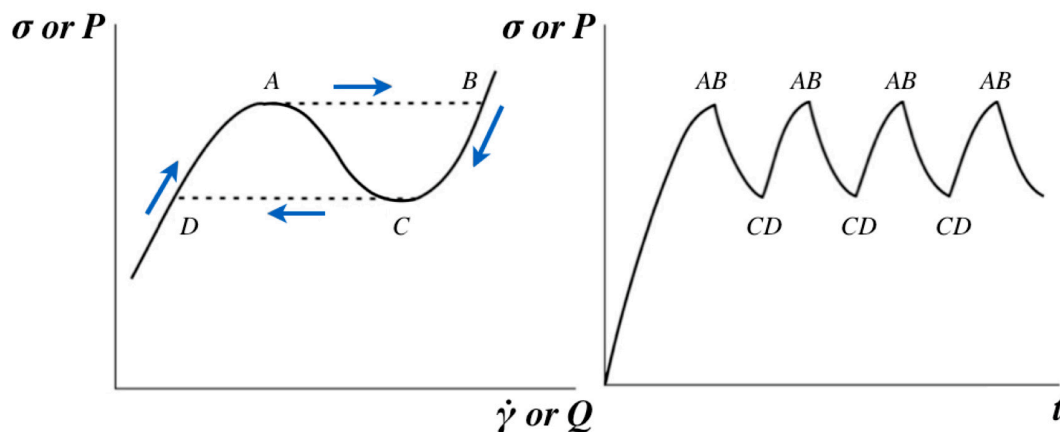


Figure 1.17: Self-induced oscillations provided by the rheological (resp. or systemic) multiplicity in the relation between shear stress  $\sigma$  (resp. pressure  $P$ ) and shear rate  $\dot{\gamma}$  (resp. flux  $Q$ ). The figure in [74] is modified here.

### 1.3.1 Multiplicity in Elastic Fluid

In the field of polymer science and industry, self-induced oscillation due to the multiplicity have been studied intensively in recent years and the phenomenon is usually referred to as spurt or stick-slip periodic transition [73, 74]. The instability is induced by rubber-like elasticity of polymer fluids, a property which causes storage of elastic energy during deformation with its subsequent release in the form of stream distortions as shown in Fig. 1.19. The key factor to generate the oscillation is mechanical fracture of a material due to concentration of stress in the experimental geometry causing transition from laminar flow to slip along the wall. Fig. 1.18 shows an example of experimental geometry, which can cause stress concentration at the outlet so as to induce the oscillation. This process becomes clear by comparison with the multiplicity in the left figure of Fig. 1.17 as following. 1) The shear rate increases to A

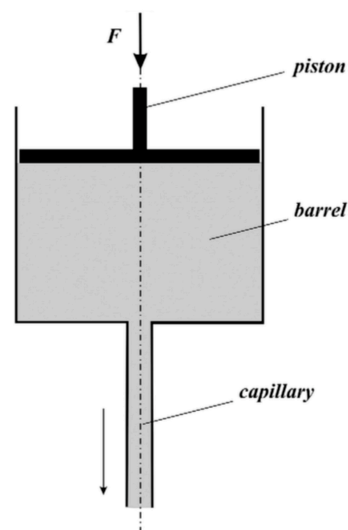


Figure 1.18: A scheme of experimental geometry to induce spurt [74].

point by increasing stress along the leftmost curve to start the experiment. 2) At the critical condition A, the fluid suddenly slips along the wall of the outlet and the shear rate jumps to the high value (A→B). 3) Reducing the elastic energy by the slip causes a decrease in the shear rate (B→C). 4) The fluid sticks along the wall due to storage of elastic energy at lower shear rates and jumps to the elasticity-dominated regime occurs (C→D). Then going back to the first process makes hysteresis loop causing self-induced oscillations. In this way, this kind of oscillation requires elasticity of the material and the geometric condition to cause concentration of stress.

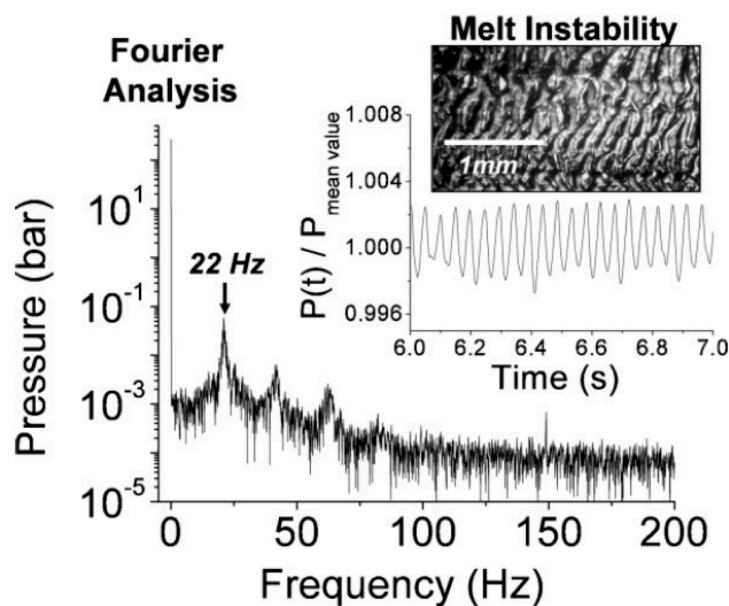


Figure 1.19: Spectrum of pressure fluctuations [95]. The inset shows the temporal change of the normalized pressure with an optical microscope picture.

### 1.3.2 Multiplicity in Gas-liquid System

Self-induced oscillations in gas-liquid system have been studied in many study fields including volcanic seismology, nuclear industry, and chemical engineering [36, 55, 68]. The dynamic instabilities take place when there is sufficient interaction and delayed feedback between the inertia of flow, heating, and compressibility of gas-liquid mixture because of change in density as a result of the rate of vapor generation. Mainly two kinds of the instabilities, density-wave oscillation and pressure-drop oscillation are applied as models of volcanic oscillation phenomena so far [35, 36, 52]. Note that although the two oscillations share the same mechanism explained by propagation time lags and feedback phenomena in gas-liquid phase, occurrence conditions are different. As in Fig. 1.21(a), the density-wave oscillation occurs at low flow rates on the positive slope of the flow curve while the

pressure-drop oscillation is observed only in the range of negative slope of the flow curve. Depending on the occurrence ranges in flow rate, they have different oscillating periods [Fig. 1.21(b)]. Since the underlying interest of this study is in oscillation phenomena caused by the multiplicity having negative slope, here we focus on the pressure-drop oscillation.

The basic idea of pressure-drop oscillation is explained by the following order according to the illustration in Fig. 1.20. 1) The surge tank pressure  $P_2$  increases due to accumulation of fluid and the operating point reaches at the peak, B point. 2) Since any higher pressure can be sustained only by a higher mass flow rate as given by the system curve, it jumps to C point in the single-phase liquid region. At C point, the amount of fluid leaving the surge tank is more than the entering amount. 3)  $P_2$  decreases until the operating point reaches the minimum, D point. 4) The mass flow rate reduces to the value at A point because it is the only way to obtain any lower pressure. 5) Now the mass leaving the surge tank is less than the entering. Hence  $P_2$  goes up again repeat this cycle. Thus perturbation at any point on the negative slope results in a flow oscillation tracing the limit cycle.

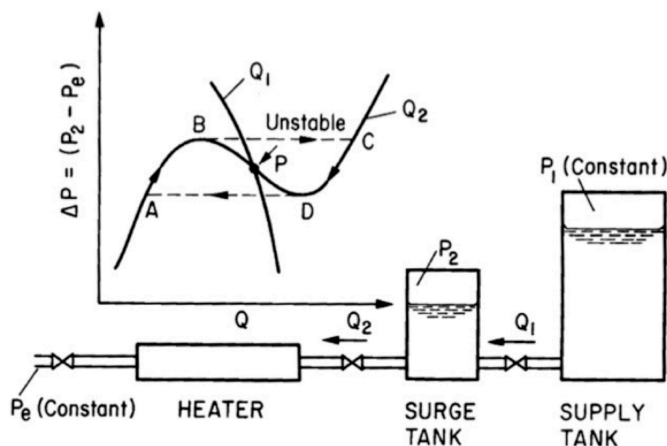
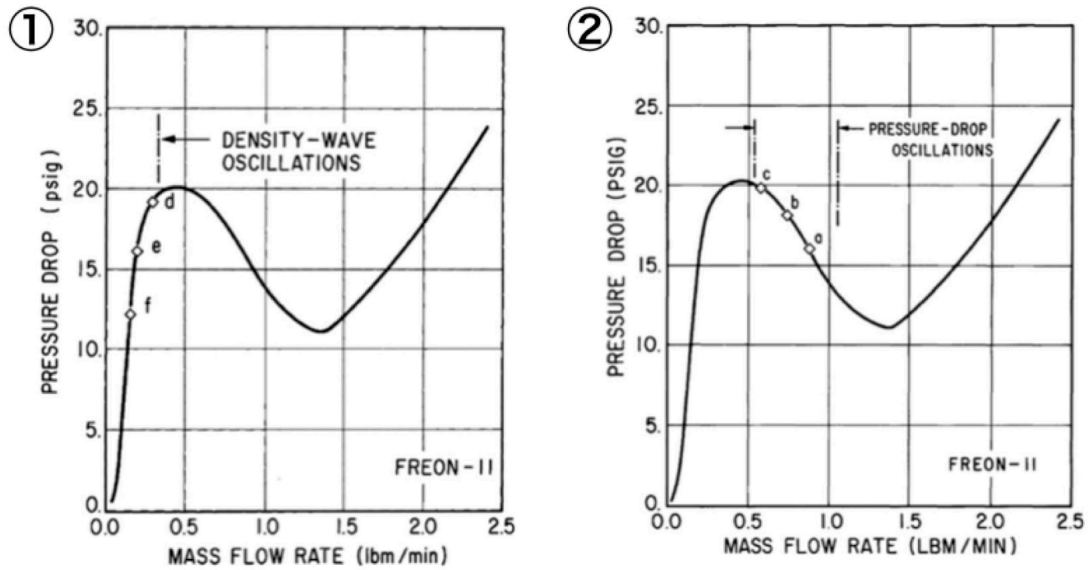
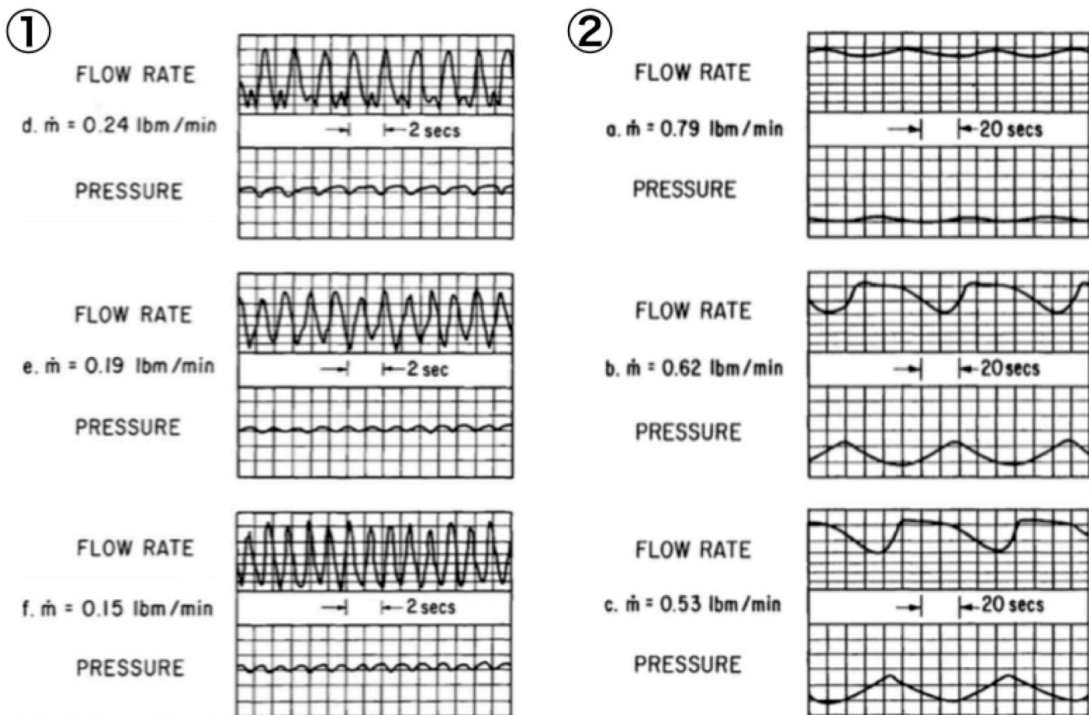


Figure 1.20: Graphic illustration of limit cycle of pressure-drop oscillation [55].



(a) Occurrence regions of the oscillations



(b) Typical recordings of the oscillations

Figure 1.21: Graphic illustrations of (a) occurrence regions and (b) typical waveform examples of ① density-wave oscillation and ② pressure-drop oscillation [55].

---

Tilt changes during the caldera formation stage in the 2000 Miyakejima eruption caused by the periodic expansion of a sill-like magma plumbing system are explained by a model of pressure-drop oscillations [35]. Fig. 1.22 shows the interpretation of relation between tilt steps and caldera formation and Fig. 1.23 illustrates the oscillation mechanism. The mechanism is described on the ground of observations as following. 1) Based on the tilt observation, the flux of magma is relatively small and more gas is accumulated in the compressible cavity along the conduit causing a gradual expansion of the cavity at shallow part (A→B). The LP events probably occur due to the instability around the cap rock. 2) When  $\Delta p$  reaches the threshold, the sill expands and the flux of magma in the sill increases abruptly, which cause a transition (B→C). The compressible cavity also expands and the cap rock collapses forming a caldera at the summit. 3) The sill and the conduit gradually shrink to reach the minimum flux (C→D). Then magma returns to the conduit and the state returns to the initial A point so as to start the next cycle.

The necessary conditions for the occurrence of pressure-drop oscillations are internal characteristics with multiplicity, external characteristics steeper than the internal characteristics as well as the existence of a compressible volume in the flow circuit [55].

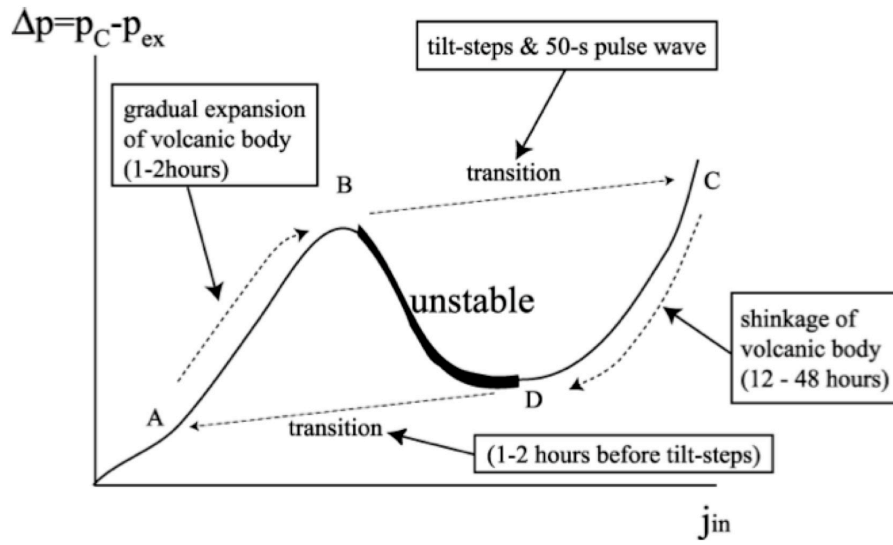


Figure 1.22: Relation between pressure loss  $\Delta p$  and flux  $j_{in}$  of the gas-liquid system [35]. Comparison with the observed tilt step cycles is also indicated.

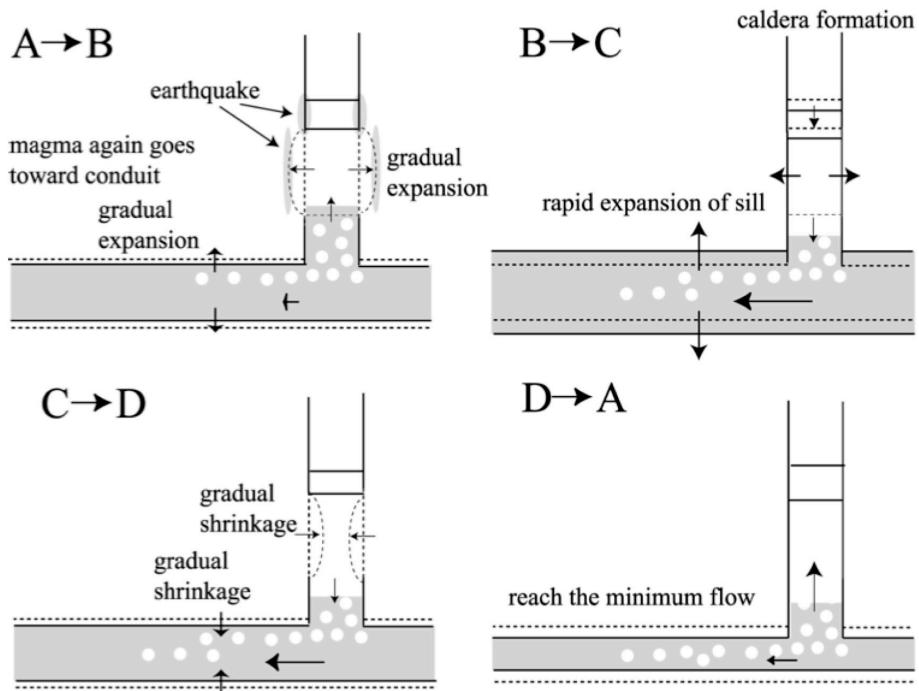


Figure 1.23: Graphic illustration of mechanism of tilt steps and caldera formation based on the pressure-drop oscillation model [35].



---

### 1.3.3 Multiplicity in Solid-liquid Magma

A considerable number of studies dedicated to self-induced oscillations of elastic fluids and gas-liquid systems reveal that key factors to induce the oscillations are elasticity of fluid, bubbles, and geometrical conditions as described in Section 1.3.1 and 1.3.3. That is to say, these are categorized as oscillations generated by systemic multiplicities that interact with material properties. By contrast, rheological multiplicity of inelastic solid-liquid magma falls behind even though the concept has been employed to describe cyclic volcanic activities such as lava dome extrusions [18, 79, 118]. As the studies numerically generate periodic variations in discharge rate due to the transition from a stable state when discharge rate is low and crystals grow efficiently leading to high magma viscosity, to another state when discharge rate is high and crystallization is negligible, rheological changes in crystal-bearing magma is an important factor [79]. However the models also consider other causes such as elasticity of the surrounding rocks, bubble growth, gas escape, chamber volume that interact with each other. Again, since the main goal of this study is exploring possible link between non-linear magma rheology and volcanic oscillation phenomena, here we purely focus on the multiplicity that solid-liquid magma could have without elasticity of surrounding rocks and bubbles.

Solid-liquid magma is a kind of dense suspension containing solid particles in a liquid. Dense suspensions are materials showing complex rheological behaviors due to properties of dispersed phase and the liquid as well as their interaction. The behaviors of suspensions are experimentally investigated in the field of non-linear physics, providing evidence for solid and liquid states in a transient shear rate from rest that is related to aging [44]. A key feature of the transition in the multiplicity is collapse and formation of the particle linked structure as shown in Fig. 1.24: particles align with the flowing direction at higher shear rates while they are entangled possessing resistance to movement at lower shear rates. In intermediate state that is the multi-valued part of the flow curve, the fluid is assumed to have shear banding [87]. Therefore such variations in arrangement have possibility to bring about flow instabilities.

At the present stage where the multiplicity is only expressed mathematically in volcanic systems, finding basic physics underlying the concept and examining the behaviors of fluids, which have the multiplicity in reality are of significance.

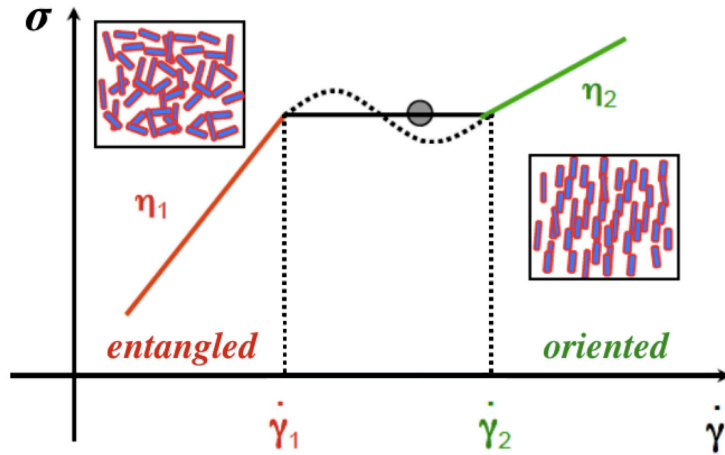


Figure 1.24: Variations of flow field in multiplicity in the relation between shear stress  $\sigma$  and shear rate  $\dot{\gamma}$  in a suspension.

## 1.4 Aim and Framework of This Thesis

As described above, elasticity of surrounding rocks and bubbles has been focused for describing volcanic tremor and LP event whereas little attention has been paid on the aspect of contribution of non-linear magma rheology. In the field of magma rheology, its non-linear nature has not well clarified yet. This is probably because efforts have been paid to construct unified rheology in steady state, which may have overlooked jerky behaviors in unsteady state. To explore possible link between volcanic oscillations and non-linear magma rheology, current researches in the field of non-linear physics that uncover interesting phenomena such as rheological instability in transient flow should provide a clue.

This thesis is written with the aim of exploring the possibility of volcanic oscillations due to non-linear magma rheology by two different approaches, experimental study and analysis of natural phenomena. First, experimental approach using analog materials of magma on two scales is adopted to comprehend underlying fundamental physics of rheological instabilities in suspensions, which possess the multiplicity in the relation between shear stress and shear rate. One experimental study explores the mechanism of pressure perturbation on macro scale linking rheological measurements and large-scale flow experiments while the other focuses on stress fluctuations by finding the relation between global rheology and local velocity profile on micro scale. Second, as another approach, analysis of actual volcanic oscillations accompanied by the 1986 Izu-Oshima eruption is performed for the purpose of comprehending the oscillation as a real phenomenon.

Chapter 2 describes experimental study of pressure perturbation arising during a transient flow. A mechanism proposed to explain this phenomenon via aging-dependent softening

---

of the fluid is supported by rheological measurements. In Chapter 3, another experimental study, the dynamics of stress fluctuation and the local dynamics during startup flow based on results of rheological measurements coupled to ultrasonic velocimetry is reported. Note that although two observed flow instabilities of different materials on different scales are shown in these two chapters, the both experiments are intended to find basic physics underlying fluctuation phenomena in unsteady flows related to the multiplicity in reality. Analysis of volcanic oscillation phenomena associated with the 1986 Izu-Oshima eruption is presented in Chapter 4. Attention points in the analysis are temporal variations in volcanic oscillations associated with the volcanic activities by estimating the source locations. Although there is still a room for further investigation, a possible link between the experimental study and the field-observational study are referred in Discussion.

# Chapter 2

## Experimental Study 1: Undershoot of Pressure Difference

### 2.1 Overview

Variation in rheological properties at rest with time, which is called as aging [62], is a typical property of suspension consisting of interacting particles. Since aging is caused by temporal change in arrangement of solid phase, it is expected to prominently affect the emergence of the rheological multiplicity, which can generate self-induced oscillations in dense suspensions as sited in Introduction 1.3.3. Aging in itself is not a new idea in the field of rheology and it is known to induce stress perturbations in the rheometry of a transient start-up flow [26]. Based on the fact, it is also expected to affect large-scale flow phenomena.

This experimental study aims to reveal the effects of aging on the pressure perturbations arising during a transient flow, and to establish a relationship between the pressure perturbations and the rheology in terms of aging. Note that understanding the relationship is required to discuss magma rheology since magma flows on a large scale in nature although the characteristics have been mainly observed in rheometers without linking to the large-scale flow, and without consideration for aging. Here the effects of aging are tested in flow experiments in a chamber and pipe system mirrored a general volcanic system consisting of a magma chamber and a conduit. Sections 2.2 and 2.3 describe the details of suspension used in this experiment and the experimental setup. Section 2.4 examines the experimental results of the start-up flow experiments. In Section 2.5, after proposing a model for pressure perturbations, the model is tested and confirmed by rheological measurements. Also the section touches on implication for volcanic system and discusses issues to be considered next.

---

## 2.2 Materials

Crystal-bearing magma is known to form crystal-clots due to the interactions (Fig. 1.13). The aggregation with high deformability results in its lower critical volume fraction  $\phi_c$  at which the yield stress first appears, 0.13–0.31 [46, 51, 105] whereas  $\phi_c$  in suspensions of hard-core particles and viscous melt is above 0.40 [69]. This fact implies that crystal-bearing magma is not a simple two-phase system and the properties are hard to be described by hard-core particles. In order to see rheological behaviors of magma due to its high deformability, using materials that can duplicate “soft” behaviors is required. For this reason, *p*-NIPAM aqueous suspension is utilized here. In fact, our measurements find that the sample has  $\phi_c$  of around 0.2 and the multiplicity, which is the fundamental concept of this study.

### 2.2.1 Microstructure

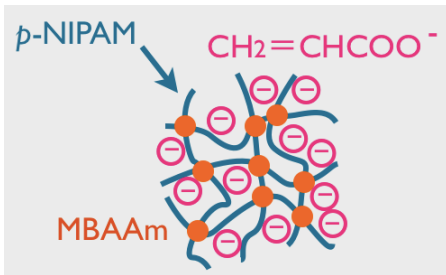


Figure 2.1: Structure of *p*-NIPAM aqueous suspension.

The *p*-NIPAM aqueous suspension comprises a mixture of distilled water and Thermogel350 (Kohjin Co., Ltd.), which itself is composed of poly (*N*-isopropylacrylamide) microgel (*p*-NIPAM) with added acrylic acid and *N,N'*-methylenebisacrylamide (MBAAm). As Figure 2.1, *p*-NIPAM is charge-free corded polymer. The acrylic acid ( $\text{CH}_2 = \text{CHCOO}^-$ ) is added to trap water, and MBAAm is cross-linker. In this case, the attractive force is entanglement of *p*-NIPAM strings while repulsion between  $\text{CH}_2 = \text{CHCOO}^-$  narrowly exists so as not to produce strong adhesion. The soft-core particles in *p*-NIPAM aqueous suspension absorb water and swell at low temperatures below 35°C while they expel water and shrink at higher temperature [108].

Although rheological variations due to the temperature change are interesting, here we focus on the behaviors at a constant temperature, 23°C in order to see the effect of particle arrangement in the absence of the temperature change in the size.

The interpretation of structural changes of crystals (resp. particles) in magmatic system (resp. *p*-NIPAM aqueous suspension) is schematically shown in Fig. 2.2. Despite the difference in the shape of crystals and particles, the two systems share a common characteristic that solid phase forms networked structure by connecting each other at rest, or by the effect of aging, while the structure is broken by shear.

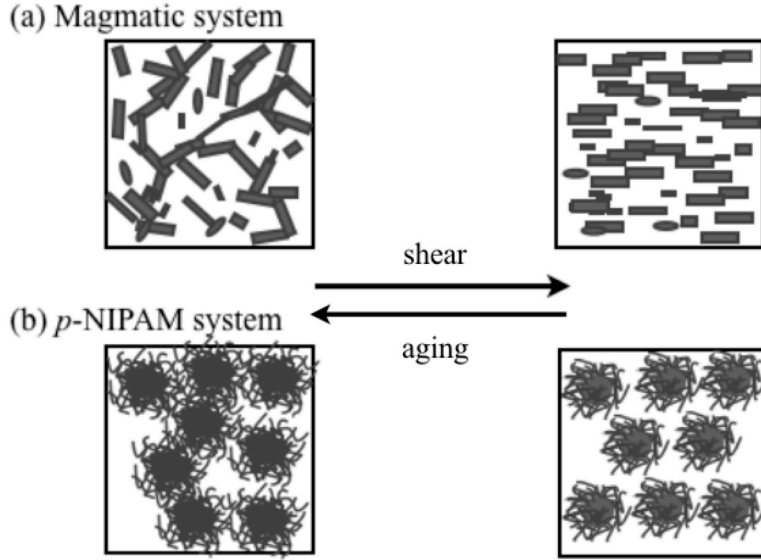


Figure 2.2: Analogy to magmatic system

Optical microscopy establishes the particle size is several hundred  $\mu\text{m}$  in water at room temperature after several minutes to absorb water and become stable (Fig. 2.3). Its production process and material structure lead the cross-linker particles to be not exactly spherical and to have a distribution of sizes, in contrast to common mono-dispersed *p*-NIPAM core-shell suspensions [21, 38].

This study focuses on aging [99, 116] in suspensions mainly containing 1.5 wt% *p*-NIPAM; the corresponding volume fraction of the solid phase in the suspensions is 0.85. The only exception is the 1.0 wt% *p*-NIPAM (volume fraction 0.72) suspension considered in Section 2.4.1. The volume fraction is determined by gravimetric estimation by separating gels from aqueous suspensions using a sieve and a centrifuge. The suspensions used in this study are dense enough to be a state above the jamming transition, 0.68 [80]. However, the suspensions are deformable above the transition, because they are composed of soft-core particles [91].

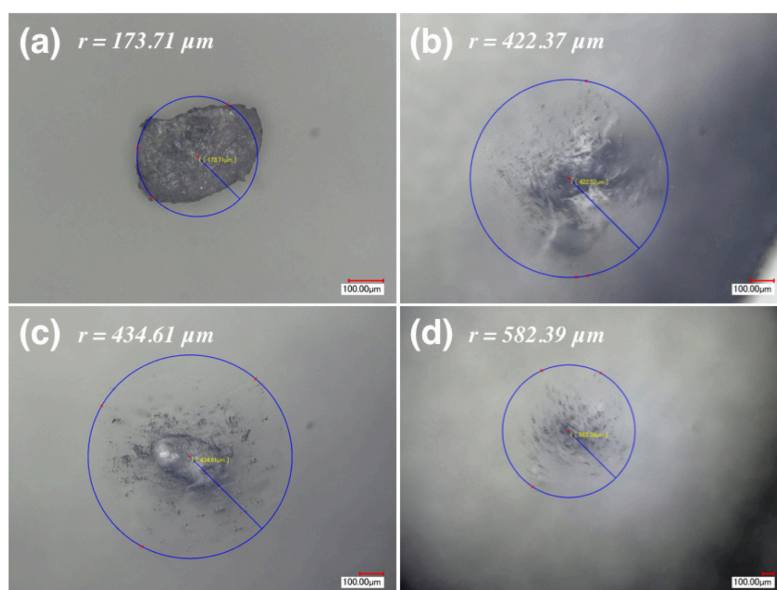


Figure 2.3: Images that show the size change of particle taken by a digital microscope (VHX-1000, Keyence Co., Ltd.). (a) Dried commercial particle in the air. (b)-(d) Time change of the particle 1-3 minutes after putting into the water, respectively.  $r$  is the radius of the particle and red lines show the scale of  $100 \mu\text{m}$ .

## 2.2.2 Fundamental Rheology

First, Fig 2.4 shows a fundamental rheology of the suspension, temporal change in the shear stress at the constant shear rate of  $0.1 \text{ s}^{-1}$ . The measurement was performed after preshearing at  $80 \text{ s}^{-1}$  for 30 s and resting for 1 min. At the beginning, the shear stress increases to the peak and then it decreases to become constant. The peak, or overshoot of the shear stress in the start-up flow is regarded as a *yield stress*. Therefore the rheological behavior indicates the change in arrangement of particles by shearing in association with the stress overshoot.

Consider aging in its rheology next. Fig. 2.5 shows the relationships between shear stress  $\sigma$  and shear rate  $\dot{\gamma}$  (flow curve) observed after various aging times in shear rate sweeping tests conducted weeks apart. The tests are conducted by increasing the shear rate from  $0.072 \text{ s}^{-1}$  to  $50 \text{ s}^{-1}$  (Lower shear rates are not tested owing to limitations of the equipment). Measurement at each shear rate is for 30 s, longer than necessary to reach a stable state in the stress-strain relation. Preshearing is imposed prior to the main measurements at  $80 \text{ s}^{-1}$  for 30 s. Aging times of 5 s to 3 h are tested. Fig. 2.5(a) shows results measured after the first sample is made, while (b) shows data taken three weeks later. During the three weeks, the sample was used for other experiments and replenished. The rheological values vary slightly due to the evaporation and supplement of water, but the trend attributable to aging is

consistent: at high shear rates all the data are similar regardless of the aging time, while at low shear rates the points show lower gradients after longer aging times. Particularly after a long aging time, two shear rates exist at one shear stress in the low shear rate range. Given that shear rate is expressed as a multiple-value function of shear stress, it is referred as multiplicity in the relation between shear stress and shear rate. The emergence of multiplicity after long aging times indicates that it is affected by aging. The existence of multiplicity in the sample caused by aging is confirmed using three different rheometers, one of which has a completely different geometry, a coaxial cylindrical rheometer.

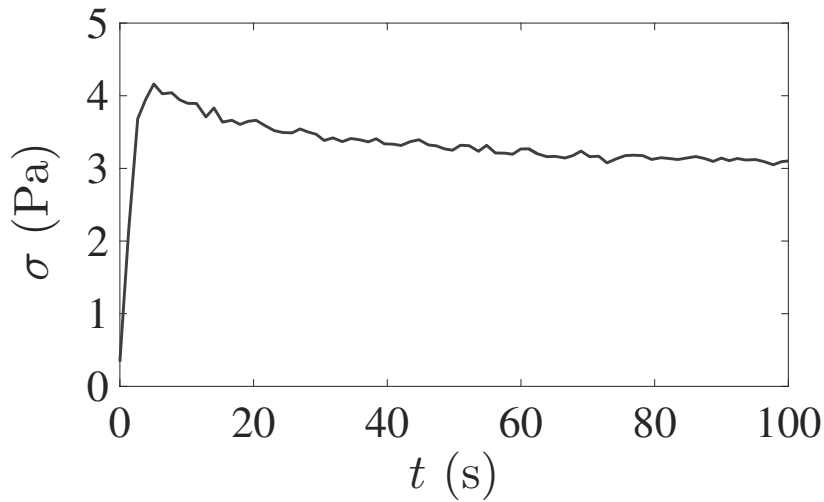


Figure 2.4: Shear stress response  $\sigma(t)$  at shear rate of  $0.1 \text{ s}^{-1}$ .

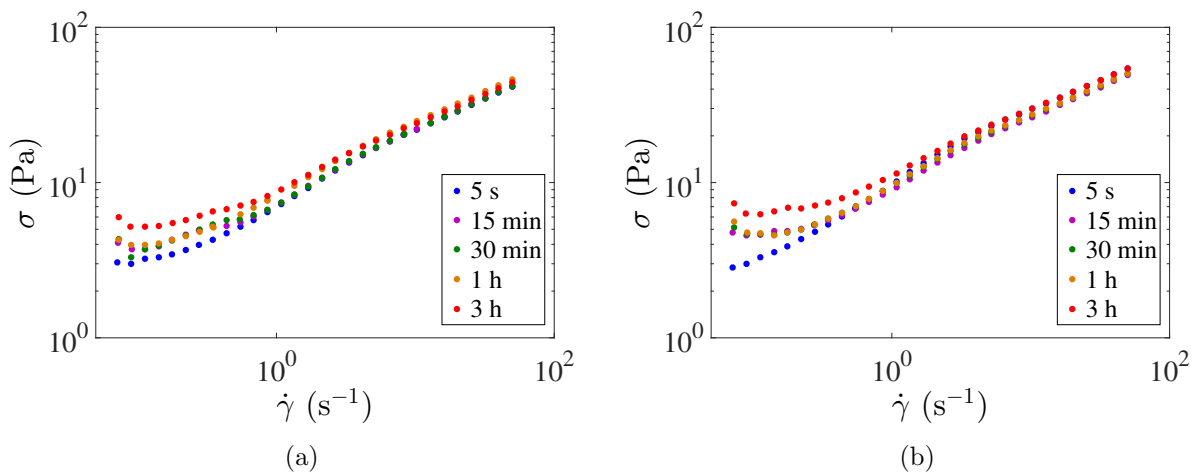


Figure 2.5: Flow curve  $\sigma$  vs  $\dot{\gamma}$  after aging times (5 s–3 h). The data in (a) are taken before the start-up flow experiments and those in (b) are taken three weeks later.



---

## 2.3 Experimental Setup

### Start-up Flow with Pump

A system using a pump for testing start-up flow in a pipe is shown in Figure 2.6(a). The system consists of a tube (diameter,  $7.5 \cdot 10^{-3}$  m), a cylindrical chamber (internal diameter, 0.06 m), and a pump. Fast flow tests are conducted using a diaphragm pump (Liquiport, KNF Flodos AG), and slow flow tests (below  $2.2 \cdot 10^{-2}$  m·s<sup>-1</sup>) are conducted using a rotary displacement pump (Hicera pump V series, Iwaki Co., Ltd.). These pumps supply fluid to the system from below. The length from the pump to the flow meter is 1.84 m, the height of the chamber is 0.11 m, and the height of the pipe is 0.40 m. The system mirrored a general volcanic system consisting of a magma chamber and a conduit with reference to [64]. The rigidity of the system is ensured by using acrylic tubes for the connections between the pump, the flow meter, and the chamber, as only the effects of fluidic behavior are desired.

Sensor heads (AP-10s, Keyence Co., Ltd.) connected to amplifier units (AP-V80, Keyence Co., Ltd.; response time 5 ms) are embedded in the pipe to measure pressures. Two pressure sensors are placed in the pipe 0.17 m apart. The flux is measured by a tension/compression load cell (TCLZ-50NA, Tokyo Sokki Kenkyujo Co., Ltd.; resonant frequency 0.45 kHz) and an amplifier (DA-16A, Tokyo Sokki Kenkyujo Co., Ltd.; set as 4 V/4000  $\mu\epsilon$ ). A PC-based measurement instrument (WE7000, Yokogawa Electric Co., Ltd.) is used for data acquisition. Sampling is at 100  $\mu\text{s}$  intervals for 90 s. The measured pressures shown below are low-pass filtered (0.1 Hz) to eliminate pump pulsation; hydrostatic components are also removed.

To conduct start-up flow experiments with variable aging times, the experimental system is first filled with fluid using the pump. This process is regarded as the preshearing, because the fluid is strongly sheared by the pump. During the subsequent aging, the fluid remains undisturbed in the experimental system for a certain duration. After the aging time, the duration between the preshearing process and the main test, the pump is then started, and the pressure at the two locations along the pipe and flux are measured.

### Start-up Flow without Pump

Start-up flow experiments are conducted without using a pump to check the effect of pump control and to clarify the nature of self-induced phenomena during the experiment. The system without a pump, shown in Figure 2.6(b), consists of a cylindrical chamber (internal diameter, 0.06 m) and a pipe (diameter,  $7.0 \cdot 10^{-3}$  m). The length of the entire system is 0.53 m, the height of the chamber is 0.16 m, and the height of the pipe is 0.37 m. The chamber and the pipe are acrylic.

Four pressure sensors are placed in the pipe  $8.5 \cdot 10^{-2}$  m apart. Pressure sensors P2 and P4 in Figure 2.6(b) are those described in Section 2.3; pressure sensors P1 and P3 (PGM-05KG, Kyowa Electronic Instruments Co., Ltd.; resonant frequency 3 kHz) are connected to an amplifier (DA-16A, Tokyo Sokki Kenkyujo Co., Ltd.; set as 4 V/1000  $\mu\epsilon$ ). The same modules as in Section 2.3 are used for data acquisition. Samples are taken at 1 ms intervals for 250 s. The measured pressures shown below are low-pass filtered (1 Hz) to eliminate noise; hydrostatic components are also removed.

The experiment is performed by the following procedure. The fluid is first presheared by stirring with a glass rod. It then flows until the system is filled and the height of the fluid in the chamber is 0.11 m. The system is closed by a plug and left for the aging time. Fluid flow is then induced by pulling out the plug. Pressures at the four positions along the pipe and flux are measured. In this case the driving force is gravity.

## Rheological Measurement

Shear-rate-controlled tests are performed using a cone-and-plate rheometer (cone diameter,  $4.0 \cdot 10^{-2}$  m with a cone angle of  $0.4^\circ$ ; CVO Rheometer, Bohlin) at 23 °C. Prior to the main measurement, preshearing is applied at  $80 \text{ s}^{-1}$  for 30 s; a subsequent aging time is applied to allow aging.

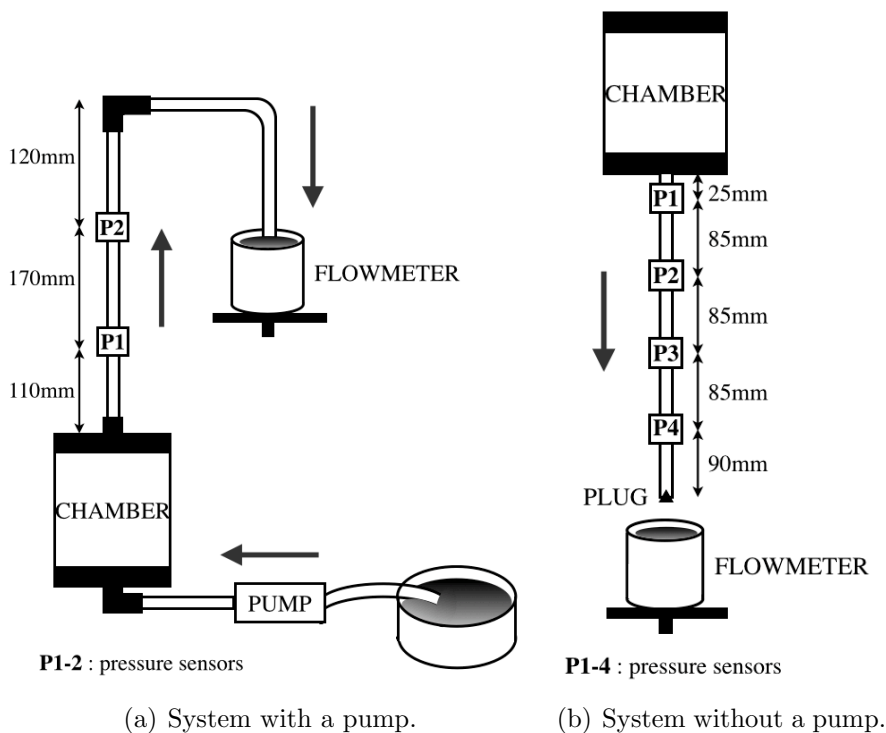


Figure 2.6: Apparatus for start-up flow measurement.

---

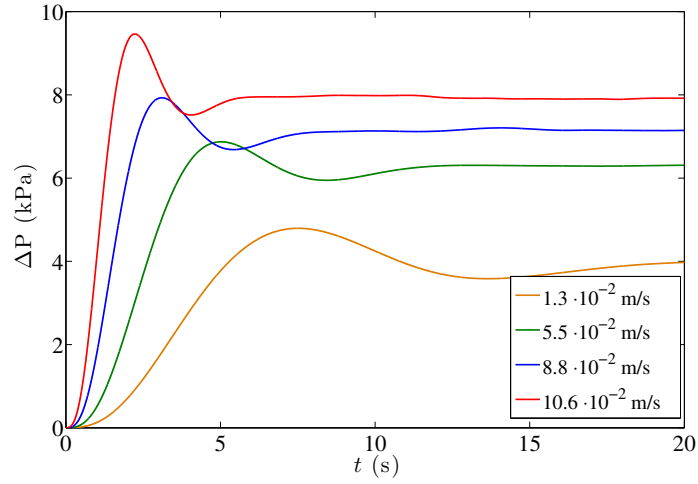
## 2.4 Results

### 2.4.1 Start-up Flow with Pump

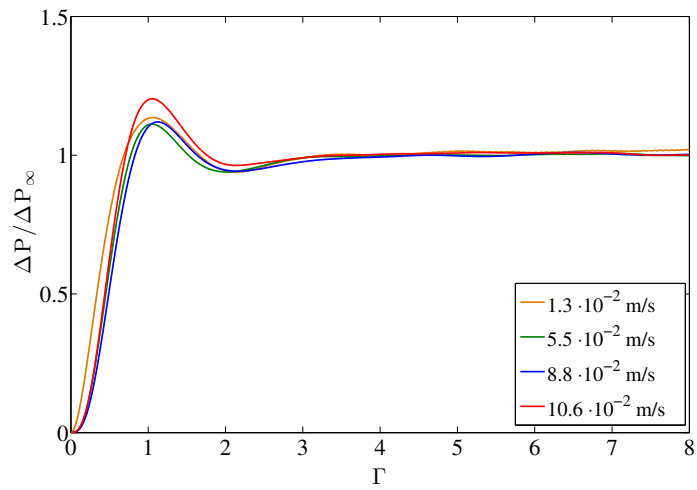
Start-up flow experiments using a pump are conducted in the system shown in Figure 2.6(a). Pressures are measured at two locations along the pipe, and the flux is also measured under changing conditions.

#### Pressure Perturbations under Different Fluxes

The temporal variations in the pressure difference along the pipe,  $\Delta P(t) = (P1(t) - P2(t)) - (P1(0) - P2(0))$  in Figure 2.6(a), are measured at different flow velocities (Figure 2.7(a)). Initial pressure perturbations are observed, and the faster the flow velocity, the shorter the time scale of these perturbations. However, converting the time to scaled time  $\Gamma = t \times v/d$  (where  $v$  is the mean flow velocity for a particular experiment measured by the flow meter, and  $d$  is the distance along the pipe between the two pressure sensors), and scaling the pressure difference by the value,  $\Delta P_\infty$ , in the steady state after the perturbation reveals identical behavior of the fluid irrespective of the type of pump and flow velocity (Figure 2.7(b)): the pressure difference reaches a maximum at  $\Gamma = 1$  after a large initial increase; it then decreases to a prominent undershoot at  $\Gamma = 2$ , before settling to a steady value. This means that the flow property does not depend on the flow velocity. Previous works have attributed the origin of the pressure/stress overshoots during flow start-up to compressibility [89, 111], viscoelasticity [30, 121], Péclet number [33, 67], or yield stress [59]. However, the pressure perturbation in the present experiment differed from the overshoots observed in previous studies, because it occurs on a much longer time scale compared with the passage time of the elastic wave or the Maxwell time for viscoelastic relaxation. That the time scale of the pressure perturbation is scaled by the travel time of the flow indicates that this pressure perturbation traveled with the flow.



(a)  $\Delta P$  vs. time.



(b)  $\Delta P/\Delta P_\infty$  vs.  $\Gamma$ .

Figure 2.7: (a) Temporal variations in the pressure difference for flow velocities of  $1.3 \cdot 10^{-2} \text{ m}\cdot\text{s}^{-1}$  to  $10.6 \cdot 10^{-2} \text{ m}\cdot\text{s}^{-1}$ . (b) Variations in the non-dimensional pressure difference with respect to the scaled time. Suspension concentration 1.0 gel wt.%; waiting 1 h. A rotary displacement pump (Hicera pump V series, Iwaki Co., Ltd.) is used for the flow velocity of  $1.3 \cdot 10^{-2} \text{ m}\cdot\text{s}^{-1}$ ; a diaphragm pump (Liquiport, KNF Flodos AG) is used in the other three tests.

---

## Effect of Aging on Start-up Flow

Figure 2.8 shows the evolution of pressure difference after aging times of 5 s to 3 h under the same experimental conditions. The shear stress at the tube wall in the right y-axis is estimated by Equation (5) in Appendix. Prominent changes due to aging are observed in the undershoot phase of the pressure perturbations. After aging time of 5 s there is no undershoot, but longer aging times lead to the appearance of undershoot, with the perturbation appearing similar to a heavily damped oscillation. These results indicate that the undershoot of  $\Delta P$  is induced by aging. A longer waiting yields a larger amplitude of the undershoot in the pressure difference at around 15 s. Hereafter we focus on the undershoot, which is affected by aging. On the other hand, all cases show similar overshoot behavior regardless of the aging time. The overshoot is observed even through a straight pipe without a chamber (see Figure 2.9) while there is no overshoot when a start-up flow is driven downward only by gravity without using a pump (see Section 2.4.2). Therefore it seems to be affected by the pump control.

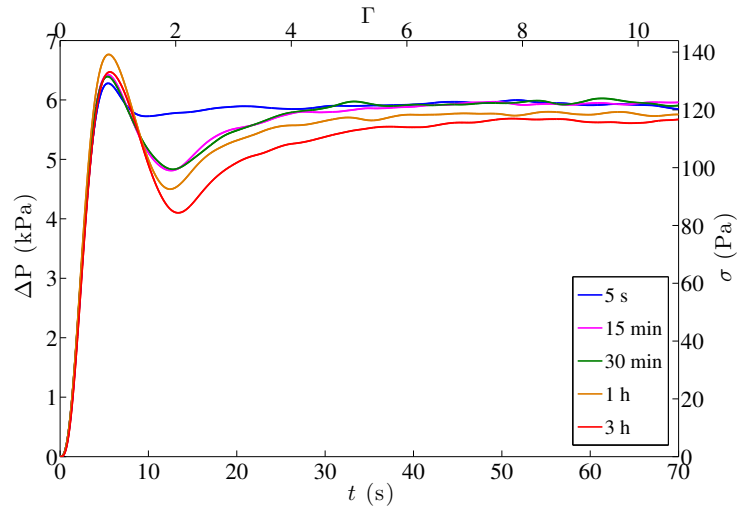


Figure 2.8: Pressure difference along the pipe  $\Delta P$  and converted shear stress  $\sigma$  vs. time  $t$  and  $\Gamma$  after different aging times of 5 s to 3 h. Suspension concentration 1.5 gel wt.%; mean flow velocity  $2.6 \cdot 10^{-2} \text{ m}\cdot\text{s}^{-1}$ .

---

## Effect of Chamber

Start-up flow experiments are conducted in two different geometries: with and without the chamber (Figure 2.9). Undershoot is observed only when the experimental system has the chamber (black line); without the chamber the steady state is reached without undershoot (gray line). A large reduction of diameter—where the chamber exit leads to the conduit—is necessary to generate the undershoot, which is the same condition necessary to induce spurt or stick slip flow [28, 74, 103]; this suggests that the mechanism causing the undershoot is related not only to aging but also to the flow geometry.

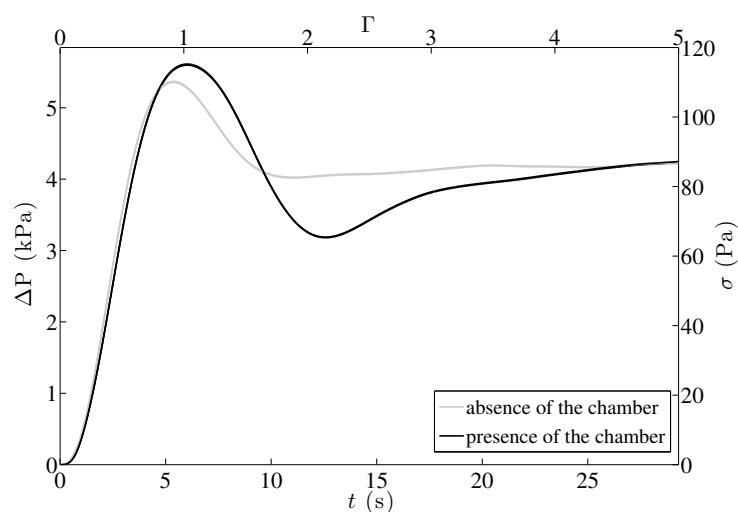


Figure 2.9: Pressure difference along the pipe  $\Delta P$  and converted shear stress  $\sigma$  vs. time  $t$  and  $\Gamma$  for configurations with (black line) and without (gray line) a chamber. Suspension concentration 1.5 gel wt.%; aging time 1 h; mean flow velocity  $2.9 \cdot 10^{-2} \text{ m}\cdot\text{s}^{-1}$ .

---

## 2.4.2 Start-up Flow without Pump

Start-up flow experiments with a pump reveal that aging and the presence of a chamber are necessary conditions for the undershoot. On the other hand, the overshoot appears owing to pump control. Therefore, because the pump affects the flow behavior, start-up flow experiments without a pump are performed in the system shown in Figure 2.6(b) to investigate the self-induced phenomena. The flow velocity in this case (around  $3.9 \cdot 10^{-3} \text{ m}\cdot\text{s}^{-1}$ ) is lower than that in the case using a pump ( $1.3 \times 10^{-2} \text{ m}\cdot\text{s}^{-1}$  to  $0.11 \text{ m}\cdot\text{s}^{-1}$ ). The four pressures along the pipe and the flux are measured under different conditions.

### Effect of Aging on Start-up Flow

#### a) Pressure Difference

Pressure differences are measured at the top, middle, and bottom of the pipe. (These being the differences between readings at positions  $P1$  and  $P2$ ,  $P2$  and  $P3$ , and  $P3$  and  $P4$ , respectively; see Figure 2.6(b).) Two behaviors relating to aging are evident in Figure 2.10: aging leads the undershoot to appear and the  $\Delta P$  to decrease. That undershoots appear with aging in a system without a pump demonstrates that it is not caused by the effect of pump control, but is rather self-induced. Conversely, the overshoot observed in the tests with a pump is not observed in these tests. Therefore, we consider the overshoot as an artifact generated by the pump that is different from the overshoots observed in previous studies [26, 33, 121]. For this reason, the overshoot is not essential in this case. However, aging led to another kind of overshoot emerging in the middle and bottom  $\Delta P$  results. This may be related to the stress overshoot of start-up flow observed in the rheometer (Fig. 2.4), which is caused by the change in particle arrangement by shear. In start-up flow experiments using a pump, it seems reasonable to suppose that the self-induced overshoot is not visible due to the large perturbation caused by the pump.

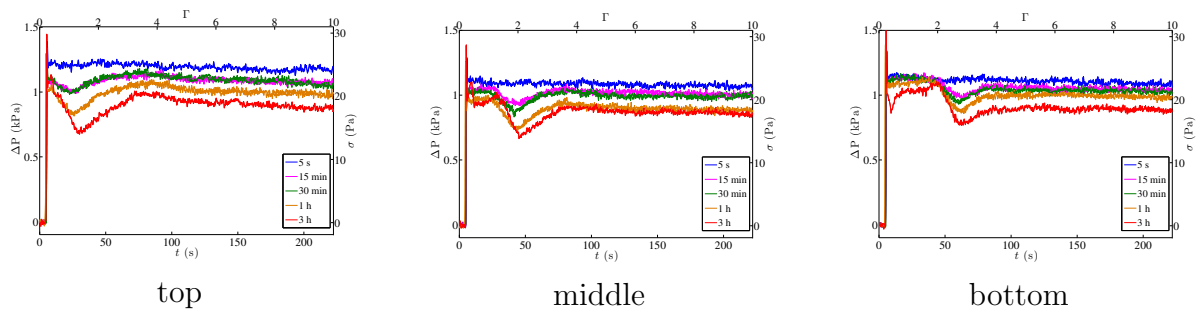


Figure 2.10: Pressure differences at different sections along the pipe  $\Delta P$  (top, middle, and bottom), and converted shear stress  $\sigma$  vs. time  $t$  and  $\Gamma$  observed after different aging times of 5 s to 3 h. Suspension concentration, 1.5 gel wt.%; mean flow velocity  $3.9 \cdot 10^{-3} \text{ m}\cdot\text{s}^{-1}$ .

## b) Pressure Profile

The pressure data taken by four pressure sensors along the pipe ( $P1$ ,  $P2$ ,  $P3$ , and  $P4$ ) form linear relationships in Figure 2.11. With increasing aging time, the pressure profile changes, and the pressure perturbation propagates with time.

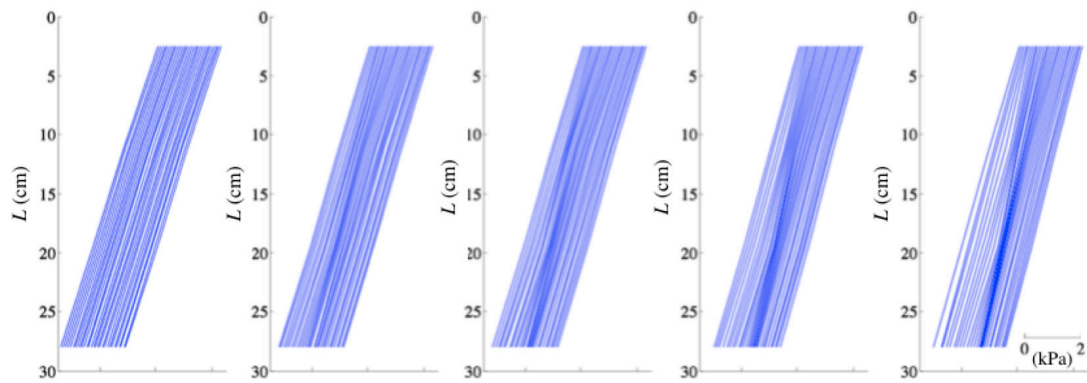


Figure 2.11: Pressure profiles along the pipe for different aging times (5 s, 15 min, 30 min, 1 h, and 3 h from left to right). Measurements at each location are taken at 4 s intervals from 7 s to 125 s. Data measured at interval are shifted on the x-axis by 0.08 kPa from those of the previous interval.



---

c) Comparison Pressure Data with Images

The above results revealed that the undershoot appears with aging regardless of the driving force. The next investigation sought to clarify the way in which the undershoot is induced. The fluid present in the chamber before the commencement of the experiment is first colored red to distinguish it from that in the pipe, thus allowing the discernment of which part of the fluid affected the undershoot. The results in Figure 2.12 show that when the front of the red fluid reached a pressure sensor, the  $\Delta P$  began to decrease. Then the  $\Delta P$  increased with time. The  $\Delta P$  perturbation propagated with the flow in the pipe from the top to the bottom. The pressure perturbation occurred when the red fluid flowed through the pipe, *i.e.*, the red fluid generated the undershoot. After the red fluid reached the end of the pipe, the pressure difference became almost constant. An interesting observation is that the time the front of the red fluid took to travel from one pressure sensor to the next became linearly shorter with time. *i.e.*, it accelerated. The front of the red fluid is softened at the chamber exit as it entered the pipe, thus it is considered to have had a lower viscosity than the white fluid. Therefore, the red fluid pushed aside the white fluid and flowed more quickly owing to the rheological change. Although these results indicate that the propagation of the fluid, which existed in the chamber before the experiment, caused the undershoot, the responsible area within the chamber is not elucidated in this test.

In the next experiment, only the fluid at the base of the chamber to an approximate height of  $5 \cdot 10^{-3}$  m (volume  $1.41 \cdot 10^{-5}$  m<sup>3</sup>) is colored red to see which part of the fluid affects the undershoot. The results indicate that a certain amount of the red fluid remained at the outer side of the chamber after the experiment. The volume of the red fluid is smaller than the estimated total volume of discharged fluid,  $4.62 \cdot 10^{-5}$  m<sup>3</sup>, suggesting that only a part of the red fluid flowed into the pipe. This indicates the fluid responsible for the undershoot came from the bottom part of chamber, while the trailing fluid were from the inner part.

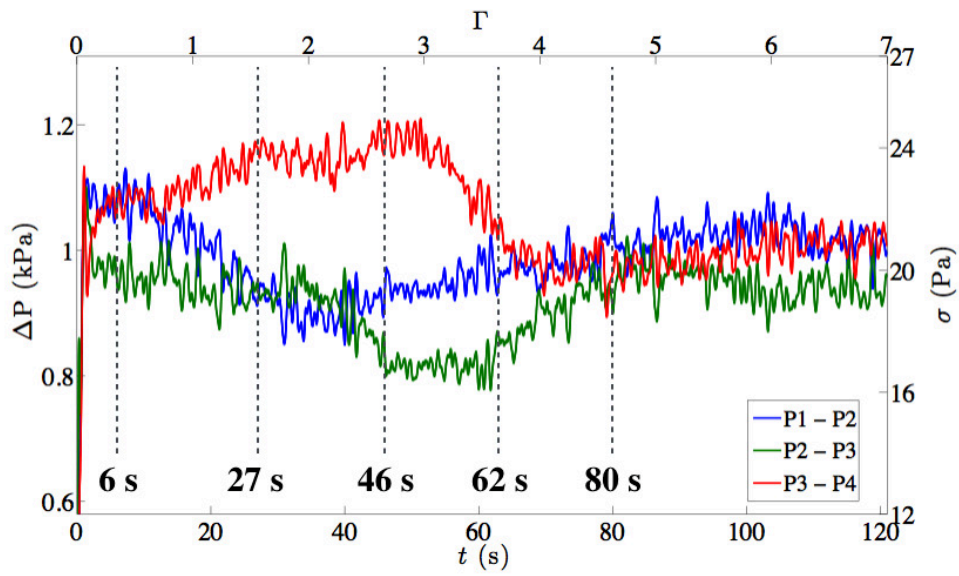
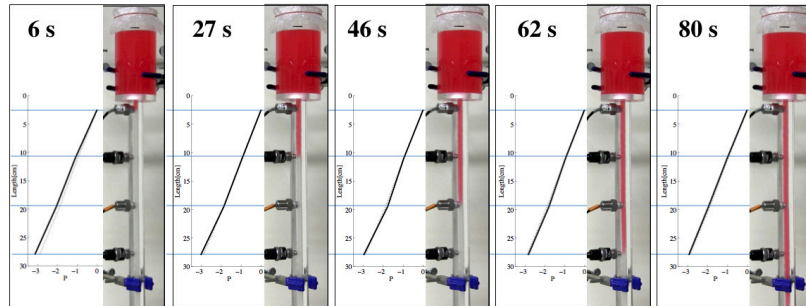


Figure 2.12: Images and pressure changes recorded at different times. Suspension concentration 1.5 gel wt %; aging time 3 h.

---

### 2.4.3 Linking Rheology and Pipe Flow in Terms of Aging

The relation between shear stress and shear rate is measured in the rheometer with changing the aging time as shown in Figure 2.5. Start-up flow experiments were also conducted changing the aging time. Here we compare the aged shear rheology and the pressure perturbation in the pipe flow.

Rheological measurements in Figure 2.5 make it possible to estimate the pressure gradient along the pipe,  $\Delta P/\Delta z$ , for a given mean flow velocity based on the method described in Appendix. Figure 2.13 shows the relation between the pressure gradient and the mean flow velocity. The lower- and the upper-limit curves of the shaded zone were obtained from the rheology data measured before the experiments (Figure 2.5(a)) and later (Figure 2.5(b)), respectively. The rheology data for the aging time of 1 h were used in the calculation and the results are compared with the measured pressure gradient for the same aging time (the circles in Figure 2.13) in the steady state of the pipe flow in Figures 2.8, 2.9, and 2.10. Although not all results in flow experiments are within the shaded zone, which is estimated by the shear rheology, they are close. This implies that the rheological measurements and start-up flow experiments were conducted properly and they are linked each other.

The pressure difference of the undershoot and that in the steady state after the undershoot for each aging time are also compared with the estimated pressure difference from the shear rheology for the corresponding aging time in Figure 2.5. The method of estimating the pressure difference by aged shear rheology is described in Appendix. The result (Figure 2.14) shows that the pressure difference estimated by the shear rheology slightly increases with aging. On the other hand, both the pressure difference of the undershoot and that in the steady state after the undershoot decrease with aging in the start-up flow experiments. In this way, the aging effect in the pipe flow cannot be expected by only the shear rate sweeping test data for aged shear rheology. It seems that there are other factors associated with aging.

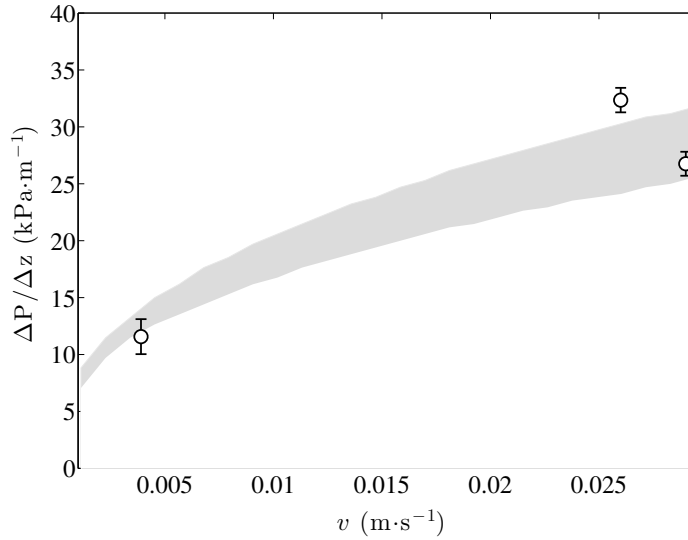


Figure 2.13: The relation between the pressure gradient  $\Delta P / \Delta z$  and the flow velocity  $v$  for the aging time of 1 h and suspension concentration of 1.5 gel wt %. Gray area is the range of pressure difference estimated by two rheological measurements shown in Figure 2.5 while circles are results in start-up flow experiments. The left circle shows the result without using the pump.

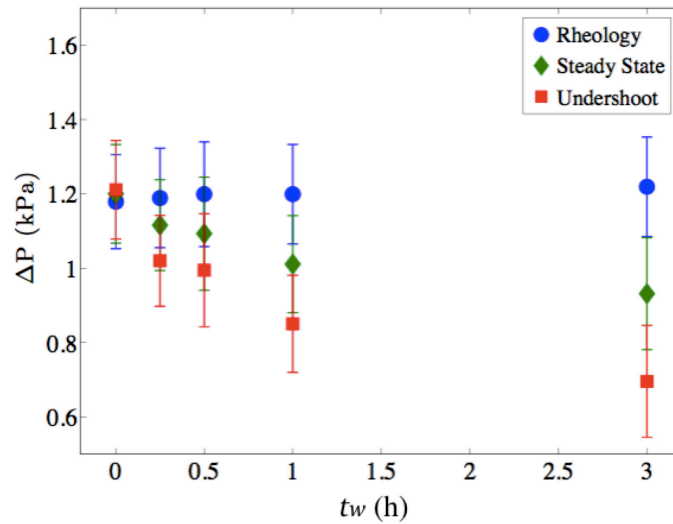


Figure 2.14: Variation in the pressure difference  $\Delta P$  with the aging time for mean velocity  $3.9 \cdot 10^{-3} \text{ m}\cdot\text{s}^{-1}$  and suspension concentration 1.5 gel wt %. Blue dots are estimated by rheological data shown in Figure 2.5. Red squares are  $\Delta P$  of the undershoots while green diamonds are  $\Delta P$  in the steady state after the undershoot in the case without using the pump.

---

## 2.5 Interpretation and Consideration

Here we propose a model to explain the undershoot in the start-up flow. The model should explain the following experimental observations.

- ① The pressure perturbation propagates with flow (Figure 2.7).
- ② The undershoot appears after sufficient aging (Figures 2.8 and 2.10).
- ③ The chamber is required for the undershoot to be induced (Figure 2.9).
- ④ The undershoot is generated when the fluid initially presented around the chamber exit flows through the pipe (Figure 2.12).
- ⑤  $\Delta P$  in the steady state after the undershoot decreases with aging (Figures 2.8 and 2.10) though it is expected to increase based on the rheological data (Figure 2.14).

The occurrence of the aging-induced undershoot requires the propagation of softened fluid (①, ②, ③). Here we consider the transport in a pipe of fluids with different shear histories, and thus with different rheological properties. Rabideau *et al.* [100] examined the velocity field during extrusion using a yield stress fluid. Their system is composed of a chamber connected to a pipe, which is similar to our system. They observed the change of velocity field with different radius ratios of pipe to chamber, from 1:2 to 1:40. Our system, with a ratio of 1:8.6, falls within their range. In all cases strong shear is observed at the geometric constriction. In our experiment, shortly after starting the flow, the fluid near the bottom wall of the chamber flowed. This fluid is labeled as the leading fluid (**LE**), with the following fluid as trailer fluid (**TR**). **TR** experienced a shear history that is different from that of **LE**, but which may nonetheless depend on aging. As shown in Figure 2.15(a), sufficient aging led to a radially narrow flow field owing to the increased yield stress of the surrounding aged fluid (**AG**) (Figure 2.5). Without aging, the flow field can spread (Figure 2.15(b)), and the shear at the chamber exit is smaller than that with aging. In this way each of the three fluids (**LE**, **TR**, and the fluid originally present in the pipe (**PF**)) had a different shear history. The rheological characteristics of the fluids are also expected to be different and dependent on their shear histories. **LE** and **TR** are assumed to have lower viscosities than **PF**, because they experienced strong shear during the extrusion into the pipe. We consider **LE** and **TR** cause the undershoot (④) and the reduced  $\Delta P$  in the steady state (⑤) respectively. Verification of the hypothesis depends on there being differences between the rheological properties of **LE** and **TR**; therefore, we performed rheological measurements of the fluids under different shear histories.

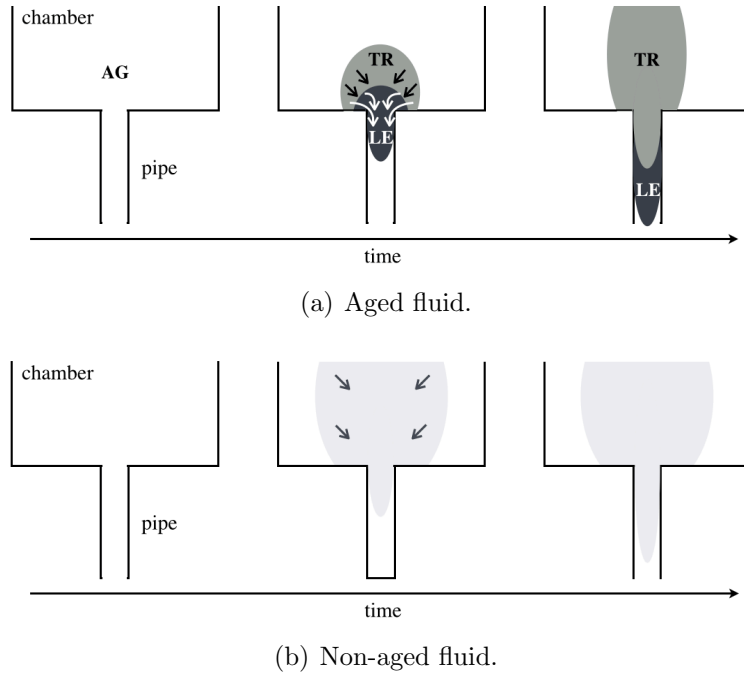


Figure 2.15: Models for the different behavior of fluid transport between aged and non-aged fluids.

### 2.5.1 Characterization of LE and TR fluids

The purpose of the rheological measurements is to clarify the distinction in the rheology of **LE** and **TR** and to confirm the mutual interaction between rheology and pipe flow. According to our model of the start-up flow, the aged fluid experiences a strong shear to change its rheology as it leaves the chamber. The shear subsequently imposed on the fluid becomes lower and constant in the pipe. This process is simulated in the rheological measurements. Preshearing is imposed in the way described in Section 2.3 prior to the aging time. After a certain aging, the first shearing is applied. It simulated the high-shear process at the chamber exit. The first shear is applied on the fluid for 3.5 s, which corresponds to the time from when the plug is removed from the pipe to when the red fluid enters the pipe (Figure 2.12). The first shear rate ( $\dot{\gamma}_{first}$ ) ranges from  $0.2 \text{ s}^{-1}$  to  $5.0 \text{ s}^{-1}$ . The main constant shear rate ( $\dot{\gamma}_{const.}$ ) then immediately follows. Its value is fixed at  $1.22 \text{ s}^{-1}$  according to the motion pictures. Shear stress is measured every 0.5 s for 200 s of which the last 50 s is regarded as the steady state. Results of the tests with aging times of 10 s and 30 min are compared, because aging effects are seen in the start-up flows after aging time of 30 min.

Figure 2.16(a) shows the shear stress in the steady state for different aging times and  $\dot{\gamma}_{first}$ . There are two points for each condition, because each experiment is conducted twice. Interestingly, the mean shear stress after aging of 30 min is lower than that after aging time

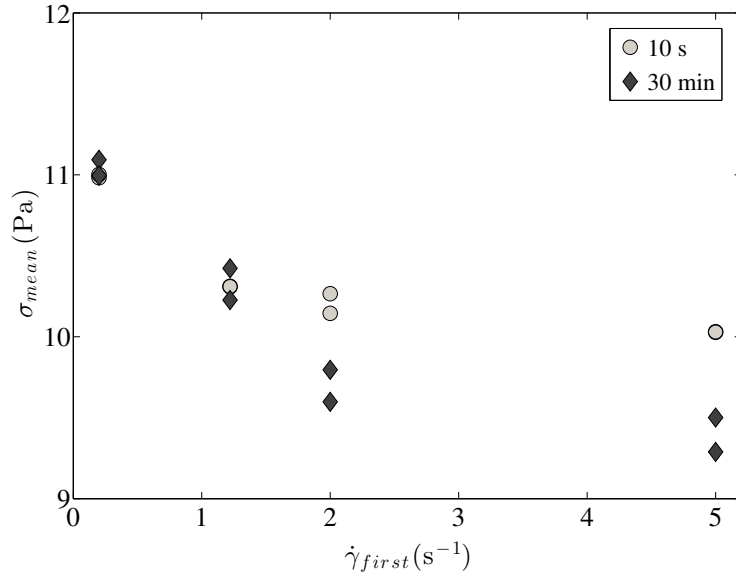
---

of 10 s when  $\dot{\gamma}_{const.} < \dot{\gamma}_{first}$ . This means that when the fluid initially receives a stronger shear than  $\dot{\gamma}_{const.}$ , the shear stress becomes lower with aging.

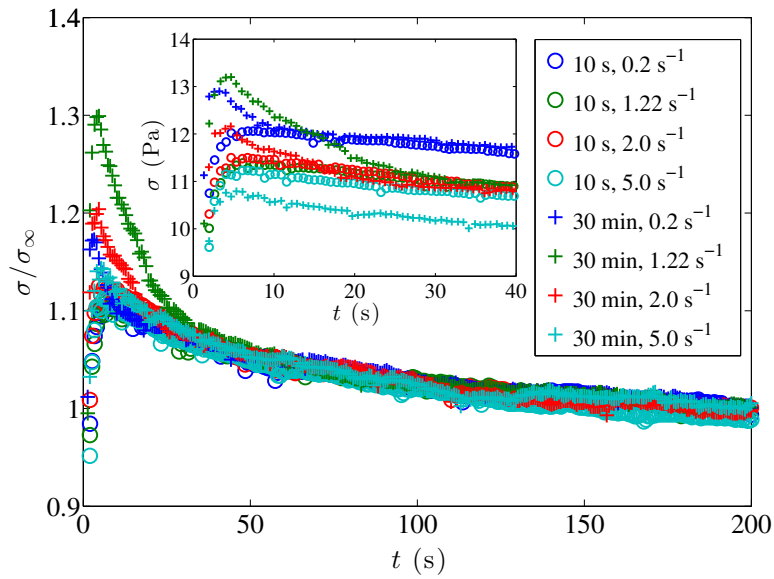
Figure 2.16(b) shows the temporal variation in the shear stress during the main constant shear rate test from which data in Figure 2.16(a) are obtained. The shear stresses in the main frame are normalized by the corresponding steady state values shown in Figure 2.16(a). The data without aging collapse into a single master curve, while the data with aging have overshoots that do not follow the master curve. The inset shows overshoot part in the un-scaled stress. Shear stresses at the peaks of the overshoots also decrease with increasing  $\dot{\gamma}_{first}$  even though the trend is different from those for the steady state values. This indicates that the critical shear stress, which breaks structures of the fluid to makes it flow at the beginning, also depends on  $\dot{\gamma}_{first}$ , or shear history when the fluid is aged. The effect of aging and shear history is different from that appeared after the overshoot, which is focused in this paper.

In Figure 2.16(a) and the inset of Figure 2.16(b), greater  $\dot{\gamma}_{first}$  is evidently correlated with lower shear stress. It is important to note that the effect continues long after the first shearing. The initial reduction rate increases with aging.

Given that the pressure difference is proportional to shear stress, this result can account for the undershoot behavior of the aged fluid in the start-up flow. The undershoot of  $\Delta P$  is induced by the propagation of the **LE** fluid, which has a lower viscosity than **TR**. This result indicates that **LE** should experience a higher shear rate than **TR**. The high shear rate may be generated because **LE** is near the bottom of the chamber. The pressure perturbations for different aging times can also be explained in this context. The viscosity reduction with the first shearing is less significant for the non-aged fluid; therefore, no undershoot is observed. The decrease of  $\Delta P$  in the steady state after the undershoot in the start-up flows shown in Figures 2.8 and 2.10 can also be explained by the memory of the first shearing that **TR** experienced at the chamber exit. Figure 2.16(b) shows that the effect of the first shearing changed with aging; the shear stress of the non-aged fluid (aging time 10 s) decreases gradually, while that of the aged fluid (aging time 30 min) decreases sharply. Given that all the shear stresses are still decreasing at 200 s, the few hundred seconds' time scale of all the experiments conducted here appears to cover a transient period. Therefore, the shear stress/viscosity of the aged fluid is lower than that of the non-aged fluid in rheology, thus the  $\Delta P$  decreased transiently with aging in the start-up flow. After the transient period, it is expected that the shear stress/viscosity would become almost constant over time regardless of aging.



(a) Shear stress  $\sigma_{mean}$  vs. shear rate  $\dot{\gamma}_{first}$  for different aging times (labeled in the inset).



(b) Shear stress normalized by corresponding steady state values  $\sigma / \sigma_{\infty}$  vs. time  $t$  with different aging times and  $\dot{\gamma}_{first}$ . Times in the legend box denote aging times; shear rates denote  $\dot{\gamma}_{first}$ . The inset shows the temporal change of the overshoots in the un-scaled shear stress.

Figure 2.16: Characterization of **LE** and **TR** by rheometer.



---

## 2.5.2 Remaining Questions to the Next Step

Start-up flow experiments of  $p$ -NIPAM aqueous suspensions were conducted to understand the aging effects on the pressure change. The observation of start-up flow in a pipe revealed that the peculiar undershoot of the pressure difference is induced by aging when the experimental system has a chamber; *i.e.*, both aging and the chamber are needed to induce the phenomenon. Based on the experimental findings, we proposed a model describing the rheological change of the fluid caused by aging and its shear rate history. The model is confirmed by rheological measurements under conditions reproducing those of the start-up flow experiments. Given that this aging effect on the start-up flow had not been expected only from conventional rheological measurements (see Figure 2.5 and 2.14), the results suggest the importance of practical-type rheological measurements to link the dynamic flow. The results also imply that both rheological measurements and flow experiments in a large scale are required to achieve greater understanding of the effect of aging. The proposed mechanism of pressure perturbation is potentially applicable to not only fluid physics but also natural phenomena. Magma demonstrates an example of pressure perturbations in nature: the multiphase fluid of a volcanic eruption flowing through a conduit (pipe) of a volcano towards a vent [20, 39]. The system considered here mirrors a general volcanic system consisting of a magma chamber and a conduit, thus the type of pressure perturbation observed here might be related to volcanic oscillation phenomena.

In the last place, let us discuss remaining matters. First, this experimental study was started in expectation of observing continual oscillations. However we only succeeded to grasp the single pressure perturbation, which never repeat again. A possible cause is that in the case of this suspension, the aging time to induce an apparent perturbation (over 30 min) is longer than the duration time of the perturbation (within two minutes). For such occasion, once the elongated structure of particles, which is formed in the process of aging, is broken by imposing shear, it cannot be rebuilt within the time scale of the experiment. Consequently aging causes the single perturbation in the start-up flow.

Secondly, although our proposed model explains the generation of the undershoot as the local change in the flow based on the rheological measurements, the local condition of the flow is not examined directly. The two outstanding issues bring about the following questions that needs to be solved as the next step:

- Can we observe continual oscillations by using a material that exhibits strong aging in a short time?
- Is there any link between rheological perturbation and the local condition in the flow?
- In the first place, do other material, which possesses the rheological multiplicity, show

---

some fluctuation phenomena, too?

One can then go on to consider these points in the next section.

# Chapter 3

## Experimental Study 2: Shear-induced Stress Fluctuation

### 3.1 Overview

The effects of aging on the pressure perturbations during start-up flow, and the relationship between the pressure perturbations and the rheology in terms of aging are described in the first experimental study. Responding to the remaining questions of the study as described in Section 2.5.2, a material that has the rheological multiplicity and exhibits strong aging in a short time, is used here. The purpose of this second experiment is to explore the aging effect on stress perturbation on microscopic scale by extensive rheological measurements coupled to ultrasonic velocimetry (USV) in shear flows. Also to confirm whether materials other than *p*-NIPAM aqueous suspension, which have the multiplicity, show fluctuation phenomena is another aim of this experiment. Sections 3.2 and 3.3 introduce the samples used in this study and the experimental setup. Section 3.4 describes the experimental results of mainly the constant-shear rate experiments together with flow-curve tests. In Section 3.5, the mechanism of stress fluctuation is proposed and the possibility to apply the process to magmatic system is explored.

### 3.2 Materials

Sample used here is a mixture of a commercial suspension of silica particles (Ludox TM-40, Sigma-Aldrich Co., Ltd., 40% wt. in silica particles) of typical diameter 20 nm [see Fig. 3.3(a) for a Scanning Electron Microscopy (SEM) image of a dilute sample (Supra 55, VP Zeiss)] and a 10% wt. deionized aqueous solution of sodium chloride (Merck Millipore Co., Ltd.). The starting sample is prepared following a recipe proposed by Moller *et al.*

---

[86]: the commercial silica suspension is first poured into the 10% wt. deionized aqueous solution of sodium chloride up to a mass ratio Ludox<sup>®</sup> : NaCl of 6 : 13, corresponding to a final volume fraction of 0.07 in silica particles. The mixture, which instantaneously becomes white and optically opaque, is then shaken intensely by hand for 2 min and left at rest for at least 15 h before being studied. Such a drastic change in the sample strongly suggests the rapid formation of aggregation. Thus the system is composed of aggregates made of silica particles (aggregated particle) and the aggregated state sensitively depends on pH and ionicity of the solution so that exact keeping the preparation procedure is essential to make reproducible samples. These aggregated particles are themselves reversibly linked in brine due to Van der Waals forces leading solid-like properties at rest.

In this system, although the volume fraction of silica particles 0.07 is quite small, the volume fraction of aggregated particles at rest is estimated to be about 0.8 by separating the liquid phase and the solid phase using a centrifuge. Note that the “hydrodynamic” volume fraction is determined by the aggregate radius rather than the much smaller actual volume fraction of silica particles [86].

### 3.2.1 Particle Interaction

The Van der Waals forces becomes strong when particles are very close together [66]. For particles in suspensions, a way to prevent from flocculating too close by the attractive force is having a surface charge that repels each other electrostatically. It is clear in Fig. 3.1 that the particles simply aggregate and settle out of solution in the absence of a stabilizing electric force while the stability is imparted via surface charge. The figure also indicates that particles have a large specific surface area due to their small size. Suspending particles in a liquid leads to charging of the surface by either surface acid or bases, and adsorption of free ions. The presence of dissociated chemical groups on the surface, of adsorbed ions, and of free counter ions and added salt ions leads to a complicated, structured electrostatic layer in solution near the particle surface [80]. Fig. 3.2 shows a double layer of positively-charged surrounding a surface with negative charges, in our case, due to  $\text{Si-O}^{-1}$ . The innermost layer of ions is absorbed to the surface and the system is electroneutral. The shading in the figure describes the density of the rest of counterions in solution. There are also cations and anions in solution arising from salt (NaCl). The thick line in Fig. 3.2 represents the electrostatic potential  $\psi(r)$  corresponding to this distribution of ions. The ions in the Stern layer (electric double layer) where the potential decays linearly are considered to be immobile. The outer limit of this region is associated with the plane of shear, beyond which the liquid around a moving particle is no longer trapped to move with the particle. In this region, the electrostatic interactions between charged surface sites and ions govern their

distribution and mobility. The potential at this point is taken to be zeta ( $\zeta$ ) potential [83].

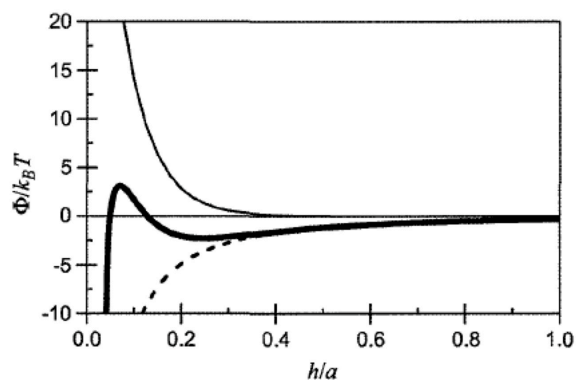


Figure 3.1: Example of interaction potential for 100 nm radius particles with a surface charge of 25 mV quoted from [80]. The thick line is the total potential, composed of the dispersion potential (dashed line) plus the electrostatic potential (thin line).

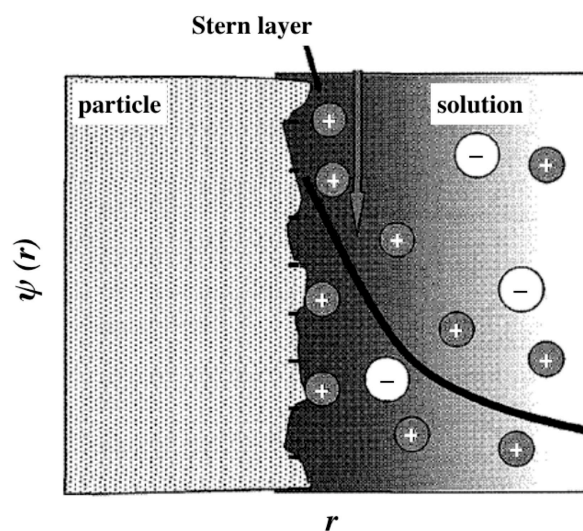


Figure 3.2: Illustration of layers in solution at the surface of a particle with reference to [80]. The Stern layer (double layer) and the electrostatic potential  $\psi(r)$  (thick line) are indicated.

Electrophoretic mobilities and zeta potentials of the commercial Ludox TM-40 and a mixture of commercial solution and HCl, which has the same pH as that measured in the sample (pH=7.6) were measured by using a Malvern ZetaSizer NanoZS as shown in Table 3.1. The fact that  $\zeta$  potential of the mixture is larger than that of commercial Ludox TM-40 means that the sample goes through dispersion stabilization and it leads an decrease in electrophoretic mobility.

	$\zeta$ potential (mV)	electrophoretic mobility ( $\mu\text{m}\cdot\text{cm}\cdot\text{V}^{-1}\cdot\text{s}^{-1}$ )
Ludox TM-40	$-29.0 \pm 0.8$	$-2.21 \pm 0.06$
Mixture of Ludox TM-40 and HCl	$-20.0 \pm 0.6$	$-1.52 \pm 0.05$

Table 3.1:  $\zeta$  potential and electrophoretic mobility of silica solutions.

Based on the interactions, the following scenario is proposed. Above pH=7, silica particles are negatively charged and bear silanol (Si–OH) and dissociated silanol groups that are poorly hydrated [43]. In most previous works, NaCl is added in a relatively small amount (typically 0.05–0.5 M) such that electrostatic repulsion is screened leading to the slow reversible aggregation of individual particles up to the formation of a gel [11, 112, 113]. Here, we add a much larger amount of salt (1.2 M) to the suspension, which leads to an ion exchange where protons are replaced by sodium ions [2, 3]. The loss of hydrogen bonding between the particles and the solvent triggers the fast and irreversible aggregation of the silica particles through the formation of interparticle siloxane bonds [22, 23, 29], resulting in the formation of the aggregated particles of silica particles described above.

### 3.2.2 Microstructures

Direct observations using different techniques confirm the existence of a much coarser microstructure than the initial nanometric silica particles. SEM images of a dried droplet extracted from a fresh sample that has been previously diluted in a NaCl solution reveal the presence of aggregated particles which size ranges from a few microns up to a hundred microns [Fig. 3.3(b)]. Images are obtained as follows: both the suspension and the sample have been diluted by a factor 1000 (except for the main figure in (b) where the sample has been diluted 100 $\times$ ), the first one in deionized water and the second one in a 6.8% wt. NaCl which corresponds to the final salt concentration in the sample. The samples are then left to dry on a pin stub before being imaged. On the other hand, bright-field microscopy images (ECLIPSE Ti, Nikon Co., Ltd.) of the sample neither altered nor diluted further confirm the existence of these micron-sized aggregated particles [Fig. 3.3(c)-(e)], which are stable in time and robust to repeated shear, as confirmed by similar observations performed

---

on samples submitted to different shear histories (Fig. 3.4). The interactions explained in Section 3.2.1 account for the formation of a large scale microstructure.

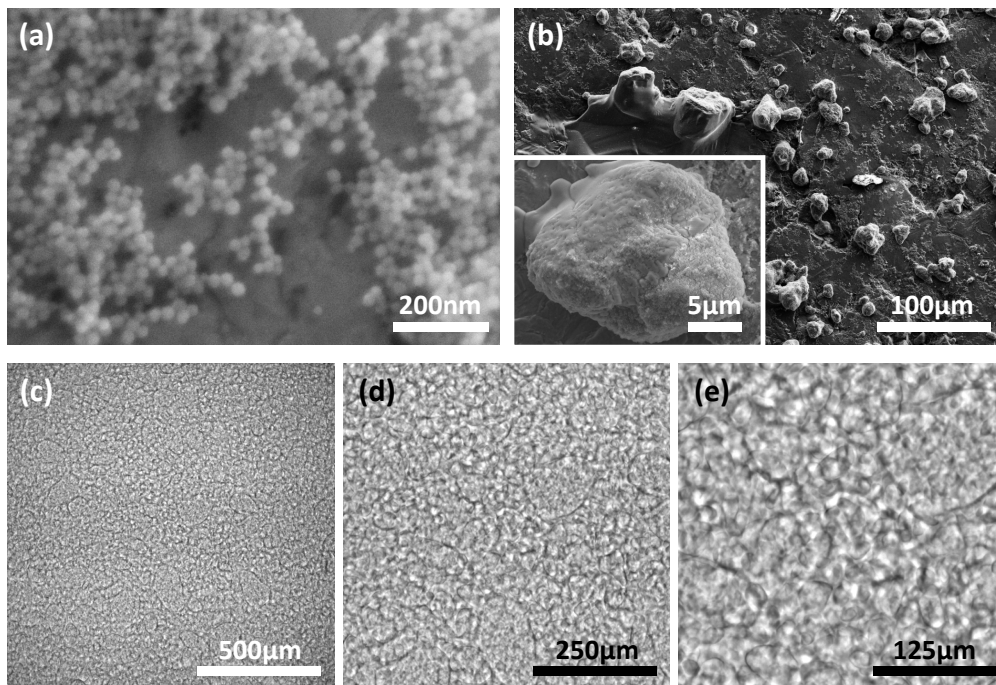


Figure 3.3: SEM images of (a) the commercial suspension (Ludox TM-40), and (b) the non-Brownian aggregates in the sample (the inset shows a typical aggregate of silica particles). (c)-(e) the microstructure at three different magnifications. The sample has been presheared for 2 min at  $500 \text{ s}^{-1}$ , 10 minutes before being imaged.

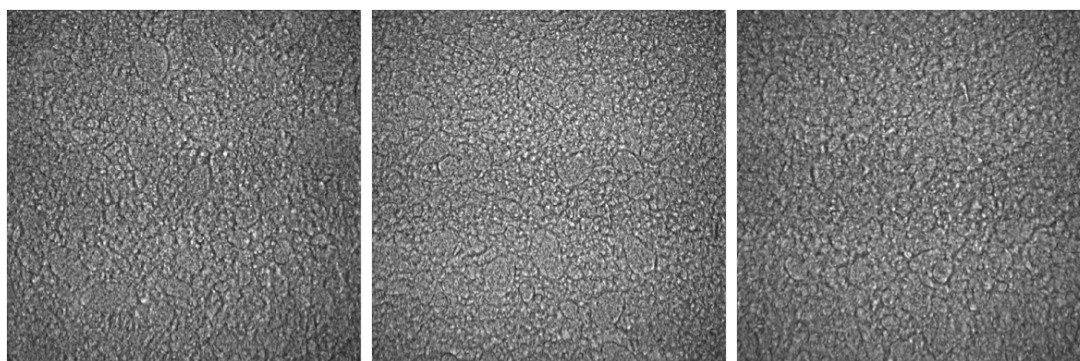


Figure 3.4: Effect of shear history on the microstructure. The images show samples at rest, after a preshear of 2 min at  $500 \text{ s}^{-1}$  and 10 min at  $1000 \text{ s}^{-1}$  from the left. The scales are same with that of Fig. 3.3 (c).

---

## 3.3 Methods

### 3.3.1 Experimental Instruments and Setup

The experimental setup allows us to perform time-resolved velocimetry simultaneously to standard rheometry as in Figure 3.5. The rheological measurements are performed in a polished Taylor-Couette (concentric cylinder) cell made of Plexiglas (gap  $e = 2$  mm) in which the inner cylinder of angle  $2.3^\circ$ , height 60 mm and radius 23 mm is connected to a stress-controlled rheometer (ARG2, TA Instruments Co., Ltd.) and positioned at  $100 \mu\text{m}$  from the bottom of the outer cylinder. A solvent trap located at the top of the rotor and a homemade lid are used to prevent evaporation efficiently up to about 9 h. The Taylor-Couette cell is embedded in a water tank connected to a thermal bath which allows us to keep the sample at a constant temperature  $T = 23.5 \pm 0.1^\circ\text{C}$ .

Local velocity profiles across the gap of the Taylor-Couette cell are recorded simultaneously to global rheology by means of two different ultrasonic probes immersed in the water tank, which also ensures acoustic coupling to the shear cell. Here, the global rheology is defined as averaged rheological data such as shear stress and shear rate obtained by a commercial rheometer. The first ultrasonic probe is a single high-frequency focused transducer that allows us to record the azimuthal velocity  $v$  as a function of the radial position  $r$  across the gap at the middle height of the shear cell *i.e.* at 30 mm from the bottom. Full technical details on this 1D ultrasonic velocimetry (1D-USV) can be found in a previous publication [77]. The second ultrasonic probe consists of a linear array of 128 transducers placed vertically at about 15 mm from the cell bottom (Fig. 3.6). This transducer array is 32 mm high and gives access to images of the azimuthal velocity as a function of the radial position  $r$  and vertical position  $z$  over about 50% of the cell height. This 2D ultrasonic velocimetry (2D-USV) technique is thoroughly described in ref. [37]. Both devices can be used simultaneously and roughly face each other in the water tank, *i.e.* they are separated by an azimuthal angle of about  $180^\circ$ . While the 1D-USV setup has the advantage of a better spatial resolution (about  $40 \mu\text{m}$  against  $100 \mu\text{m}$ ), only the 2D-USV setup allows us to detect and monitor the presence of flow heterogeneities along the vorticity direction.

Both velocimetry techniques require that the ultrasonic beam crossing the gap of the shear cell is backscattered either by the fluid microstructure itself or by acoustic tracers added during sample preparation when the system is acoustically transparent [37, 77]. Here, the microstructure of our sample further detailed above, which conveniently backscatters ultrasound in the single scattering regime, opens the way to monitor the fluid velocity in a fully non-invasive way. This is a great advantage of the sample, because in most cases impurities are added as tracers to backscatter the ultrasonic beams. This process is better to avoid because addition of impurities can affect the rheological characteristics. The same



problem would happen if we used *p*-NIPAM aqueous suspension that is used in the first experimental study. Moreover, precise tracking of the velocity profile in the suspension would be difficult since the tracers can intrude inside of the entangled soft particles, which have the size of several hundred  $\mu\text{m}$ . In this case, velocity profiles of in water and inside the particles are confused and hard to interpret. This is the technical reason why we chose the sample for this experiment.

In order to calibrate the experiment, the speed of sound in the working sample ( $c_0$  in Fig. 3.6) has to be measured. A classical transmission setup consisting of two transducers facing each other (one is the fixed emitter and the other is a receiver, which can be moved) is used for the calibration. After pulses are recorded for various displacements of the receiver and the time-shifts between the arrival times of the pulses are measured, the sound speed  $c_0 = 1570 \pm 2 \text{ m}\cdot\text{s}^{-1}$  is given. Then, calibrations of incident angle,  $\theta$  and stator position in a 7% wt. NaCl solution with 1% wt. glass beads, which have the same sound speed with that in the sample obtain good statical convergences by averaging over 1,000 pulses.

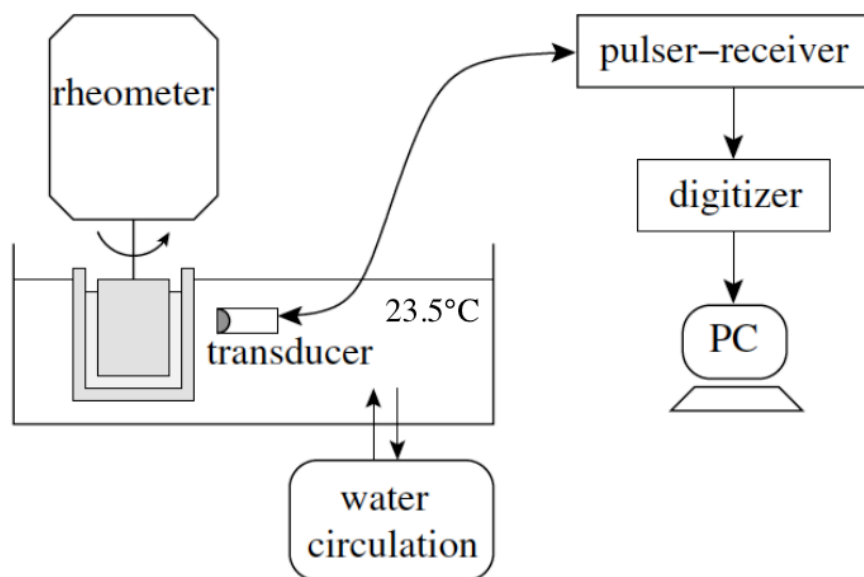


Figure 3.5: Experimental system with reference to [77].

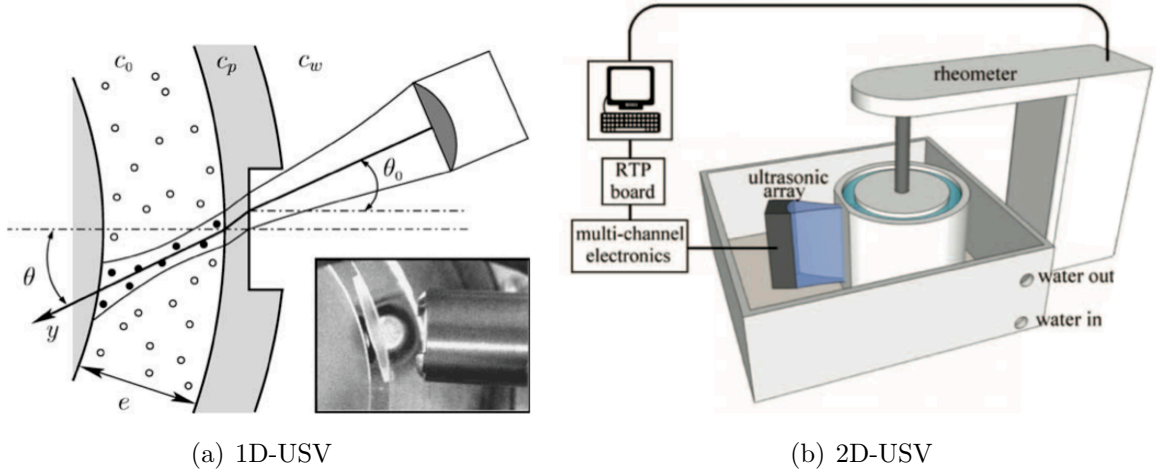


Figure 3.6: (a) 1D-USV setup [77]. Ultrasonic pulses are incident on the stator with a given angle  $\theta_0$  while  $\theta$  is the incidence angle and  $c_0$ ,  $c_p$ , and  $c_w$  stand for the speed of sound in the sample, in Plexiglas, and in water, respectively. The inset shows the 1D transducer and the stator as seen above. (b) General view of 2D-USV setup [37].

### 3.3.2 Experimental Protocol

Prior to any shear start-up experiment, the sample is presheared at  $500 \text{ s}^{-1}$  for 2 min in order to erase any previous shear history [117]. We check systematically that the velocity profiles during the preshear step become homogeneous across the gap within a duration shorter than 2 min. The system is then left to rebuild for a duration  $t_w$  (aging time) that ranges between 1 and 100 min, and during which we apply negligible small amplitude oscillatory shear stress (stress amplitude  $\sigma = 0.05 \text{ Pa}$ , frequency  $f = 1 \text{ Hz}$ ) to monitor the evolution of the linear viscoelastic properties and make sure that for a given value of  $t_w$ , the sample reaches an initial state that is reproducible from one experiment to another. Finally, a constant global shear rate  $\dot{\gamma}$  is applied to the material over a long duration ( $> 1000 \text{ s}$ ) monitoring the stress response together with local velocity profiles. In this geometry, global shear rate and global shear stress are expressed as  $\dot{\gamma} = R_i \Omega / e = v_0 / e$  and  $\sigma = \Gamma / 2\pi R_i l$ , respectively, where  $R_i$  is the radius of inner cylinder,  $\Omega$  is the angular velocity,  $v_0$  is the rotor velocity,  $e$  is the gap between two walls of the cell,  $\Gamma$  is the torque, and  $l$  is the height of the cell. The global viscosity  $\eta$  is computed from the rheological data as  $\eta = \sigma / \dot{\gamma}$  as long as the flow remains laminar and stationary. In the presence of wall slip, slip velocity is given by  $v_s = v_0 - v(0)$  where  $v(0)$  is the sample velocity at the rotating wall obtained by the USV. The local shear rate is defined as  $v(0) / \delta$  where  $\delta$  is the width of shear banding.

---

## 3.4 Results

### 3.4.1 Fundamental Rheology

The sample is known to exhibit strong aging by rheological measurements and light scattering investigations [86, 110]. In this study the aging feature should be checked at first. Fig. 3.7 displays variations of the elastic modulus  $G'$  and the viscous modulus  $G''$  with time. The measurement is performed under oscillatory shear stress with frequency 1 Hz and stress amplitude 0.05 Pa after a strong preshear at  $500 \text{ s}^{-1}$  for 2 min. Although the preshear fully fluidizes the sample, the elastic modulus instantly becomes larger than the viscous modulus within about 20 s of the start and it further increases logarithmically over more than 2 h. Such reproducible aging behavior to the formation of a solid-like state was confirmed in all samples used in this study.

Aging behaviors are also found in other measurements. Fig. 3.8 shows the flow curve  $\sigma$  vs  $\dot{\gamma}$  measured by sweeping down the shear rate from  $10^3$  to  $10^{-2} \text{ s}^{-1}$  in 75 logarithmically spaced points of duration  $\delta t = 8 \text{ s}$  and back up. The flow curve displays a complex multiplicity in the relation together with strong hysteresis (further discussion on the flow curve is presented in Section 3.4.6).

The present experiments are all performed after laying a sample to rest, so as to investigate the shear-induced fluctuant behavior of the aged sample in unsteady state. In practice, after preparing the sample in a reproducible initial state, we monitor the stress response of the material to a constant shear rate over long durations to 1 h.

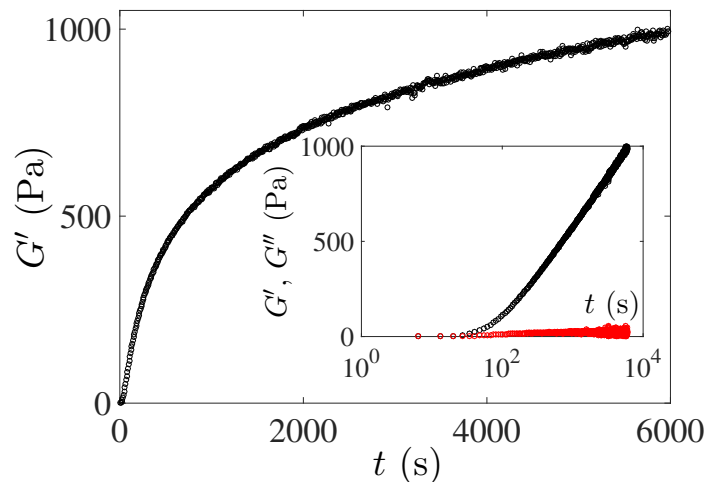


Figure 3.7: Elastic modulus  $G'$  vs time  $t$  after preshearing. Inset: same data set in semilogarithmic scales with viscous modulus  $G''$  (red).

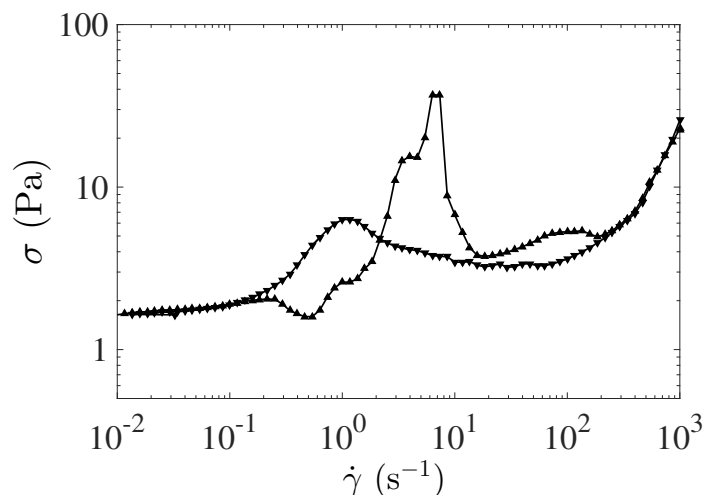


Figure 3.8: Flow curve  $\sigma$  vs  $\dot{\gamma}$  obtained by decreasing ( $\blacktriangledown$ ) and then increasing  $\dot{\gamma}$  ( $\blacktriangle$ ).

### 3.4.2 Global Rheology and 1D Velocity Profiles

The effects of applied global shear rate  $\dot{\gamma}$  and aging time  $t_w$ , on the flow are first described by comparing global stress response and velocity profiles obtained by 1D-USV. Here we focus on the behaviors after the global shear rate applied by the rheometer reaches constant. The effects of shear rate and aging time on the very first start-up flow including peak stress are described in Appendix.

#### Effect of Shear Rate

First constant-global shear rate experiments with the prescribed aging time of  $t_w = 60$  min are performed at shear rates of 100, 150, 200, and 250  $\text{s}^{-1}$  as illustrated in Fig. 3.9. At the lowest shear rate of 100  $\text{s}^{-1}$ , the stress relaxes smoothly towards a constant value. Although the stress response seems to indicate a smooth stable flow, the internal flow structure is different from that in homogeneous flow. Velocity profiles acquired simultaneously reveal that the material is separated into two regions: the outer region near the stator remains at rest while the inner region near the rotor is flowing, which means that the sample displays steady-state shear banding. Furthermore there exists strong wall slip [Fig. 3.9(b)]. The result points out the importance of simultaneous measurements of global rheology and velocity profiles because the stable shear banding could not be expected only by the stress response without monitoring velocity profiles.

At larger shear rates, a completely different behavior appears both in the global and local measurements. In the global measurement, the stress displays a series of spike-like fluctuation events, during which stress increases of small amplitude are followed by large drops [Fig. 3.9(a)]. Local measurements show that the sample starts flowing heterogeneously

with shear band at first as is the case of the stable shear banding at the lowest shear rate of  $100 \text{ s}^{-1}$  [Fig. 3.9(b)]. However, this shear band is transient and the width of shear banding grows wider with time. Then the system always reaches the state of being homogeneously sheared at steady state [Fig. 3.9(c)–(e)]. The width of the shear band increases while strong wall slip is observed at the rotor, until the whole gap is fluidized and wall slip becomes negligible. This behavior is robustly observed at different shear rates and the full fluidization is attained sooner for larger shear rates. The result indicates plural cycles of the stress fluctuation occur during the course towards fluidization with changing the width of shear band when a certain level of high shear rate is imposed as in Fig. 3.10.

This kind of stress fluctuation for a flowing system at the stress relaxation is highly unexpected and quite original behavior, which have never been reported before [63]. Large stress drop in relatively short time scale resembles the stress drop behavior during the fracturing of solid materials under stress. The fact that a flowing material at one side exhibits a solid nature should be a key in distinction between the solid and the liquid.

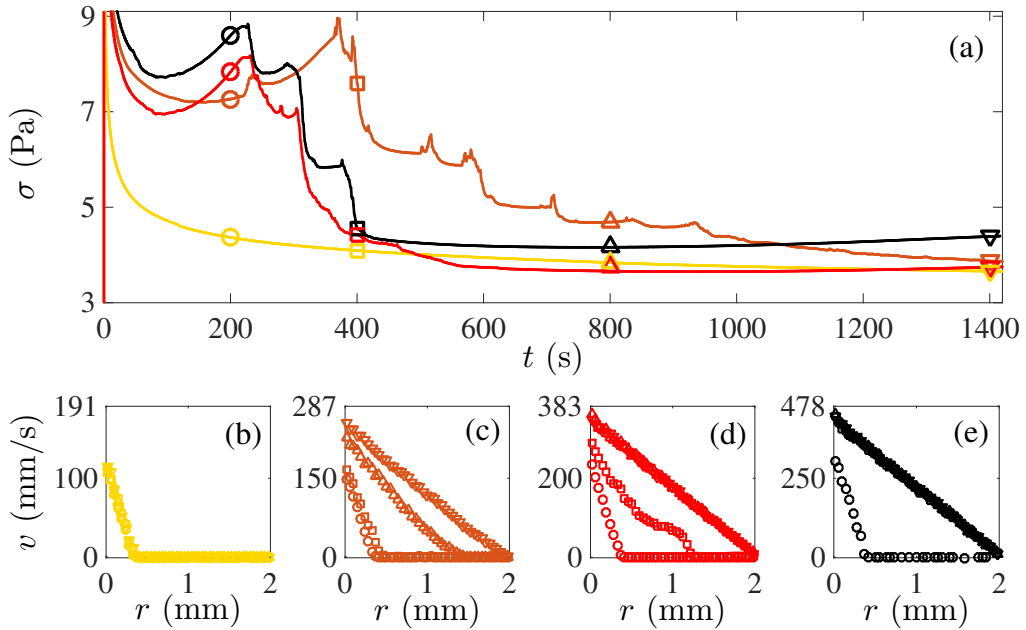


Figure 3.9: (a) Shear stress response  $\sigma(t)$  for different shear rates [color,  $\dot{\gamma}$  ( $\text{s}^{-1}$ )]: [—, 100]; [—, 150]; [—, 200]; [—, 250]. (b)–(e) Velocity profile  $v(r)$  across the gap, where  $r$  is the distance to the rotor at different times [symbol, time (s)]: [○, 200]; [□, 400]; [△, 800]; [▽, 1400]. Each color corresponds to each applied shear rate in (a). The rotor velocity corresponds to the upper bound of the vertical axis. The sample is left to age during  $t_w = 60$  min before each experiment.

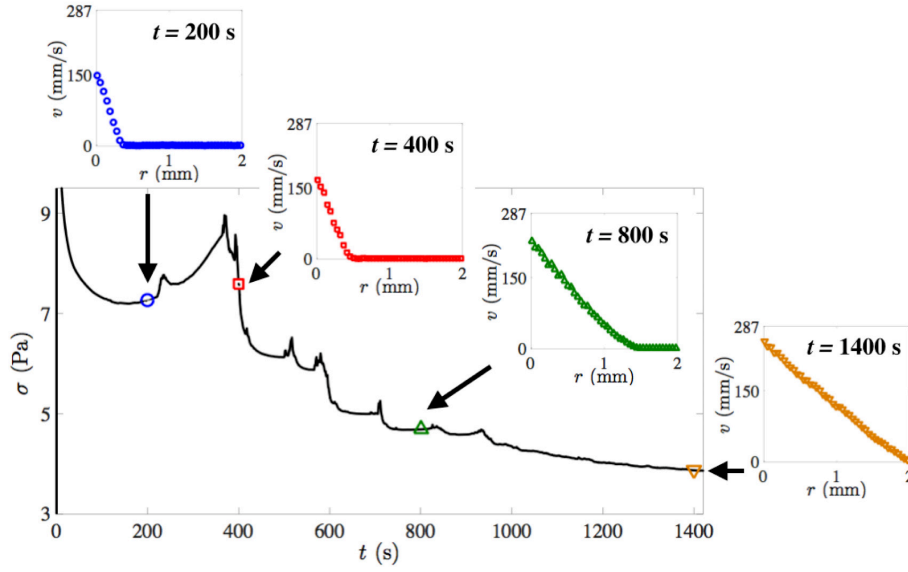


Figure 3.10: Excerpt data at shear rate  $150 \text{ s}^{-1}$  and  $t_w = 60 \text{ min}$  from Fig. 3.9. Shear stress response  $\sigma(t)$  with velocity profiles  $v(r)$  at different times are shown.

### Effect of Aging Time

To demonstrate the impact of the aging time  $t_w$  on the material response, Figs. 3.11(b)–(e) show similar experiments performed for different  $t_w$  at the same shear rate  $\dot{\gamma} = 100 \text{ s}^{-1}$ . For long aging times, e.g.  $t_w = 100 \text{ min}$ , a smooth stress relaxation is displayed. At the same period, steady shear-banded velocity profiles are obtained [Fig. 3.11(a) and (b)]. This behavior is the same with that observed at  $100 \text{ s}^{-1}$  and  $t_w = 60 \text{ min}$  [Fig. 3.9(b)], which is called as the case of stable shear banding. Then, decreasing  $t_w$  results in a decrease in aging effect on a sample leading lower viscosity. Local measurements further reveal that these weaker aged samples go through a transient shear-banding regime and reach the homogeneous steady state [Fig. 3.11(c) and (d)]. Unlike the case of transient shear banding reported in Fig. 3.9(a) for large shear rates where fluidization corresponds to a long series of successive stress relaxations, here it proceeds in a single stress drop together with small noisy fluctuations [Fig. 3.11(a)]. Finally, one observes that very young samples ( $t_w = 1 \text{ min}$ ) barely show any heterogeneous velocity profile during start-up flow and reach a homogeneous steady state within a few tens of seconds [Fig. 3.11(e)]. In summary, the longer the sample ages after preshear, the more likely it is to exhibit long-lasting transient shear banding or steady shear banding. The result also indicates occurrence of similar stress fluctuations with changing the width of shear banding during fluidization as in Fig. 3.10. Note that the fluctuation occurs only when a sample is aged to some extent.

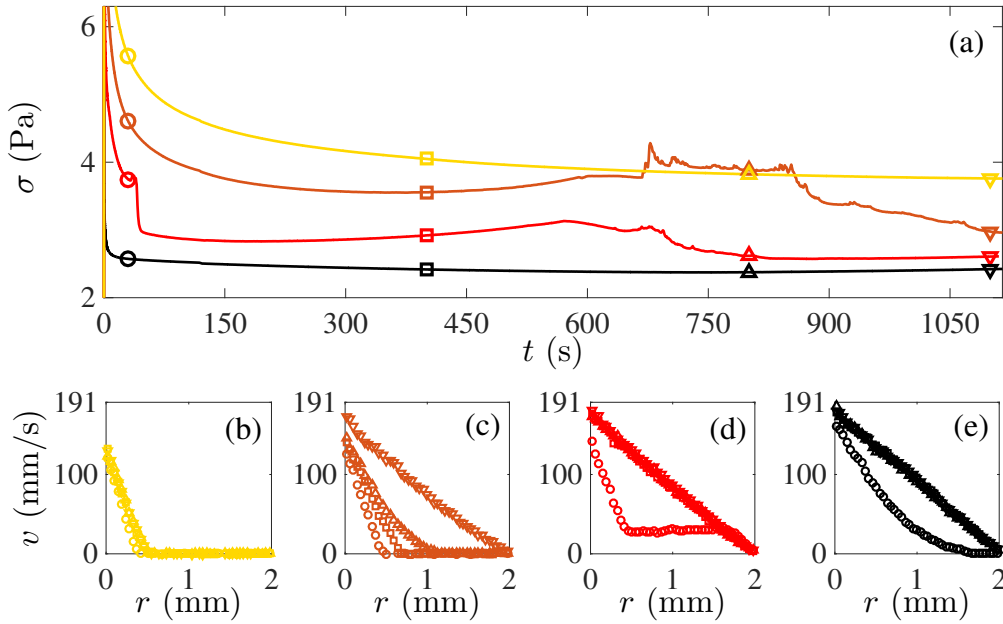


Figure 3.11: (a) Shear stress response  $\sigma(t)$  for different aging times  $t_w$  [color,  $t_w$  (min)]: [—, 100]; [—, 30]; [—, 5]; [—, 1]. Experiments performed at  $\dot{\gamma} = 100 \text{ s}^{-1}$ . (b)-(e) Velocity profile at different times [symbol, time (s)]: [ $\circ$ , 30]; [ $\square$ , 400]; [ $\triangle$ , 800]; [ $\nabla$ , 1100]. Each color corresponds to each value of  $t_w$  in (a). The rotor velocity corresponds to the upper bound of the vertical axis.

### 3.4.3 Flow State Diagram

To get an overall picture of the material response, we have performed extensive shear start-up experiments by varying systematically both the aging time ( $1 \leq t_w \leq 100$  min) and the applied shear rate ( $10 \leq \dot{\gamma} \leq 250 \text{ s}^{-1}$ ). The entire data set is summarized in the flow state diagram pictured in Fig. 3.12, where the different symbols code for the three different behaviors distinguished at the end of each experiment. First is full fluidization case after a transient phase involving strong fluctuations ( $\blacklozenge$  in Fig. 3.12), as observed in the upper part of the state diagram for large shear rates quite independently of the sample age.

The other two types can be discriminated by the existence of persistent shear banding. One is *steady* shear banding ( $\bullet$  in Fig. 3.12), for which both the width  $\delta$  of the shear band and the slip velocity  $v_s$  display negligible fluctuations in steady state. The behaviors are observed in particular at low aging times  $t_w \lesssim 20$  min and under low enough shear rates, typically below  $100 \text{ s}^{-1}$ . The other is *unsteady* shear banding ( $\blacklozenge$  in Fig. 3.12). In this case, both global and local measurements continue to display significant fluctuations. These fluctuations are strikingly similar to those observed during the transients leading to complete fluidization in the upper part of the diagram. However here the material never gets entirely fluidized and the width  $\delta$  of the shear band does not show a systematic evolution towards  $\delta = e$  so that an unsteady shear band persists at least within the finite duration

of the experiments. The unsteady shear banding with fluctuations appears near the border between full fluidization range and steady shear banding range according to the flow state diagram.

Fig. 3.13 illustrates many result examples of the three types of stress response. The difference in the types: full fluidization, unsteady shear banding, and steady shear banding is clearly recognized as the stress response: stabilization after fluctuations, persistent fluctuations, and smooth stabilization, respectively. Since the main interest of this study is fluctuation phenomena, the two former cases are investigated in more details in the next section.

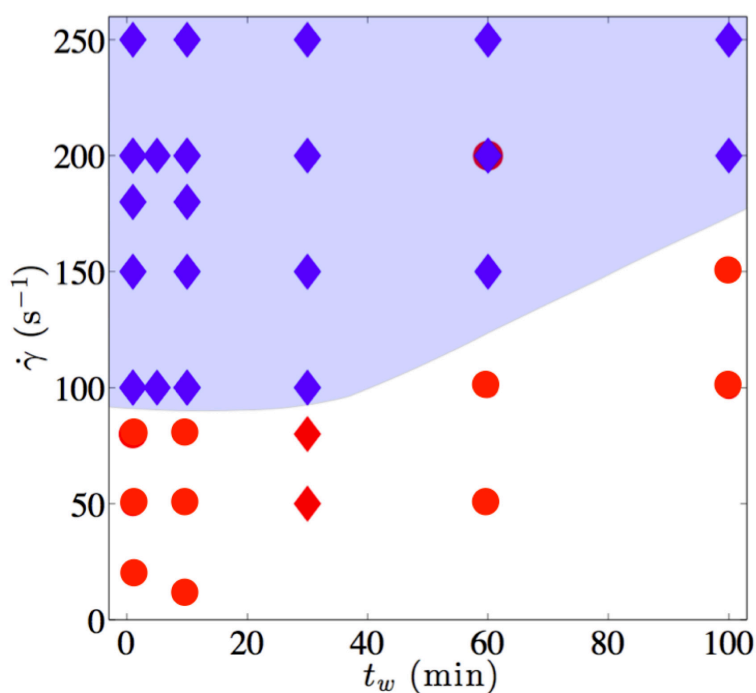
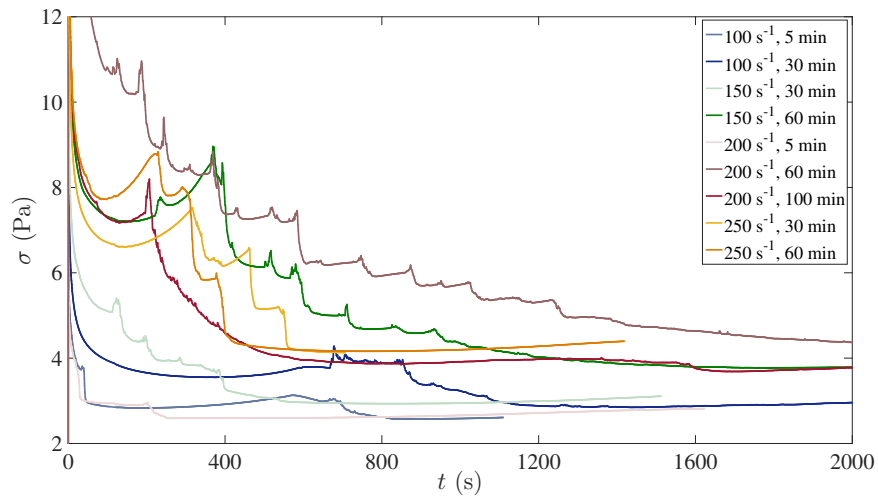
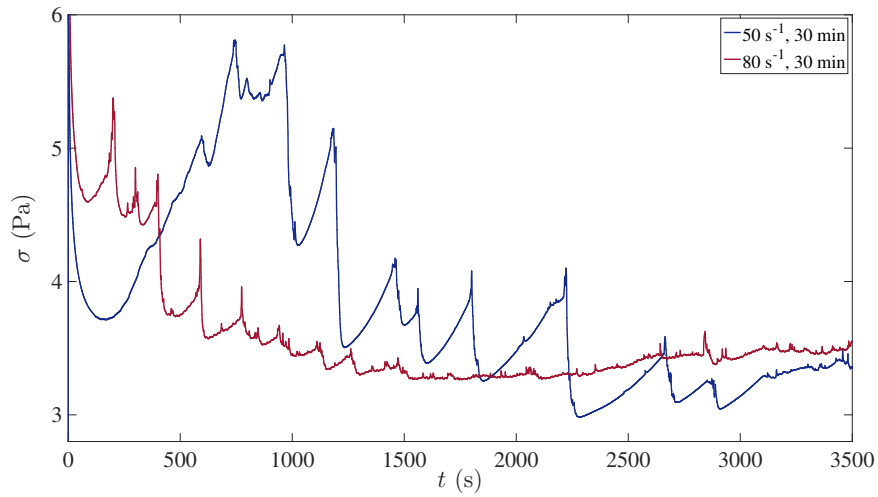


Figure 3.12: Flow state diagram in the (sample age  $t_w$ , applied shear rate  $\dot{\gamma}$ ) plane. In steady state, the sample may either be fully fluidized (◆) or display shear banding. Steady shear banding is represented in (●). Unsteady banding, which denotes flows where the band width and the slip velocity display significant fluctuations, is represented by (◆).

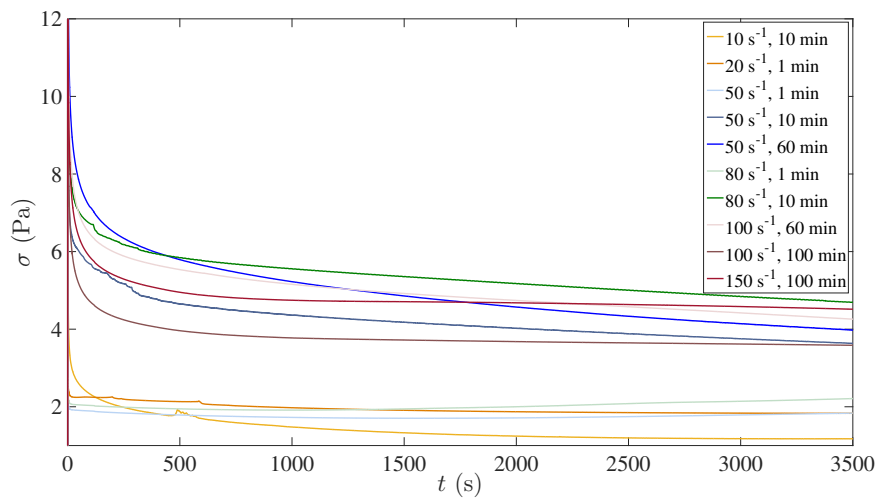




(a) Full fluidization



(b) Unsteady shear banding



(c) Steady shear banding

Figure 3.13: Numerous examples of the three types, full fluidization, unsteady shear banding, and steady shear banding indicated as  $\blacklozenge$ ,  $\blacklozenge$ ,  $\bullet$  in the flow state diagram (Fig. 3.12), respectively. The insets show each applied shear rate and waiting time.

---

### 3.4.4 Linking Global Rheology to Local Dynamics

This section focuses on the strong fluctuations that are observed (i) during transient regimes leading to complete fluidization and (ii) during persistent unsteady shear-banded flows. We report here results at  $150 \text{ s}^{-1}$  with  $t_w = 30 \text{ min}$  and at  $50 \text{ s}^{-1}$  with  $t_w = 30 \text{ min}$  as representative cases of (i) and (ii), respectively. Global rheology data together with the detailed analysis of the corresponding local measurements of velocity profile are reported in Figs. 3.14 and 3.15. Local data are analyzed as follows: linear fits of the velocity profiles in the fluidized part of the gap are used to estimate the local shear rate  $\dot{\gamma}_l$  imposed on the flowing part and to extrapolate the sample velocity  $v(0)$  at the rotor. The width  $\delta$  of the shear band is obtained as the intersection between the fit and the zero velocity axis.

Fig. 3.14 shows a case of full fluidization for  $\dot{\gamma} = 150 \text{ s}^{-1}$  with  $t_w = 30 \text{ min}$ . The stress relaxes by successive drops up to full fluidization which occurs at  $t = \tau_f \simeq 507 \text{ s}$  and after that,  $\sigma$  remains roughly constant [Fig. 3.14(a)]. The normalized width of shear band  $\delta/e$  [Fig. 3.14(b)] increases to the entire gap in the first 507 s with steps and pulse-like jerky fluctuations. The fact that  $\delta/e$  stays 1 after  $t = \tau_f \simeq 507 \text{ s}$  means that the entire part of the sample is homogeneously fluidized. In the whole fluidization stage, the slip velocity at the rotor  $v_s$  decreases towards a negligible value at  $t = \tau_f$ , diminishing by jumps that are almost in phase with the stress evolution.

Fig. 3.15 focuses on persistent fluctuations observed during unsteady shear-banded flows at a lower shear rate of  $50 \text{ s}^{-1}$  for  $t_w = 30 \text{ min}$ . The stress exhibits periods of increase followed by drops [Fig. 3.15(a)]. Looking at Fig. 3.15(b), about half of the sample gets fluidized within an hour and the size of the fluidized band shows pronounced increase during short period of times, that are synchronized with the stress drops. The dynamics of the fluid at the rotor is also correlated to the stress fluctuations, as evidenced by the sudden peaks of the slip velocity when the stress drops. Note that, although the slip velocity decreases in average over the whole duration of the experiment, it remains at a high level of about 20%, in noticeable contrast with that in the fully fluidized case described in the previous paragraph.

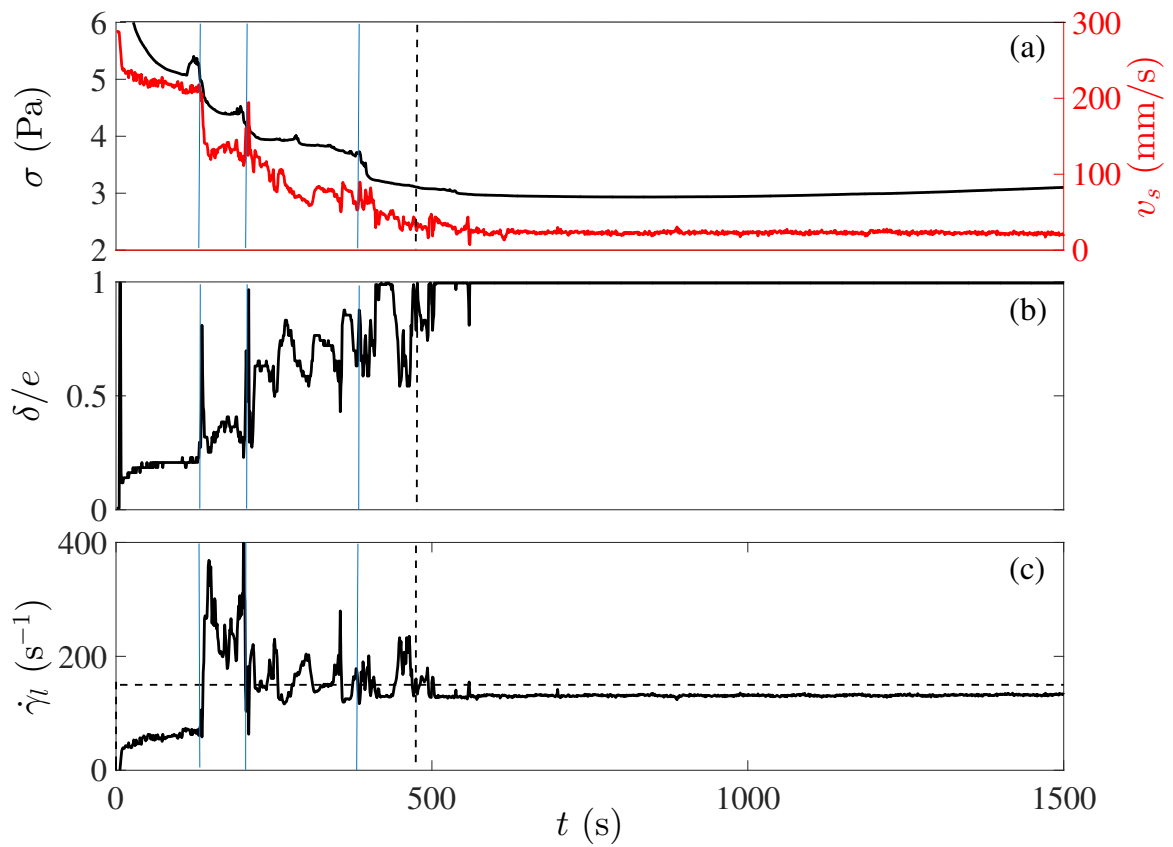


Figure 3.14: Full fluidization observed for  $\dot{\gamma} = 150 \text{ s}^{-1}$  and  $t_w = 30 \text{ min}$ . (a) Shear stress  $\sigma$  and slip velocity  $v_s$  vs time. (b) Width  $\delta$  of the fluidized shear band normalized by the gap width  $e$  vs time. (c) Local shear rate within the shear band vs time. The horizontal dotted line indicates the global shear rate applied and measured by the rheometer. In (a)-(c), the vertical dashed line indicates the fluidization time while the blue lines show the peak times.

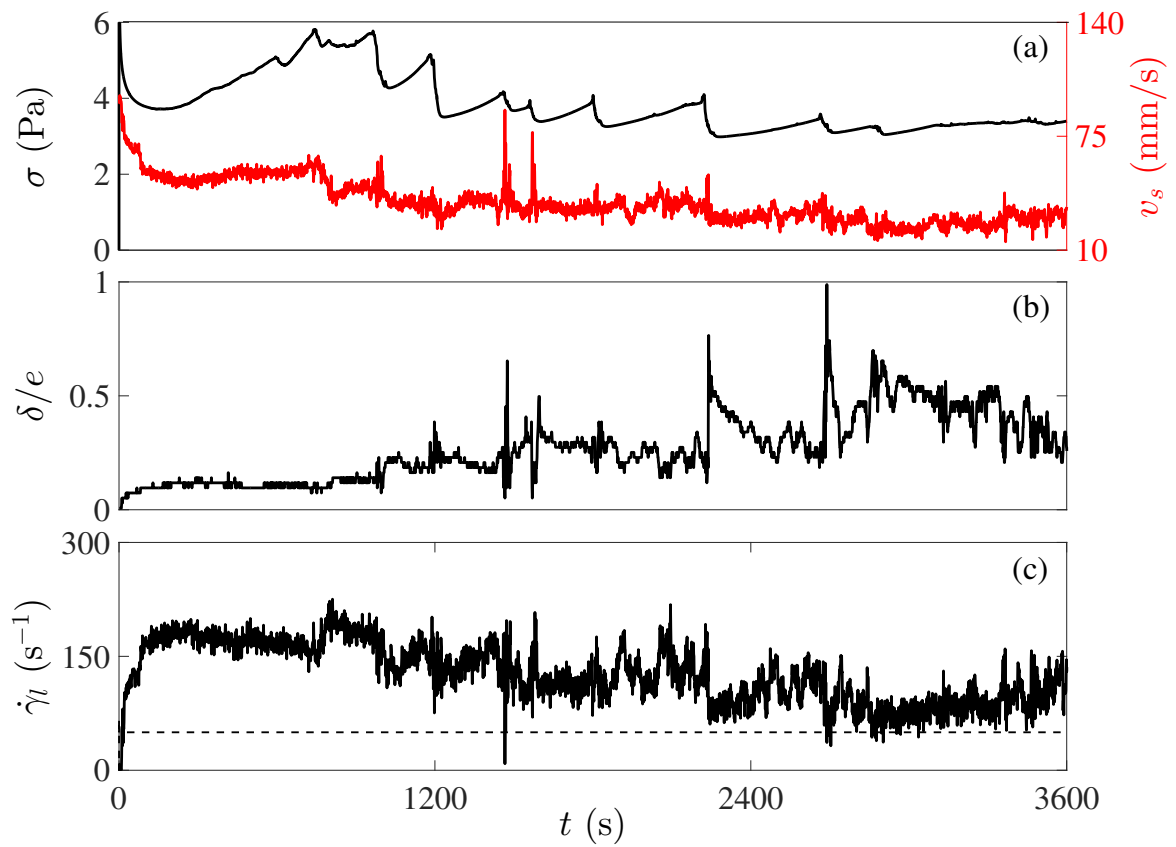


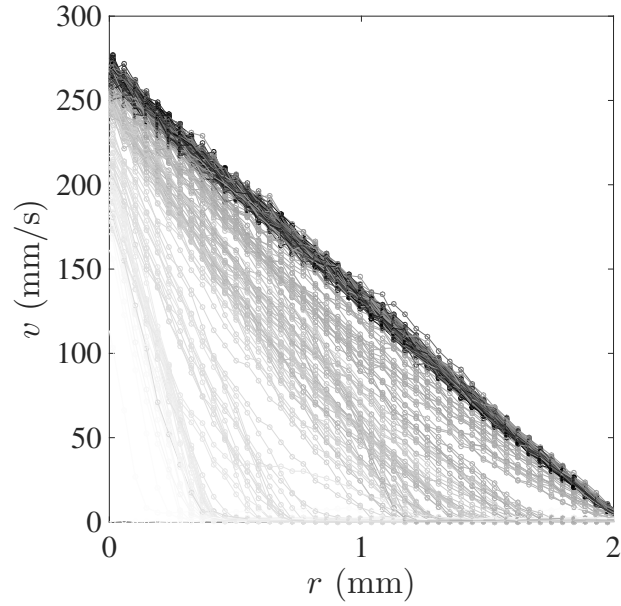
Figure 3.15: Unsteady shear banding observed for  $\dot{\gamma} = 50 \text{ s}^{-1}$  and  $t_w = 30 \text{ min}$ . (a) Shear stress  $\sigma$  and slip velocity  $v_s$  vs time. (b) Width  $\delta$  of the fluidized shear band normalized by the gap width  $e$  vs time. (c) Local shear rate within the shear band vs time. The horizontal dotted line indicates the global shear rate applied and measured by the rheometer.

---

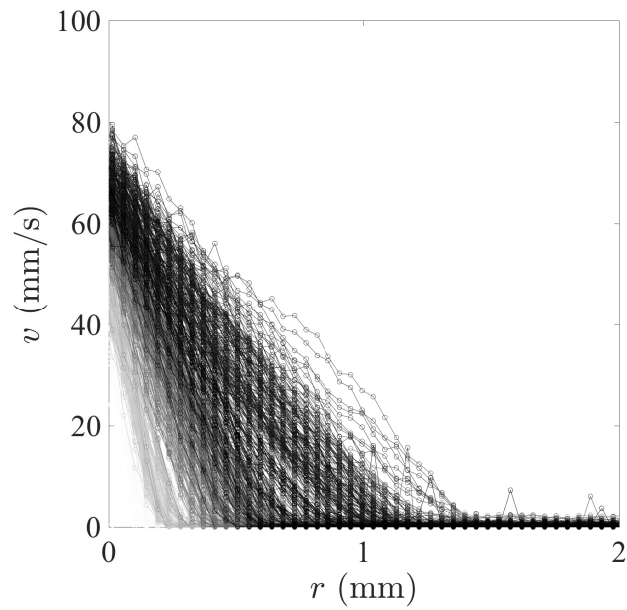
Fig 3.16 shows temporal change in velocity profile in the both cases of full fluidization and unsteady shear banding as in Figs. 3.14 and 3.15. In the case of full fluidization ( $\dot{\gamma} = 150 \text{ s}^{-1}$ ,  $t_w = 30 \text{ min}$ ), the velocity profile becomes straight line after shear banding while in the case of unsteady shear banding ( $\dot{\gamma} = 50 \text{ s}^{-1}$ ,  $t_w = 30 \text{ min}$ ), it goes back and force keeping shear banding state. Although these peculiar dynamics suggest a coupling between flow and its microstructure, the mechanism of the stress fluctuation is still unclear.

In order to provide a more complete picture of the coupling during the fluctuation, a single stress fluctuation event is picked up for detailed analysis, which shows apparent link to the local dynamics as shown in Fig. 3.17. A single stress fluctuation event can be divided into three stages. At first, the stress increases gradually after the stress drop in the previous event. During this stage, it is clear in Figs. 3.17(a) and (b) that the slip velocity increases while the width of shear banding decreases. Above all, the decrease in the width of shear banding is predominant. On the other hand, looking at Fig. 3.17(c), the global viscosity increases while the viscosity of the flowing part decreases. The changes in the width of shear banding and the viscosities mean that solid-like part extends into the flowing part while the flowing shear-banded part becomes less viscous because the local shear rate increases due to  $\delta$  decrease, causing shear-thinning and/or expelling the aggregated particles to the aged solid-like part. The second stage is the last part of stress-increasing to the peak. At this stage, the local dynamics becomes unstable with showing perturbations while the stress smoothly increases without undergoing major change from the first stage. The third is the stress drop stage. A significant increase in the width of shear band indicates fluidization of great part of the aged solid-like part. Since the solid-like part moves to the flowing part in this process, the local viscosity increases. Moreover, the fact that the slip velocity shows apparent perturbations and becomes larger before the fluidization implies the importance of the wall slip.

However looking at the fluctuations carefully, occasionally the stress fluctuates without clear correlation with the local dynamics as the first part of Fig. 3.15 ( $t < 1200 \text{ s}$ ). This suggests a possibility that intrinsic internal changes may occur outside the area of 1D-USV measurements. To confirm this, 2D-USV measurements to cover the broad region were performed and the results are described in the next section.

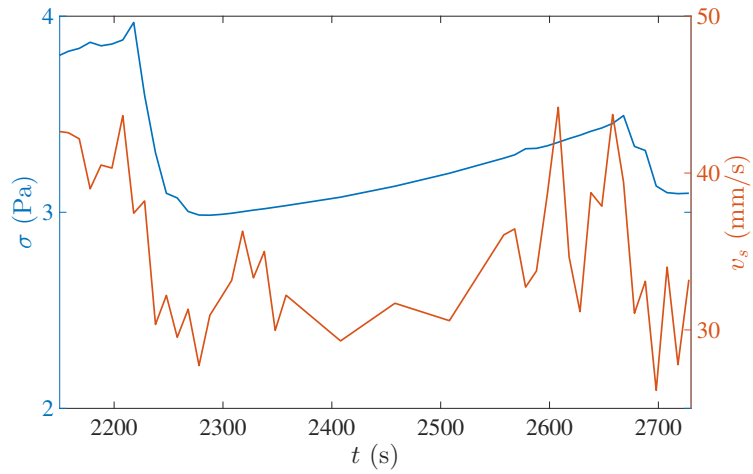


(a) Full fluidization

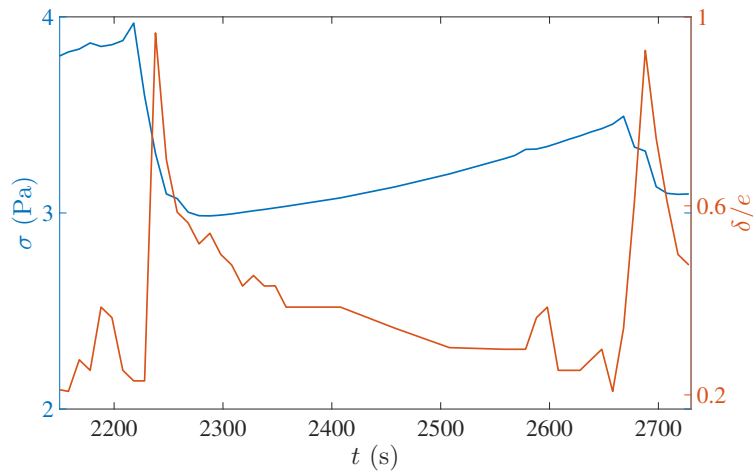


(b) Unsteady shear banding

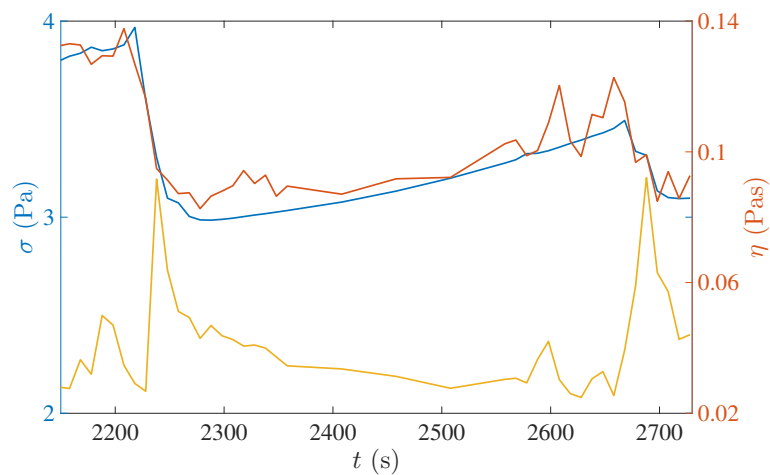
Figure 3.16: Temporal change in velocity profile in the cases of full fluidization ( $\dot{\gamma} = 150 \text{ s}^{-1}$ ,  $t_w = 30 \text{ min}$  in Fig. 3.14) and unsteady shear banding ( $\dot{\gamma} = 50 \text{ s}^{-1}$ ,  $t_w = 30 \text{ min}$  in Fig. 3.15). The color variation from white to black indicates the elapsed time of the experiment. The velocity data are plotted at 5 s intervals.



(a) Stress  $\sigma(t)$  and slip velocity  $v_s(t)$



(b) Stress  $\sigma(t)$  and normalized width  $\delta(t)/e$  of shear banding



(c) Stress  $\sigma(t)$  and viscosities  $\eta$  (red: global viscosity  $\sigma \cdot e/v_{wall}$ , orange: viscosity of the flowing part  $\sigma \cdot \delta/v_{wall}$ )

Figure 3.17: Comparison between global rheology and local dynamics at  $\dot{\gamma} = 50 \text{ s}^{-1}$  and  $t_w = 30 \text{ min}$  during measurement time of  $2150 \text{ s} < t < 2730 \text{ s}$  (*ref.* Fig. 3.15).

---

### 3.4.5 Local Scenario of Stress Fluctuation

To approach further details of the fluctuation process, 2D measurements at  $\dot{\gamma} = 180$  and  $200 \text{ s}^{-1}$  in the full fluidization region of the state diagram (Fig. 3.12) are performed. The reason why such high shear rates are chosen is that condition in which a fast fluidization process proceeds is required for a technical reason: once the 2D-USV measurement starts, it is impossible to stop for two minutes and it takes few minutes to start it again due to the large data processing.

The temporal evolution of the shear stress is given in Figs. 3.18(a) and 3.19(a) while the corresponding 2D-USV measurements  $v(r_0, z, t)$  are displayed as spatiotemporal diagrams in Figs. 3.18(b) and 3.19(b) for a radial position  $r_0 = 0.7 \text{ mm}$ . The results of 2D-USV measurements distinctly show that temporal evolution of the velocity field is strongly heterogeneous along the vertical direction in the both experiments. In Fig. 3.18, at first the lower part of the sample starts fluidizing during the first stress drop while the upper part necessitates supplemental avalanches in turn to be fluidized after that. On the other hand, the fluidization process shown in Fig. 3.19 starts from the upper part of the sample before extending to the lower part of the cell. Here, each avalanche-like event involves large pieces of the sample with a typical vertical extension of about 5 mm [see events marked by white dotted lines in Fig. 3.19(a)]. Some of these events only show up in the stress response as very small peaks while their local signature is much more impressive (*e.g.* the event at  $t \simeq 600 \text{ s}$ ). For  $t \simeq 400$  to  $500 \text{ s}$ , the sample even appears to fluidize, or at least to be set into motion, through regular steps occurring from top to bottom with a characteristic time of 10–20 s. In this way, the results in Figs. 3.18 and 3.19 allow us to conclude that the fluctuations in the stress signal encompass very different local scenarios. For that reason, 1D-USV measurement cannot get the whole story of the two-dimensional fluctuation as in Fig. 3.15 ( $t < 1200 \text{ s}$ ). Since the both 2D experiments were performed with the same aging time  $t_w = 1 \text{ min}$ , these results illustrate the high sensitivity to “initial conditions,” i.e. to the possibly different arrangement of the heterogeneous microstructure after the aging process, and the subtle interplay between aging and shear banding with no systematic failure scenario along the cell height.



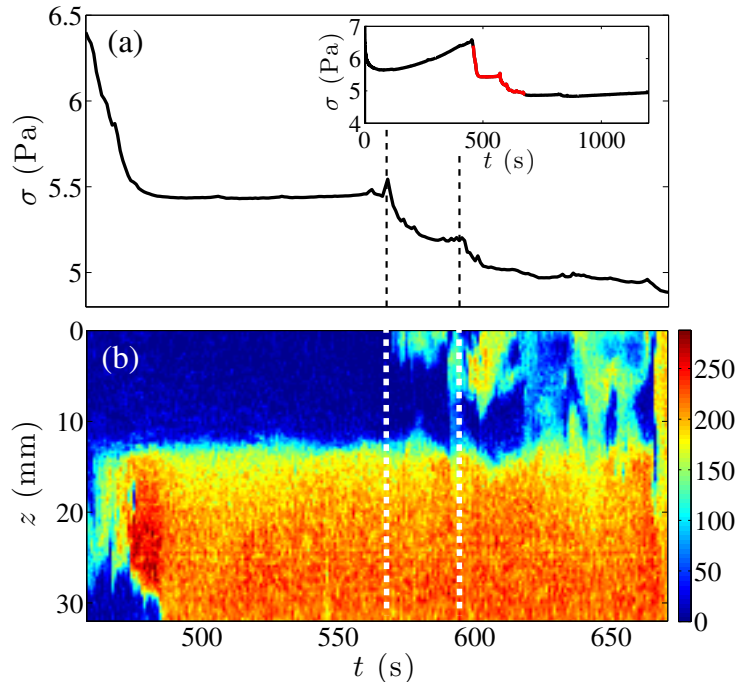


Figure 3.18: (a) Stress  $\sigma$  vs time  $t$  during a single stress fluctuation ( $\dot{\gamma} = 180 \text{ s}^{-1}$ ,  $t_w = 1 \text{ min}$ ). (b) Spatiotemporal diagram of the velocity  $v(r_0, z, t)$  as a function of the vertical position  $z$  and  $t$  at  $r_0 = 0.7 \text{ mm}$  obtained with 2D-USV. The fluid velocity is color coded in  $\text{mm}\cdot\text{s}^{-1}$ .

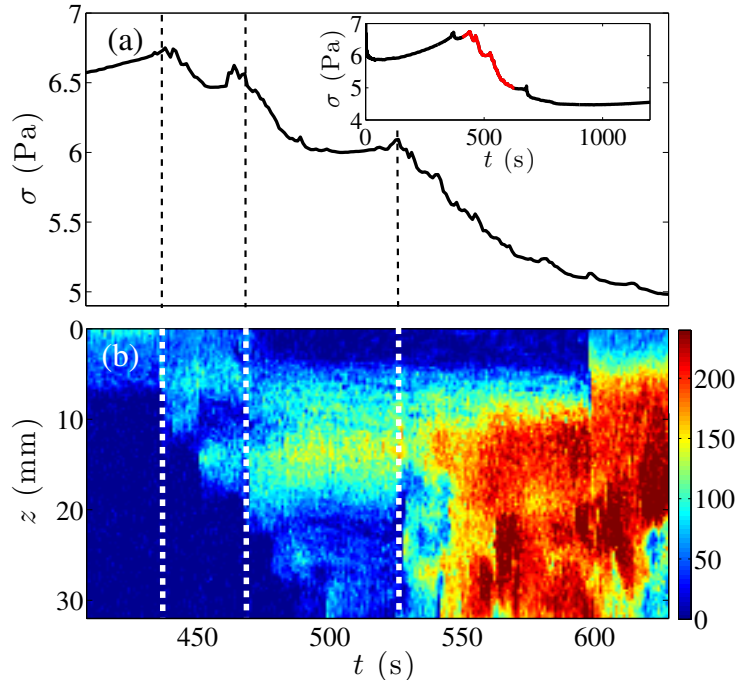


Figure 3.19: (a) Stress  $\sigma$  vs time  $t$  during a single stress fluctuation ( $\dot{\gamma} = 200 \text{ s}^{-1}$ ,  $t_w = 1 \text{ min}$ ). (b) Spatiotemporal diagram of the velocity  $v(r_0, z, t)$  as a function of the vertical position  $z$  and  $t$  at  $r_0 = 0.7 \text{ mm}$  obtained with 2D-USV. The fluid velocity is color coded in  $\text{mm}\cdot\text{s}^{-1}$ .

---

### 3.4.6 Local Scenario of Flow Curve

Fig. 3.20 shows time variations in global rheology and the corresponding 2D velocity profiles of the flow curve ( $\sigma$  vs  $\dot{\gamma}$ ) in Fig. 3.8. Again, the measurement was performed by sweeping down the shear rate from  $10^3$  to  $10^{-2}$   $\text{s}^{-1}$  in 75 logarithmically spaced points of duration  $\delta t = 8$  s and back up. The change in the width of shear banding at a given height ( $z_0 \simeq 15$  mm) in the cell [Fig. 3.20(b)], and spatiotemporal plots of the velocity as a function of the vertical position  $z$ , at a given radial position inside the gap ( $r_0 = 0.5$  mm) [Fig. 3.20(c)] are presented. Velocity data are shown only for  $\dot{\gamma} < 460$   $\text{s}^{-1}$  due to the limitation in the USV [37]. Fig. 3.20(b) reveals that the initial linear flow transforms into the shear-banded flow stepwisely showing fluctuations in the width of shear banding without a significant decrease in the shear stress. On the other hand, the velocity decreases homogeneously in the vertical direction [Fig. 3.20(c)]. It suggests that the sample ages with decreasing the shear rate with time. The wall slip and shear-banded flows are involved over large ranges of shear rates, below  $40$   $\text{s}^{-1}$  during the decreasing ramp and up to about  $100$   $\text{s}^{-1}$  during the increasing ramp. In particular, at the large stress peak suddenly observed at  $\dot{\gamma} \simeq 7$   $\text{s}^{-1}$  during the shear rate increasing process, the partial fluidization of the sample, which moves as a fast plug flow with slipping at the walls happens and persists to  $\dot{\gamma} \simeq 10$   $\text{s}^{-1}$ . Then above about  $100$   $\text{s}^{-1}$ , fluidization process undergoes. In contrast to the first transformation from linear flow to shear-banded flow with wall slip, this fluidization process is inhomogeneous in the vertical direction that is reminiscent of fluidization with stress fluctuations at a constant shear rate (Fig. 3.18 and 3.19).

The flow curve exhibits a large hysteresis mainly at low shear rates. During the decreasing ramp of  $\dot{\gamma}$ , the sample which is first sheared homogeneously at large shear rates, enters a total wall slip regime where the fluid just slips at the walls without flowing at  $t \simeq 400$  s after experiencing shear banding. This regime persists until  $\dot{\gamma}$  is increased back up again. The subsequent fluidization of the material is abrupt and occurs in a narrow range of shear rates,  $1 \lesssim \dot{\gamma} \lesssim 10$   $\text{s}^{-1}$ , which coincides with the brutal increase of the stress. Figure 3.20 (b, c) reveal that the subsequent drop in the stress corresponds to flow arrest, i.e. total wall slip, until the sample fluidizes again for  $\dot{\gamma} \gtrsim 100$   $\text{s}^{-1}$ .

The same flow curve test was performed whenever a new sample was poured into the rheometer. In the all samples, the hysteresis and the two apparent stress peaks were observed in the flow curves at much the same shear rates. This suggests that the reproducible samples have something like a “yield stress” to show the invariable hysteresis. In this way, the multiplicity with the two stress peaks is also related to the local changes in velocity profiles, especially shear banding and wall slip.

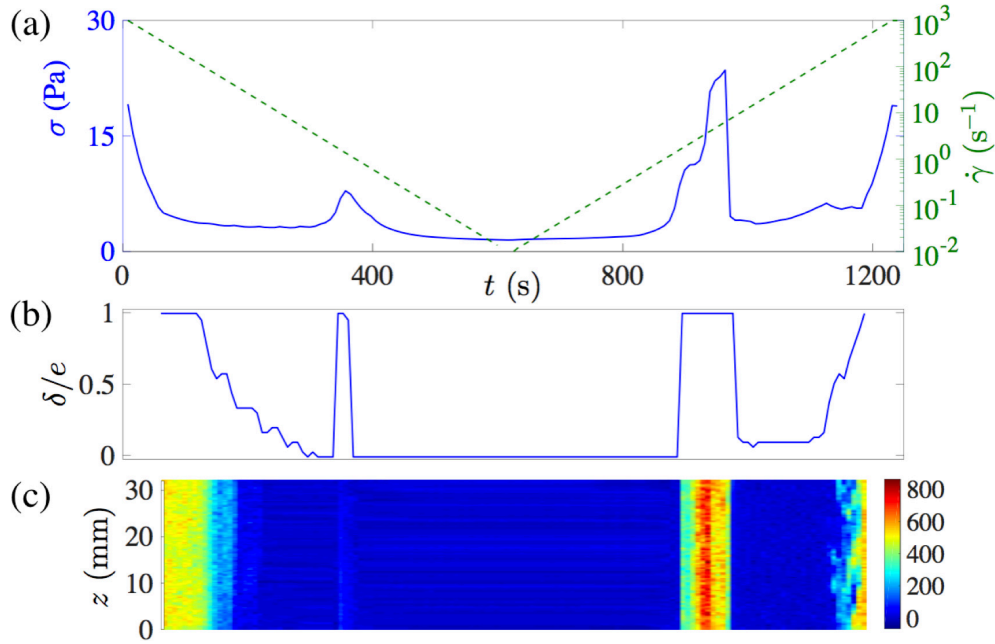


Figure 3.20: Local dynamics of flow curves. (a) Shear rate  $\dot{\gamma}$  and shear stress  $\sigma$  vs time  $t$ . (b) Width of shear banding at  $z_0 \simeq 15$  mm vs time. (c) Spatiotemporal diagram of the velocity data  $v(r_0, z, t)$  as a function of the vertical position  $z$  and  $t$ , at  $r_0 = 0.5$  mm. The fluid velocity is color-coded in  $\text{mm}\cdot\text{s}^{-1}$ .

### 3.4.7 Difference in Rate-control and Stress-control

Flow curves obtained by sweeping shear rate and shear stress are compared in Fig. 3.21. The shear rate is swept down from  $10^3$  to  $10^{-2}$   $\text{s}^{-1}$  in 75 logarithmically spaced points of duration  $\delta t = 8$  s and back up. In the case of stress-control test, the shear stress is swept down from 30 to 0.01 Pa with 15 points per decade in 15 min ( $\delta t = 16.5$  s), followed by the reverse way. The flow curve obtained by sweeping shear rate stays about the same with Fig. 3.8 although slight difference due to the use of a sample made on a different day, is found. On the other hand, the flow curve obtained by sweeping shear stress displays a significant difference: no multiplicity in the both down and up processes. We have performed constant shear stress tests in this range in order to understand what the difference brings about. The experimental results indicated that the sample did not flow. This may be because the imposed stress is slightly lower than the yield stress. Therefore we have tried to make a flow by using weakly-aged sample or by applying higher stress. In that case, however, once the sample flows, the measurement is forcibly stopped reaching the rotational limitation of the rheometer because viscosity of fluidized sample is too low to obtain the stress. In this way, it was impossible to see fluctuation phenomena under the control of stress in our system. The fact indicates that responses of the fluid can change depending on controlled parameter, shear rate or shear stress.

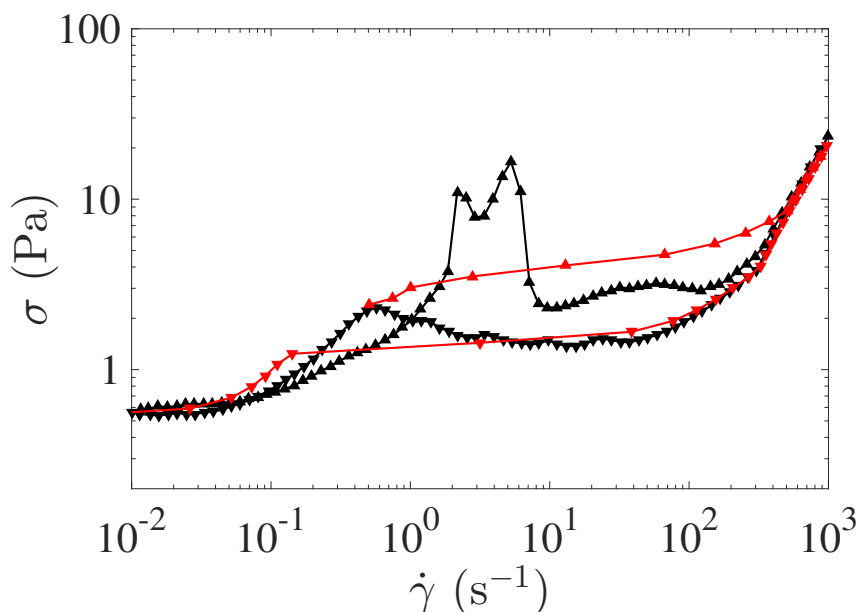


Figure 3.21: Flow curve  $\sigma$  vs  $\dot{\gamma}$  obtained by decreasing ( $\blacktriangledown$ ,  $\blacktriangledown$ ) and then increasing  $\dot{\gamma}$  or  $\sigma$  ( $\blacktriangle$ ,  $\blacktriangle$ ). Black (resp. red) data indicate results of shear-rate (resp. shear-stress) controlled test.

## 3.5 Interpretation and Consideration

### 3.5.1 Common Characteristics of Stress Fluctuation

A number of stress fluctuation data have been reported in the series of experiments with different  $t_w$  and  $\dot{\gamma}$ . This section focuses on common characteristics of the fluctuations.

At first, Fig. 3.22 indicates the time correlation between global fluctuation and local fluctuation. In each rheological measurement coupled to 1D-USV, times when the shear stress reaches the peak and when the width of shear banding achieves the maximum peak during the fluctuation process are examined. Despite the fact that data, in which fluctuations are seen both in stress and width of shear banding, are selected unintentionally within  $\dot{\gamma}$  of  $50 - 250 \text{ s}^{-1}$  and  $t_w$  of  $30 - 100 \text{ min}$ , apparently there is a linear correlation. The result indicates that the stress fluctuation is strongly related to the change in width of shear banding. Having noticed the relationship, one can then go on to consider rheological process of the stress fluctuation next.

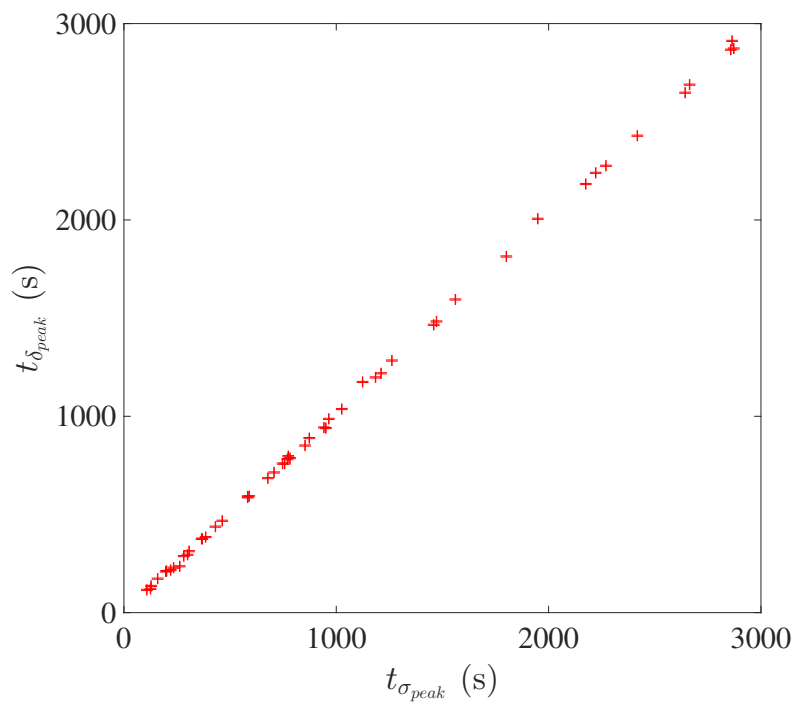


Figure 3.22: Relation between times when the width of shear banding achieves the peak,  $t_{\delta_{peak}}$  and when the stress reaches the peak,  $t_{\sigma_{peak}}$  during experiments for the cases of observing fluctuations by both the rheometer and the 1D-USV. The line length represents the error.

In order to focus on the rheology of the fluctuation process, let us focus on the occurrence of stress drop events. Fig. 3.23 shows one example picked from the result at  $\dot{\gamma} = 50 \text{ s}^{-1}$  and  $t_w = 30 \text{ min}$ . After the stress reaches the peak, it sharply drops. Then it increases again and repeats the process. To understand the fluctuation process, four physical amounts are defined as in the figure. The non-dimensional preparing time is defined as  $t_p^n = t_p \cdot \dot{\gamma}$  where  $t_p$  is the time from when the stress becomes the lowest in the previous drop to when it reaches the stress peak, and  $\dot{\gamma}$  is the applied shear rate.  $\sigma_p$  is the stress at the peak,  $\Delta\sigma$  is the amount of stress drop, and  $t_d$  is the duration time of the stress drop.

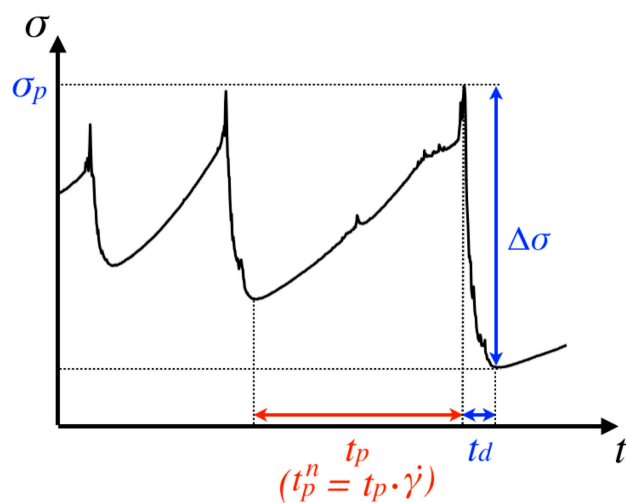
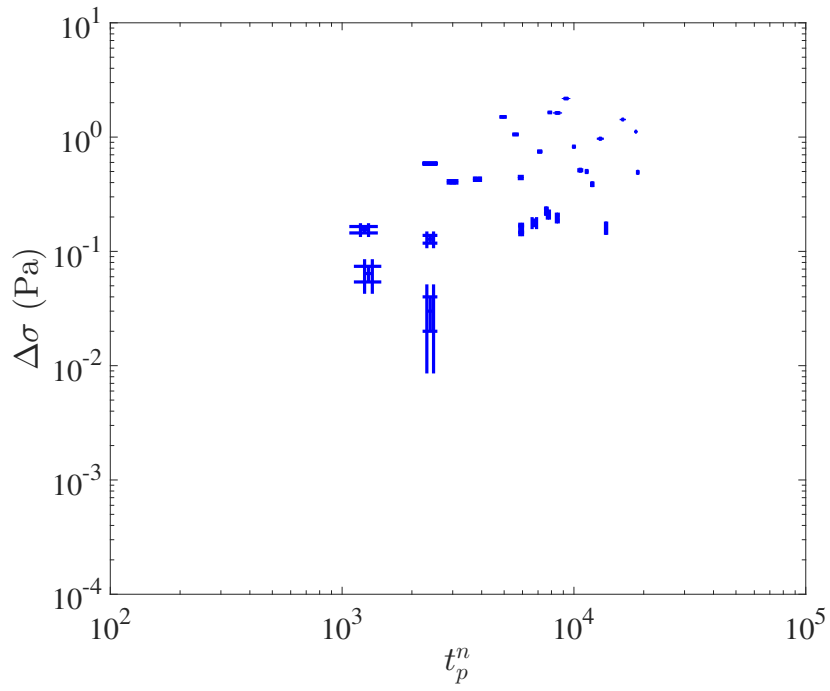


Figure 3.23: Variable definition in fluctuation

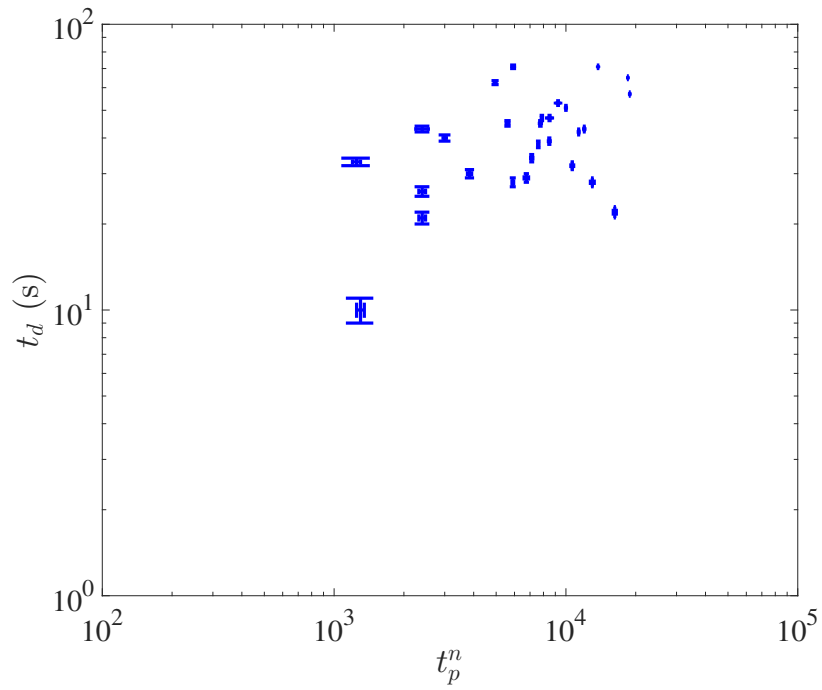
Effects of the preparing time  $t_p^n$  is displayed in Fig. 3.24 where  $\Delta\sigma$  vs  $t_p^n$  and  $t_d$  vs  $t_p^n$  are given in all cases when stress fluctuations are observed. The fact that both  $\Delta\sigma$  and  $t_d$  increase with increasing  $t_p^n$  means that a long preparing time triggers a predominant stress fluctuation, which is an analogical property to stick-slip phenomena. Note that the trend does not depend on the applied shear rate and the aging time.

The relation between the peak stress  $\sigma_p$  and  $\Delta\sigma$  shown in Fig. 3.25 infers the existence of a kind of *yield stress* since the all fluctuations appear only when  $\sigma_p > 3.2 \text{ Pa}$ , approximately. In this case, the *yield stress* is the stress threshold to observe the stress fluctuations that is different from the so-called yield stress, which is difficult to determine experimentally [85], but it would be related to the yield stress.

When it is compared with the flow curve as in Fig. 3.26, it is clear that the stress fluctuations are observed within the unstable zone. In this way, the stress fluctuations are consistent with the flow curve, which is obtained by a different experimental protocol and shows the link to local dynamics such as wall slip and shear banding.



(a)  $\Delta\sigma$  vs  $t_p^n$



(b)  $t_d$  vs  $t_p^n$

Figure 3.24: (a) Amount of stress drop  $\Delta\sigma$  vs non-dimensional preparing time  $t_p^n$  (b) Duration time of stress drop  $t_d$  vs  $t_p^n$  for all cases of stress fluctuations.

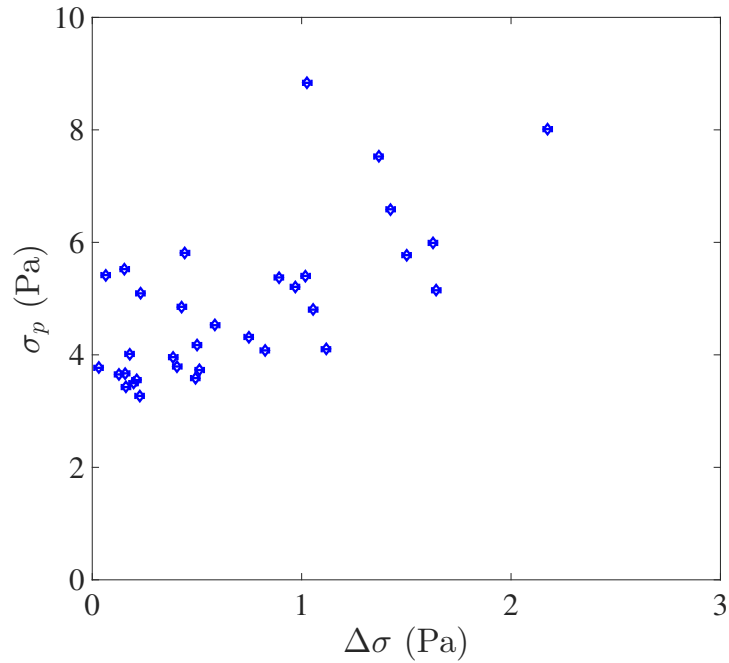


Figure 3.25: Peak stress  $\sigma_p$  vs amount of stress drop  $\Delta\sigma$  for all cases of stress fluctuations.

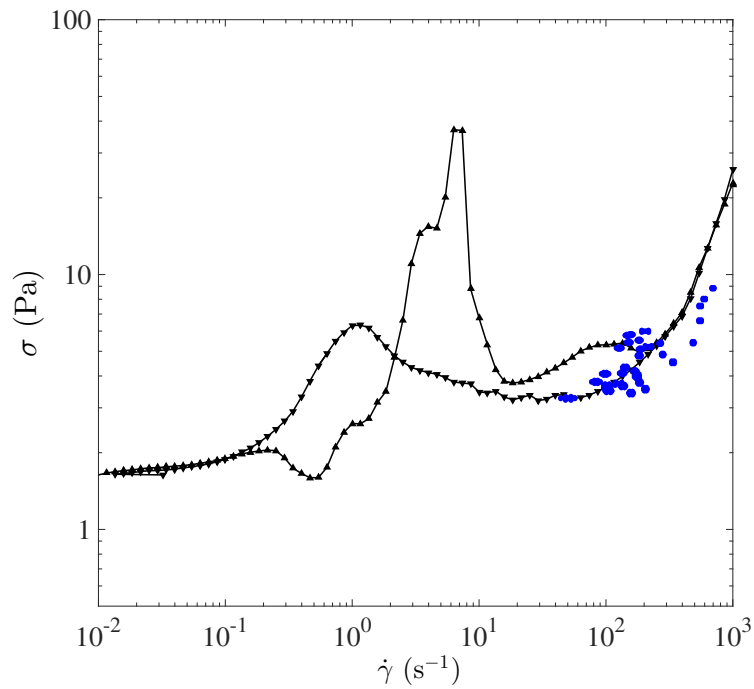


Figure 3.26: Flow curve, shear stress  $\sigma$  vs. applied shear rate  $\dot{\gamma}$  shown in Fig. 3.8 superimposed results of the stress fluctuations. As for the blue dots, stresses, at which the stress drops occur are measured by the rheometer while shear rates are local shear rates in the shear-banded part estimated by USV data. The dot size depends on the errors.



---

### 3.5.2 How is Stress Fluctuation Induced?

In combination of global stress history and associated evolution of the internal velocity structure, this work unravels the existence of unique fluctuations in the stress that correspond to local changes associated with the abrupt fluidization of shear-banded flow and aging. With reference to the experimental results, here we consider the fluctuation process in two steps as shown in Fig. 3.27. ①–② : While the stress slowly increases, the sample evolves as evidenced by the decrease of the width of shear banding and the increase of the global viscosity [see Figs. 3.17(b)(c)], which implies that solid-like part extends into the flow due to the aggregation of particles. On the other hand, the decrease in viscosity at the shear-banded part and the increase of the local shear rate [see Figs. 3.17(b)(c)] induces shear-thinning in the flowing part and/or expelling the aggregated particles to the solid-like part. ②–③ : The sample suddenly fluidizes beyond sufferance causing the stress drop. In this process, separation of the aggregated particles and destruction of the particle in itself are considered to happen since the two phenomena have been practically observed in microfluidic experiments by using a microscope (Wild Makroskop Mk20, Heerbrugg Co., Ltd., objective Makrozoom 1/5, Leica Co., Ltd.) as shown in Fig. 3.28. Although the microfluidic experiments are not well-controlled by imposing hand-built shear, the formation and destruction of shear banding accompanied by fragmentations of aggregated particles and changes in contacts of aggregated particles were confirmed.

In conclusion, the key finding in this experimental study is that the stress shows distinct fluctuations in flowing fluids, which is strongly reminiscent of stick-slip phenomena in solid materials [45, 82]. Also the conditions to induce the stress fluctuation are revealed in terms of shear rate. We have shown that for higher shear rates, the fluidization of the sample involves successive local avalanche-like fluctuation events that are heterogeneously distributed along the cell height. The dynamics is strongly coupled to both the slip behavior at the wall and the width of the shear band. For intermediate shear rates, the stress fluctuations occur repeatedly. Based on observations of the local dynamics, aging process proceeds when the stress increases, while abrupt fluidization occurs somewhere in the fluid when the stress drops. That is to say, the persistent stress fluctuations are seen as the result of the competition, *aging* vs. *rejuvenation*.

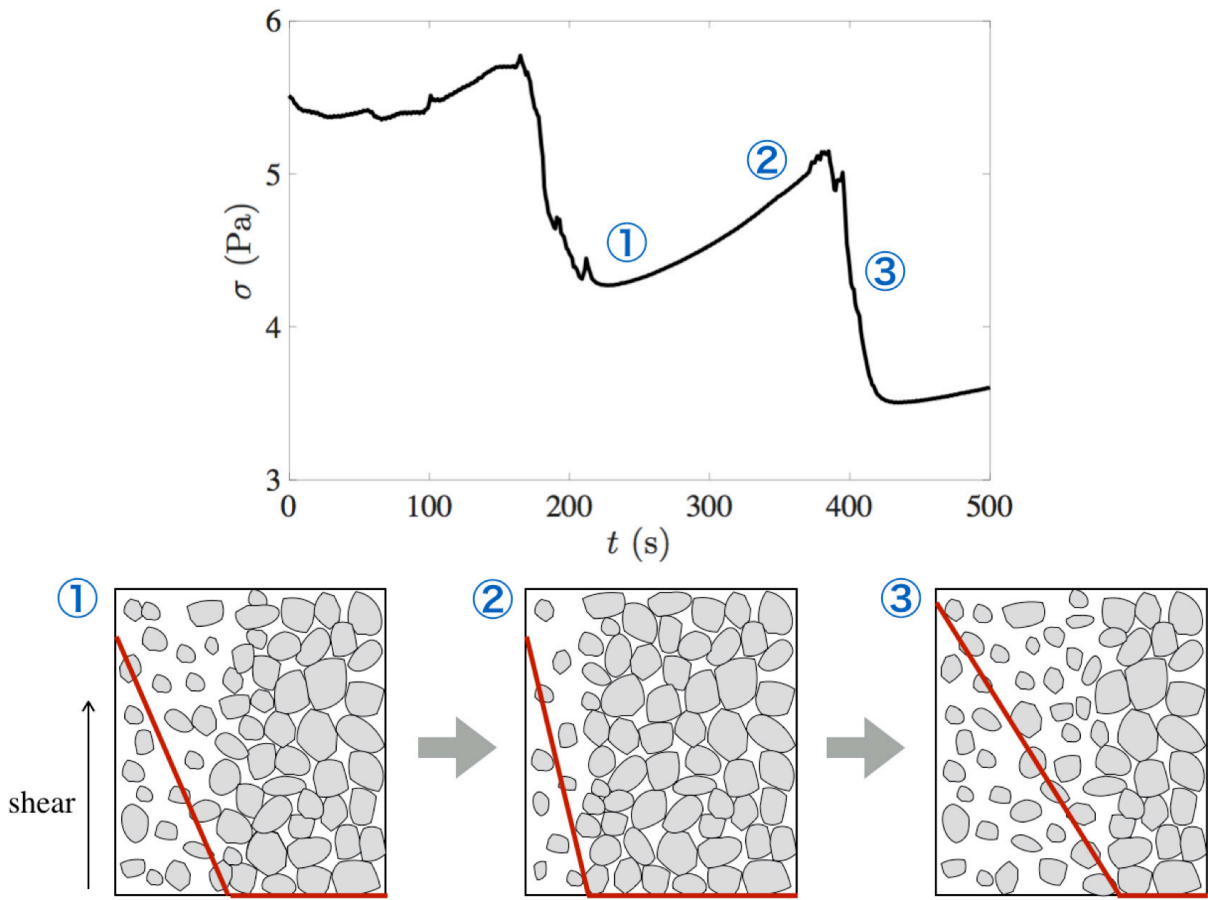
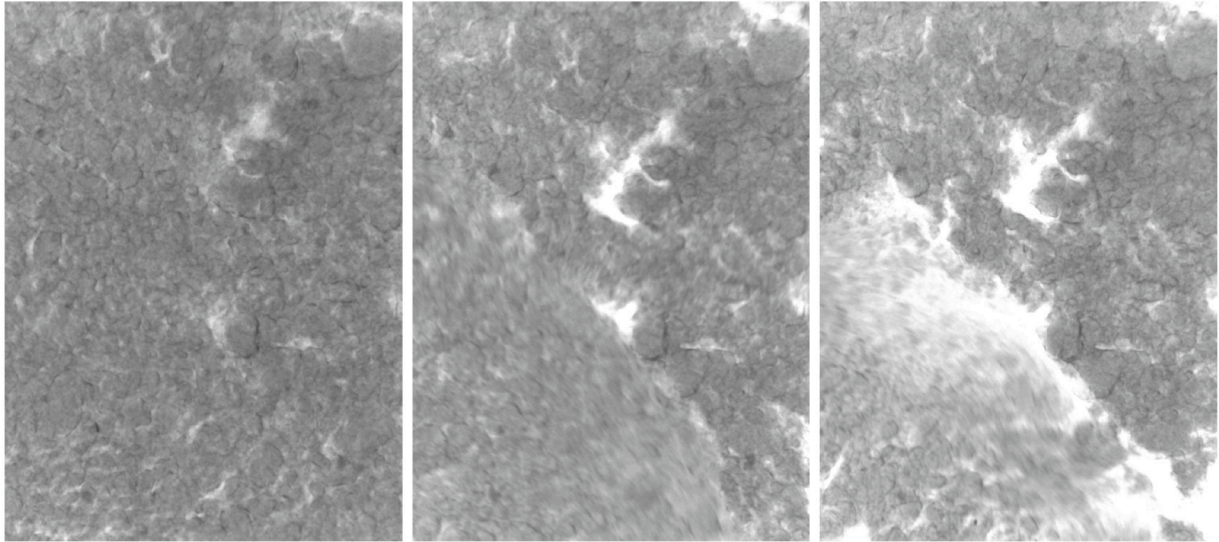
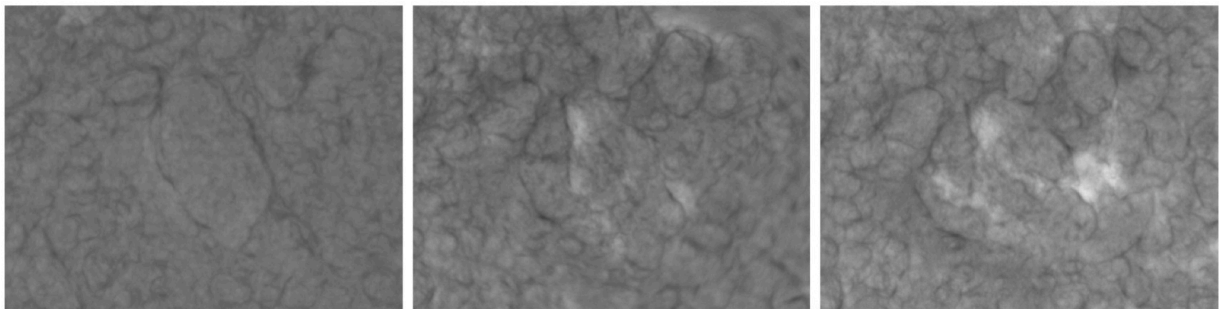


Figure 3.27: Graphic illustration of proposed mechanism of the stress fluctuation. The red lines show velocity profiles.



(a) Rearrangement



(b) Fracturing

Figure 3.28: Images of rearrangement and fracturing processes of aggregated particles taken by a microscope (Wild Makroskop Mk20, Heerbrugg Co., Ltd., objective Makrozoom 1/5, Leica Co., Ltd.).

---

### 3.5.3 Implication for Oscillation Induced by Non-linear Magma Rheology

Shear banding plays a key role to generate stress fluctuations in the experiments. At moment, significance of the shear banding has not been well recognized in the field of magma rheology although shear-banded structures have been observed in eruptive products at volcanoes. However there exist several pioneering experimental works on natural magma, which suggest shear banding and stress fluctuations.

[13, 119] adopted torque measurements by using rotational rheometers and observed the texture of quenched products. Fig. 3.29 shows a temporal change in viscosity during crystallization at a constant shear rate and sub-liquidus temperature [13]. The sample is the dense pyroclastic flow erupted during the 2006 Plinian activity of Tungurahua Volcano, Ecuador. The figure indicates that the viscosity increases with progress of crystallization (Fig. 3.29). The interesting point is that the change is not always smooth but it sometimes has step-like increases and even decreases in a short time scale. Since the viscosity reported here is calculated by the measured torque, the result corresponds to short time-scale stress fluctuations. This behavior is similar to what we reported in the experimental suspension.

The cross-sectional view of the experimental product after deformation (Fig. 3.30) reveals existence of three-layered structure: two plagioclase-bearing layers along the inner wall and the outer wall separated by thick crystal-free layer. From the information in Fig. 3.30, the crystal volume fractions in the three layers are estimated as  $0.22 \pm 0.01$ ,  $0.02 \pm 0.02$ , and  $0.14 \pm 0.01$  from the inner part to the outer part. The significant difference in crystal volume fraction brings about a difference in viscosity, that is shear banding. In the study [13], the authors propose that crystal redistribution and alignment in the flow field generates the viscosity fluctuations. The mechanism is reminiscent of the results of our experimental study: stress fluctuations caused by the variation in width of shear band and wall slip due to the change in arrangements of particles by aging and shearing. However since their work is not *in-situ* measurement but based on observations of the quenched product, more-straightforward and *in-situ* experiments are needed to explore physical mechanism of the stress/viscosity fluctuation.

Until this point, experimental approaches are discussed. The next session will focus on a different approach, analysis of observed volcanic tremor and LP events at an active volcano, to look for the link between non-linear rheology and volcanic oscillation phenomena induced by magma movements from the other direction.

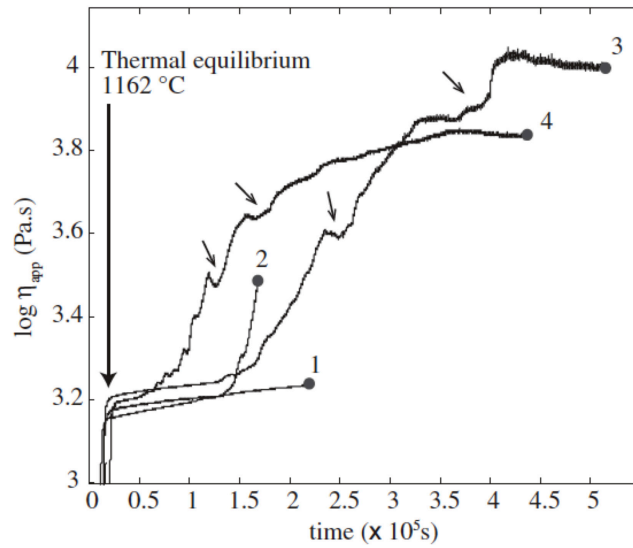


Figure 3.29: Temporal change in viscosity during crystallization at  $0.042 \text{ s}^{-1}$  and  $1162 \text{ }^{\circ}\text{C}$  [13]. The same measurement is repeated four times with different termination times.

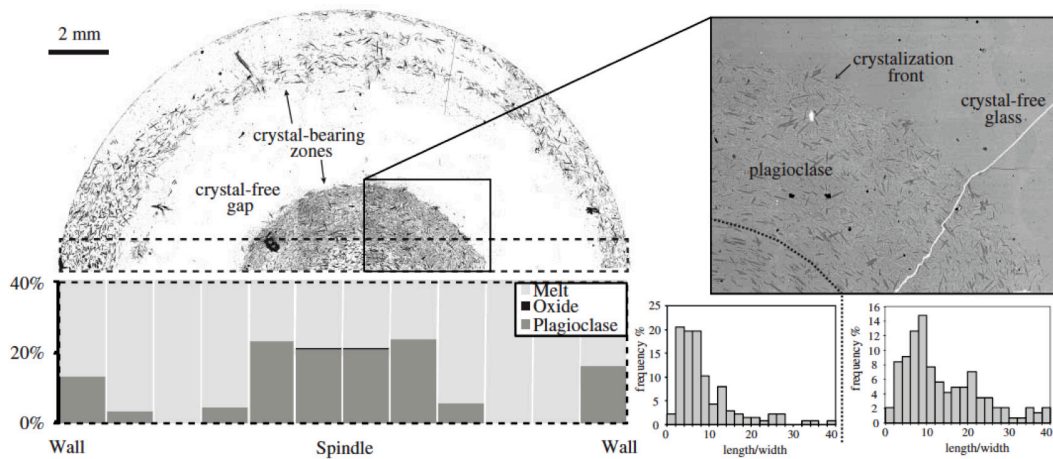


Figure 3.30: Image of the product quenched after run 2 in Fig 3.29 with the corresponding crystal fraction across the sample in reference to [13]. The right image shows the crystallization front and two crystal-bearing zones with plagioclase aspect-ratio frequency plots.

# Chapter 4

## Analysis of Volcanic Oscillations Accompanied by 1986 Izu-Oshima Eruption

### 4.1 Overview

In this thesis, volcanic tremors and LP events associated with 1986 eruption of Izu-Oshima volcano are analyzed as representative cases to infer rheological controls in generation of oscillation phenomena. Although some observational data have been damaged and lost after many years and the instruments at that time were quite old and inaccurate in the present day standard, there still exist four important factors to focus even in such severe situations.

First it shows a remarkable change in eruption style from summit eruption to fissure eruptions, and the small summit eruption. The change in eruption style during the major activity is quite unique on a global scale and expected to link to the movement of magma inside the volcano. Since the main interest of this study is to explore possible relation between non-linear magma rheology and volcanic oscillation phenomena, the change of eruption style can prepare suitable test case to focus the control of magmatic properties with keeping same geometrical conditions. In comparing oscillation phenomena between different volcanoes or different eruption episodes, we could not focus only the magmatic properties because varied geometrical situations should always obscure the arguments.

The second reason comes from more broad interest. One of the major concerns in volcanology is how to conduct real-time monitoring of eruption processes. The change of eruption style in this case could provide an indispensable chance to check the idea/procedure of real-time monitoring by using volcanic tremor and LP events.

Thirdly, Earthquake Research Institute (ERI) undertook digitization of analog seismic

---

records of the 1986 Izu-Oshima eruption a few years ago and luckily the data became available at just the right time. In this way, it was a good opportunity to reveal remaining mysteries, which have not been unraveled by previous studies, using digitized data with recent analytical approaches.

As the last reason, Izu-Oshima is known to have the eruption interval of about 30 years and 27 years had already passed when we planned to analyze the data. Based on the history, the volcano is expected to be at the preparatory stage to the next eruption. Therefore it was the time to undertake the analysis in order to understand the past eruption in detail for utilizing the results for the next.

In association with the 1986 Izu-Oshima eruption, volcano-tectonic earthquakes, tremors, and long-period (LP) events were observed. Among them, tremors and LP events are known to provide clues to magma migration pathways since they are often associated with the movement of fluids through conduits or dykes as presented in Introduction. Again, the main goal of this study is to understand volcanic oscillation phenomena induced by non-linear magma rheology. Toward the goal, we report analytical results on tremors and LP events associated with the 1986 Izu-Oshima eruption in this chapter. In the first place, Section 4.2 explains chronology of the eruption. Then after explaining the analytical methods in Section 4.3, the activities during the large eruption stage are focused in Section 4.4.1. Next, Section 4.4.2 describes oscillation phenomena during the terminal stage after the active eruption stage, including the small summit eruption. Then the temporal variation of volcanic oscillations accompanied by the change in eruption style is summarized in Section 4.4.3.

## 4.2 Sequence of 1986 Izu-Oshima Eruption

Izu-Oshima Island is one of the most active volcanoes in Japan that locates 110 km SSW of Tokyo (see the map in Fig. 4.1). It typically erupts in vulcanian or strombolian explosions that produce emanations of basaltic lava. The most recent eruption occurred in 1986, consisted of the most active stage with three eruption episodes at craters A, B, and C as in Fig. 4.1, and a minor summit eruption followed about one month after the active stage. The eruption began at the summit crater A at 17:25 (GMT+9) on November 15, initially in a strombolian style with a continuous lava fountain. The eruption then changed to a vulcanian style, gradually became intermittent and explosive accompanied by infrasound and shock waves with decreasing magma discharge rate. This observation indicates that gas discharge gradually became dominant over magma discharge [31, 106]. The eruption suddenly ceased at the end of November 19 and was followed by a quiet period with very small explosions at the summit that continued until the morning of November 23. Two

---

subplinian eruptions occurred in parallel at 16:15 and 17:47 on November 21 producing fissures in the caldera floor (crater B) and in the flank of the outer rim (crater C). Lava flow from these unexpected fissure eruptions approached inhabited regions on the island and forced the evacuation of all residents. However, the two fissure eruptions were short-lived and subsided by 2:00 on November 22. After the fissure eruptions, silent period had lasted for 26 days on the surface preceding a small strombolian eruption at the summit on December 18. The summit eruption is far smaller in scale than the former three eruptions and the duration time is just a few hours. As for the former active eruptions, the eruption sequence is distinctive in that the duration of fissure eruptions ( $< 10$  h) was much shorter than that of the summit eruption ( $> 4$  days), while the total volume erupted from the fissures ( $0.0351 \text{ km}^3$ ) was larger than that ejected from the summit ( $0.0178 \text{ km}^3$ ) [31, 75].

## 4.3 Analytical Methods

### 4.3.1 Data

Intensive volcanic tremors during the eruptions and LP events in the intervals were recorded by seismometers on the island [42, 124]. The seismometers are velocity type with the natural period of 1 s (Katsujima Co. Ltd.). In this study, analog signals recorded by the short-period seismometers were digitized and analyzed. The locations and names of five stations mainly used for this analysis are shown in Fig. 4.1. The original signals were transmitted to Oshima Volcano Observatory of ERI by radio and recorded in magnetic tapes as analog signals. The digitization was performed at a sampling rate of 200 Hz with a 12-bit amplitude resolution. Due to the low signal-to-noise ratio of the analog recording, the actual dynamic range of the digitized data is 10 to 11 bits. The analyses are conducted only for the UD component, since other components could not be digitized successfully due to tape deterioration. The deterioration was also found in data of the UD component: the open-reel films extended with age. The degree of extension was estimated by comparison to the information of standard-time and frequency-signal emission (JJY clock data). The estimation found that the films extended  $1.015 \pm 8.7 \cdot 10^{-4}$  times longer than in reality on average. Hence all data used in this study were corrected in terms of time by dividing by the value. The gain of amplitude was also altered by reference to documents written at the time.



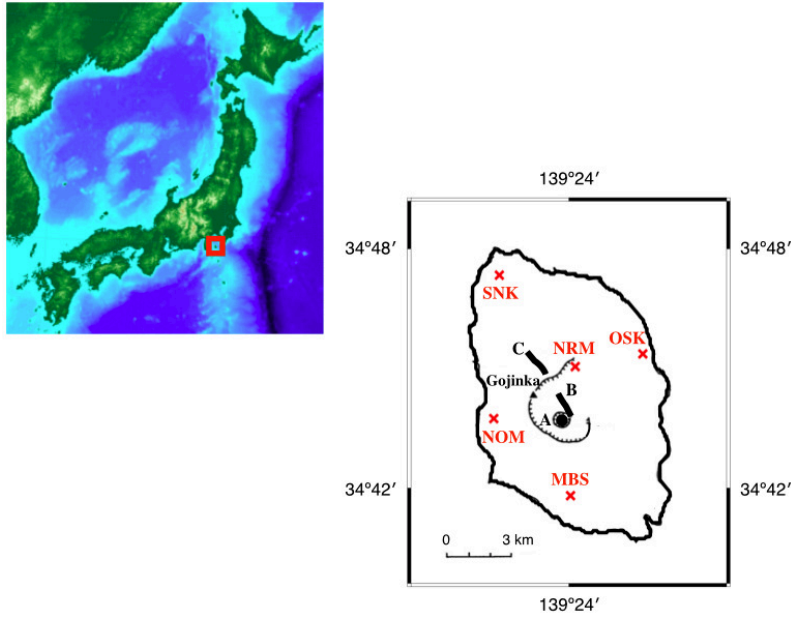


Figure 4.1: Names and positions of the five seismic stations used in this analysis. The map of Izu-Oshima, which shows the locations of the summit crater (A) and the fissures (B and C) is based on [123]. The map left above indicates the location of the Izu-Oshima Island in Japan as red square.

### 4.3.2 Estimation of Source Location

Conventional arrival time methods for tectonic earthquakes cannot adapt to locations of volcanic tremor and LP event due to the absence of clear onset. Over the last decade, several techniques have been developed to estimate the source locations, including the cross-correlation method [72, 92], the time reversal method [40, 65, 70], and the amplitude inversion method (AIM) [7, 61, 93]. The former two methods require the accurate time information because those are based on the phase coherence of the signals observed among the seismic stations, while accuracy of amplitude information has a greater significance than time in AIM. As mentioned in Section 4.3.1, our original data had a time lag due to the tape deterioration. It was corrected in use, however application of methods that require the accuracy of time is preferable to be avoided. For that reason, this study adopted AIM that utilizes the amplitude attenuation of the seismic signal with distance from the source. The fact that AIM can estimate the source location by using a single component is another reason to prefer since only UD component data is available in this study.

Although AIM does not require accurate time data, it is critically dependent on the path attenuation and the local amplification factor. We used coda waves from seven earthquakes (utilizing six seconds of the wave trains starting two seconds after the S wave peak) that occurred in November 1986 near the Izu Peninsula. Details of the effects are described in

---

Appendix. In recent years, AIM has been developed and successfully applied to the emergent signals of volcanic tremors and LP events [7, 61, 93]. AIM applied in this study assumes that wave consists of body wave because in the case of volcanic tremor and LP events during active eruptions, the sources are expected to locate beneath the seismic stations and the waves arrive at the stations directly while for instance, rockfalls are surface phenomena and the waves would be dominated by surface waves. The adaptive possibility of the method to volcanic tremor and LP event is evaluated in [6].

The seismic amplitude at the  $i$ -th station at time  $t$  is expressed as follows:

$$A_i(r_i, t) = A_0(t) \frac{e^{-Br_i}}{r_i} S_i \quad (4.1)$$

where  $A_0$  is the source amplitude calculated as  $A_0 = \frac{1}{N} \sum_{i=1}^N A_i r_i e^{Br_i}$  ( $N$  is the number of seismic stations),  $r_i$  is the distance between the source and the  $i$ -th station, and  $S_i$  is the site amplification factor.  $B = \frac{\pi f}{Q\beta}$ , where  $f$  is the characteristic frequency,  $Q$  is the quality factor for medium attenuation, and  $\beta$  is the velocity of the medium. We set  $f$  to 3 Hz and  $Q$  to 50 with reference to [60], and  $\beta$  to the shear wave velocity with reference to [81]. To estimate the source location, the point that minimizes the normalized residual error between the observed root-mean square amplitude  $A_{obs}$ , and the calculated amplitude in Equation (4.1) is searched by changing  $r_i$  as follows:

$$\delta = \sqrt{\frac{\sum_{i=1}^N \left( A_{obs} - A_0 S_i \frac{e^{-Br_i}}{r_i} \right)^2}{\sum_{i=1}^N A_{obs}^2}} \quad (4.2)$$

To minimize  $\delta$ , a grid search is performed using a 10 m mesh numerical map produced by the Geospatial Information Authority of Japan. The search area is within the Izu-Oshima Island and the vertical dimension is limited to between 4 km depth and the surface. Previous studies that have adopted AIM regarded the estimated error as the residual,  $\delta$  in Equation (4.2). For example, [7] showed tremor sources in the  $\delta$  range of 0.1 to 0.3 while [61] indicated spatial distributions of  $\delta$  in the time windows, which have about  $\delta$  of 0.2 as the maximum. By reference to the studies, we set the residual threshold as  $\delta < 0.2$ . However since the main concern of this study is the migration of sources, it is more straightforward to present errors in the spatial domain rather than the amplitude domain. The error in the spatial domain,  $\Delta z$  is calculated by partial differentiation of Equation (4.2) in the main part with respect to  $r_i$ :

$$\Delta A_i = A_0 S_i \left( -\frac{B e^{-Br_i}}{r_i} - \frac{e^{-Br_i}}{r_i^2} \right) \Delta r_i \quad (4.3)$$

---


$$\Delta r = \frac{1}{N} \sum_{i=1}^N |\Delta r_i| = \frac{1}{NA_0} \sum_{i=1}^N \Delta A_i \cdot \frac{r_i^2 e^{Br_i}}{S_i(1 + Br_i)} \quad (4.4)$$

Assuming the isotropy,  $\Delta r = \sqrt{3\Delta z^2}$  :

$$\Delta z = \frac{1}{\sqrt{3}} \frac{1}{NA_0} \sum_{i=1}^N \Delta A_i \cdot \frac{r_i^2 e^{Br_i}}{S_i(1 + Br_i)} \quad (4.5)$$

As thresholds, we set  $\delta < 0.2$  and  $\Delta z < 1$  km to ensure reliable results.

---

## 4.4 Results and Consideration

### 4.4.1 Volcanic Tremor in Active Eruption Stage

During the most active stage including the summit eruption and the fissure eruptions, intensive volcanic tremors have been observed. This section focuses on temporal variations in waveform characteristics of the tremors and the source locations with comparing the change in eruption style.

#### Waveform Characteristics of Volcanic Tremors

Fig. 4.2 shows temporal variations in the root-mean square (RMS) amplitude,  $\sqrt{\frac{1}{n} \sum_{k=1}^n A(k)^2}$  ( $n$  is the number of data,  $A$  is the observed amplitude), of the tremor with those in magma discharge rate and eruption activities. In this case, RMS amplitude is calculated every 1 min with 10-second overlap. The data show two distinct types of volcanic tremor: 1) continuous tremor that occurred during the initial activity period including the summit eruption stage; and 2) episodic tremor that occurred during the latter activity period that include fissure eruption stage. Looking at the time variation in the RMS amplitude, the continuous tremor persists without a break showing the gradual change in amplitude with time on a long time scale. On the other hand, the episodic tremor occurs intermittently with large amplitude shift in a short time. Thus the difference in the two types of volcanic tremors is found in characteristics of the amplitude.

In chronological order, the amplitude of the continuous tremor increases gradually from the beginning of the summit eruption on November 15, synchronous with a decreasing rate of magma discharge from the summit eruption. This behavior is unique because volcanic tremor is generally considered to represent magma migration, and positive correlations between tremor amplitude and magma discharge have previously been reported [7]. In contrast, the episodic tremor is in agreement with this general relationship. Waveform examples of the two tremor types (Fig. 4.3) show that the episodic tremor lasts up to several minutes while the continuous tremor occurs without interruption. As concerns the dominant frequency, although significant difference between the two types is not detected in the narrow frequency responses of the seismometers, the results in Fig. 4.4 show that the both dominant frequencies are around 1 Hz. A previous study about the eruption [124] reports the time change in spectra using three-components data of Japan Meteorological Agency (JMA). According to the study, waves with frequencies above 1 Hz become dominant in the continuous tremor from November 17 to 19. The shift is apparent especially in NS component. On the other hand, the dominant frequency of 1Hz does not change even after the volcanic tremor transformed into the episodic type, which supports our results. Their

results of particle motion of episodic tremor occurred on November 20-21 indicates the prevailing directions of oscillation from NNE-SSW to NW-SE composed of Rayleigh and SV types of wave motion.

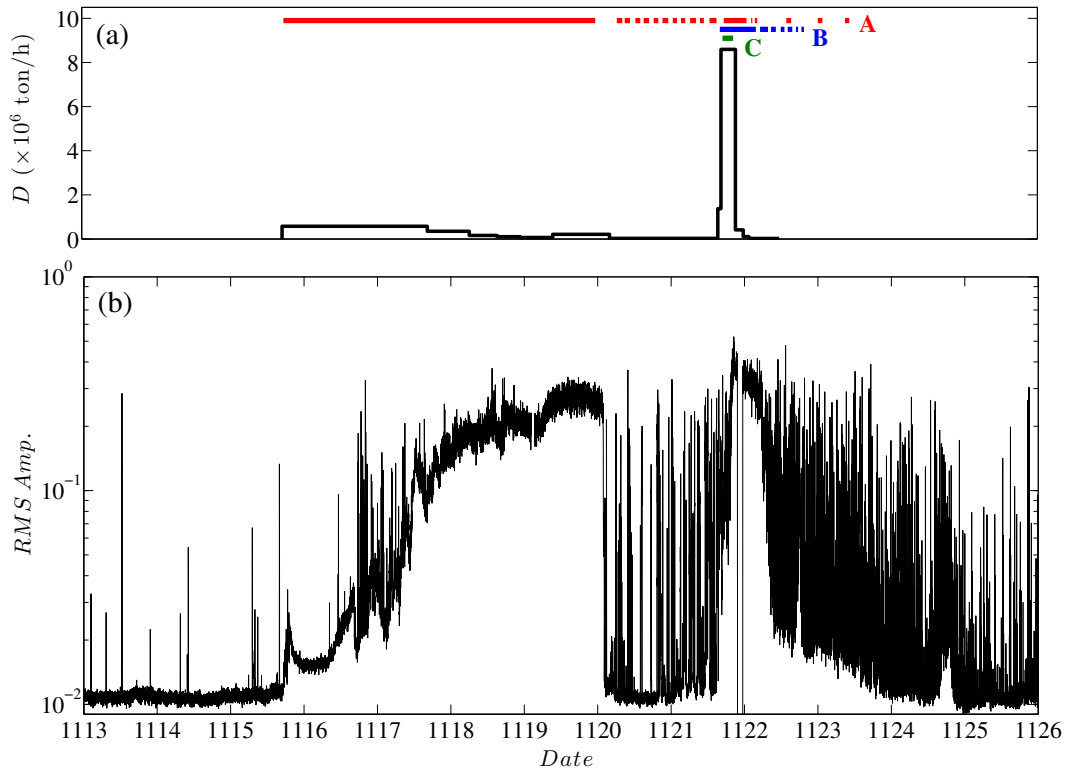


Figure 4.2: (a) Magma discharge rate of November 15 – 22 given by [31]. Red, blue, and green lines indicate activities of the summit eruption at A crater, the fissure eruptions at B and C craters, respectively with reference to [106]. (b) RMS amplitude of volcanic tremor during November 13 – 25 at MBS calculated every 1 min.

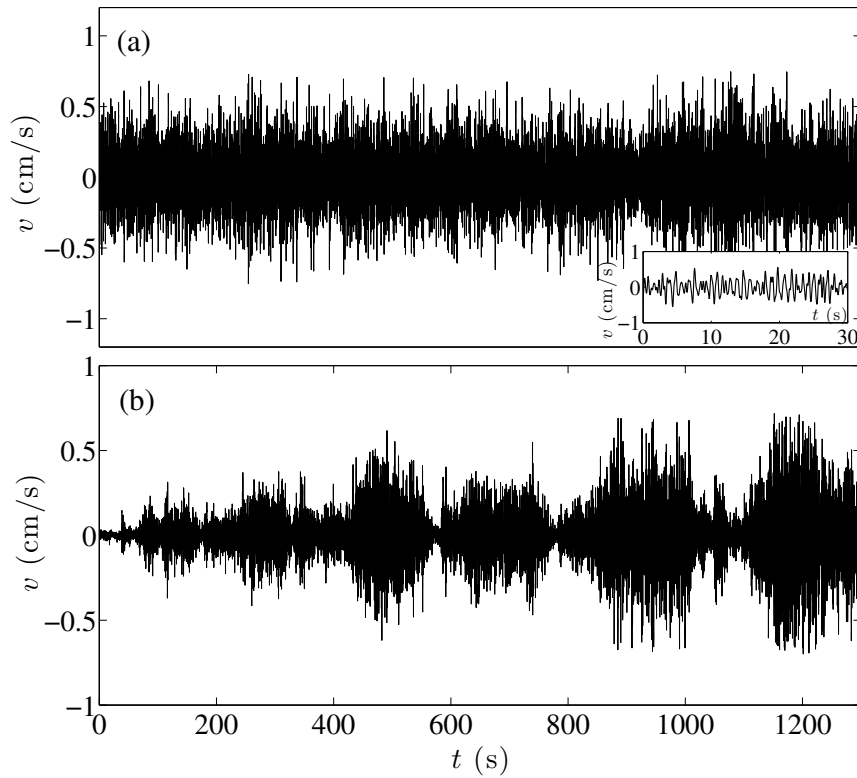


Figure 4.3: Comparison of waveforms observed at OSK. (a) Example of continuous tremor starting at 1:00 am on November 19. Inset: magnified figure of the same data set. (b) Examples of episodic tremor starting at 9:32 am on November 23.

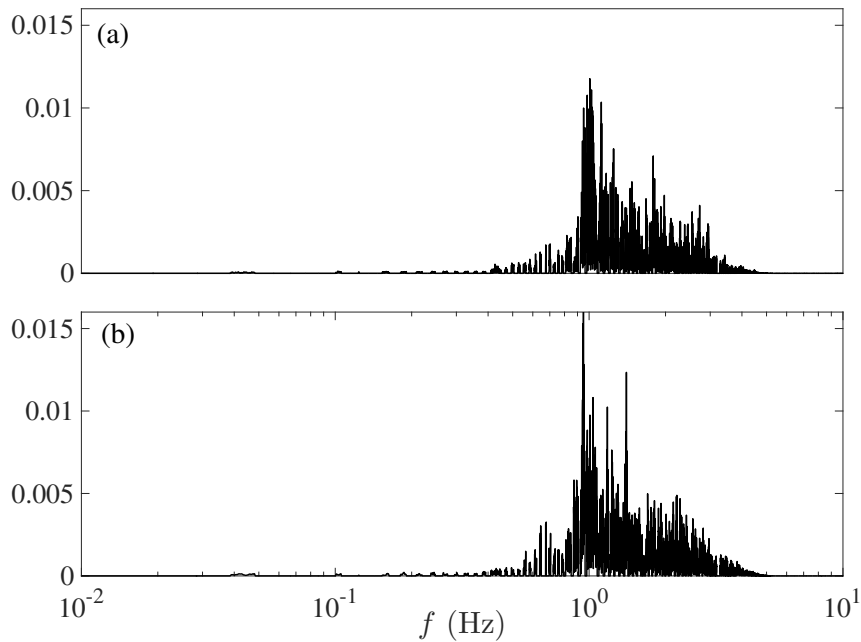


Figure 4.4: Comparison of spectra of waveforms in Fig. 4.3(a) and (b). Noises come from the tape characteristic are filtered out from the data.

## Temporal Variation in Tremor Source

Fig. 4.5 represents example waveforms of the continuous tremor used for source location by AIM. In this case, the tremor source is determined below the summit. The amplitude corrected by the site amplification factor decreases exponentially with increasing the distance from the determined source location. The trend follows the relation in Equation (4.1) that represents the attenuation of amplitude as a function of the distance to the source.

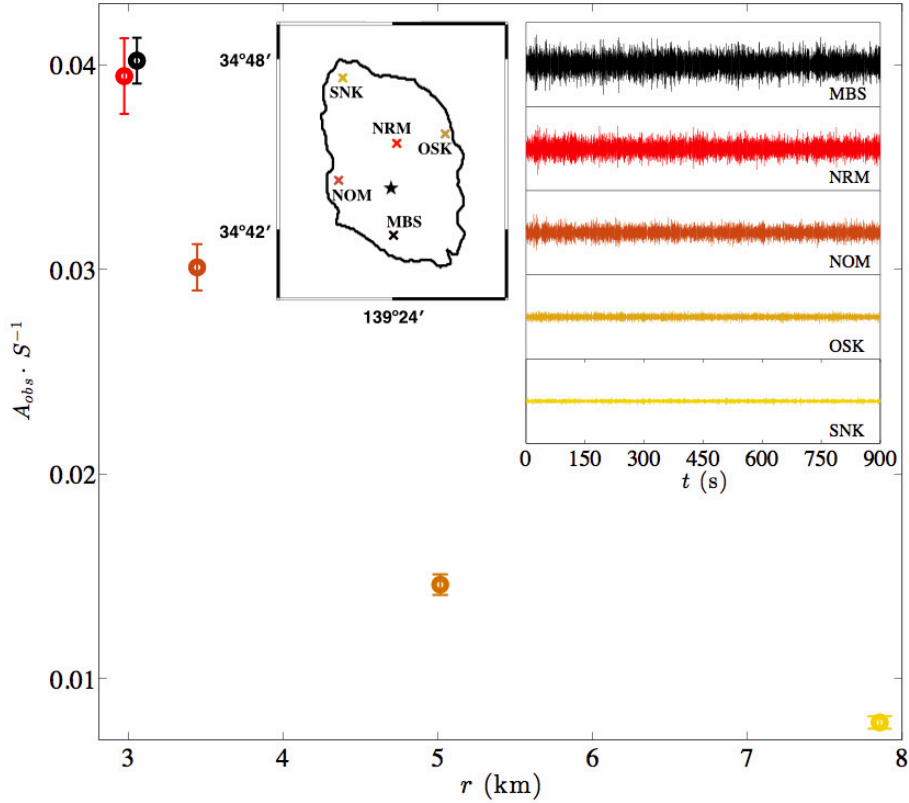


Figure 4.5: Relation between source amplitude  $A_{obs} \cdot s^{-1}$  and distance to the source  $r$ , occurred from 8 pm for 15 minutes on November 15. The right insets show waveforms at the five seismic stations. The scale of y-axes is  $\pm 0.3$  cm/s and the waveforms filtered from 1 Hz to 5 Hz are used in the AIM method. The left inset marks locations of the tremor source ( $\star$ ) and the seismic stations ( $\times$ ).

---

The temporal variation in tremor source location from November 13 to November 23 are shown in coordinates of longitude and latitude (Fig. 4.6) and in the depth direction (Fig. 4.8). The estimation of source location is made using RMS amplitudes in each 15-minute time window with the purpose of future application for automatic real-time monitoring. The RMS amplitude at the  $i$ -th seismic station is written as  $\sqrt{\frac{1}{n} \sum_{k=1}^n A_i(k)^2}$ , where  $n$  is the number of data for 15 min and  $A_i$  is the bandpass-filtered amplitude (1–5 Hz) at  $i$ -th seismic station. The results of source location meet the threshold condition,  $\delta < 0.2$  and  $\Delta z < 1$  km. In Fig. 4.6, most tremor sources cluster in a narrow region around the summit crater on November 13 to November 19. It is consistent with the fact that the summit eruption has lasted from November 15 to November 19. In association with the onset of the eruption, the depth of tremor source also shows reasonable result, moving toward the surface (Fig 4.8). On the other hand, the epicenters of volcano-tectonic earthquakes do not cluster around the summit crater during this period as in Fig. 4.7 [123]. This result indicates the source location of volcanic tremor is a better indicator of magma migration than earthquake epicenter since magma was drastically effused from the summit during the eruption.

After the summit eruption suddenly calmed down in the middle of night on November 19, the location of tremor sources changes significantly. The sources spread along a NW–SE trending line that includes the region of the surface fissures B and C already on November 20, the day before the fissure eruptions day. The result suggests an important possibility that if real-time monitoring of tremor source had been performed, the fissure eruptions would have been expected. The trend of clustering NW–SE line continues till November 23 as in Fig. 4.6. At the stage, epicenters of earthquakes also align with the same direction accompanied by the fissure eruptions as indicated in Fig. 4.7.

On the other hand, the source depth produces few meaning in this fissure eruption period (Fig. 4.8) while source locations using the same AIM determine the depths well as indicated in Fig. 1.4 in Introduction. As possible explanations for the difference in accuracy of the depth direction, the number of seismic stations, the height of volcano, and the dominant frequency are considerable. When it is compared to the previous study as in Table 4.1, the smaller number of seismic stations located on the Izu-Oshima island recording waves with lower dominant frequency while it is known that the AIM works well for signals with relatively-high frequency as the case of the previous study. Moreover at Piton de la Fournaise, which is much higher than Izu-Oshima and has plumbing system at shallower part mostly above the sea level, the large number of seismic stations surround at different altitudes. The observation condition would be another advantage to use AIM because the method is suitable for source location of waves generated at shallower part beneath the stations.



---

	$N$	$H$ (m)	$f$ (Hz)
Izu-Oshima	5	758	1
Piton de la Fournaise	12	2631	5-10

Table 4.1: Comparison of analysis conditions at Izu-Oshima and Piton de la Fournaise Volcanoes as in Fig. 1.4.  $N$  is the number of seismic stations,  $H$  is the altitude of volcano, and  $f$  is the dominant frequency of analyzed data.

To sum up, the results in Fig. 4.2 and 4.6 show that the waveform characteristics and source locations of the volcanic tremor undergo simultaneous and significant transformations from midnight of November 19 to the early morning of November 20 when the summit eruption calmed down. In addition, as other simultaneous change, the tilt measured at Gojinka (the position is shown in Fig. 4.1) also exhibits an inflation in a NNW direction [122]. The inflation can be explained if magma moves to the direction of fissures under the ground. These observations imply that precursory injections of magma beneath the fissures is expected to occur at least 41 hours before the first fissure eruption at B crater. Up to now, only phenomenon that can be interpreted as a precursor of the fissure eruptions was clustering epicenters of volcano-tectonic earthquakes 2 hours before the fissure eruption at B crater [123]. Therefore the migration of tremor source demonstrated in this analysis evidently precedes the epicenter clustering.

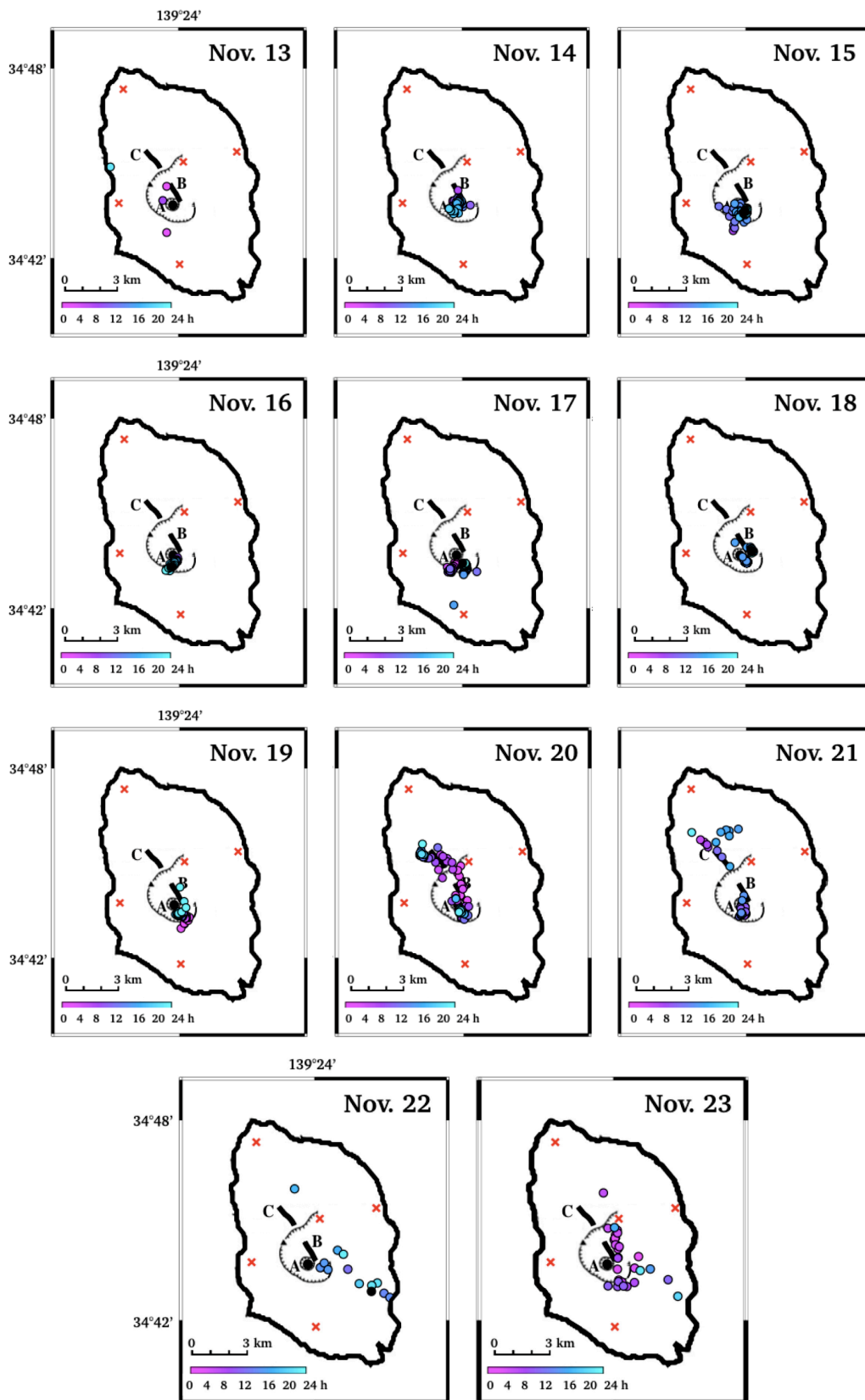


Figure 4.6: Temporal variations in source location on November 13 to November 23. The results shown here are 61.8 % of the total that meet the threshold condition. The color gradation represents the hour in a day and red cross marks indicate the locations of seismic stations.

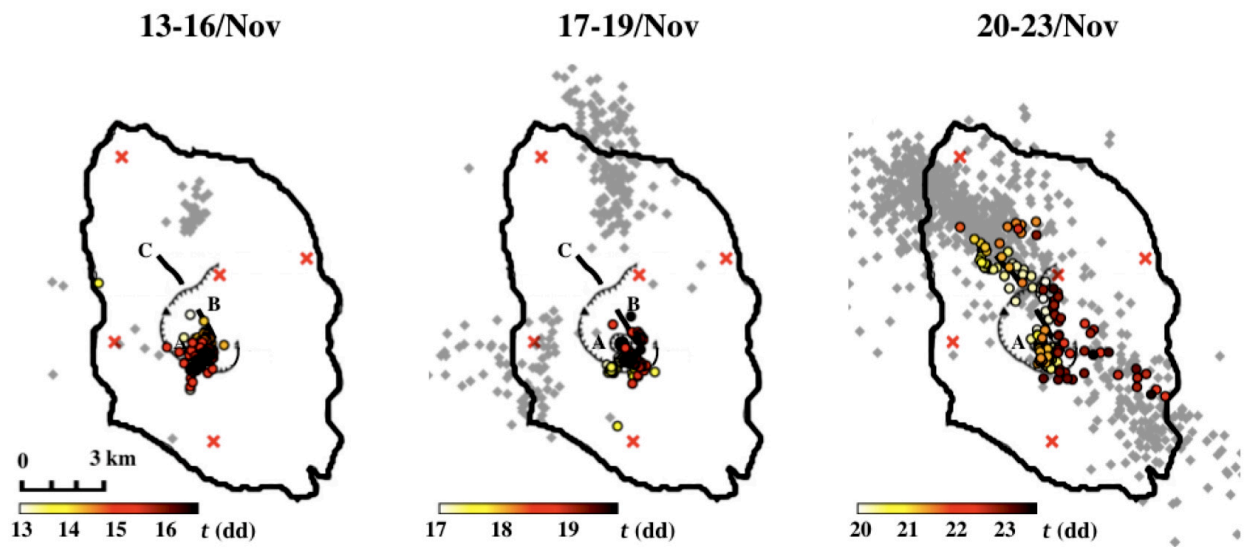


Figure 4.7: Comparison between source locations of tremor and earthquake on November 13 to November 23. The color gradation of tremor sources shows the time in the day unit and red cross marks indicate the locations of seismic stations. Gray diamonds mark source locations of earthquakes during the same period with reference to [123].

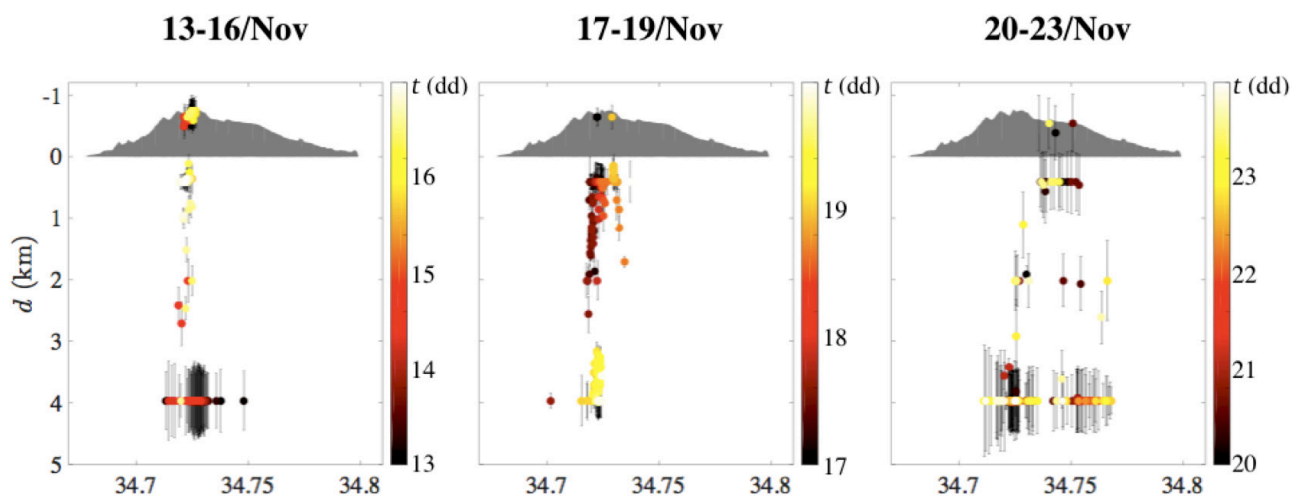


Figure 4.8: Temporal variation in source depth with the distance error estimated by Equation 4.5 on November 13 to November 23 is shown on a cross-section of the island. The color gradation of tremor sources shows the time in the day unit. The planar source locations are indicated in Fig. 4.6 and 4.7.

---

## Precursory Activity of Tremors

The tremor activity on November 16 and 17 is conspicuous because prominent episodic tremors are superimposed on continuous tremor (see Fig. 4.2). We extract 40 episodic tremors from 16:16 on November 16 to 4:20 am on November 17 and apply AIM to wave trains of the tremors that have the average duration time of 46.4 s. Waveforms in Fig 4.9 indicate that the episodic tremors superimpose on the continuous tremor. As concerns the relative difference of amplitude, although it is in the course of the summit eruption, the episodic tremors have a different trend (amplitude at SNK is dominant) from that of the continuous tremor (an increase in amplitude with decreasing distance to the summit). This fact may account for the difference in the source locations. In fact, Fig. 4.10 clearly shows that the tremor sources cluster along the same NW–SE trending line as those from the fissure eruption stage (November 20 – 23). However, this trend is not seen in Fig. 4.7 even though the figure includes data of this same period. The source locations for each 15-minute time window shown in Fig. 4.7 are strongly affected by the base amplitude of the continuous tremor because the 46.4 s average duration of the episodic tremors is shorter than the time window. Therefore, the precursory trend of the tremor sources along the fissures only becomes apparent when the episodic sections are picked. It is noteworthy that these episodic tremors began five days before the fissure eruptions.

As concerns precursory activity of the continuous tremor, [42] reports that the continuous tremor already started at the end of October in 1986 based on the record of the intermediate band seismometer on the Izu-Oshima Island. Since the waveform characteristics seem similar to those during the period of the summit eruption, the precursory activity may already have started below the summit crater two weeks before the eruption, although the tremor source during the period cannot be determined without the digitized data. Thus in both cases of the summit eruption and the fissure eruptions, precursory tremor activities are described. In contrast, the epicenters of volcano-tectonic earthquakes are spread out within and around the island as shown in Fig. 4.7, and do not show precursory clustering until 2 hours before the fissure eruption [123]. The fact confirms the primary importance of using volcanic tremors in adaptive real-time monitoring of volcanic eruptions.

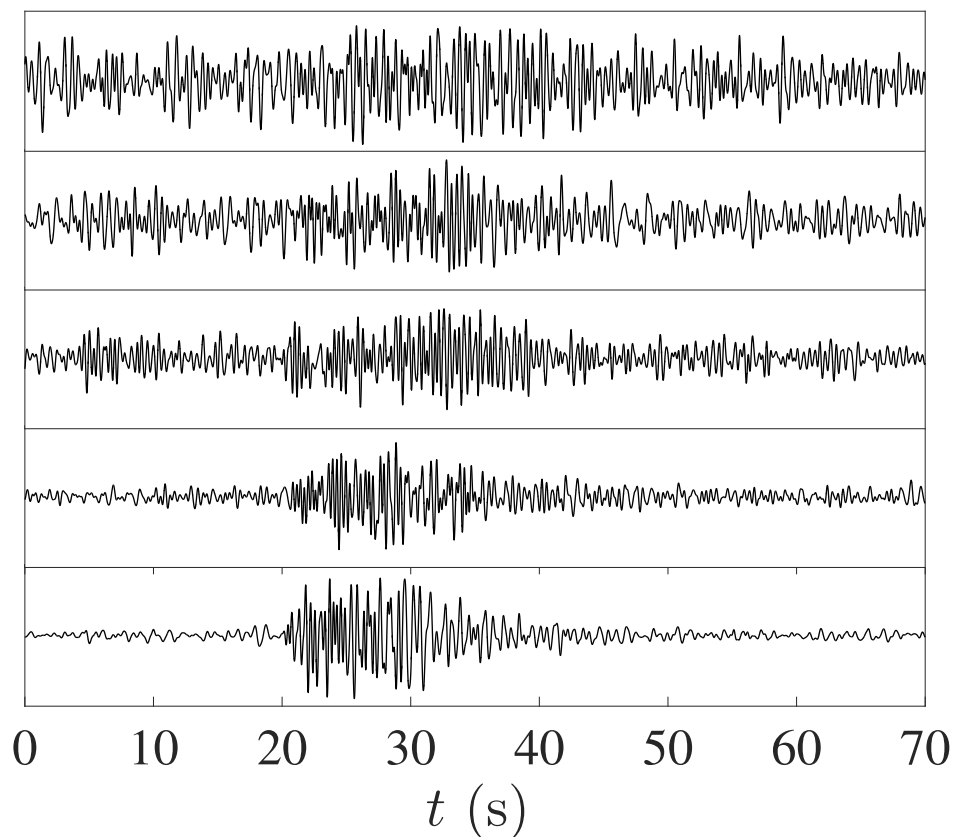


Figure 4.9: Examples of episodic tremors superimposed on the continuous tremor observed at all stations (MBS, NOM, NRM, OSK, SNK from the top to the bottom. The positions are shown in Fig. 4.1), which have y-axis range of  $\pm 1 \text{ cm.s}^{-1}$ . The figures show data at 6:42 am on November 17.

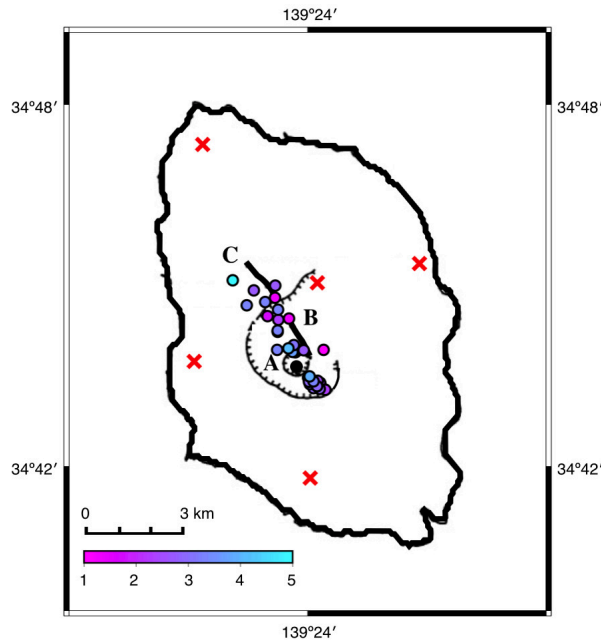


Figure 4.10: Source locations of 40 episodic tremors from 16:16 on November 16 to 4:20 on November 17. The color gradation shows the magnitude of source amplitudes and red cross marks indicate the locations of seismic stations.

### Difference in Two Eruption Styles

There exists a clear correlation between the waveform characteristics and the source locations: continuous tremor occurred during the summit eruption stage and episodic tremor occurred during the fissure eruption stage. Although this strongly suggests that the excitation mechanism differs between the two stages, unfortunately it is impossible to perform in-depth analysis such as the moment-tensor inversion due to the shortage of available data in our case. Under the circumstances, the only way to approach the mechanism of the two types of eruption is comparing temporal changes in the tremor radiation energy and magma discharge rate. Here tremor energy is defined as the time integrated value of mean square amplitude calculated every 1 min. Fig. 4.11 indicates that after the beginning of the summit eruption, the tremor energy increases with decreasing magma discharge. Concerning on the period, previous studies report that hydrovolcanic explosions occurred due to an increase in gas below the summit and the shock waves were observed throughout the South of Kanto area [31]. For this reason, the gas emission seems to become more predominant than magma effusion during the eruption and it causes the negative correlation between the tremor energy and magma discharge, since nucleation and migration of bubbles in the conduit would affect the occurrence of continuous tremor. By contrast, an increase in energy of the episodic tremors associated with the fissure eruptions is large during the period of high magma discharge (November 21 – 22). This result with the fact that volcanic earthquakes

drastically start occurring with the fissure eruptions [123], suggests the episodic tremors may reflect fissure formation by magma migration through fissures.

A distinct difference in the eruption style is found in the eruptive products [4, 34, 106]. The previous studies propose that the two types of products are supplied independently from the different magma sources based on the fact that products ejected from the summit (A) and from the fissures (B, C) are completely different. In particular, products from the summit are rich in crystals, especially plagioclase, while those from the fissures scarcely contain crystals. Therefore rheological properties are expected to be significantly different between the two eruption stages, which may affect the movement of magma.

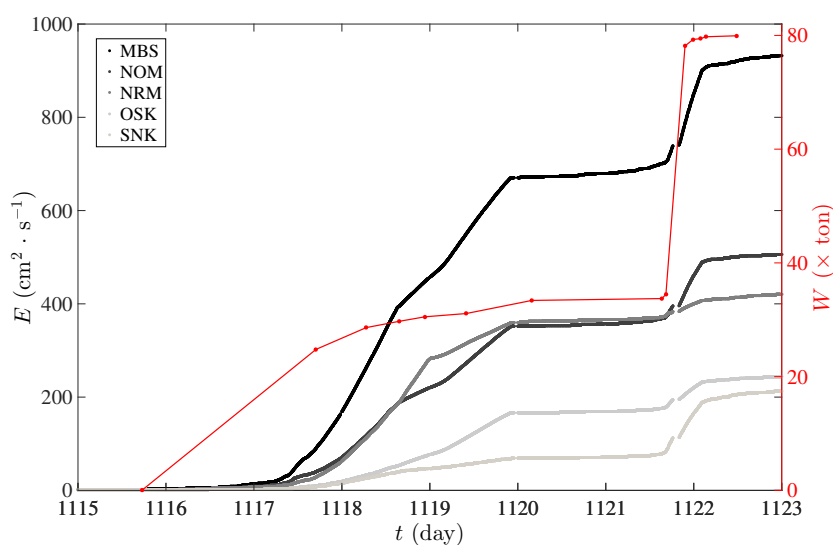


Figure 4.11: Temporal change in tremor energies at the five stations  $E$  (black to gray lines) and cumulative discharge weight ( $W$  in red) by reference to [31].

---

#### 4.4.2 LP Events and Volcanic Tremor in Terminal Stage

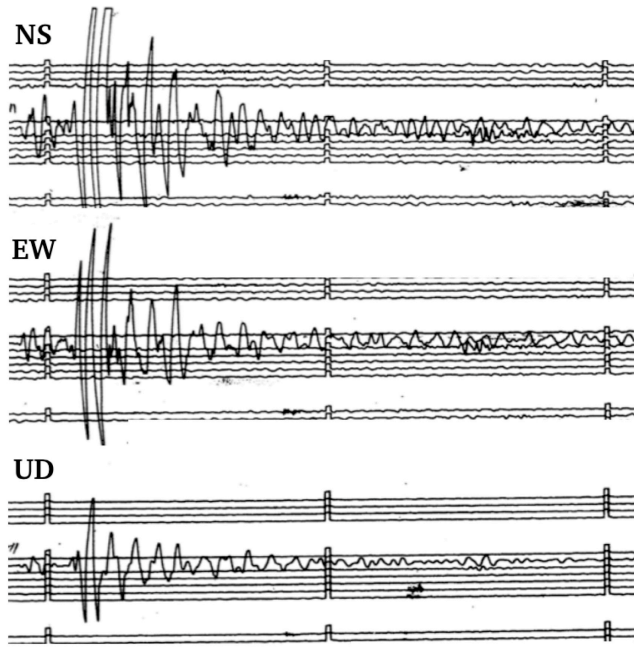
As described in the previous section, two types of volcanic tremors, continuous tremor and episodic tremor that occurred during the active eruption stage in the 1986 Izu-Oshima eruption, are understood as oscillation phenomena associated with the change in eruption style from the summit eruption to the fissure eruptions. Then shortly after the end of fissure eruptions, long-period (LP) events start appearing on November 22 and have occurred intermittently to the last part of December. Within that time frame, a small-scale summit eruption broke out with accompanying tremor activity from 17:23 to about 20 pm on December 18. Up to now, most of previous studies about the 1986 Izu-Oshima eruption draw attention to the active eruption stage in November and only few attempts have been made on the terminal stage. Hence it remains questions, why and where LP events have continued to occur intermittently and what kind of difference exists in terms of oscillation phenomena between the large summit eruption in November and the much smaller one in December. This section explores the questions by discussing characteristics of LP events and tremor in the terminal stage.

##### LP Events

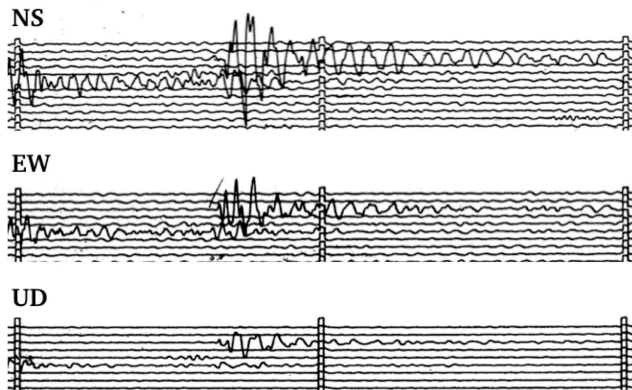
Data of LP events used in this study were extracted with reference to observation daybook written by ERI researchers at the time and seismic data recorded by a long-period electromagnetic seismograph (59B type) sited on the Island (latitude of  $34.76^\circ$ , longitude of  $139.38^\circ$ , and altitude of 190.2 m) by JMA till the end of December in 1986. Here LP event is defined as the event that has detectable amplitude (30 points in tiff image) in record by the JMA long-period seismometer, although it depends on activities of volcanic tremor and noise level.

In total, 123 LP events that show clear waveforms in both ERI and JMA recordings are detected and analyzed. Figs. 4.12 and 4.13 show some of the waveform examples observed by the JMA long-period seismometer (59B type) in November and December 1986, respectively. In the figures, LP events are clearly detectable by the human eye. Especially LP events in November have large amplitudes while the duration times of all events are close to the same, 1–2 min.

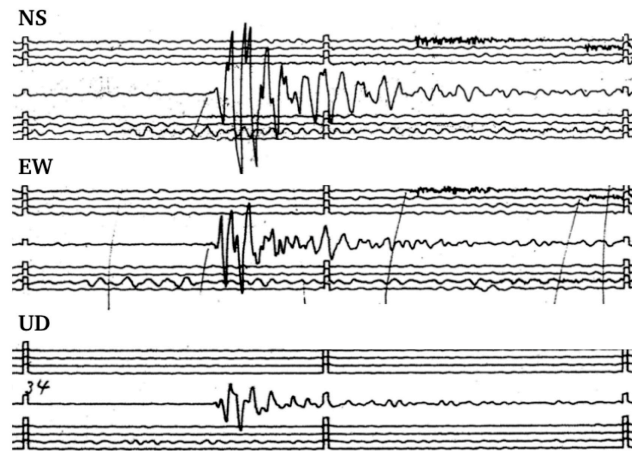




(a) 15:24 on November 23

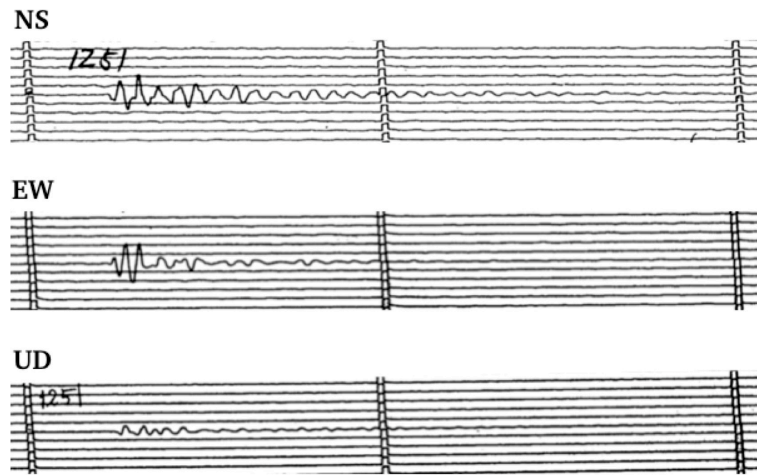


(b) 08:05 on November 24

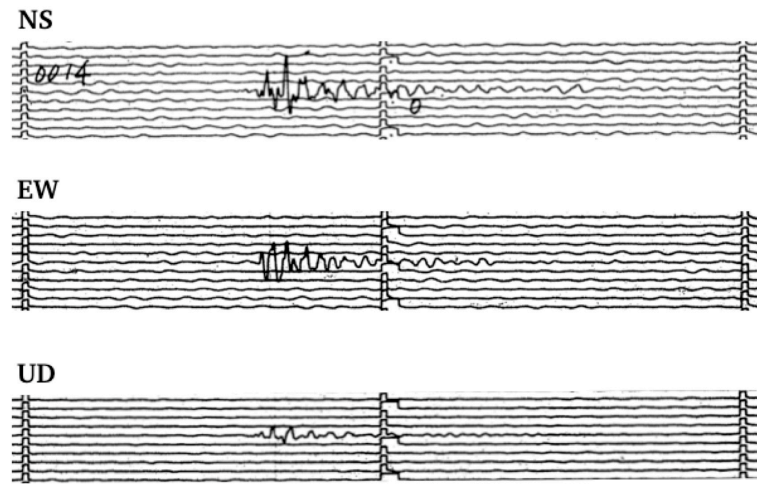


(c) 10:34 on November 24

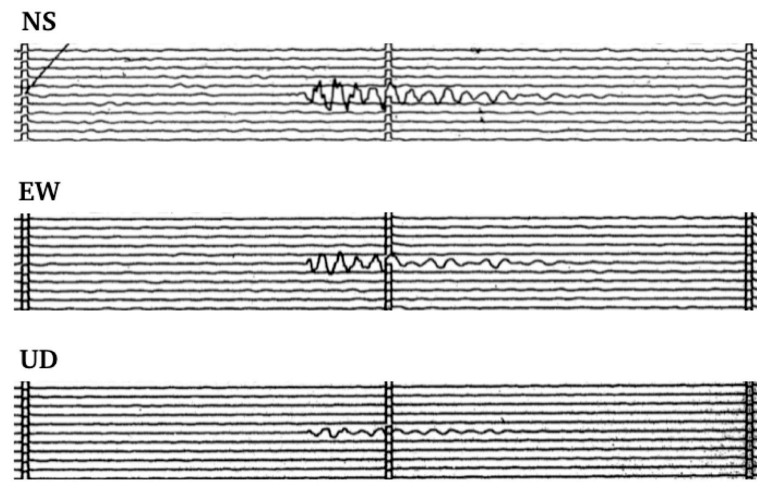
Figure 4.12: Examples of LP waveforms observed by the long-period seismometer in November. The length between squares indicates 1 min.



(a) 12:51 on December 10



(b) 00:14 on December 17



(c) 14:19 on December 23

Figure 4.13: Examples of LP waveforms observed by the long-period seismometer in December. The length between squares indicates 1 min.

---

In order to compare amplitudes of the LP events at the five seismic stations and to see the changing trend, amplitude at each station is normalized by the mean value of the five amplitudes. The normalized root-mean square amplitudes of LP events are shown in Fig. 4.14. The result indicates that its relative trend at the five stations drastically changes from the early stage (November 23 – December 2) to the late stage (December 10 – December 23); one in the early stage have a dominant amplitude at OSK while the other in the late stage have a dominant amplitude at MBS. Since the two different trends switched clearly on December 2, we call the one occurred before December 2 as the early LP events and the other after the day as the late LP events.

Fig. 4.15 shows the source locations of both, early and late LP events estimated by AIM. It is clear that the sources of early LP events locate near B and C fissures whereas those of late LP events cluster around the summit. Depths of the sources concentrate on a velocity boundary of 2 km probably due to the reason described above in Section 4.4.1. One explanation for the difference in source location may be that the early LP events are generated by magma movements inside the fissures because it first occurred within a day after the fissure eruptions and there would exist residual magma, which flows maintaining a high temperature. On the other hand, the concentration of the sources of late LP events near the summit [Fig. 4.15(b)] implies that those occurred inside the conduit below the summit about 25 days after the large summit eruption (here late LP events occurred from December 2 – 14 are excluded because the sources locate outside of the crater). The result means that after the large summit eruption calmed down, LP events start occurring below the summit for the first time breaking the 25-day silence. Since magma is expected to stay in the conduit during the terminal period, the LP events seem related to the movement of magma in the conduit.

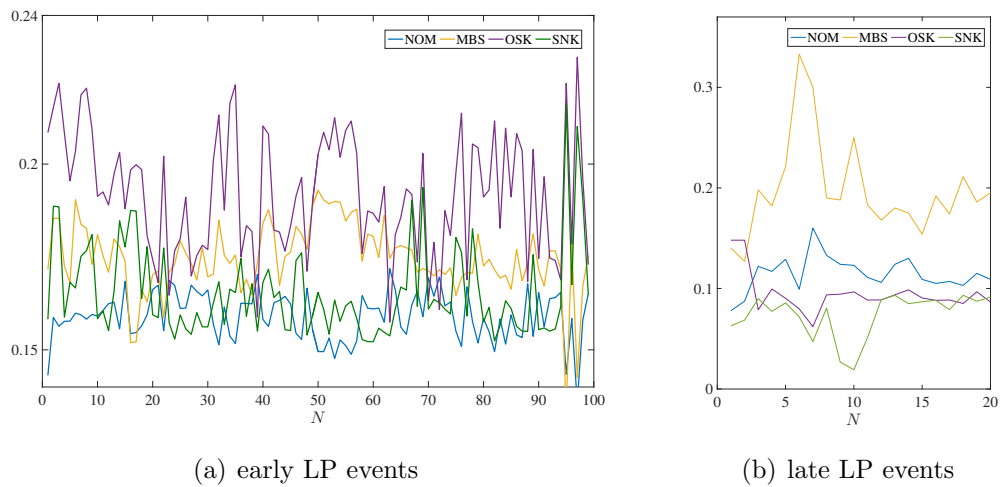


Figure 4.14: RMS amplitudes of early and late LP events normalized by the sum total.  $N$  is the number of events and each color represents each seismic station. Locations of the seismic stations are shown in Fig. 4.1.

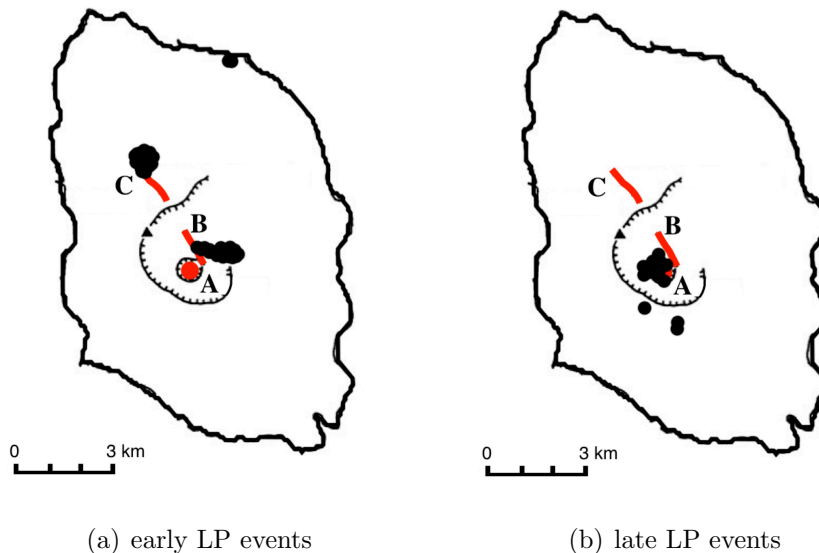
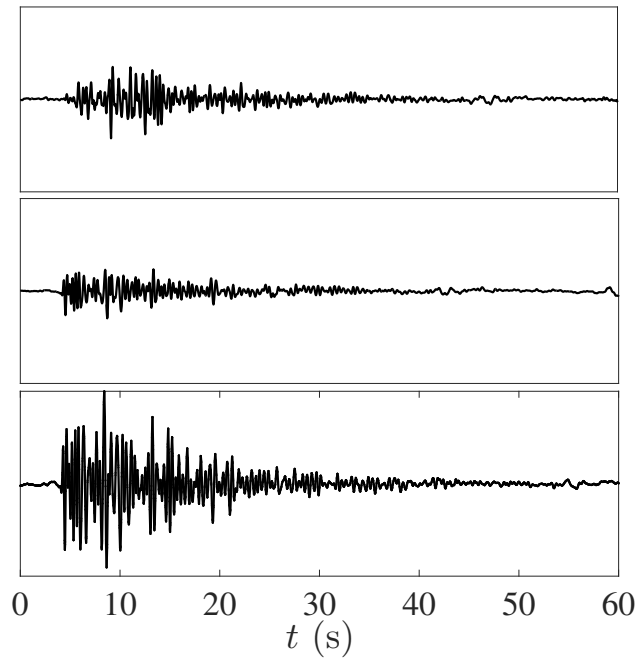


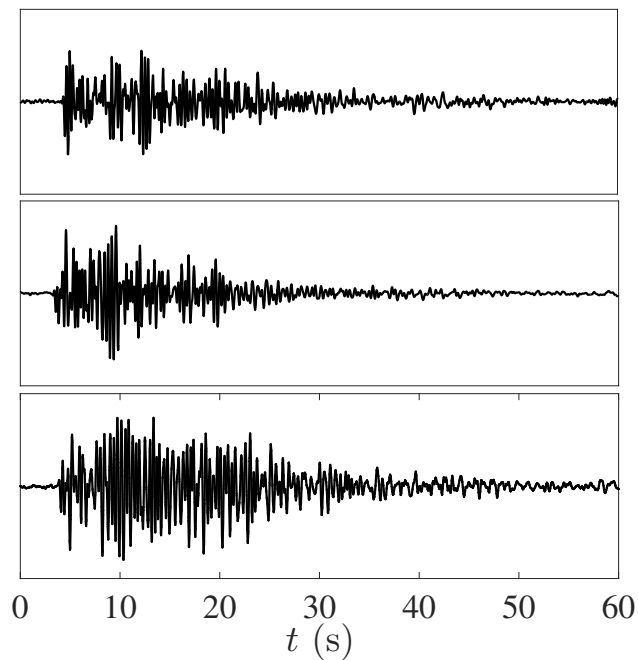
Figure 4.15: Source locations of early and late LP events. Red dot and lines written as A, B and C, indicate the places where the summit eruption and the two fissure eruptions occurred.

---

There exist several differences in the waveforms between early LP events and late LP events. Hence turning now to look at seismic data of the LP events. Fig. 4.16 shows waveforms of early LP events occurred near the fissures whereas those of late LP events occurred below the summit are shown in Fig. 4.17. It is clearly the case in the figures that the two kinds of LP events have totally different waveform characteristics. As for the early LP events, the waveforms have relatively-high dominant frequency, which does not attenuate with time. This characteristic is found in data observed at all stations. On the other hand, waveforms of late LP events have a common trend: long-period wave has continued and short-period wave superimposes when the amplitude is large as examples in Fig. 4.17. On the basis of the finding, let us now return to Figs. 4.12 and 4.13. The waveform difference between early and late LP events is also found in the waves taken by the long-period seismometer: early LP events have large amplitudes with high frequencies while late LP events start with relatively-high frequencies but only low-frequency waves remain at the end. Again although revealing source mechanism by obtaining the moment tensor solution is impossible by using the present data, the similarity of late LP waveforms implies a same process, acceleration with the high frequency and then relaxation keeping low-frequency oscillation. Based on the results, the late LP events seem to be excited by sudden changes inside the conduit related to the movement of magma.

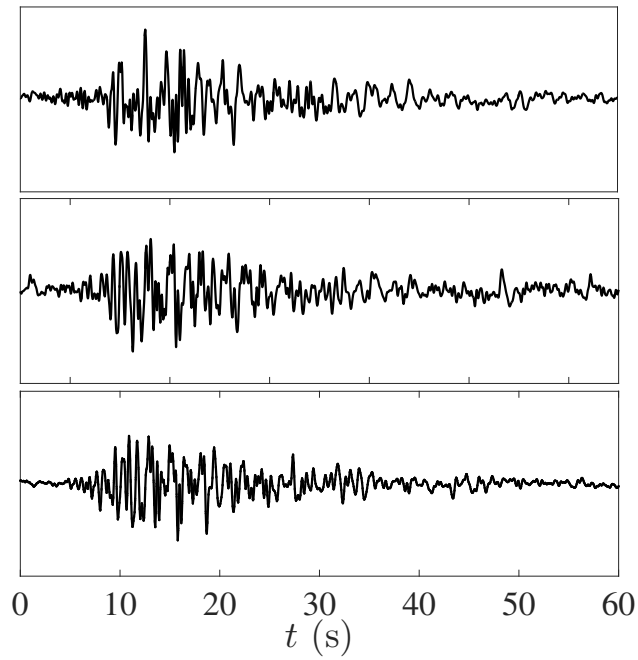


(a) Waveforms observed at MBS

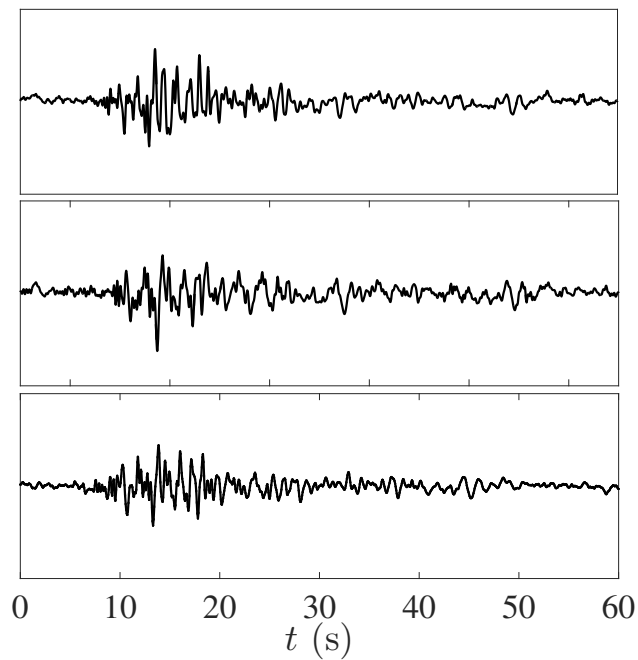


(b) Waveforms observed at OSK

Figure 4.16: Examples of early LP waveforms observed at MBS and OSK (ref. Fig. 4.1), which have y-axis range of  $\pm 0.8 \text{ cm.s}^{-1}$ . The three events started at 15:56 on November 23, 6:47 on November 24, and 10:10 on November 25, from top to bottom.



(a) Waveforms observed at MBS



(b) Waveforms observed at OSK

Figure 4.17: Examples of late LP waveforms observed at MBS and OSK (ref. Fig. 4.1), which have y-axis range of  $\pm 0.2 \text{ cm.s}^{-1}$ . The three events started at 1:10 am on December 19, 4:58 am on December 19, and 6:09 am on December 21, from top to bottom.

---

## Volcanic Tremor Associated With Small Summit Eruption

During the small summit eruption on December 18, tremor activity becomes remarkable again. Here we discuss 9 episodic tremors occurred from 17:18 to 19:35 on December 18. The period when the tremors occurred almost corresponds to the duration time of the small summit eruption (three hours from 17:23). This fact supports results shown in Fig. 4.18 that source locations of the tremors cluster below the summit. As for other observations, tilt observation stays unchanged just 40 minutes before the eruption that suggests relaxation process [122] while caldera subsidence proceeds in a step-by-step manner since before the beginning of the small summit eruption [48]. In the previous study, drain-back process of magma is proposed based on the observations. According to their estimation, the total amount of drain-back magma ( $50 \times 10^4 - 130 \times 10^4$  t) is 1000 times larger than that of product of the small summit eruption if the subsidence amount at the summit crater after the large eruption to the small eruption compares the amount of drain-back magma. Other data to support the idea of drain-back process is gravity anomaly [48, 120]. Under the condition of the ground subsidence trend, a reduction in gravity is observed,  $50 \mu\text{gal}$  near the summit and  $20 \mu\text{gal}$  on the caldera floor from December 1986 to March 1987. The negative gravity change, which is especially predominant near the summit, can be interpreted as a mass decrease that corresponds to the drain-back process of magma [48, 120].

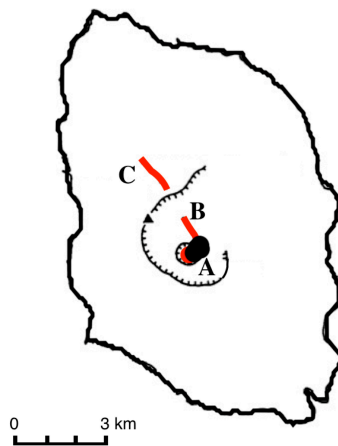


Figure 4.18: Source locations of tremors accompanied by the small summit eruption on December 18. Red dot and lines written as A, B and C, indicate the places where the summit eruption and the two fissure eruptions occurred.



Now let us compare two kinds of tremors accompanied by summit eruptions: intensive continuous tremor in the large summit eruption stage (November 15 – 19) as described in Section 4.4.1 and the tremor observed during the small summit eruption on December 18. For confirmation, the results in Fig. 4.7 and 4.18 that indicate the convergence of tremor sources near the summit are consistent with the case that the tremors are accompanied by the summit eruptions. However the two tremors reflect a remarkable difference with respect to the waveform as indicated in Fig. 4.19. It clearly shows the transformation from continuous tremor to episodic tremor. The remaining question is why tremor waveform shifts to the episodic type although the source locations are same, below the summit.

Difference in products of the two summit eruptions gives a hint. As compared to the product of the large summit eruption, the latter small summit eruption effused products that have much higher crystal contents and the crystals are mainly composed of plagioclase with coarse surface [106]. Based on the fact, the most likely explanation for the waveform transformation is related to change in magma rheology inside the conduit. If the temperature stays about the same in the conduit, crystals in magma need to be localized having a higher viscosity during the drain-back process to achieve the observational fact. When the drain-back magma reaches the magma chamber, it would be mixed with existing magma, which is considered as volatile-rich and high temperature. The small summit eruption might be related to the interaction although a detailed discussion should be avoided here because of the lack of well-supported evidence.

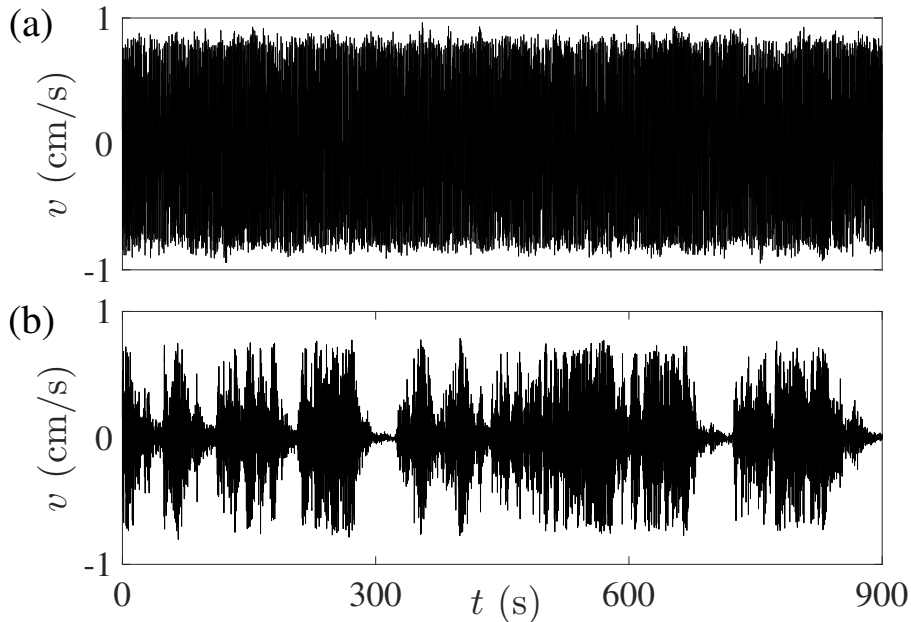


Figure 4.19: Comparison of waveforms observed at MBS. (a) Examples of continuous tremor starting at 12:30 on November 18 during the large summit eruption. (b) Example of tremor starting at 16:43 on December 18 during the small summit eruption.

---

### 4.4.3 Summary of Temporal Variation in Volcanic Oscillations

Volcanic tremors and LP events associated with the 1986 Izu-Oshima eruption are analyzed. The most important finding in this study is that the volcanic oscillation activities are clearly categorized in terms of the waveform property, the source location by the eruption style. The result, at the same time, denotes the high-accuracy source location. So far, temporal changes in source location of volcanic tremor and LP event accompanied by shift in eruption site are also presented at different volcanoes such as Mt. Piton de la Fournaise and Mt. Etna in previous studies [7, 10, 25, 126]. However little attention has been given to the relation between temporal variations in the volcanic oscillations and changes in eruption style. Our work brings about valuable data on correlation between eruption style, waveform characteristics, and source locations of volcanic tremors and LP events.

Fig. 4.20 summarizes the results in chronological order. First is the large summit eruption stage (stage 1 in Fig. 4.20), in which continuous tremor keeps on arising. Second is the fissure eruption stage (stage 2 in Fig. 4.20). Three types of seismicities, episodic tremor, volcano-tectonic earthquake, and LP event are accompanied by the fissure eruptions. In particular, the analysis reveals that the appearance of episodic tremor precedes the beginning of fissure eruptions by approximately 5 days. The fact confirms the primary importance of volcanic tremors in adaptive real-time monitoring of volcanic eruption. Then the final stage is the terminal stage including the small summit eruption (stage 3 in Fig. 4.20). During the stage, tens of LP events occur below the summit and episodic tremors are observed while the small summit eruption is lasting. The interesting point here is that the type of volcanic oscillation phenomena below the summit drastically changed from continuous tremor in stage 1 to LP events and episodic tremors in stage 3. One possible explanation for the remarkable transformation may be related to rheological change of magma inside the conduit since the silent time of 25 days would be enough to bring about the change, which is considered as a kind of aging process in magma rheology.



# Chapter 5

## Discussion

### 5.1 Difference in Aging Effect on the Two Fluctuations

In this research, two kinds of pressure/stress fluctuation phenomena were experimentally investigated using the two different materials that have the rheological multiplicity in the relation between shear stress and shear rate. One is the undershoot of pressure difference along the pipe during the start-up flow of *p*-NIPAM aqueous suspension. The perturbation is explained by rheological change of the aged flow generated by shear history. The other is the persistent stress fluctuation in the silica suspension, whose properties are strongly reminiscent of stick-slip phenomena. Thus although these are produced by different mechanisms, the important factor is common, that is aging. Aging is a term extensively used in the fields of rheology and non-linear physics describing slowly changing phenomena. At the present stage, it is more or less phenomenological description, which includes wide range of physical processes [27, 99, 104]. In this study, “aging” is defined as a structure build-up process due to attractive interactions between the individual components, which progresses slowly with time resulting in viscosity increase or solidification. In an opposite manner, “rejuvenation” is a structure destruction process by sufficient shear that brings about viscosity decrease [85]. According to the definition, structural build-up processes such as crystallization and chemical aging in some clay suspensions are also regarded as aging [9, 88, 109]. However the difference is that those processes cannot be rejuvenated by shear. Here aging is defined as the process that advances structure formation with time repeatedly after shear rejuvenation, which means that the process of aging and rejuvenation is reversible. In our case, the two samples show the aging after imposing sufficient shear. The following discusses the effect of aging on the fluctuation phenomena observed in the two samples.

The major difference in the two kinds of fluctuations is that the undershoot of pressure difference has a single-shot nature that does not repeat once it passes whereas the stress fluctuation repeats and persists for a long time. This study found that internal and external

factors are both necessary to induce each fluctuation as described in Chapters 2 and 3. Among them, first let us focus on the common internal factor, which is aging to understand the reason for the major difference.

The stress fluctuation can occur repeatedly due to the cyclicity originated from two competing processes: aging and rejuvenation (fluidization) in the flow. We presume that aging advances due to aggregation of particles whereas rejuvenation proceeds by disintegration of the particle aggregates and fracturing of each particle by shear as shown in Fig. 5.1. This is based on the microfluidic inspections (Fig. 3.28), which indicates the microstructural changes during the flow. As in Fig. 5.1, aging proceeds with an increase in the stress until the critical limit where structural destruction accompanied by the stress drop suddenly occurs. Then after this rejuvenation, the growth of the solid-like particle layer starts again. Repeating the process within the process time of measurement makes the stress fluctuation recurring in the silica suspension. This means that the time scale of aging should be shorter than the deformation time or flow time. The fact may explain the case of *p*-NIPAM aqueous suspension: only a single-shot perturbation occurs if the time scale of aging is longer than the process time. In order to confirm this, comparative experiments were performed by using a cone-and-plate rheometer (cone diameter,  $4.0 \cdot 10^{-2}$  m with a cone angle of  $0.4^\circ$ ; CVO Rheometer, Bohlin), which was handled in the experimental study 1 (Chapter 2). The purpose of the experiments is to clarify the difference in aging characteristics of the two samples used in this study.

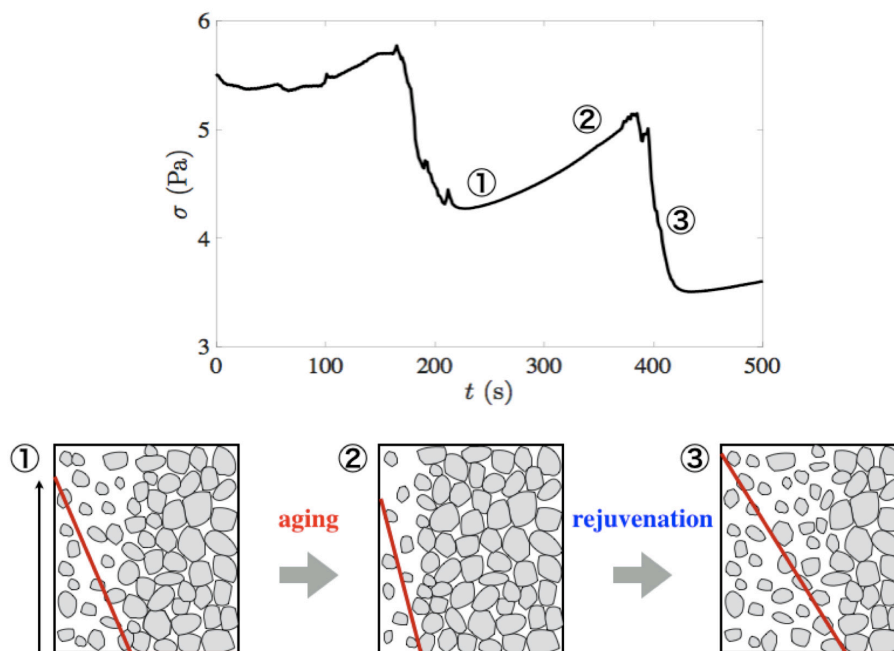
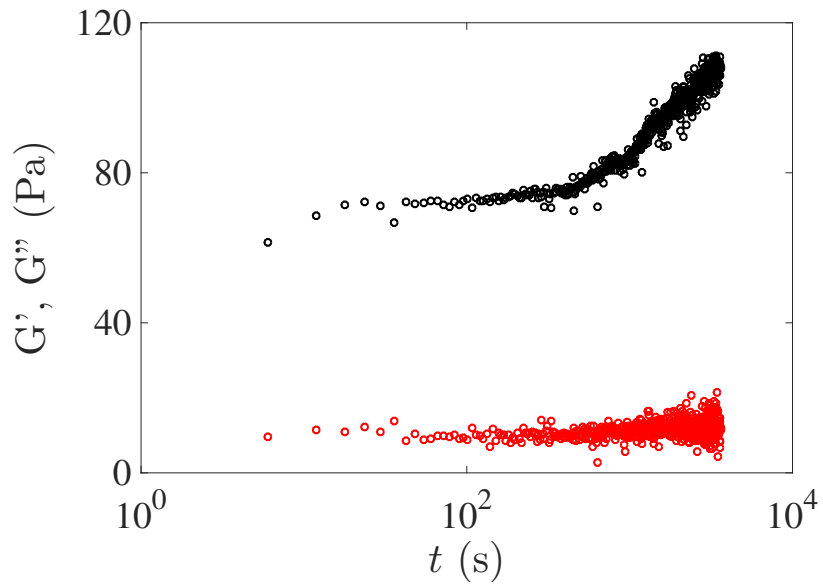


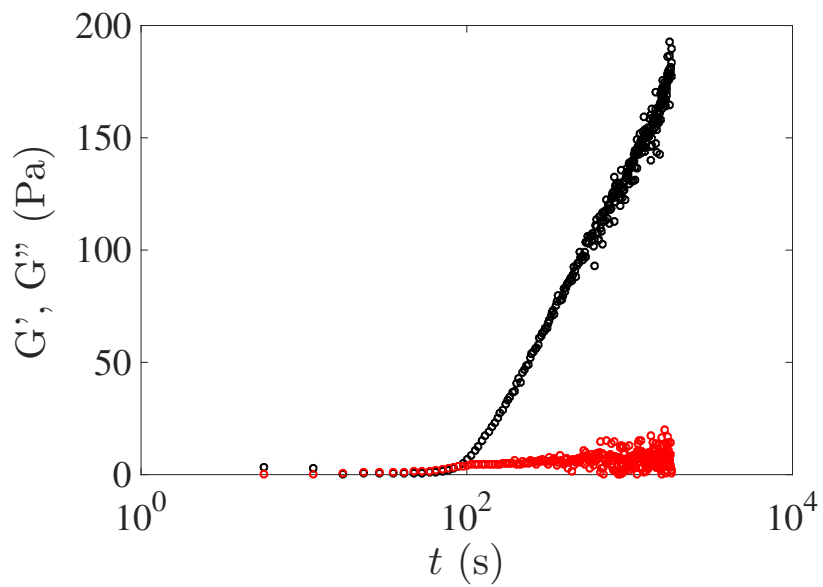
Figure 5.1: Graphic illustration of proposed mechanism of the stress fluctuation. Fig. 3.27 is modified here. The red lines show velocity profiles.

---

Fig. 5.2 compares temporal variations in the elastic modulus  $G'$  and the viscous modulus  $G''$  of the two samples. After the preshear at  $100 \text{ s}^{-1}$  for 1 min, the measurement is started under oscillatory shear with frequency 1 Hz and stress amplitude 0.05 Pa. Under the slight oscillatory situation, the sample scarcely moves and it is regarded as stationary state. In this state, the elastic modulus becomes larger with time in the both samples. This solidification with time represents the aging. However there exist three differences between them. First of all, the time scale of aging process is different:  $G'$  starts increasing at about 450 s in the *p*-NIPAM aqueous suspension while the drastic build-up of  $G'$  occurs at approximately 80 s in the silica suspension. Secondly, the silica suspension shows more rapid aging ( $\Delta G'/\Delta t \sim 0.084 \text{ Pa}\cdot\text{s}^{-1}$ ) than that in the *p*-NIPAM aqueous suspension ( $\Delta G'/\Delta t \sim 0.009 \text{ Pa}\cdot\text{s}^{-1}$ ). Thirdly, the crossover of  $G'$  and  $G''$  is observed only in the case of the silica suspension. These results indicate that pronounced aging process proceeds much faster in the silica suspension, which support our proposed idea that the cycle between aging and rejuvenation repeats in the course of measurement leading to the stress fluctuation. As for *p*-NIPAM aqueous suspension, it takes about 450 s of incubation time to start aging process from the presheared initial state, which is approximately twice of the longest flow time ( $\sim 230 \text{ s}$ ) in the series of experiments. This may be the reason why the perturbation does not repeat in few-minutes experiment since the sample cannot be aged again during the flow time. Also whether the *p*-NIPAM aqueous suspension shows aging process under shear as with the case of silica suspension remains unclear.



(a) *p*-NIPAM aqueous suspension



(b) Silica suspension

Figure 5.2: Elastic modulus  $G'$  (black) and viscous modulus  $G''$  (red) vs time  $t$  after preshear at 23.5 °C.

---

Based on the results, we propose that the time scale of aging is a key to generate lasting fluctuations. Although the time scale of rejuvenation is also essential to generate repeatable fluctuations, it strongly depends on the shear rate. This is an important constraint to consider similar phenomena in different materials such as magma. Aging time scale whatever it is should be comparable to the flow time scale to generate stress fluctuation repeatedly. However at current stage, the physics of aging in this system has not been clarified well because of lack of suitable inspection techniques in micro-scale during flow. We estimate attractive force working between colloidal particles enhances aggregation [11]. Entanglement of irregular-shaped particles under shear is another proposed mechanism. Moller *et al.* [86] estimates the size of aggregated particles and their growth with time by light scattering measurements using the same sample. On the basis of the results, they consider aging as the progress of entanglement. To specify the physical mechanism of aging in this system is important when we apply this phenomenon to other materials such as magma.

In this way, by focusing on the roles for aging and rejuvenation processes, it was revealed that the stress fluctuation is generated due to the cycle of structure formation and destruction, or aging and rejuvenation in the flow. In addition to the internal factor, this study found that external factors are also essential to induce the fluctuation phenomenon such as shear rate, boundary condition, and gap width. The next section discusses roles of the external conditions for the stress fluctuation after explaining the fluctuation mechanism linked to the multiplicity. An applicable kinetic model for the stress fluctuation is also proposed conceptually in the last part of the section.



---

## 5.2 Understanding Mechanism of the Stress Fluctuation

### 5.2.1 Link to the Multiplicity

As described in Introduction, one of common concepts to explain self-induced oscillations is a looped cycle in the multiplicity relation between shear stress and shear rate ( $A \rightarrow B \rightarrow C \rightarrow D \rightarrow A$  in Fig. 1.17). However the experimental study 2 in Chapter 3 revealed that the observed stress fluctuation has a different mechanism. As indicated in Figs. 3.9, 3.10, and 3.11, the fluctuation occurs in the presence of shear banding and it is coupled to the change in the width of shear banding (Fig. 3.17). Therefore the fluctuation should occur within the negative slope where the flow is separated into solid-like part and flowing part, which is referred to as shear banding as pictured in Fig. 5.3 whereas it can move as a plug flow with wall slip at lower shear rates where the stress is below the static yield stress  $\sigma_{st}$ . In the negative slope, the stress decreases with increasing the width of shear banding due to the fluidization while the stress increases when the width of shear banding decreases and the solid-like part extends with progression of aging. Consequently, the stress fluctuation occurs by going back and forth within the negative slope [(a) process in Fig. 5.3]. After (a) process, if it escapes from the negative slope and moves to the regime of the positive slope as (b) process in Fig. 5.3, the sample experiences complete fluidization. The flow state diagram obtained by extensive shear start-up experiments (Fig. 3.12) indicates whether it stays (a) process or it moves to (b) process depends on the aging time and the applied shear rate. Since the aging time in this case means the time in which aging proceeds at stationary state before the measurement, the physical mechanism may differ from aging under shear. On the basis of the observation, it is reasonable to assume that rapid aging process corresponds to aggregation of particles dispersed in the fluid while structural strengthening of the aggregated particles brings about aging over long period of time. A similar “two-step” aging process is also proposed in [104]. However note that the both are caused by structure build-up process.

Till now the effect of aging was discussed as the internal factor to induce the stress fluctuation whereas the effect of external factors including the applied shear rate is not mentioned yet. Therefore next let us focus on external factors for the stress fluctuation.

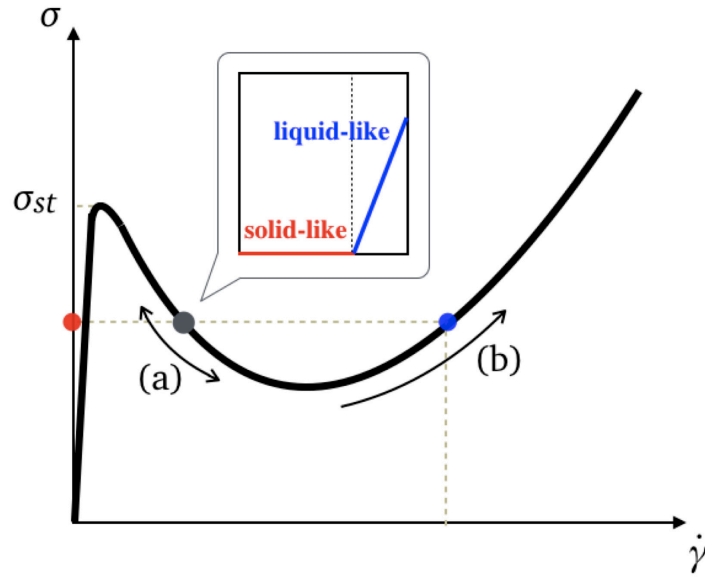


Figure 5.3: Proposed mechanism of the stress fluctuation with the flow curve  $\sigma$  vs  $\dot{\gamma}$ .  $\sigma_{st}$  is the static yield stress above which the system starts flowing from the solid state [27]. Gray dot represents the apparent state, and red (resp. blue) dot shows the solid (resp. liquid) state in shear banding. The liquid state is defined as shear banded part. (a) describes the stress fluctuation process while (b) shows the fluidization process.

## 5.2.2 External Factors of the Stress Fluctuation

The experiments exhibit that external factors are also important to induce the stress fluctuation in addition to the internal factor. Firstly as shown in Fig. 3.12, the stress fluctuates at higher shear rates at a fixed aging time. This result means that a certain level of shear is required for breaking aggregation of particles (rejuvenation) to cause the stress fluctuation. Moreover, since the time when the sample is fluidized completely after some stress fluctuations systematically increases with decreasing the shear rate as shown in Fig. 3.9, the balance between the time scale of aging and the strength of shearing should be considered.

Other external factors are boundary condition (smooth or rough) and gap width as described in Appendix. With respect to the boundary condition, “rough” is the case in a sand-blasted Plexiglas Taylor-Couette cell with typical roughness of  $1 \mu\text{m}$  while “smooth” is the case with typical roughness of a few tens of nanometers. The major distinction in the two situations is that wall slip is found only in the case of smooth boundary with which the stress fluctuation occurs. In the case of the rough boundary, the stress does not fluctuate and wall slip is negligible even in the presence of shear banding as in Fig. 5.4. This is a significant difference with the case in the smooth boundary where wall slip and shear banding coexist at all times. Since the stress fluctuation is coupled to not only the shear

banding but also the wall slip as shown in Figs. 3.14 and 3.15, the necessary condition of the boundary may imply the importance of wall slip or degree of freedom at the wall. On the other hand, the narrower the gap width of flow, the faster the sample fluidizes at the same shear rate as Fig. 7 in Appendix. The fact that the stress fluctuates prominently with wide gap indicates that the gap width also affects the phenomenon. However it is expected that prominent fluctuations occur at lower shear rates with narrow gaps according to the tendency.

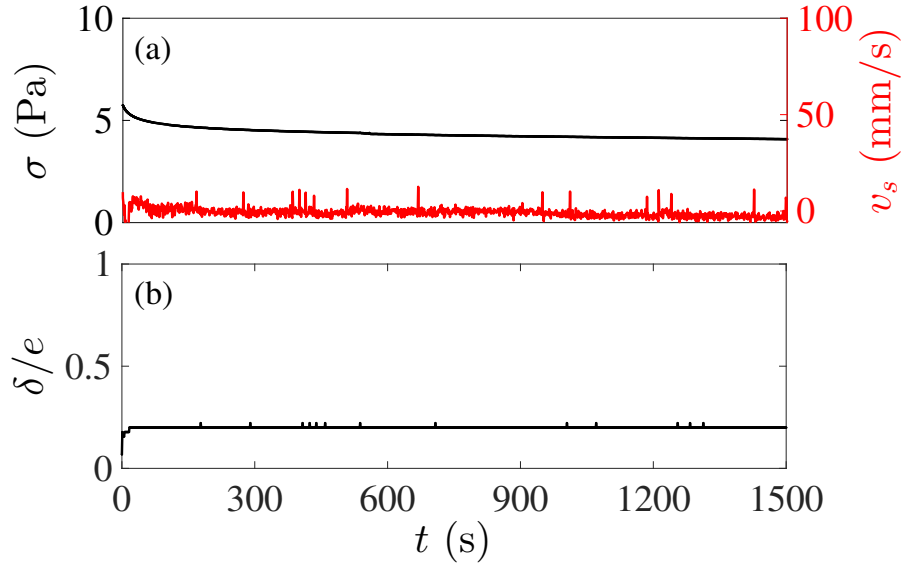


Figure 5.4: Stable shear banding observed for  $\dot{\gamma} = 80 \text{ s}^{-1}$  and  $t_w = 10 \text{ min}$  with the rough boundary condition. (a) Shear stress  $\sigma$  and slip velocity  $v_s$  vs time. (b) Width  $\delta$  of the fluidized shear band normalized by the gap width  $e$  vs time.

The last point, which should be noted as an external factor is that fluctuation phenomenon never happen and the multiplicity fades out under the stress-control system (Fig. 3.21). Interestingly absence of the multiplicity under stress-control is reported in other material, too [44]. This previous study reports that the microstructure of the suspensions is more sensitive in the rate-control mode because the suspension is forced to deform under the condition. By contrast, an abrupt structural change corresponds to a step-like increase of shear rate at a critical shear stress in the stress-control mode. A key is that the stress response at a constant shear rate reflects internal reactions of the sample. For such occasion, the stress decreases or fluctuates if the structural changes such as aging and rejuvenation occur. On the other hand, applying the constant stress makes a simple increase in the shear rate and it never get back once the shear rate becomes high. This systemic difference is a possible reason why fluctuation phenomenon is observed only in the rate-control system.

Based on the findings about necessary conditions, we conclude that the shear-induced stress fluctuation can be explained by interworking between multiplicity of the rheological

relation of the constituent materials and the external environments. This is an important lesson in applying to other systems. In application to volcanic systems in particular, some recent models of magma flow in a volcanic conduit take account of shear banding and wall slip [20, 39]. Although it is not a direct link at present, it is worth exploring the possibility and considering what the necessary conditions mean in the volcanic system because the existence of shear banding and wall slip is a key for the stress fluctuation. In preparation for the application, next we suggest a conceptual model to explain the stress fluctuation kinetically.

### 5.2.3 Suggestion of Kinetic Model for the Stress Fluctuation

Focusing on the kinetic mechanism, properties of the persistent stress fluctuation are strongly reminiscent of stick-slip phenomena that bring about large stress drop in relatively short time scale in frictional sliding behavior of solid materials as we noted in Chapter 3. The stress fluctuation in a flowing system reported in this study is quite original result that has never been reported before, so that there is no model for describing such fluctuation in fluid. In order to understand the original phenomenon and to find future applications to other fluids, we conceptually propose a model of the stress fluctuation based on stick-slip phenomena of solid materials.

Fig. 5.5 shows the simplified model composed of a spring and a dashpot. The system is assumed to be pressed at a constant velocity  $v_c$  since the experiments were performed under the control of shear rate. Generally system composed of a spring and a dashpot in series represents Maxwell viscoelastic property. However in this case, the spring is employed to express the progression of aging, which is the build-up process of  $G'$  as in Figure 5.2. The energy injected by shearing is accumulated at the frame of external driver, which is wall of rheometer in our experiments. For such occasion, examining effects of shear rate, boundary condition, and gap width of the rheometer as described in Section 5.2.2 is of great account because the external stiffness affects the phenomenon. This point is a clear difference from the stick-slip behavior in solid materials, in which the energy is accumulated internally as elastic energy.

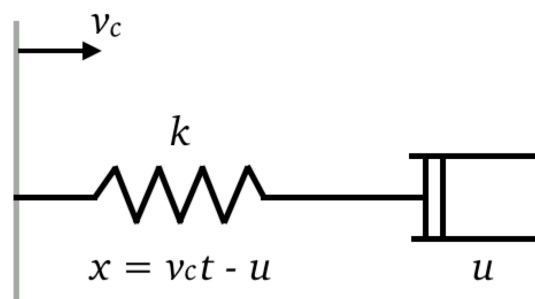


Figure 5.5: Conceptual diagram of the stress fluctuation model

The fluctuation mechanism is summarized as follows. First, pressing the system at the constant velocity leads to gradual increase of stress due to aging accumulating the energy

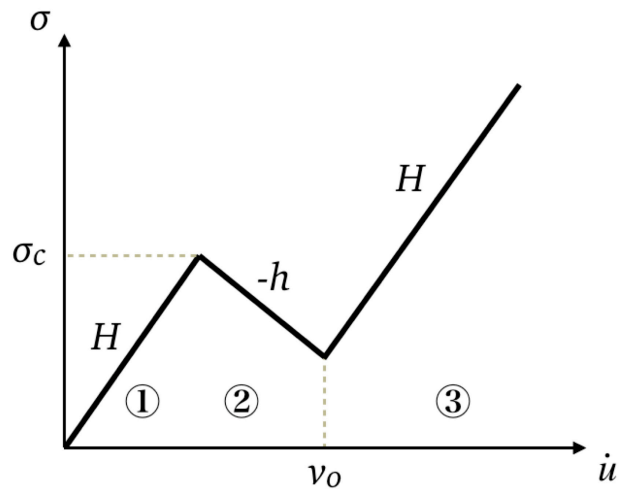
---

at the wall of rheometer (① in Fig. 5.6). Then when it reaches the critical stress  $\sigma_c$ , the fluid abruptly flows that triggers succeeding stress drop (② in Fig. 5.6). Repeating this process induces stress fluctuations as indicated in Fig. 5.6(b).

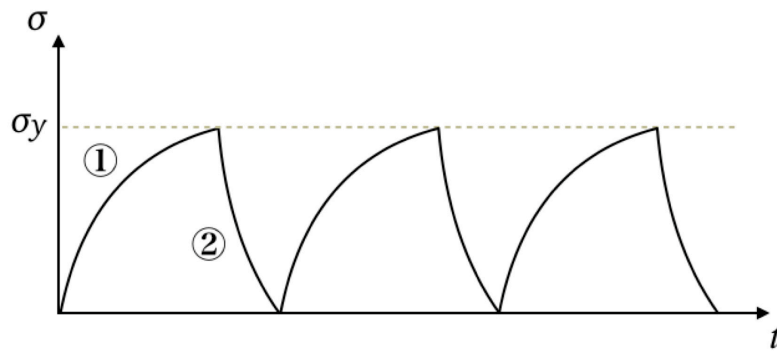
In this model, the equation of motion is given as Equation 5.1 with the viscous intensity of the fluid in the dashpot  $\sigma$  (Equation 5.2) where  $m$  is the mass of movable part of the dashpot,  $u$  is the displacement,  $k$  is the spring constant,  $v_c$  is the applied constant velocity, and  $t$  is the time. The viscous intensity  $\sigma(\dot{u})$  depends on the shear rate and the critical stress  $\sigma_c$  is regarded as a function of aging time: when the sample becomes more solid-like by structure build-up process or aging, larger critical stress is required to break the structure. This represents that aging affects both of the spring and the dashpot individually. In order to express the experimental condition, the relation between the stress and the shear rate of this model approximates the multiplicity that is simplified by straight lines with positive constants  $H$  and  $h$  as described in Equation 5.2 and Figure 5.6(a). Although the proposed process in the flow curve [Figure 5.6(a)] is not exactly same with the (a) process in Figure 5.3 because it is impossible to see the effect of local flow in this model, it describes temporal variations in rheology by employing the spring and the dashpot. Figure 5.6(b) shows a possible picture of stress fluctuation on the assumption of  $m\ddot{u} = 0$ . By considering initial conditions and external factors, this model has a possibility to explain the mechanism of the observed stress fluctuation. This would be an important future work.

$$m\ddot{u} = k(v_c t - u) - \sigma(\dot{u}) \quad (5.1)$$

$$\sigma(\dot{u}) = \begin{cases} H\dot{u} & \text{if } \sigma < \sigma_c \\ -h\dot{u} + a & \text{else if } \dot{u} < v_o \\ H\dot{u} + b & \text{else} \end{cases} \quad (5.2)$$



(a) Flow curve  $\sigma$  vs  $\dot{u}$



(b) Stress response  $\sigma(t)$  in the case of stress fluctuations

Figure 5.6: Graphic illustrations of the model where  $\sigma_c$  is the critical stress,  $v_0$  is the cut-off velocity,  $H$  is the gradient of positive slopes, and  $-h$  is that of negative slope.

---

## 5.3 Implication for Future Works

### 5.3.1 Possible Link between Stress Fluctuation and LP Event

This study attempted to find a link between non-linear rheology and volcanic oscillation phenomena by experimental study and analysis of natural phenomena. However at the present stage, it is difficult to find a direct connection between the experimental results and the occurrence of magma-driven volcanic oscillation phenomena analyzed in this study because the link demands careful consideration and more information regarding non-linear magma rheology. Here as a first step, a possible link that can give a hint for future works is mentioned.

The analysis of volcanic tremors and LP events associated with the 1986 Izu-Oshima eruption revealed that the volcanic oscillations below the summit display the clear transition, from continuous tremor to LP events and episodic tremors after breaking about one month-silence. This shift in oscillation phenomena can be understood if rheology of magma existed in the conduit changes with time. In that case, the following scenario can be considered. After the large summit eruption, magma starts drain-back due to the gravity as previous studies proposed [48, 120]. During this stage, magma is expected to be subject to slight shear and slow change in the internal structure such as crystal rearrangements is expected. This is aging phenomena: crystals contact and link each other over time. As the aging process proceeds, local increase of viscosity becomes predominant with aggregation of crystals. The process can occur everywhere inside the conduit generating shear-banded flow. If the shear-banded structure suddenly breaks with the change in the width of shear banding, it would make shear-induced fluctuation, which can excite LP events. If the proposed excitation mechanism applies, LP event would possess a potential to be an indicator of decline period in eruption because the condition is likely to be produced in degassing magma at low temperature as time proceeds.

This idea comes from new findings in this experimental study 2: aging proceeds even in flows and it causes stick-slip like stress fluctuations in fluids. From the experimental viewpoint, aging is an important factor to induce self-induced oscillations and the rheological multiplicity is *apparent sign* that implies possibility of flow instability. However there is no direct study that clarifies existence of aging of magma rheology till now. Furthermore the physics of aging in magma is unclear. Although controlling the condition of magma for a prolonged time would be much more difficult than expected, exploring the possibility of self-induced oscillations of magma due to aging is an important future work in order to search the direct link between non-linear magma rheology and magma-driven volcanic oscillations. In the last section, we propose experimental plan to approach the direct link based on verified characteristics of magma rheology.

---

### 5.3.2 Proposal of Rheological Measurements in Non-linear Magma

Complex non-linearity of magma rheology due to change in the crystal alignments is becoming apparent recently [13, 50, 119]. Among them, shear-thinning and decrease in viscosity with time by constant shear are experimentally supported in high crystal concentrations (dense suspension) where strong constraints between crystals exist because these characteristics are produced in the process of contact-breakage.

Nowadays microscopic observations of eruption products from volcanoes reveal that crystals in melt interact each other forming linked structures and clusters that are called as crystal agglomeration [98], plagioclase chains [96] and so on. As shown in Fig. 1.13, it seems that some attractive force exists between crystals. Although practical factors to induce the attractive interaction between crystals are unsolved at present, drawing effects by pressure shadow and shear-thinning melt can be hydrodynamic factors to force crystals to connect externally. Shear-induced solidification that is observed in other materials may also be a possible factor in magma [97, 125]. If the complex non-linear rheology of magma is generated by changes in the crystal structure due to these proposed factors, the aging process may be reproducible by shear rejuvenation.

With respect to the relation between rheology and local field in the flow, viscosity fluctuations of shear-banded magma during crystallization (Figure 3.29 and 3.30) provides a clue to understand effects of build-up process in crystal structure on non-linear rheology [13]. Note that although this process can be categorized as a kind of aging process, it is not reproducible by shear because the crystal volume increases with time due to crystallization. However it is worth emphasizing that in the crystallization process, the viscosity fluctuations occur under constant shear in magma that is separated into layers, one is crystal-free and the others are plagioclase-bearing [13]. This study offers an essential clue about fluctuation phenomena coupled to the local dynamics in magma.

We consider non-linear nature of magma rheology should be critical in understanding volcanic oscillation phenomena although the nature has not been clarified yet. Only quite few numbers of pioneering work exist such as [13]. Hence here we propose several future research subjects to fulfill the gap. In the first place, we propose an experimental verification of the role of aging in magma rheology: perform flow curve test by sweeping the shear rate changing the aging time by using conventional rotary-type rheometer at high temperatures. The direct aim of this experiment is to elucidate physics of aging phenomena. The apparent change of the rheology with time should be investigated by inspection of microstructure. Expected physics behind aging is gradual progress of crystal entanglement from an analogy of colloidal suspensions [84, 86]. To observe this process, the sample cell in the rheology measurement should be large enough in comparison with the crystal size. In situ inspection of the internal structure such as USV adopted in this work is not an easy task and it would



---

be impossible in the present technology. Instead, inspection will be conducted over the quenched products. In this procedure we should carefully remove the effects of quenching. Sometimes insufficient quenching produces crystals and enhances overgrowth of existing crystals. Specification of the aging physics is important and particularly the estimate of the time scale of aging is critical whether it competes with the time scale of the actual flow phenomena.

Next step in the proposal is to perform simultaneous measurement of global rheology and local dynamics such as flow field for high temperature magma. To conduct this measurement, several technical advancements are required. By using high speed X ray imaging camera at synchrotron facilities, we can measure local velocity field based on the radiography technique. In this experiment, stress fluctuation phenomena should be revealed.

# Chapter 6

## Conclusions

Generation of LP event and volcanic tremor are related to movement of magmatic fluid in volcanic system, whereas complexity of non-linear magma rheology gradually starts coming to light in late years. Under the circumstances, it is important to explore the possible link between the magma-driven volcanic oscillations, that is LP event and volcanic tremor, and non-linear magma rheology.

Toward the goal, two approaches were adopted in this study. First, experimental approach using analog materials was performed to comprehend underlying physics of fluctuation phenomena in suspensions, which possess the rheological multiplicity. The experiments substantiated two kinds of fluctuations at different levels of scale by using different materials: pressure undershoot in the pipe flow and continual stress fluctuations coupled to the local dynamics such as shear banding and wall slip. Although the mechanisms to induce the two fluctuation phenomena are different, the common key factor for the generations is aging caused by change in solid phase with time. Based on the results, we emphasize that this aging is the most important next target in the field of magma rheology for finding a direct connection with volcanic oscillation phenomena.

Analysis of volcanic tremors and LP events accompanied by the 1986 Izu-Oshima eruption was also performed as another approach for the purpose of promoting a better understanding toward actual volcanic oscillations. The analysis results demonstrated the clear relationship between variations in the eruption style and characteristics of LP events and tremors in terms of waveform and source location. Especially the fact that volcanic oscillations below the summit changes from continuous tremor to LP events and episodic tremors after silent period is interpreted as indication of rheological change in magma inside the conduit with time, or aging.

On the basis of the results by the two approaches, finally we discussed the possible link between non-linear magma rheology caused by the change in crystal alignment and temporal shift in magma-driven volcanic oscillations at Izu-Oshima volcano. Although the link is an assumption at the present stage, this study proposes the importance of aging in order to

---

understand oscillation phenomena caused by non-linear magma rheology.

# Appendix

## Supplementary Data on Experimental Study 1

### Fundamental Equations

The Navier–Stokes equation in this case is described as an incompressible stationary flow with the axis of the flow direction taken as the  $z$ -axis and the perpendicular distance from the cylinder axis is designated by  $r$ :

$$0 = -\frac{dP}{dz} + \frac{1}{r} \frac{\partial}{\partial r}(r\sigma_{rz}) + \rho g, \quad (1)$$

$$\frac{d}{dz}(P - \rho g z) = \frac{1}{r} \frac{\partial}{\partial r}(r\sigma_{rz}). \quad (2)$$

Where  $P$  is the pressure;  $\rho$  is the fluid density;  $\sigma_{rz}$  is the  $z$ -axial shear stress at  $r$ ;  $g$  is the acceleration due to gravity and  $g = 9.8 \text{ m/s}^2$  when the  $z$ -axis is downward and  $-9.8 \text{ m/s}^2$  when it is upward. Shear stress is given by the integral of Equation (2):

$$\int_0^R r \frac{d}{dz}(P - \rho g z) dr = \int_0^R \frac{\partial}{\partial r}(r\sigma_{rz}) dr, \quad (3)$$

$$\sigma_{rz}^w = \frac{R}{2} \left( \frac{dP}{dz} - \rho g \right). \quad (4)$$

Where  $R$  is the radius of the pipe and  $\sigma_{rz}^w$  is the value of  $\sigma_{rz}$  at the pipe wall ( $r = R$ ). Because  $\Delta P$  already accounts for the deduction of the hydrostatic component,  $P1(0) - P2(0) =$

---

$-\rho g \Delta z$ :

$$|\sigma_{rz}^w| = \frac{R \Delta P}{2 \Delta z}. \quad (5)$$

Where  $\Delta z$  is the distance of two pressure sensors. Note that the shear stress expresses the amount of change from a state of rest.

Equation (5) can be converted as shear stress at arbitrary radius of the pipe,  $r$ :

$$|\sigma_{rz}| = \frac{r \Delta P}{2 \Delta z}. \quad (6)$$

Since  $|\sigma_{rz}|$  and  $|dV_z/dr|$  are shear stress and shear rate respectively, their relation was determined by the rheological measurements shown in Figure 2.5. Here we presents the relation by  $|dV_z/dr| = f(|\sigma_{rz}|)$ . Below, the absolute value sign  $||$  is omitted.

The velocity at  $r$  and the flux are related to the rheology curve in the following way:

$$V_z = \int_R^r \frac{dV_z}{dr} dr = \frac{2\Delta z}{\Delta P} \int_{\frac{R\Delta P}{2\Delta z}}^{\frac{r\Delta P}{2\Delta z}} f(\sigma) d\sigma. \quad (7)$$

$$Q = \int_0^R 2\pi r V_z dr = \frac{4\pi\Delta z}{\Delta P} \int_0^R r \int_{\frac{R\Delta P}{2\Delta z}}^{\frac{r\Delta P}{2\Delta z}} f(\sigma) d\sigma dr. \quad (8)$$

Equation (8) is the relation between the flux and the pressure difference and other parameters are known quantities. Equation (8) gives the relation between the mean velocity ( $Q/\pi R^2$ ) and the pressure gradient  $\Delta P/\Delta z$ , which is compared with the measured mean velocity and the pressure gradient in the pipe flow experiments.

The relation between shear stress and shear rate,  $dV_z/dr = f(\sigma_{rz})$  used in the above calculation, was specifically estimated in the following way. The rheology curves in Figure 2.5 are different depending on the aging time, but are all similar at high shear rates. Therefore, for the shear rates  $> 8.2 \text{ s}^{-1}$ , in which  $\frac{1}{N} \sum_i |\sigma_i - \bar{\sigma}|/\bar{\sigma} < 0.25$  ( $\sigma_i$  is the shear stress at a certain shear rate for the  $i$ -th waiting time and  $N$  is the number of the aging time),  $f$  is expressed as a power-law function fitting all the data in the shear rate rage. In the lower shear rates,  $f$  is expressed as a cubic function to fit the rheology curve individually for each aging time. The shear rate is set to zero at lower shear rate than the minimum measured shear stress regarding that the minimum shear stress represents the yield stress below which the fluid never flows.

---

## Supplementary Data on Experimental Study 2

### Oscillatory Experiments

Figs. 1 and 2 show the elastic modulus  $G'$  and the viscous modulus  $G''$  that are nearly frequency independent and a critical yield strain of about 7% that weakly depends on the sample age.

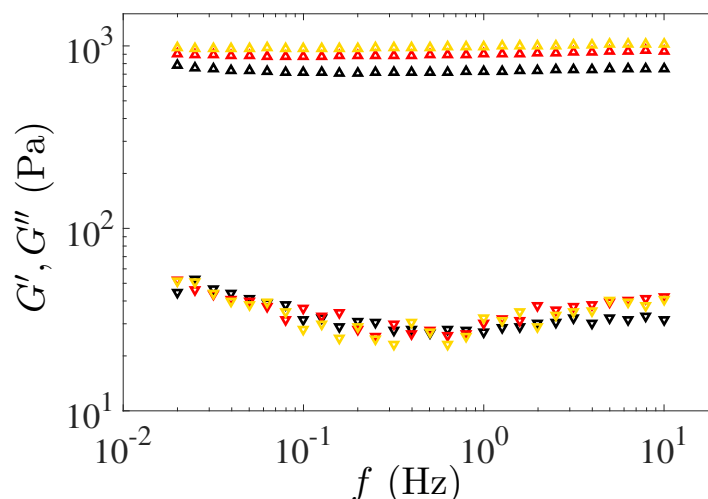


Figure 1: Elastic ( $\triangle$ ) and viscous ( $\nabla$ ) moduli vs frequency  $f$ . The frequency sweep is performed at a constant strain  $\gamma = 0.5$  % and at different aging times  $t_w$  after preshear. [color,  $t_w$  (min)]: (-, 30); (-, 60); (-, 100).

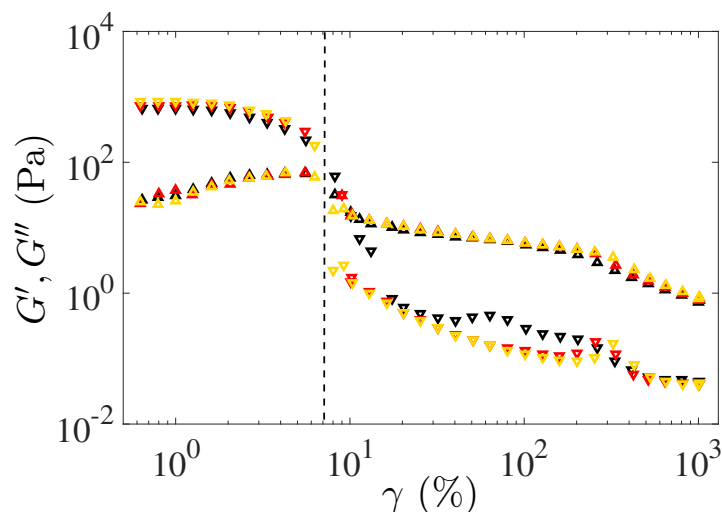


Figure 2: Elastic ( $\triangle$ ) and viscous ( $\nabla$ ) moduli vs the strain amplitude  $\gamma$ . The strain sweep is performed at a fixed frequency  $f = 1$  Hz with an aging time of 8 s per point, and at different times  $t_w$  after the preshear. [color,  $t_w$  (min)]: (-, 30); (-, 60); (-, 100).

---

## Effects of shear rate and aging time on the very first start-up flow

Figs. 3 and 4 show effects of shear rate and aging time on very first start-up flows, respectively. The both figures indicate that it takes about 0.3 s to have a constant shear rate. It means that the results discussed in the main context are obtained after the relaxation time of the applied shear rate. At the very beginning of the measurement where the shear rate is not stable yet, a large stress peak exists. Although it is regarded as a *yield stress*, which is also an important non-linear characteristic [26], it is not discussed in detail because it appears during the initial rise of shear rate, which is affected by technical properties of the rheometer. The only evident characteristic of the stress peak is that the stress value at the peak depends on the aging time, not on the global applied shear rate.

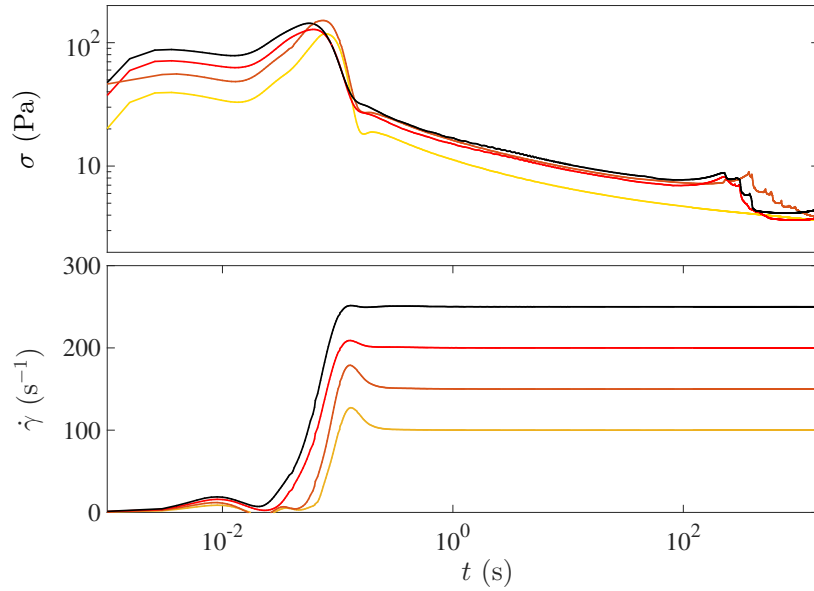


Figure 3: Shear stress response  $\sigma(t)$  and shear rate response  $\dot{\gamma}(t)$  in the start-up flow for different applied shear rates [color,  $\dot{\gamma}$  ( $\text{s}^{-1}$ )]: [—, 100]; [—, 150]; [—, 200]; [—, 250]. The sample is left to age during  $t_w = 60$  min before each experiment.

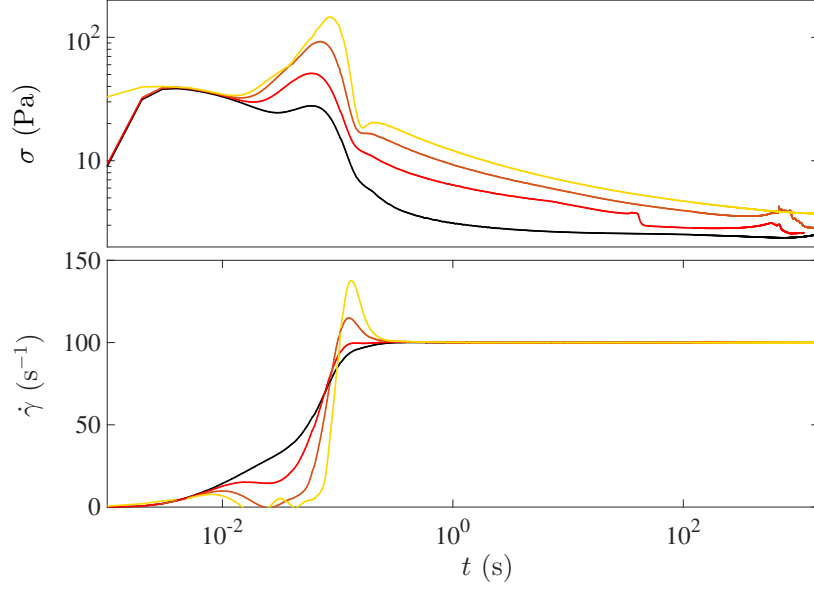


Figure 4: Shear stress response  $\sigma(t)$  and shear rate response  $\dot{\gamma}(t)$  in the start-up flow for different aging times  $t_w$  [color,  $t_w$  (min)]: [—, 100]; [—, 30]; [—, 5]; [—, 1]. Experiments performed at  $\dot{\gamma} = 100 \text{ s}^{-1}$ . Experiments performed at  $\dot{\gamma} = 100 \text{ s}^{-1}$ .

## Comparison of 1D and 2D-USV observations

A single stress drop event is extracted from a startup experiment performed at  $\dot{\gamma} = 150 \text{ s}^{-1}$  for  $t_w = 10 \text{ min}$  [inset of Fig. 5(a)]. The 1D velocity profiles are plotted as a spatiotemporal diagram in Fig. 5(b). Surprisingly the 1D flow profiles before and after the stress drop are very similar as they all show shear localization over about half the gap. By the time the stress reaches its maximum value, about 80% of the gap is sheared. Then shear abruptly localizes again over about 1 mm close to the rotor at the beginning of the stress relaxation. Therefore, although the strong fluctuations of  $v(r, t)$  observed before the stress peak appear to be correlated to those of  $\sigma(t)$ , the drop of about 15% in the stress value cannot be explained by these 1D data at a given height of the cell so that they may reflect the evolution of global rheology only if the flow is homogeneous along the vorticity direction. As a matter of fact, velocity profiles  $v(r, z, t)$  recorded simultaneously over the whole height of the cell through 2D-USV demonstrate that the flow is strongly heterogeneous in the vertical direction  $z$ . Fig. 5(c) shows a spatiotemporal plot of the fluid velocity along the vertical axis  $z$  at a fixed radial position  $r_0 = 0.2 \text{ mm}$  close to the rotor. Depending on the position along the  $z$ -axis, the material can be either solid-like or fluid-like. Note that the 1D-USV measurements are performed at  $z_0 \simeq 15 \text{ mm}$  and are fully consistent with the 2D-USV data.



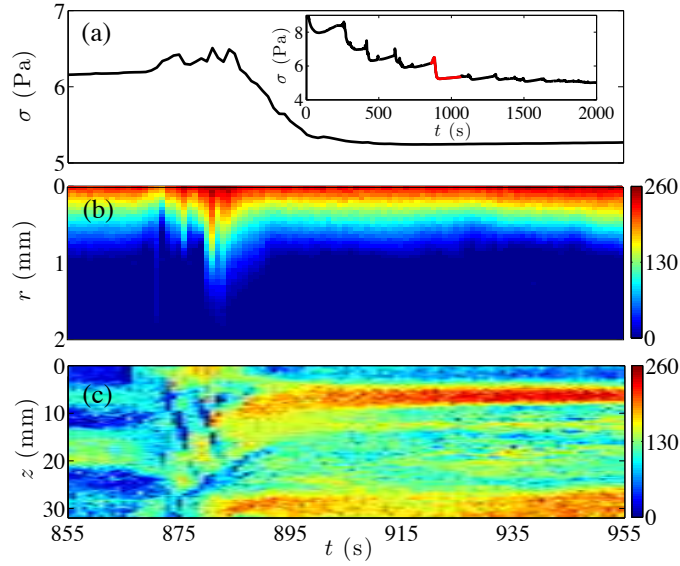


Figure 5: (a) Stress response  $\sigma(t)$  at  $\dot{\gamma} = 150 \text{ s}^{-1}$ ,  $t_w = 10 \text{ min}$ . Inset:  $\sigma(t)$  for the whole experiment. The signal of the main graph appears in red. (b) Spatiotemporal diagram of the velocity  $v(r, t)$  as a function of position  $r$  and  $t$  obtained with 1D-USV. The radial position  $r$  is measured from the rotor. (c) Spatiotemporal diagram of the velocity  $v(r_0, z, t)$  as a function of the vertical position  $z$  and  $t$  at  $r_0 = 0.2 \text{ mm}$  obtained by 2D-USV.  $z$  is measured from the top of the transducer. The velocity is color coded in  $\text{mm}\cdot\text{s}^{-1}$ .

## Effect of the Boundary Condition

The flow curve changes when the boundary condition becomes rough in a sand-blasted Plexiglas Taylor-Couette cell with typical roughness of  $1 \mu\text{m}$  (to be compared to a few tens of nanometers for the “smooth” cell used so far). Fig. 6 shows the rheological and 2D-USV data obtained in rough boundary conditions (b.c.) by the same protocol of the results in smooth b.c. in the main text. In the case of rough b.c. in Fig. 6, the rheological hysteresis is far less pronounced in comparison to the data obtained with smooth b.c. Here the flow remains homogeneous along the vertical axis during both ramps. As for results of shear-rate controlled tests with 1D-USV, although there exists shear banding as it is for the smooth boundary, interestingly, the wall slip is negligible in the case of the rough boundary. Also the fluidization proceeds smoothly without stress fluctuations.

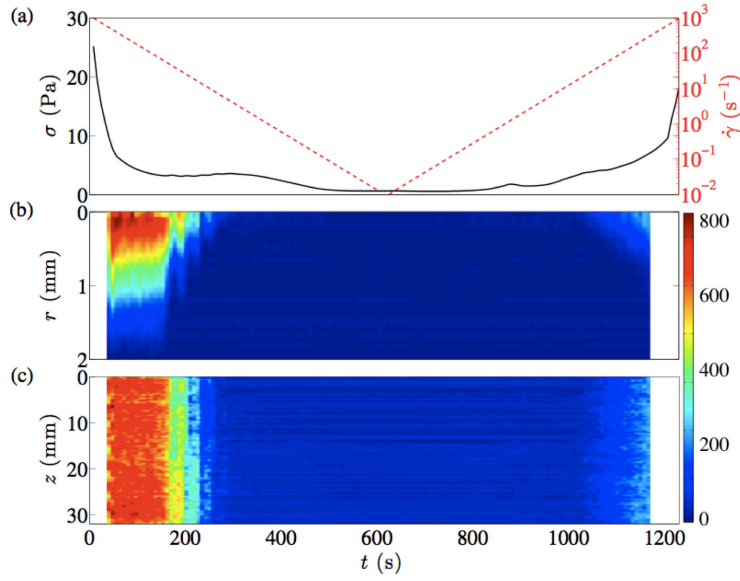


Figure 6: 1D and 2D velocity profiles of flow curves in rough b.c. (a) Shear rate  $\dot{\gamma}$  and shear stress  $\sigma$  vs time  $t$ . (b) Spatiotemporal diagram of the velocity data  $v(r, z_0, t)$  as a function of the distance  $r$  to the rotor and  $t$ , at  $z_0 \simeq 15$  mm. (c) Spatiotemporal diagram of the velocity data  $v(r_0, z, t)$  as a function of the vertical position  $z$  and  $t$ , at  $r_0 = 0.5$  mm. The fluid velocity is color-coded in mm/s.

## Effect of the Gap Width

Fig. 7 shows the influence of the gap size on the fluid response to a shear startup experiment performed at  $\dot{\gamma} = 50 \text{ s}^{-1}$  on a sample left at rest for  $t_w = 10$  min. In a gap of size  $e = 2$  mm, the same value as in the main text, the stress response displays a large number of peaks together with unsteady shear banding over 2400 s. Decreasing the size of the gap changes radically the sample behavior. In a gap twice as small ( $e = 1$  mm), the stress response exhibits less peaks and the sample fluidizes entirely in about  $t = 200$  s. Decreasing the gap by a factor of 4 ( $e = 0.5$  mm) leads to a smooth stress response and to homogeneous velocity profiles from the beginning of the experiments, with significant slip at the moving boundary.

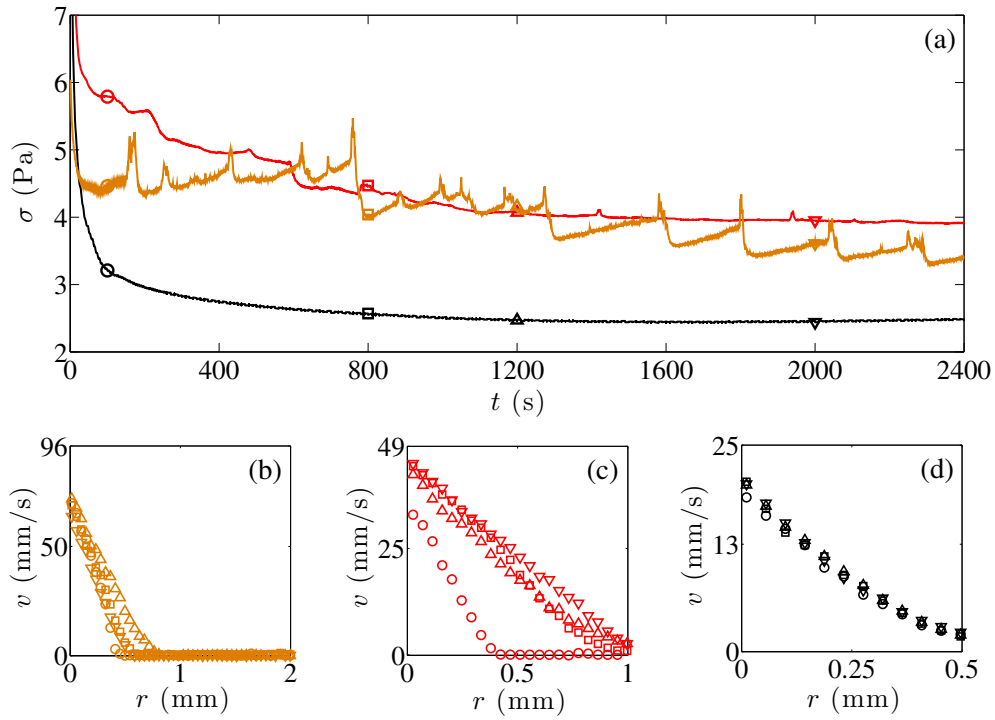


Figure 7: (a) Stress response  $\sigma(t)$  to a shear startup experiment performed at  $\dot{\gamma} = 50 \text{ s}^{-1}$  for different gap sizes: [color, gap (mm)] = [—, 2], [—, 1], [—, 0.5]. (b)-(d) Velocity profile, where  $r$  is the distance to the rotor at different times in (a) [symbol, time (s)]: [ $\circ$ , 100]; [ $\square$ , 800]; [ $\triangle$ , 1200]; [ $\nabla$ , 2000]. The rotor velocity corresponds to the upper bound of the vertical axis. The sample is aged during  $t_w = 10 \text{ min}$  before each experiment.

---

# Supplementary Data on Analysis of 1986 Izu-Oshima Eruption

## Evaluation of the Method

### Evaluation of Site Amplification Factor

The site amplification factor  $S_i$  in Equation (4.3) is difficult to evaluate properly due to its empirical determination, although it has a large effect on the source location. We use coda waves from seven earthquakes (utilizing six seconds of the wave trains starting two seconds after the S wave peak) that occurred in November 1986 near the Izu Peninsula (gray stars in Fig. 8 (a)). It is better to use earthquakes with various locations as these ensure homogenized path directions; however, all the usable earthquakes during the period occurred near the Izu Peninsula, west of Izu-Oshima Island. Therefore, it is necessary to evaluate the effects of the biased path direction on the location determination.

To evaluate the possible bias effect, we estimate site amplification factors at five recently-operated stations close to the stations operated in November 1986 using the same method described above. Since the seismometers were newly installed at slightly different places, the local situation may be different. The analyzed data are 10 earthquakes in January 2013 that occurred near Izu Peninsula, Tokyo Bay, and Boso Peninsula (that is, west, north, and north-east from Izu-Oshima, respectively) as shown in Fig. 8 (a). The hypocenters are given in the Japan Meteorological Agency Earthquake Catalog [115]. Fig. 8 first indicates that the trend of site amplification factors in 2013 is different from that in 1986. This may be caused because the positions of the seismometers and underground condition varied. However, the variation among the stations in 1986 case is relatively smaller compared to that in 2013 case, especially for the data recorded at NRM and OSK stations. Note that shallow earthquakes happened near Izu Peninsula and deep earthquakes near Tokyo Bay and Boso Peninsula are used for the evaluation. Therefore, for the seismic ray paths coming from Izu Peninsula, there exists a systematic bias in OSK data since the amplitude attenuates by crossing shallow parts of the Island to reach the seismic station. Fig. 8 shows the effect that the paths crossing the Island (blue) have lower value than those without crossing (red and green) at the OSK station. To evaluate variations in the source location caused by the bias effect, we set a reference location for tremor source and change  $S_i$  of NRM and OSK within the estimated range. Results show that the tremor source location moves 1.7 km in a NE–SW direction when the reference source is set along the fissures. Although the changes in the estimated range in  $S_i$  cause a shift perpendicular to the strike of the fissures,

it does not affect the NW–SE trend of tremor source locations along the fissures, which is an essential point in this study.

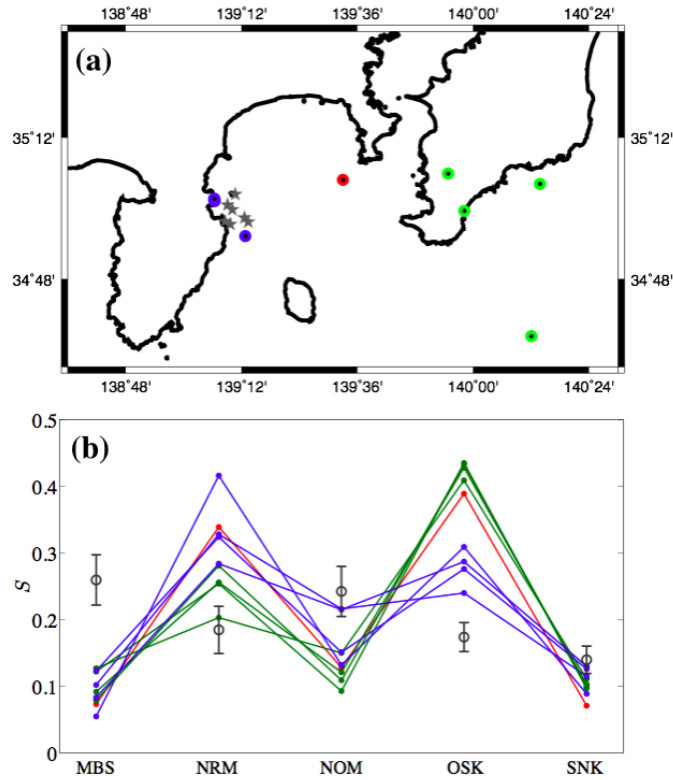


Figure 8: (a) Epicenters of earthquakes utilized in estimation of site amplification factors. Red, green, and blue dots represent those occurred in January 2013 (Tokyo Bay, Boso Peninsula, and Izu Peninsula, respectively) while gray stars are those happened in November 1986. (b) Normalized site amplification factors at the stations estimated by earthquakes in (a) with the same color coordination.

---

## Evaluation of AIM

We evaluate the AIM itself by applying the method to recent earthquakes in central Izu-Oshima in January 2014 and in northwestern Izu-Oshima in July 2014 by using the amplification factors of 2013, as shown in Fig. 9. Fig. 9 compares the AIM results and hypocenter locations determined by ERI and Japan Metrological Agency (JMA). Although different seismic stations and three different methods were used, the estimated hypocenter locations approximately coincide as shown in Table 1.

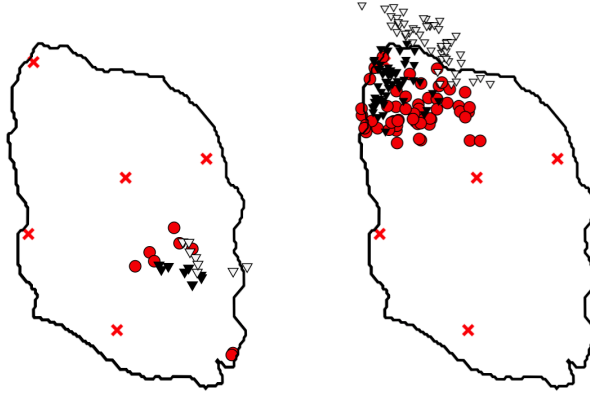


Figure 9: Seismic sources of earthquakes that occurred in January (left) and July (right) of 2014. White and black inverted triangles are the locations of hypocenters determined by ERI and JMA, respectively. The results of our estimation using AIM are shown as red dots. Seismic data recorded at five stations indicated by cross marks were used in the estimation.

	$ \Delta r_{AIM-JMA} $ (km)	$ \Delta r_{AIM-ERI} $ (km)	$ \Delta r_{JMA-ERI} $ (km)
Jan.	1.32	2.04	1.25
Jul.	2.38	2.96	2.45

Table 1: Mean horizontal distance between seismic sources estimated by the three, ERI, JMA, and our analysis. The source locations are plotted in Fig. 9.

# Bibliography

- [1] ALIDIBIROV, M. & DINGWELL, D.B. (1996). Magma fragmentation by rapid decompression. *Nature*, **380**, 146–148. [8](#)
- [2] ALLEN, L.H. & MATIJEVIC, E. (1969). Stability of Colloidal Silica: I. Effect of Simple electrolytes. *J. Colloid Interface Sci.*, **31**, 287–296. [52](#)
- [3] ALLEN, L.H. & MATIJEVIC, E. (1970). Stability of Colloidal Silica II. Ion Exchange. *J. Colloid Interface Sci.*, **33**, 420–429. [52](#)
- [4] ARAMAKI, S. & FUJII, T. (1988). Petrological and geological model of the 1986-1987 eruption of Izu-Oshima Volcano. *Bull. Volcanol. Soc. Japan.*, **33**, S297–S306. [101](#)
- [5] BARNES, H.A., HUTTON, J.F. & WALTERS, K. (1989). *An introduction to rheology*, vol. 3. Elsevier. [12](#)
- [6] BATTAGLIA, J. & AKI, K. (2003). Location of seismic events and eruptive fissures on the Piton de la Fournaise volcano using seismic amplitudes. *Journal of Geophysical Research: Solid Earth*, **108**, 2364. [88](#)
- [7] BATTAGLIA, J., AKI, K. & FERRAZZINI, V. (2005). Location of tremor sources and estimation of lava output using tremor source amplitude on the Piton de la Fournaise volcano: 1. Location of tremor sources. *Journal of Volcanology and Geothermal Research*, **147**, 268–290. [vi](#), [5](#), [6](#), [87](#), [88](#), [90](#), [112](#)
- [8] BINGHAM, E.C. (1916). An investigation of the laws of plastic flow. *U.S. Bureau of Standards Bulletin*, **13**, 309–353. [12](#)
- [9] BONN, D., KELLAY, H., TANAKA, H., WEGDAM, G. & MEUNIER, J. (1999). Laponite: What is the difference between a gel and a glass? *Langmuir*, **15**, 7534–7536. [114](#)
- [10] CANNATA, A., DI GRAZIA, G., MONTALTO, P., FERRARI, F., NUNNARI, G., PATANÈ, D. & PRIVITERA, E. (2010). New insights into banded tremor from the

- 2008–2009 Mount Etna eruption. *Journal of Geophysical Research: Solid Earth*, **115**, B12318. [vi](#), [5](#), [9](#), [10](#), [112](#)
- [11] CAO, X.J., CUMMINS, H.Z. & MORRIS, J.F. (2010). Structural and rheological evolution of silica nanoparticle gels. *Soft Matter*, **6**, 5425–5433. [52](#), [118](#)
- [12] CHENG, D.C.H. (2003). Characterisation of thixotropy revisited. *Rheologica Acta*, **42**, 372–382. [17](#)
- [13] CHEVREL, M.O., CIMARELLI, C., DEBIASI, L., HANSON, J.B., LAVALLÉE, Y., ARZILLI, F. & DINGWELL, D.B. (2015). Viscosity measurements of crystallizing andesite from Tungurahua volcano (Ecuador). *Geochemistry, Geophysics, Geosystems*, **16**, 870–889. [xi](#), [82](#), [83](#), [126](#)
- [14] CHOUET, B. (1985). Excitation of a buried magmatic pipe: A seismic source model for volcanic tremor. *Journal of Geophysical Research*, **90**, 1881–1893. [7](#)
- [15] CHOUET, B. (1988). Resonance of a fluid-driven crack: Radiation properties and implications for the source of long-period events and harmonic tremor. *Journal of Geophysical Research*, **93**, 4375–4400. [vi](#), [8](#), [9](#)
- [16] CHOUET, B.A. (1996). Long-period volcano seismicity: its source and use in eruption forecasting. *Nature*, **380**, 309–316. [vi](#), [1](#), [2](#), [3](#)
- [17] CHOUET, B.A., PAGE, R.A., STEPHENS, C.D., LAHR, J.C. & POWER, J.A. (1994). Precursory swarms of long-period events at Redoubt Volcano (1989–1990), Alaska: Their origin and use as a forecasting tool. *Journal of Volcanology and Geothermal Research*, **62**, 95–135. [2](#)
- [18] COSTA, A., MELNIK, O., SPARKS, R.S.J. & VOIGHT, B. (2007). Control of magma flow in dykes on cyclic lava dome extrusion. *Geophysical Research Letters*, **34**, L02303. [23](#)
- [19] COSTA, A., CARICCHI, L. & BAGDASSAROV, N. (2009). A model for the rheology of particle-bearing suspensions and partially molten rocks. *Geochemistry, Geophysics, Geosystems*, **10**, Q03010. [15](#)
- [20] COSTA, A., WADGE, G. & MELNIK, O. (2012). Cyclic extrusion of a lava dome based on a stick-slip mechanism. *Earth and Planetary Science Letters*, **337–338**, 39–46. [47](#), [122](#)



- 
- [21] CRASSOUS, J.J., SIEBENBÜRGER, M., BALLAUFF, M., DRECHSLER, M., HENRICH, O. & FUCHS, M. (2006). Thermosensitive core-shell particles as model systems for studying the flow behavior of concentrated colloidal dispersions. *The Journal of Chemical Physics*, **125**, 204906. [28](#)
- [22] DEPASSE, J. (1997). Coagulation of Colloidal Silica by Alkaline Cations: Surface Dehydration or Interparticle Bridging? *J. Colloid Interface Sci.*, **194**, 260–262. [52](#)
- [23] DEPASSE, J. & WATILLON, A. (1970). The stability of Amorphous Colloidal Silica. *J. Colloid Interface Sci.*, **33**, 430–438. [52](#)
- [24] DEREK, C., DUCOURET, G., AJDARI, A. & LEQUEUX, F. (2003). Aging and non-linear rheology in suspensions of polyethylene oxide-protected silica particles. *Physical Review E*, **67**, 061403. [16](#)
- [25] DI LIETO, B., SACCOROTTI, G., ZUCCARELLO, L., ROCCA, M.L. & SCARPA, R. (2007). Continuous tracking of volcanic tremor at Mount Etna, Italy. *Geophysical Journal International*, **169**, 699–705. [112](#)
- [26] DIVOUX, T., BARENTIN, C. & MANNEVILLE, S. (2011). Stress overshoot in a simple yield stress fluid: An extensive study combining rheology and velocimetry. *Soft Matter*, **7**, 9335–9349. [16](#), [26](#), [37](#), [133](#)
- [27] DIVOUX, T., FARDIN, M.A., MANNEVILLE, S. & LEROUGE, S. (2015). Shear banding of complex fluids. *Annual Review of Fluid Mechanics*, **48**, 81–103. [xiv](#), [114](#), [120](#)
- [28] DOELDER, C.F.J.D., KOOPMAND, R.J., MOLENAAR, J. & VAN DE VEN, A.A.F. (1998). Comparing the wall slip and the constitutive approach for modelling spurt instabilities in polymer melt flows. *Journal of Non-Newtonian Fluid Mechanics*, **75**, 25–41. [36](#)
- [29] DRABAREK, E., BARTLETT, J.R., HANLEY, H.J.M., WOOLFREY, J.L. & MUZNY, C.D. (2002). Effect of processing variables on the structural evolution of silica gels. *International journal of Thermophysics*, **23**, 145–160. [52](#)
- [30] DUARTE, A.S.R., MIRANDA, A.I.P. & OLIVEIRA, P.J. (2008). Numerical and analytical modeling of unsteady viscoelastic flows: The start-up and pulsating test case problems. *Journal of Non-Newtonian Fluid Mechanics*, **154**, 153–169. [33](#)
- [31] ENDO, K., CHIBA, T., TANIGUCHI, H., SUMITA, M., TACHIKAWA, S., MIYAHARA, T., UNO, R. & MIYAJI, N. (1988). Tephrochronological study on the 1986-1987

- eruptions of Izu-Oshima Volcano, Japan. *Bull Volcanol Soc Japan*, **33**, S32–S51. [xii](#), [85](#), [86](#), [91](#), [100](#), [101](#)
- [32] FEHLER, M. (1983). Observations of volcanic tremor at Mount St. Helens Volcano. *Journal of Geophysical Research*, **88**, 3476–3484. [1](#), [7](#)
- [33] FOSS, D.R. & BRADY, J.F. (1999). Self-diffusion in sheared suspensions by dynamic simulation. *Journal of Fluid Mechanics*, **401**, 243–274. [33](#), [37](#)
- [34] FUJII, T., ARAMAKI, S., KANEKO, T., OZAWA, K., KAWANABE, Y. & FUKUOKA, T. (1988). Petrology of the lavas and ejecta of the November, 1986 eruption of Izu-Oshima Volcano. *Bull. Volcanol. Soc. Japan.*, **33**, S234–S254. [101](#)
- [35] FUJITA, E., UKAWA, M. & YAMAMOTO, E. (2004). Subsurface cyclic magma sill expansions in the 2000 Miyakejima volcano eruption: Possibility of two-phase flow oscillation. *Journal of Geophysical Research: Solid Earth*, **109**, B04205. [vii](#), [18](#), [21](#), [22](#)
- [36] FUJITA, E., ARAKI, K. & NAGANO, K. (2011). Volcanic tremor induced by gas-liquid two-phase flow: Implications of density wave oscillation. *Journal of Geophysical Research: Solid Earth*, **116**, B09201. [18](#)
- [37] GALLOT, T., PERGE, C., GRENARD, V., FARDIN, M.A., TABERLET, N. & MANNEVILLE, S. (2013). Ultrafast ultrasonic imaging coupled to rheometry: Principle and illustration. *Review of Scientific Instruments*, **84**, 045107. [ix](#), [54](#), [56](#), [72](#)
- [38] GAN, D. & LYON, L.A. (2001). Tunable Swelling Kinetics in CoreShell Hydrogel Nanoparticles. *Journal of the American Chemical Society*, **123**, 7511–7517. [28](#)
- [39] HALE, A.J. (2007). Magma flow instabilities in a volcanic conduit: Implications for long-period seismicity. *Physics of the Earth and Planetary Interiors*, **163**, 163–178. [47](#), [122](#)
- [40] HANEY, M.M. (2014). Backprojection of volcanic tremor. *Geophysical Research Letters*, **41**, 1923–1928. [87](#)
- [41] HARRINGTON, R.M. & BRODSKY, E.E. (2007). Volcanic hybrid earthquakes that are brittle-failure events. *Geophysical Research Letters*, **34**, L06308. [2](#)
- [42] HASHIMOTO, M. & TADA, T. (1988). Crustal deformation before and after the 1986 eruption of Izu Oshima Volcano. *Bull. Volcanol. Soc. Japan.*, **33**, S136–S144. [86](#), [98](#)

- 
- [43] HESTON, W.M., ILER, R.K. & SEARS, G.W. (1960). The adsorption of hydroxyl ions from aqueous solution on the surface of amorphous silica. *The Journal of Chemical Physics*, **64**, 147–150. [52](#)
- [44] HEYMANN, L. & AKSEL, N. (2007). Transition pathways between solid and liquid state in suspensions. *Physical Review E*, **75**, 021505. [23](#), [121](#)
- [45] HIROSE, T. (2005). Growth of molten zone as a mechanism of slip weakening of simulated faults in gabbro during frictional melting. *Journal of Geophysical Research: Solid Earth*, **110**, B05202. [79](#)
- [46] HOOVER, S.R., CASHMAN, K.V. & MANGA, M. (2001). The yield strength of subliquidus basalts - experimental results. *Journal of Volcanology and Geothermal Research*, **107**, 1–18. [13](#), [27](#)
- [47] ICHIHARA, M., RITTEL, D. & STURTEVANT, B. (2002). Fragmentation of a porous viscoelastic material: Implications to magma fragmentation. *Journal of Geophysical Research: Solid Earth*, **107**, 2229–2243. [8](#)
- [48] IDA, Y., YAMAOKA, K. & WATANABE, H. (1988). Model of volcanic activity associated with magma drain-back: Implication for eruptions of Izu-Oshima Volcano after December, 1986. *Bull. Earthq. Res. Inst.*, **63**, 183–200. [110](#), [125](#)
- [49] IGUCHI, M., YAMAMOTO, K., TAKAYAMA, T., MAEKAWA, T., NISHIMURA, T., HASHINO, H., YAKIHARA, H. & HIRANO, S. (2001). Characteristics of Volcanic Earthquakes at Kuchierabujima Volcano. *Annuals of Disaster Preview Research Institute of Kyoto University*, 317–326. [4](#)
- [50] ISHIBASHI, H. & SATO, H. (2007). Viscosity measurements of subliquidus magmas: Alkali olivine basalt from the Higashi-Matsuura district, Southwest Japan. *Journal of Volcanology and Geothermal Research*, **160**, 223–238. [vii](#), [15](#), [16](#), [126](#)
- [51] ISHIBASHI, H. & SATO, H. (2010). Bingham fluid behavior of plagioclase-bearing basaltic magma: Reanalyses of laboratory viscosity measurements for Fuji 1707 basalt. *Journal of Mineralogical and Petrological Sciences*, **105**, 334–339. [15](#), [27](#)
- [52] IWAMURA, K. & KANESHIMA, S. (2005). Numerical simulation of the steam-water flow instability as a mechanism of long-period ground vibrations at geothermal areas. *Geophysical Journal International*, **163**, 833–851. [18](#)
- [53] JELLINEK, A.M. & BERCOVICI, D. (2011). Seismic tremors and magma wagging during explosive volcanism. *Nature*, **470**, 522–525. [vi](#), [2](#), [4](#)

- 
- [54] JULIAN, B.R. (1994). Volcanic tremor: Nonlinear excitation by fluid flow. *Journal of Geophysical Research*, **99**, 11859–11877. [vi](#), [7](#), [8](#)
- [55] KAKAC, S. & BON, B. (2008). A Review of two-phase flow dynamic instabilities in tube boiling systems. *International Journal of Heat and Mass Transfer*, **51**, 399–433. [vii](#), [18](#), [19](#), [20](#), [21](#)
- [56] KAWAKATSU, H. & YAMAMOTO, M. (2007). Volcano Seismology. *Treatise on Geophysics*, **4**, 389–420. [vi](#), [1](#), [8](#)
- [57] KIEFFER, S.W. (1984). Seismicity at old faithful geyser: An Isolated source of geothermal noise and possible analogue of volcanic seismicity. *Journal of Volcanology and Geothermal Research*, **22**, 59–95. [9](#)
- [58] KONSTANTINOU, K.I. & SCHLINDWEIN, V. (2002). Nature, wavefield properties and source mechanism of volcanic tremor: a review. *Journal of Volcanology and Geothermal Research*, **119**, 161–187. [vi](#), [1](#), [7](#), [9](#)
- [59] KOUMAKIS, N., LAURATI, M., EGELHAAF, S.U., BRADY, J.F. & PETEKIDIS, G. (2012). Yielding of Hard-Sphere Glasses during Start-Up Shear. *Physical Review Letters*, **108**, 098303. [33](#)
- [60] KOYANAGI, S., AKI, K. & MAYEDA, K. (1995). Inferred attenuation from site effect-corrected T phases recorded on the island of Hawaii. *Pure Applied Geophysics*, **144**, 1–17. [88](#)
- [61] KUMAGAI, H., PALACIOS, P., MAEDA, T., CASTILLO, D.B. & NAKANO, M. (2009). Seismic tracking of lahars using tremor signals. *Journal of Volcanology and Geothermal Research*, **183**, 112–121. [87](#), [88](#)
- [62] KUROKAWA, A., ICHIHARA, M. & KURITA, K. (2015). Softening of aged fluids in start-up flows of dense suspensions. *Journal of Non-Newtonian Fluid Mechanics*, **217**, 14–22. [16](#), [26](#)
- [63] KUROKAWA, A., VIDAL, V., KURITA, K., DIVOUX, T. & MANNEVILLE, S. (2015). Avalanche-like fluidization of a non-brownian particle gel. *Soft Matter*, **11**, 9026–9037. [59](#)
- [64] LANE, S.J., CHOUET, B.A., PHILLIPS, J.C., DAWSON, P., RYAN, G. & HURST, E. (2001). Experimental observations of pressure oscillations and flow regimes in an analogue volcanic system. *Journal of Geophysical Research*, **106**, 6461–6476. [31](#)

- 
- [65] LARMAT, C.S., GUYER, R.A. & JOHNSON, P.A. (2010). Time-reversal methods in geophysics. *Physics Today*, 31–35. [87](#)
- [66] LARSON, R.G. (1999). *The structure and rheology of complex fluids*. Oxford University Press. [50](#)
- [67] LAURATI, M., MUTCH, K.J., KOUMAKIS, N., ZAUSCH, J., AMANN, C.P., SCHOFIELD, A.B., PETEKIDIS, G., BRADY, J.F., HORBACH, J., FUCHS, M. & EGELHAAF, S.U. (2012). Transient dynamics in dense colloidal suspensions under shear: shear rate dependence. *Journal of Physics: Condensed Matter*, **24**, 464104. [33](#)
- [68] LEDINEGG, M. (1938). Instability of flow during natural and forced circulation. *Waerme*, **61**, 891–898. [18](#)
- [69] LEJEUNE, A.M. & RICHEL, P. (1995). Rheology of crystal-bearing silicate melts: An experimental study at high viscosities. *Journal of Geophysical Research*, **100**, 4215–4229. [12](#), [27](#)
- [70] LOKMER, I., O'BRIEN, G.S., STICH, D. & BEAN, C.J. (2009). Time reversal imaging of synthetic volcanic tremor sources. *Geophysical Research Letters*, **36**, L12308. [87](#)
- [71] LYONS, J.J., ICHIHARA, M., KUROKAWA, A. & LEES, J.M. (2013). Switching between seismic and seismo-acoustic harmonic tremor simulated in the laboratory: Insights into the role of open degassing channels and magma viscosity. *Journal of Geophysical Research: Solid Earth*, **118**, 277–289. [4](#)
- [72] MAEDA, T. & OBARA, K. (2009). Spatiotemporal distribution of seismic energy radiation from low-frequency tremor in western Shikoku, Japan. *Journal of Geophysical Research: Solid Earth*, **114**, B00A09. [87](#)
- [73] MALKIN, A.Y. (2006). Flow instability in polymer solutions and melts. *Polymer Science Series C*, **48**, 21–37. [17](#)
- [74] MALKIN, A.Y., SEMAKOV, A.V. & KULICHIKHIN, V.G. (2010). Self-organization in the flow of complex fluids (colloid and polymer systems) Part 1: Experimental evidence. *Advances in Colloid and Interface Science*, **157**, 75–90. [vii](#), [17](#), [36](#)
- [75] MANNEN, K. (2006). Total grain size distribution of a mafic subplinian tephra, TB-2, from the 1986 Izu-Oshima eruption, Japan: An estimation based on a theoretical model of tephra dispersal. *Journal of Volcanology and Geothermal Research*, **155**, 1–17. [86](#)

- [76] MANNEVILLE, S. (2008). Recent experimental probes of shear banding. *Rheologica Acta*, **47**, 301–318. [15](#)
- [77] MANNEVILLE, S., BÉCU, L. & COLIN, A. (2004). High-frequency ultrasonic speckle velocimetry in sheared complex fluids. *The European Physical Journal Applied Physics*, **28**, 361–373. [ix](#), [54](#), [55](#), [56](#)
- [78] MCNUTT, S.R. (1996). *Seismic monitoring and eruption forecasting of volcanoes: A review of the state-of-the-art and case histories*. Springer. [vi](#), [2](#)
- [79] MELNIK, O. & SPARKS, R.S.J. (2005). Controls on conduit magma flow dynamics during lava dome building eruptions. *Journal of Geophysical Research: Solid Earth*, **110**, B02209. [23](#)
- [80] MEWIS, J. & WAGNER, N.J. (2013). *Colloidal suspensions rheology*. Cambridge University Press. [ix](#), [28](#), [50](#), [51](#)
- [81] MIKADA, H., WATANABE, H. & SAKASHITA, S. (1997). Evidence for subsurface magma bodies beneath Izu-Oshima volcano inferred from a seismic scattering analysis and possible interpretation of the magma plumbing system of the 1986 eruptive activity. *Physics of the Earth and Planetary Interiors*, **104**, 257–269. [88](#)
- [82] MIKUMO, T., OLSEN, K.B., FUKUYAMA, E. & YAGI, Y. (2003). Stress-breakdown time and slip-weakening distance inferred from slip-velocity functions on earthquake faults. *Bulletin of Seismological Society of America*, **93**, 264–282. [79](#)
- [83] MØLLER, P. (2008). *Shear banding and the solid/liquid transition in yield stress fluids*. Ph.D. thesis, University Pierre et Marie Curie. [51](#)
- [84] MØLLER, P., FALL, A., CHIKKADI, V., DERKS, D. & BONN, D. (2009). An attempt to categorize yield stress fluid behaviour. *Philosophical Transactions of the Royal Society A: Mathematical, Physical and Engineering Sciences*, **367**, 5139–5155. [126](#)
- [85] MØLLER, P.C.F., MEWIS, J. & BONN, D. (2006). Yield stress and thixotropy: on the difficulty of measuring yield stresses in practice. *Soft Matter*, **2**, 274–283. [12](#), [76](#), [114](#)
- [86] MØLLER, P.C.F., RODTS, S., MICHELS, M.A.J. & BONN, D. (2008). Shear banding and yield stress in soft glassy materials. *Physical Review E*, **77**, 041507. [50](#), [57](#), [118](#), [126](#)

- [87] MOORCROFT, R.L. & FIELDING, S.M. (2013). Criteria for shear banding in time-dependent flows of complex fluids. *Physical Review Letters*, **110**, 086001. [23](#)
- [88] MUELLER, S., LLEWELLIN, E.W. & MADER, H.M. (2010). The rheology of suspensions of solid particles. *Proceedings of the Royal Society A: Mathematical, Physical and Engineering Sciences*, **466**, 1201–1228. [114](#)
- [89] NEGRAO, C.O.R., FRANCO, A.T. & ROCHA, L.L.V. (2011). A weakly compressible flow model for the restart of thixotropic drilling fluids. *Journal of Non-Newtonian Fluid Mechanics*, **166**, 1369–1381. [33](#)
- [90] NISHIMURA, T., NAKAMICHI, H., TANAKA, S., SATO, M., KOBAYASHI, T., UEKI, S., HAMAGUCHI, H., OHTAKE, M. & SATO, H. (2000). Source process of very long seismic events associated with 1998 activity of Iwate Volcano, northeastern Japan. *Journal of Geophysical Research*, **105**, 19135–19147. [vi](#), [11](#)
- [91] NORDSTROM, K.N., VERNEUIL, E., ARRATIA, P.E., BASU, A., ZHANG, Z., YODH, A.G., GOLLUB, J.P. & DURIAN, D.J. (2010). Microfluidic Rheology of Soft Colloids above and below Jamming. *Physical Review Letters*, **105**, 175701. [28](#)
- [92] OBARA, K. (2002). Nonvolcanic deep tremor associated with subduction in southwest Japan. *Science*, **296**, 1679–1681. [87](#)
- [93] OGISO, M. & YOMOGIDA, K. (2012). Migration of tremor locations before the 2008 eruption of Meakandake Volcano, Hokkaido, Japan. *Journal of Volcanology and Geothermal Research*, **217-218**, 8–20. [5](#), [87](#), [88](#)
- [94] OKUMURA, S. & UESUGI, K. (2014). Transition between frictional sliding and viscous flow in magmatic fractured zone. In *RHEOVOLC 2014*. [vii](#), [15](#)
- [95] PALZA, H., NAUE, I.F.C. & WILHELM, M. (2009). In situ pressure fluctuations of polymer melt flow instabilities: Experimental evidence about their origin and dynamics. *Macromolecular Rapid Communications*, **30**, 1799–1804. [vii](#), [18](#)
- [96] PHILPOTTS, A.R. & DICKSON, L.D. (2000). The formation of plagioclase chains during convective transfer in basaltic magma. *Nature*, **406**, 59–61. [126](#)
- [97] POGODINA, N.V., LAVRENKO, V.P., SRINIVAS, S. & WINTER, H.H. (2001). Rheology and structure of isotactic polypropylene near the gel point: quiescent and shear-induced crystallization. *Polymer*, **42**, 9031–9043. [126](#)

- [98] PUPIER, E., DUCHENE, S. & TOPLIS, M.J. (2008). Experimental quantification of plagioclase crystal size distribution during cooling of a basaltic liquid. *Contributions to Mineralogy and Petrology*, **155**, 555–570. [vii](#), [13](#), [14](#), [126](#)
- [99] PURNOMO, E.H., ENDE, D.V.D., MELLEMA, J. & MUGELE, F. (2006). Linear viscoelastic properties of aging suspensions. *Europhysics Letters (EPL)*, **76**, 74–80. [28](#), [114](#)
- [100] RABIDEAU, B.D., MOUCHERONT, P., BERTRAND, F.O., RODTS, S.P., ROUSSEL, N., LANOS, C. & COUSSOT, P. (2010). Journal of Non-Newtonian Fluid Mechanics. *Journal of Non-Newtonian Fluid Mechanics*, **165**, 394–408. [43](#)
- [101] RIPEPE, M. & GORDEEV, E. (1999). Gas bubble dynamics model for shallow volcanic tremor at Stromboli. *Journal of Geophysical Research*, **104**, 10639–10654. [vi](#), [8](#), [9](#)
- [102] RIPEPE, M., MARCHETTI, E., BONADONNA, C., HARRIS, A.J.L., PIOLI, L. & ULIVIERI, G. (2010). Monochromatic infrasonic tremor driven by persistent degassing and convection at Villarrica Volcano, Chile. *Geophysical Research Letters*, **37**, L15303. [4](#)
- [103] ROBERT, L., DEMAY, Y. & VERGNES, B. (2004). Stick-slip flow of high density polyethylene in a transparent slit die investigated by laser Doppler velocimetry. *Rheologica Acta*, **43**, 89–98. [36](#)
- [104] ROGERS, S.A., VLASSOPOULOS, D. & CALLAGHAN, P.T. (2008). Aging, Yielding, and Shear Banding in Soft Colloidal Glasses. *Physical Review Letters*, **100**, 128304–4. [114](#), [119](#)
- [105] SAAR, M.O., MANGA, M., CASHMAN, K.V. & FREMOUW, S. (2001). Numerical models of the onset of yield strength in crystal-melt suspensions. *Earth and Planetary Science Letters*, **187**, 367–379. [vii](#), [14](#), [15](#), [27](#)
- [106] SAKAGUCHI, K., TAKADA, A., UTO, K. & SOYA, T. (1988). The 1986 eruption and products of Izu-Oshima volcano, Japan. *Bull. Volcanol. Soc. Japan.*, **33**, S20–S31. [xii](#), [85](#), [91](#), [101](#), [111](#)
- [107] SCHMINCKE, H.U. (2004). *Volcanism*. Springer. [13](#)
- [108] SENFF, H. & RICHTERING, W. (1999). Temperature sensitive microgel suspensions: Colloidal phase behavior and rheology of soft spheres. *The Journal of Chemical Physics*, **111**, 1705. [27](#)



- [109] SHAHIN, A. & JOSHI, Y.M. (2010). Irreversible Aging Dynamics and Generic Phase Behavior of Aqueous Suspensions of Laponite. *Langmuir*, **26**, 4219–4225. [114](#)
- [110] SRIVASTAVA, S., SHIN, J.H. & ARCHER, L.A. (2012). Structure and rheology of nanoparticle–polymer suspensions. *Soft Matter*, **8**, 4097. [57](#)
- [111] TANG, H.S. & KALYON, D.M. (2008). Time-dependent tube flow of compressible suspensions subject to pressure dependent wall slip: Ramifications on development of flow instabilities. *Journal of Rheology*, **52**, 1069. [33](#)
- [112] TROMPETTE, J.L. & CLIFTON, M.J. (2004). Influence of ionic specificity on the microstructure and the strength of gelled colloidal silica suspensions. *Journal of Colloid and Interface Science*, **276**, 475–482. [52](#)
- [113] TRUZZOLILLO, D., ROGER, V., DUPAS, C., MORA, S. & CIPELLETTI, L. (2014). Bulk and interfacial stresses in suspensions of soft and hard colloids. [52](#)
- [114] TSURUGA, K., YOMOGIDA, K., HONDA, S., ITO, H., OHMINATO, T. & KAWAKATSU, H. (1997). Spatial and temporal variations of volcanic earthquakes at Sakurajima Volcano, Japan. *Journal of Volcanology and Geothermal Research*, **75**, 337–358. [7](#)
- [115] TSURUOKA, H. (1998). Development of earthquake information retrieval and analysis system on WWW. *IPJS SIG Technical Report*, **1998-115-9**, **1998-49-9**, 65–70. [138](#)
- [116] VAN DEN ENDE, D., PURNOMO, E.H., DUTS, M.H.G., RICHTERING, W. & MUGELE, F. (2010). Aging in dense suspensions of soft thermosensitive microgel particles studied with particle-tracking microrheology. *Physical Review E*, **81**, 011404. [28](#)
- [117] VIASNOFF, V. & LEQUEUX, F. (2002). Rejuvenation and overaging in a colloidal glass under shear. *Phys. Rev. Lett.*, **89**, 065701. [56](#)
- [118] VOIGHT, B. (1999). Magma flow instability and cyclic activity at Soufriere Hills volcano, Montserrat, British west indies. *Science*, **283**, 1138–1142. [23](#)
- [119] VONA, A., ROMANO, C., DINGWELL, D.B. & GIORDANO, D. (2011). The rheology of crystal-bearing basaltic magmas from Stromboli and Etna. *Geochimica et Cosmochimica Acta*, **75**, 3214–3236. [15](#), [82](#), [126](#)
- [120] WATANABE, H., OKUBO, S., SAKASHITA, S. & MAEKAWA, T. (1998). Drain-back process of basaltic magma in the summit conduit detected by microgravity observation at Izu-Oshima volcano, Japan. *Geophysical Research Letters*, **25**, 2865–2868. [110](#), [125](#)

- [121] WATERS, N.D. & KEELEY, A.M. (1987). Start-up of an elastico-viscous liquid draining from a vertical surface. *Journal of Non-Newtonian Fluid Mechanics*, **22**, 325–334. [33](#), [37](#)
- [122] YAMAMOTO, E., KUMAGAI, T., SHIMADA, S. & FUKUYAMA, E. (1988). Crustal tilt movements associated with the 1986–1987 volcanic activities of Izu-Oshima Volcano. *Bull. Volcanol. Soc. Japan.*, **33**, S170–S178. [95](#), [110](#)
- [123] YAMAOKA, K., WATANABE, H. & SAKASHITA, S. (1988). Seismicity during the 1986 eruption of Izu-Oshima Volcano. *Bull. Volcanol. Soc. Japan.*, **33**, S91–S101. [xi](#), [xii](#), [87](#), [94](#), [95](#), [97](#), [98](#), [101](#)
- [124] YAMASATO, H., CHUREI, M., SEINO, M. & ANDO, K. (1988). Behavior of volcanic tremors during the eruptions of Izu-Oshima Volcano. *Bull. Volcanol. Soc. Japan.*, **33**, S120–S127. [86](#), [90](#)
- [125] ZACCONE, A., GENTILI, D., WU, H., MORBIDELLI, M. & GADO, E.D. (2011). Shear-driven solidification of dilute colloidal suspensions. *Physical Review Letters*, **106**, 138301. [126](#)
- [126] ZUCCARELLO, L., BURTON, M.R., SACCOROTTI, G., BEAN, C.J. & PATANÈ, D. (2013). The coupling between very long period seismic events, volcanic tremor, and degassing rates at Mount Etna volcano. *Journal of Geophysical Research: Solid Earth*, **118**, 4910–4921. [112](#)